Design and characterization of subwavelength grating (SWG) engineered silicon photonics devices fabricated by immersion lithography

Warren Kut King Kan

THÈSE DE DOCTORAT

NNT : 2024UPAST099

université PARIS-SACLAY

Design and characterization of subwavelength grating (SWG) engineered silicon photonics devices fabricated by immersion lithography

Conception et caractérisation de composants photoniques sur silicium, nano-structurés à échelle sub-longueur d'onde, fabriqués par lithographie à immersion

Thèse de doctorat de l'université Paris-Saclay

École doctorale n° 575 : Electrical, Optical, Bio-physics and Engineering (EOBE)
Spécialité de doctorat : Electronique, Photonique et Micro-Nanotechnologies
Graduate School : Sciences de l'ingénierie et des systèmes
Référent : Faculté des sciences d'Orsay

Thèse préparée dans les unités de recherche de l'**Université Paris-Saclay, CNRS, Centre de Nanosciences et de Nanotechnologies, 91120 Palaiseau, France** et du **Commissariat à l'énergie atomique et aux énergies alternatives, 38054, Grenoble** sous la direction de **Carlos ALONSO-RAMOS**, chargé de recherche, le co-encadrement de **Daivid FOWLER**, ingénieur-chercheur au CEA-LETI

Thèse soutenue à Paris-Saclay, le 09 octobre 2024, par

Warren KUT KING KAN

Composition du Jury

Membres du jury avec voix délibérative

Christian SEASSAL Ecole Centrale de Lyon	Président
Gilles RENVERSEZ Université d'Aix-Marseille	Rapporteur & Examinateur
Gonzalo WANGÜEMERT-PÉREZ Université de Málaga	Rapporteur & Examinateur
Daniel BENEDIKOVIC Université de Zilina	Examinateur

université PARIS-SACLAY
ÉCOLE DOCTORALE
Physique et ingénierie : Electrons, Photons, Sciences du vivant (EOBE)

Titre : Conception et caractérisation de composants photoniques sur silicium, nano-structurés à échelle sub-longueur d'onde, fabriqués par lithographie à immersion

Mots clés : Métamatériaux à base de réseaux sub-longueur d'onde, lithographie à immersion en ultraviolet profond, correction optique de proximité, interféromètre multi-mode, réseaux de couplage, antennes optiques à réseau de phases

Résumé : La technologie photonique sur silicium s'appuie sur les procédés matures de fabrication de l'industrie du semi-conducteur pour produire des composants opto-électroniques à échelle industrielle. Les métamatériaux à base de réseaux sub-longueur d'onde permettent de contrôler le confinement du mode et la dispersion, et ont ainsi été implémentés pour démontrer des performances de pointe de composants photoniques intégrés.

Les effets de diffraction et de réflexions sont supprimés dans les matériaux sub-longueur d'onde. Leurs dimensions sont petites et sont environ de 100 nm. Jusqu'à présent, la majorité des composants sub-longueur d'onde ont été fabriqués par lithographie électronique. Or, cette technique n'est pas compatible avec une production à large échelle. Aujourd'hui, la lithographie à immersion se déploie dans les fonderies photoniques sur silicium. Elle permet de définir des dimensions aussi petites que 70 nm, avec un modèle de correction d'effets optiques de proximité.

Le but principal de cette thèse est d'étudier la faisabilité de l'utilisation de la lithographie à immersion avec la correction d'effets optiques de proximité pour la fabrication de composants photoniques sub-longueur d'onde de pointe. Ces composants ont été développés sur des plaques de 300 mm de diamètre au CEA-Leti. Trois composants ont été étudiés, chacun avec une spécificité technologique : i) un diviseur de puissance avec une seule étape de gravure complète, ii) un réseau de couplage puce-fibre alternant des gravures partielles et complètes, et iii) une matrice d'antennes optiques, couvrant une large surface, avec une étape de gravure partielle.

Le diviseur de puissance est constitué d'un coupleur par interférométrie multi-mode (MMI) avec des réseaux sub-longueur d'onde pour contrôler la dispersion des modes optiques et ainsi pour obtenir une très large bande passante spectrale, qui a été mesurée expérimentalement à 350 nm, et qui en bon accord avec les simulations. La bande passante d'un MMI conventionnel sans structures sub-longueur d'onde n'est que de 100 nm environ.

Le réseau de couplage puce-fibre s'appuie sur une géométrie en forme de « L », avec des structures sub-longueur d'onde gravés partiellement et complètement, pour augmenter l'efficacité de couplage. Celle-ci a été mesurée à -1.70 dB (68 %) à une longueur d'onde de 1550 nm et représente la meilleure performance pour une telle structure complexe, utilisant une technologie autre que la lithographie électronique. Néanmoins, la valeur mesurée est inférieure à la valeur simulée de -0.80 dB (83 %). Une des raisons principales de cette performance limitée est la sensibilité de cette structure aux erreurs d'alignement entre les deux étapes de gravure pendant la fabrication.

L'antenne optique est constituée de structures sub-longueur d'onde partiellement gravées pour obtenir une grande surface d'émission de 48 µm×48 µm, réduisant ainsi la divergence du faisceau. Cette antenne a été implémentée comme antenne unitaire dans une matrice 4×4 à réseau phasé avec un pas de 90 µm×90 µm. A une longueur d'onde de 1550 nm, le faisceau émis par l'antenne unitaire a une divergence à mi-hauteur mesurée de 1.40° et celui émis par la matrice d'antennes a une divergence à mi-hauteur de 0.25°. Ces valeurs sont en accord avec les valeurs simulées. Ces résultats servent comme preuve de concept de l'implémentation d'une telle antenne dans une matrice à réseau phasé.

En résumé, les résultats de cette thèse illustrent le grand potentiel de la lithographie à immersion avec la correction d'effets optiques de proximité pour la fabrication de composants photoniques sub-longueur d'onde, ouvrant ainsi la voie pour la commercialisation de ces derniers.

ÉCOLE DOCTORALE
Physique et ingénierie : Electrons, Photons, Sciences du vivant (EOBE)

Title: Design and characterization of subwavelength grating (SWG) engineered silicon photonics devices, fabricated by immersion lithography

Keywords: Subwavelength grating metamaterials, immersion deep ultra-violet (DUV) lithography, optical proximity correction (OPC), multi-mode interferometer (MMI), grating couplers, optical phased array (OPA)

Abstract: Silicon photonics technology leverages the mature fabrication processes of the semi-conductor industry for the large-volume production of opto-electronic devices. Subwavelength grating (SWG) metamaterials enable advanced engineering of mode confinement and dispersion, that have been used to demonstrate state-of-the-art performance of integrated photonic devices.

SWGs generally require minimum feature sizes as small as a 100 nm to suppress reflection and diffraction effects. Hitherto, most reported SWG-based devices have been fabricated using electron beam lithography. However, this technique is not compatible with large volume fabrication, hampering the commercial adoption of SWG-based photonic devices. Currently, immersion lithography is being deployed in silicon photonic foundries, enabling the patterning of features of only 70 nm, when used in conjunction with optical proximity correction (OPC) models.

The main goal of this PhD is to study the feasibility of immersion lithography and OPC for the realization of high-performance SWG devices. The SWG devices developed here have been fabricated using the OPC models and 300 mm SOI wafer technology at CEA-Leti. Three devices have been considered as case studies, each with a specific technological challenge: i) a power splitter requiring a single full etch step, ii) a fiber-chip grating coupler interleaving full and shallow etch steps, and iii) an optical antenna array covering a large surface area with a shallow etch step.

The power splitter is implemented using a SWG-engineered multi-mode interferometer (MMI) coupler. The SWG is used to control the dispersion of the optical modes to achieve an ultrawide operating spectral bandwidth. This device experimentally showed state-of-the-art bandwidth of 350 nm, in good agreement with simulations. Note that the bandwidth of a conventional MMI without SWG is around 100 nm.

The fiber-chip coupler relies on an L-shaped geometry with SWG in full and shallow etch steps to maximize the field radiated towards the fiber. The measured coupling efficiency, of - 1.70 dB (68 %) at a wavelength of 1550 nm, is the highest value reported for an L-shaped coupler fabricated without electron-beam lithography. Still, this value differs from the calculated efficiency of -0.80 dB (83 %), and compares to experimental values achieved with fiber-chip grating couplers without SWG (~ -1.50 dB). One of the main reasons for the limited experimental performance is the strong sensitivity of the structure to errors in the alignment between the full and shallow etch steps.

The optical antenna uses shallowly etched SWG teeth to minimize the grating strength, allowing the implementation of a large area emission aperture, of 48 × 48 µm, which is required to minimize the beam divergence. A two-dimensional (2D) optical phased array (OPA) with an antenna pitch of 90 µm × 90 µm, comprising 16 antennas was designed and fabricated. The SWG-based unitary antenna has a measured full width at half maximum divergence of 1.40° at a wavelength of 1550 nm, while the beam emitted from the phased array has a divergence of 0.25°, both in very good agreement with expected values. These results serve as a good proof-of-concept demonstration of this novel antenna architecture.

In summary, the results shown in this PhD illustrate the great potential of immersion lithography and OPC for harnessing SWG-engineering, paving the way for their commercial adoption. Devices with full or shallow etch steps exhibited excellent performance close to that predicted by simulations. The fiber-chip grating couplers deviated from expected results, probably due to the tight fabrication tolerances associated with the combination of full and shallow etch steps.

ACKNOWLEDGEMENTS (REMERCIEMENTS)

Cette thèse de doctorat fut une expérience très enrichissante, tant sur le plan professionnel que sur le plan personnel. J'ai eu la chance d'avoir pu rencontrer et collaborer avec des personnes bienveillantes et motivées.

Je souhaite remercier Daivid FOWLER et Carlos ALONSO-RAMOS, qui m'ont bien encadré pendant ces trois ans et demi. Merci beaucoup pour votre aide, vos conseils, votre bonne humeur et votre bon humour ! Je souhaite aussi remercier Cécilia DUPRÉ, qui a m'a encadré pendant la première année et qui m'a encouragé à écrire un rapport bibliographique en début de thèse. J'ai beaucoup appris de toi.

Je remercie aussi Karim HASSAN et Bertrand SZELAG, chef et ex-chef du LIPS, pour leur soutien pendant la thèse. Merci aussi à Sylvain et à Léopold pour vos conseils en design et caractérisation d'OPA. Merci à l'équipe filière pour votre dévouement à EYELIT. Je sais, ce n'est pas facile. Merci en particulier à Stéphanie, Laeticia et à Jonathan FT (Est-ce que tu viens pour les vacances ?) de m'avoir accompagné en salle blanche pour faire des belles images SEM. Merci aussi à Quentin pour le suivi de NPG1 et à Stéphanie pour le suivi de 3PH3. Merci à l'équipe caractérisation, notamment Philippe, Karen et André de m'avoir aidé pendant mes manips. Merci Imène aussi de ton précieux coup de main pendant les mesures ! J'espère que la taxe GROSSE rapporte toujours !

Je souhaite remercier aussi les doctorants, post-doctorants et stagiaires du LIPS avec qui j'ai passé de très bons moments. Merci à Linda, Sara, Anna-Lara et Giuliano de m'avoir appris quelques mots de base en italien qui me se seront très utiles quand j'irai en Italie. Merci aux GNOCCHOS, Mattéo, Valentin et Clément pour leur bonne ambiance. Merci à Baptiste, le pro de python, Jonathan quantique et Pierre pour votre soutien et discussions. Je souhaite également remercier les thésards ST, Cyrille, Josserand, Louise-Eugénie, et Guillaume. Je me souviendrai de nos sorties ensemble comme « Chez Emile », de nos karaokés et de nos randos.

Je remercie toute l'équipe du LIPS de façon générale pour leur soutien, et pour les nombreuses viennoiseries et galettes des rois. J'espère que les équipements (probers, PCs et SEM) vont bien depuis mon départ. La garantie Warren c'est 10 ans normalement…

Je remercie également l'équipe OPC, notamment Estelle et Jean-Baptiste et l'équipe CDSEM, notamment Tristan, Haidar et Cyril. Je remercie aussi l'équipe communication du CEA-Leti, notamment Hélène et Kim, avec qui j'ai pu réaliser une vidéo « PhD Generation », disponible sur Youtube.

Je remercie également l'équipe MINAPHOT, au C2N, avec qui j'ai passé ces derniers mois pendant la rédaction. Merci pour les nombreux pots. Je me souviendrai de notre sortie à l'Ile d'Oléron, de nos parties de babyfoot et de beach volley. Je souhaite remercier Sara, David <3, Paula pour leur aide dans la mesure des MMIs SWG et aussi Jianhao et David Spanish pour leur aide quand je commençais à faire des mesures de réseaux de couplage. Merci à Natnicha aussi pour le dépôt de métal sur les OPAs. Merci à Andrès et à Mouad, mes fameux co-bureaux de l'ambiance.

Je souhaite aussi remercier IPCEI/Nano 2022 pour le financement de la thèse. Merci au CEA-Leti et au C2N pour l'accueil.

Finalement je souhaite remercier ma famille, à qui je dédie cette thèse. Merci de votre soutien et de vos encouragements.

FRENCH SUMMARY (RESUME EN FRANÇAIS)

La photonique sur silicium permet l'intégration de fonctions optiques sur une puce en silicium. La fabrication des dispositifs exploite les procédés CMOS, qui sont des procédés matures souvent utilisés dans la fabrication de semi-conducteur. Les applications de la photonique sur silicium sont diverses et incluent les télécommunications, le LiDAR pour l'automobile, l'optique quantique entre autres.

Cette thèse présente les travaux effectués sur des dispositifs photoniques sur silicium, nano-structurés à échelle sub-longueur d'onde, et fabriqués par lithographie à immersion avec un modèle de correction d'effets optiques de proximité. Cette thèse a été faite en partenariat avec le CEA-LETI, à Grenoble et le C2N, à Paris-Saclay.

LES STRUCTURES SUB-LONGUEUR D'ONDE (SWG)

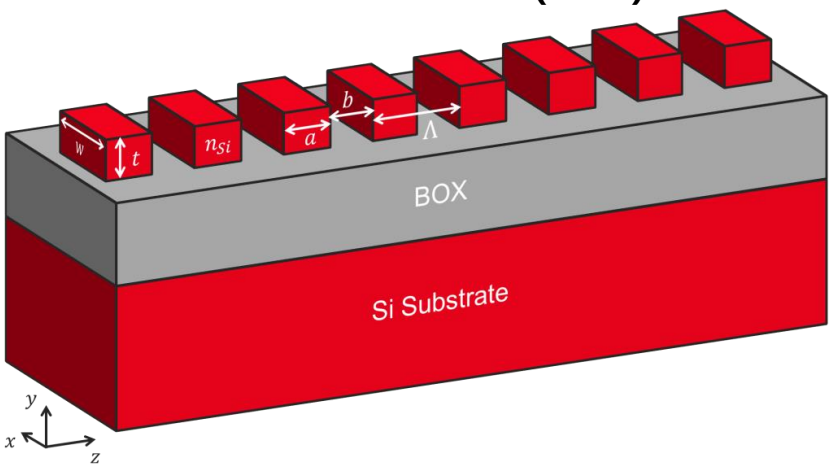

Figure 1: Guide d'onde silicium (Si) périodique, structuré avec un pas Λ. Le guide est encapsulé de silice (SiO_2), qui n'est montré dans la figure pour des raisons de clarté. Dans le régime sub-longueur d'onde, $\Lambda \ll \lambda$, où λ est la longueur d'onde.

La Figure 1 montre un guide d'onde silicium (Si) structuré de façon périodique. Le guide est encapsulé de silice (SiO_2). Le pas du réseau est Λ. La longueur d'onde de la lumière est λ et on considère que l'axe de propagation est selon l'axe z. L'indice effectif du mode supporté par le guide périodique est n_{eff}. On considère λ = 1550 nm (longueur d'onde télécom usuelle). A cette longueur d'onde, l'indice de réfraction du Si est de n_{Si} = 3.48, est celui du SiO_2 est de n_{SiO_2} = 1.44. Une valeur

approximative de l'indice effectif est n_{eff} ~ 2.5. La longueur d'onde de Bragg est définie comme $\lambda_B = \lambda/2n_{eff}$ et vaut approximativement λ_B ~ 300 nm avec les valeurs considérées. Le comportement de ce réseau peut être décrit selon trois régimes différents, selon les valeurs de Λ devant λ_B.

1. $\boldsymbol{\Lambda > \lambda_B}$ **: régime de diffraction**. Le mode s'échappe graduellement principalement vers le haut et vers le bas. Ce régime diffractif est exploité dans les réseaux de couplage pour coupler de la lumière entre un guide d'onde sur une puce et une fibre optique externe placée presque verticalement sur la surface de la puce.
2. $\boldsymbol{\Lambda = \lambda_B}$ **: régime de réflexion** (aussi appelé régime de Bragg). Le réseau se comporte comme un miroir et réfléchi le mode incident. Ce régime réflectif est exploité dans les filtres de Bragg et dans les cristaux photoniques.
3. $\boldsymbol{\Lambda < \lambda_B}$ **: régime sub-longueur d'onde**. Les effets de diffraction et de réflexions sont supprimés. La lumière se propage dans le réseau sub-longueur d'onde (abrévié SWG pour subwavelength grating en anglais) qui se comporte comme un matériau anisotrope homogène, avec un indice de réfraction équivalent, n_{SWG} . Cet indice équivalent dépend de la direction de propagation et de l'axe de polarisation de la lumière. n_{SWG} peut être égal à l'indice ordinaire, $n_{\parallel}$, ou à l'indice extraordinaire, $n_{\perp}$ du matériau anisotrope. En changeant les paramètres géométriques du réseau (voir les longueurs a, b et Λ sur la Figure 1), n_{SWG} peut être contrôlé, ce qui donne plus de degrés de liberté dans la conception de composants photoniques.

Grâce à ces nouveaux degrés de liberté, les SWG ont amélioré la performance de dispositifs photoniques sur silicium. Certains exemples sont l'amélioration de l'efficacité de couplage de coupleurs par la tranche et de réseaux de couplage en surface, l'augmentation de la bande passante spectrale de coupleurs MMI, ou le contrôle de la polarisation. Néanmoins, les dimensions des SWG sont très petites, ~ 100 nm aux longueurs d'onde et ont été majoritairement fabriqués par lithographie électronique. Cet outil permet de définir de très faibles dimensions, ~ 30 nm, mais a un temps d'écriture très long. Il

est ainsi adapté pour des démonstrations en laboratoire, mais ne peut pas être utilisé pour une production industrielle. Or, la production industrielle de dispositifs SWG pourrait se faire aujourd'hui en utilisant la lithographie à immersion, qui est un outil récent et qui commence à se déployer dans les fonderies de photoniques sur silicium. En effet, elle peut définir de faibles dimensions, ~ 70 nm, à échelle industrielle.

LA LITHOGRAPHIE A IMMERSION ET LA CORRECTION D'EFFETS OPTIQUES DE PROXIMITE (OPC)

La résolution, R, d'un système de lithographie est la taille du plus petit motif que le système peut définir. Elle est donnée par l'Equation (1).

$$R = k_1 \frac{\lambda}{NA} = k_1 \frac{\lambda}{n \sin\theta} \qquad \text{Equation (1)}$$

où λ est la longueur d'onde d'imagerie, k_1 est un facteur lié au procédés de fabrication, NA est l'ouverture numérique (numerical aperture en anglais), n est l'indice de réfraction du milieu entre le système d'imagerie et la résine sur le wafer, θ est la demi-ouverture angulaire du système d'imagerie. A noter que $NA = n \sin\theta$.

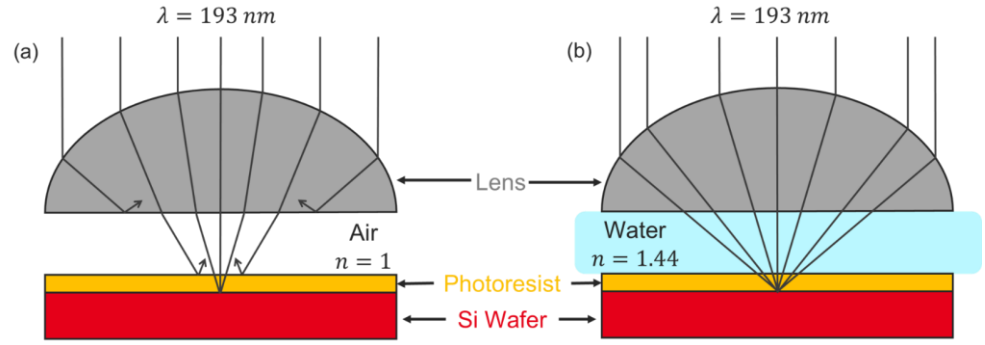

Figure 2: (a) Lithographie dite « sèche ». (b) Lithographie dite « à immersion ». En rajoutant de l'eau entre le système d'imagerie et la surface de la résine sur le wafer, la résolution, R, est améliorée. La lithographie sèche a une résolution de ~ 110 nm tandis que la lithographie à immersion a une résolution de ~ 70 nm.

La Figure 2 illustre les principes de la lithographie à immersion. En rajoutant de l'eau, qui a un indice de réfraction plus fort que l'air (n = 1.44 pour l'eau et n = 1 pour l'air à la longueur d'onde d'imagerie λ = 193 nm), entre le système d'imagerie et la résine sur le wafer, l'ouverture numérique du système, NA, est augmentée, ce qui permet

d'améliorer la résolution, R. Ainsi la lithographie sèche possède une résolution de ~ 110 nm tandis que la lithographie à immersion possède une résolution plus fine de ~ 70 nm pour la fabrication de dispositifs photonique sur silicium.

Néanmoins, pendant l'étape de lithographie, des effets optiques de proximité sont présents, ce qui rend les motifs fabriqués différents des motifs voulus en conception, en termes de formes et de tailles. Ainsi, un algorithme de correction d'effets optiques de proximité (abrévié OPC pour optical proximity correction en anglais) est appliqué. L'OPC change les formes nominales des motifs sur le masque de lithographie pour compenser les effets de proximité pendant l'étape de lithographie, pour que les motifs fabriqués correspondent au mieux aux motifs voulus. La Figure 3(a) montre un exemple d'OPC sur des motifs SWG, dont la plus petite taille est de 70 nm. La Figure 3(b) montre les motifs correspondant après fabrication. Ainsi, l'OPC est essentielle pour pouvoir pleinement profiter de la très haute résolution que peut offrir la lithographie à immersion.

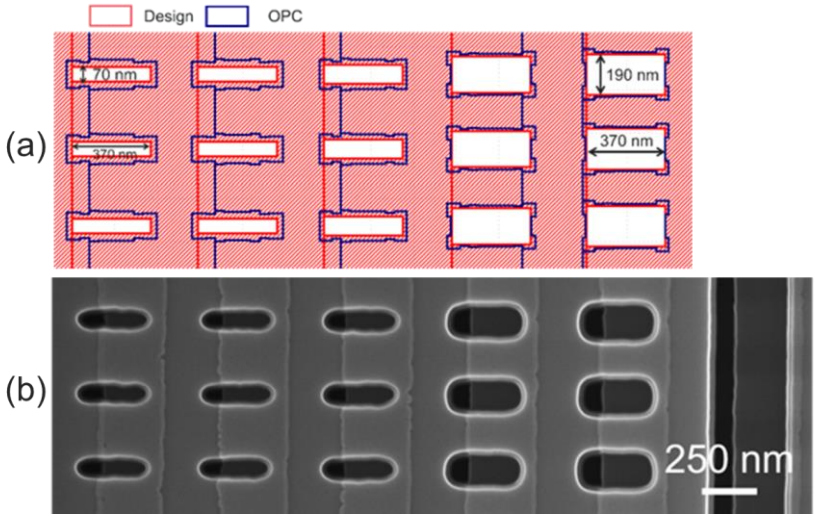

Figure 3: (a) L'OPC change les motifs présents sur le masque de lithographie pour compenser les effets optiques de proximité. (b) Les motifs fabriqués respectent au mieux les motifs voulus en conception.

OBJECTIFS DE LA THESE

Le but principal de cette thèse a été de concevoir et de caractériser des dispositifs photoniques sur silicium sub-longueur d'onde, fabriqués par lithographie et l'OPC sur la ligne pilote du CEA-LETI. Ainsi, trois

différents dispositifs ont été étudiés : un coupleur MMI SWG, un réseau de couplage en forme de L basé sur des SWG, et une antenne optique SWG pour des réseaux phasés.

COUPLEUR MMI SWG AVEC UNE LARGE BANDE PASSANTE

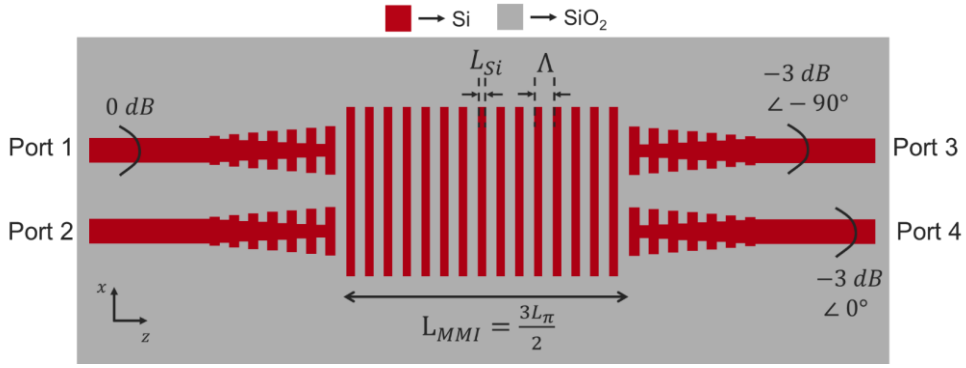

Figure 4: Coupleur MMI sub-longueur d'onde, Λ=190 nm, L_{Si}= 95 nm

La Figure 4 montre un coupleur par interférométrie multimode (MMI) 2x2, avec 2 entrées et 2 sorties, avec des structures SWG. Il sert de coupleur à 3-dB et consiste principalement à diviser la puissance du faisceau optique d'entrée injecté du port 1 par deux, ce qui donne une transmission de 50 % (-3 dB) dans les ports de sortie 3 et 4. Il y a aussi un déphasage de 90° entre les faisceaux dans les ports 3 et 4. Le coupleur MMI fonctionne de la façon suivante. Le faisceau d'entrée (du port 1) vient exciter des modes d'ordres supérieures dans la région multimode, qui est plus large. Les modes excités interférent entre eux, formant des images le long du MMI de façon périodique. Des images doubles, mais contenant 50 % de la puissance d'entrée sont formées à une distance $L = 3L_\pi/2$, où L_π est la longueur de battement du MMI.

En structurant le coupleur MMI à échelle sub-longueur d'onde, L_π, peut être rendue moins dépendante de la longueur d'onde, ce qui permet d'augmenter la bande passante du MMI car les images seront formées à la même position sur une plus grande gamme spectrale.

Les figures de mérites du MMI sont définies comme suit. Les pertes du MMI sont égales à la somme des transmissions dans les ports 3 et 4, en dB. Le déséquilibre du MMI est égal à la valeur absolue du rapport des transmissions des ports 3 et 4, en dB. Les erreurs de phases du MMI sont égal à l'écart du déphasage entre les ports 3 et 4, par rapport au déphasage idéal de 90°.

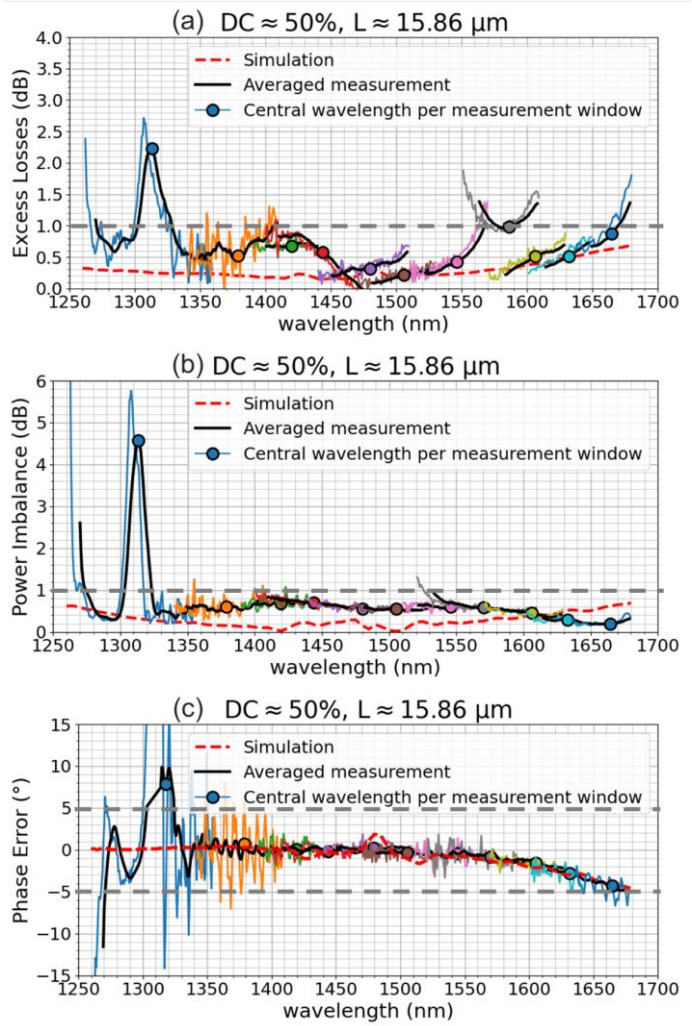

Figure 5: Figures de mérite du MMI SWG. (a) Pertes. (b) Déséquilibre. (c) Erreurs de phase. Les mesures ont été faites sur plusieurs bandes spectrales puis été attachées ensemble, et ont été moyennées, donnant la courbe noire. Les valeurs données en simulation sont indiquées par la courbe en pointillés rouges.

La Figure 5 montre les figures de mérites du MMI mesurées et simulées. Le mode du guide d'entrée était le mode transverse électrique (TE) fondamental. Des pertes < 1 dB, un déséquilibre < 1 dB et des erreurs de phase < ± 5° ont été mesurés sur une très large gamme de longueur d'onde de λ =1330 – 1680 nm, conférant au MMI une très large bande passante de $\Delta\lambda$ = 350 nm. Ces résultats sont comparables à ceux obtenus par un MMI SWG similaire fabriqué par lithographie électronique, démontrant le potentiel de ce dispositif à être fabriqué à échelle industrielle par lithographie à immersion avec un modèle OPC. Néanmoins, des effets de résonance ont été observés pour des

longueurs d'onde autour de 1300 nm. Ceux-ci limitent la bande passante, et n'étaient pas prévus par la simulation. L'origine de ces effets doit être investiguée. La bande passante du MMI SWG de 350 nm reste cependant supérieure à celle d'un MMI conventionnel, sans SWG, qui a une bande passante d'environ de 100 nm.

RESEAUX DE COUPLAGE EN FORME DE L A BASE DE SWG A FORTE EFFICACITE DE COUPLAGE

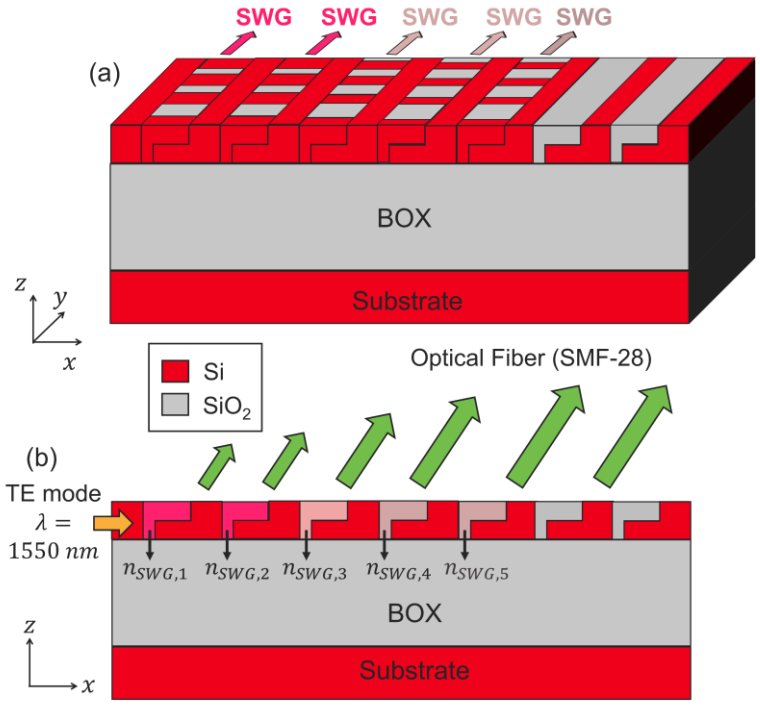

Figure 6: (a) Vue 3D du réseau de couplage en forme de L et SWG (qui sont selon l'axe des y). (b) Coupe 2D du réseau de couplage. Les SWG ont des indices de réfractions équivalents $n_{SWG,i}$ où i est l'indice de la période respective.

La Figure 6 montre des schémas du réseau de couplage en forme de L avec des SWG. Ce dispositif sert à coupler de la lumière entre un guide d'onde sur la puce photonique et une fibre optique externe, placée à un angle de 11.5° par rapport à la verticale au-dessus de la surface de la puce. Son efficacité de couplage, η_{CE}, est définie comme étant le rapport de la puissance optique couplée dans la fibre à la puissance incidente du guide d'onde. L'efficacité de couplage est aussi égale à $\eta_{CE} = \eta_{up} \times \eta_{OL}$, où η_{up} est la transmission de puissance optique vers le haut, en direction de la fibre, et η_{OL} est le recouvrement modal entre le mode émis par le réseau et le mode Gaussien de la fibre qui a un

diamètre de ~ 10.4 µm à une longueur d'onde de λ = 1550 nm. Ainsi, afin de maximiser η_{CE}, le réseau est blazé en formes de L, pour le rendre plus directionnel en diffractant plus de lumière vers le haut que vers le bas, et contiennent des SWG pour réduire les réflexions et pour apodiser le réseau. Apodiser un réseau consiste à adapter la force du réseau pour augmenter le recouvrement modal par rapport à un réseau uniforme, dont la force du réseau est constante. La simulation en 3D du réseau prédisait, à une longueur d'onde λ = 1550 nm et pour le mode fondamental transverse électrique (TE) dans le guide d'entrée, η_{up}= 0.96, η_{OL} = 0.87 et donc, η_{CE} = 0.84 = -0.80 dB.

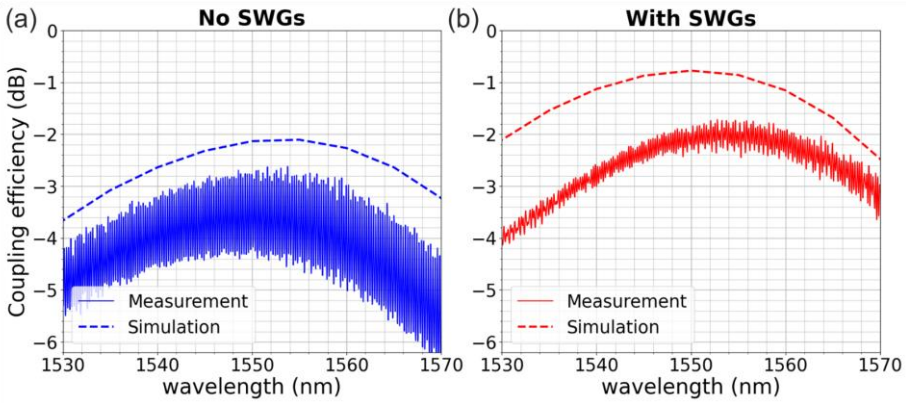

Figure 7: Efficacité de couplage mesurée et simulée sur des réseaux en formes de L : (a) uniformes et sans SWG (b) apodisés avec des SWG.

La Figure 7 montre les efficacités de couplage mesurées et simulées de réseaux de couplage en forme de L uniformes sans SWG et apodisés des SWG. Avec des SWG, l'efficacité mesurée est meilleure. $n_{CE}(avec\ SWG)$ = -1.90 dB alors que $n_{CE}(sans\ SWG)$ = -2.70 dB à la longueur d'onde pic λ ~ 1550 nm. Ceci montre l'importance des SWG pour augmenter l'efficacité de couplage. Cependant, l'efficacité mesurée avec des SWG reste inférieure à celle qui a été simulée η_{CE} = -0.80 dB. Ceci montre que même si le réseau en forme de L avec des SWG peut potentiellement avoir une forte efficacité de couplage de < -1 dB, il reste tout de même complexe à fabriquer. Son efficacité est comparable à des réseaux de couplage plus simple à fabriquer (à un niveau de gravure partielle avec des SWG). Cependant, il serait possible de continuer à optimiser le réseau, en prenant en compte et en compensant des effets de fabrication que l'OPC ne peut pas corriger dans la conception, pour augmenter l'efficacité de couplage.

ANTENNE OPTIQUE DE RESEAU PHASE A BASE DE SWG A FAIBLE DIVERGENCE CONÇUE POUR DES COMMUNICATIONS OPTIQUES EN ESPACE LIBRE

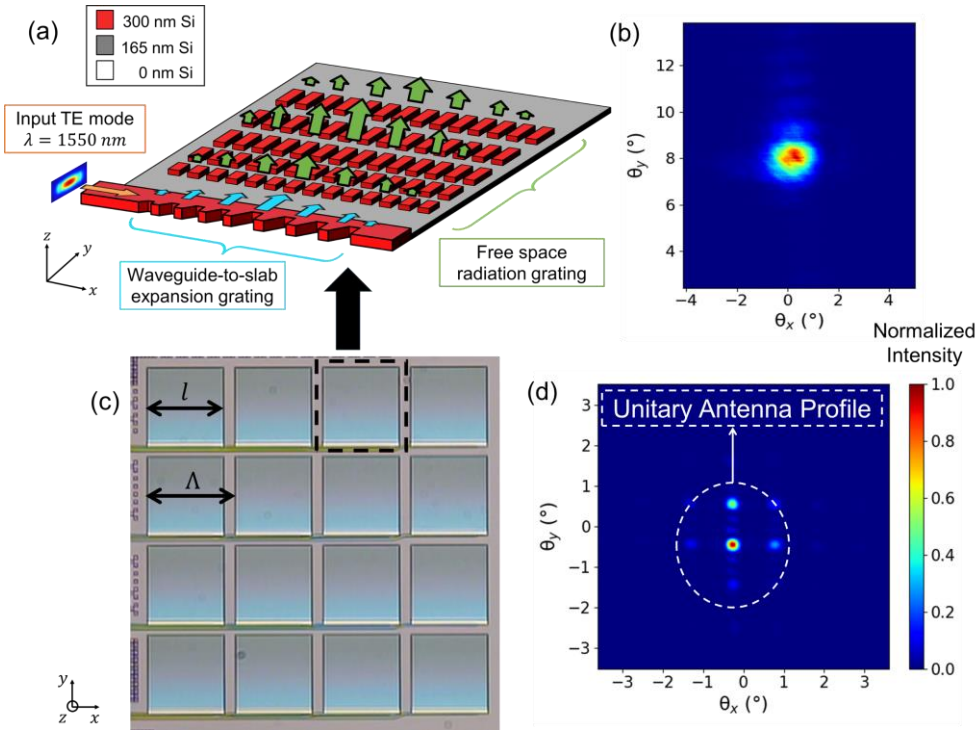

Figure 8: (a) Antenne unitaire d'un réseau phasé (abrévié OPA pour optical phased array en anglais) à base de SWG. (b) Champ lointain de l'antenne unitaire mesuré. (c) Réseau d'antennes de l'OPA, l est la longueur de l'antenne, Λ est le pas du réseau. (d) Champ lointain de l'OPA, calibré en phase, mesuré.

La Figure 8(a) montre un schéma de l'antenne unitaire étudié qui sert à émettre un faisceau Gaussien dans l'espace libre avec une faible divergence à partir du mode fondamental transverse électrique (TE) du guide d'entrée. Il est constitué de deux réseaux de diffraction indépendants. Le premier est constitué de corrugations quasi-triangulaires. Il sert d'extenseur de mode et diffracte la lumière dans le plan de la puce (plan x-y) pour créer un mode Gaussien se propageant selon l'axe y (voir les flèches bleus) avec un large diamètre (~ 48 µm) selon l'axe des x. L'extenseur de mode permet de donner une configuration compacte à l'antenne car le deuxième réseau peut être placé à une distance très proche du guide d'entrée. Le deuxième réseau sert à diffracter le mode produit par le premier vers l'espace libre (voir les flèches vertes). Le champ proche émis par l'antenne est quasi-Gaussien, selon les deux axes x et y, avec un même diamètre

~ 48 µm. Le deuxième réseau est fait de blocs SWG selon l'axe des x, qui permettent de réduire le contraste d'indice par rapport à des blocs en Si pure. Le pouvoir de diffraction est réduit, ce qui permet de diffracter le mode sur une plus grande distance. Comme la divergence angulaire en champ lointain est inversement proportionnelle au diamètre du champ proche, la divergence angulaire du faisceau est réduite grâce aux SWG. Les simulations en 3D prévoient une divergence angulaire à mi-hauteur de $\Delta\theta_{FWHM}$ ~ 1.40° à une longueur d'onde λ = 1550 nm. La Figure 8(b) montre le champ lointain imagé expérimentalement à λ = 1550 nm. La divergence mesurée selon les axes x et y et correspondent aux valeurs simulées. Cette antenne a été implémentée dans une matrice 4x4 (voir la Figure 8(c)) d'antennes optiques à réseaux phasés (abrévié OPA pour optical phased array en anglais). Le taux de remplissage de l'OPA, l/Λ, où l est la taille de l'antenne, et Λ est le pas du réseau, a pu être maximisé grâce à la configuration compacte de l'antenne. Ce fort taux de remplissage permet d'atténuer l'intensité des lobes secondaires de l'OPA, qui ne sont pas souvent utilisés pour des applications de communications en espace libre. La Figure 8(d)) montre le champ lointain de l'OPA, à λ = 1550 nm, après une calibration de phase pour maximiser l'intensité du lobe principal. Un rapport ~ -5 dB (30 %) a été mesuré entre l'intensité du lobe principal et l'intensité du lobe secondaire, démontrant une preuve de concept de l'implémentation de cette antenne dans un OPA en 2D, pour l'atténuation de l'intensité des lobes secondaires et pour l'augmentation de l'intensité du lobe principal. Néanmoins, la transmission énergétique de l'antenne vers l'espace libre, mesurée à -8 dB (15 %) à λ = 1550 nm doit être optimisée.

CONCLUSION ET PERSPECTIVES DE LA THESE

Les travaux menés dans cette thèse ont étudié le potentiel de la lithographie à immersion et un modèle OPC pour la fabrication à échelle industrielle de dispositifs photoniques sur silicium sub-longueur d'onde. Ces derniers montrent que les dispositifs sub-longueur d'onde ainsi fabriqués fonctionnent, mais que leur performance étaient légèrement moins bonnes que celles qui étaient attendues. Il faudrait donc continuer à optimiser l'OPC et/ou alors compenser en conception les effets que l'OPC ne peut pas corriger.

TABLE OF CONTENTS

LIST OF ABBREVIATIONS

2D	Two dimensional
3D	Three dimensional
APC	Angle polished fiber
ArF	Argon Fluoride
BOX	Buried oxide
CD	Critical dimension
CMOS	Complementary metal oxide semiconductor
DC	Duty cycle
DUV	Deep ultra-violet
EC	Edge coupler
EL	Excess loss
ER	Extinction ratio
EUV	Extreme ultra-violet
FDE	Finite difference eigenmode
FDTD	Finite difference time domain
FF	Fill factor
FIB	Focus ion beam
FSO	Free space optical
FSR	Free spectral range
FWHM	Full width at half maximum
GC	Grating coupler
IB	Imbalance
LiDAR	Light detection and ranging
MFD	Mode field diameter
MFS	Minimum feature size
MMI	Multi-mode interferometer
MPW	Multi-project wafer
MZI	Mach-Zehnder interferometer
NA	Numerical aperture
OPA	Optical phased array
OPC	Optical proximity correction
OPE	Optical proximity effect
OWC	Optical wireless communication
PDK	Process design kit
PE	Phase errors

PIC	Photonic integrated chip
PM	Polarization maintaining
RF	Radio frequency
SEM	Scanning electron microscope
Si	Silicon
SiO_2	Silicon Dioxide
SLL	Side lobe level
SMF	Single mode fiber
SOI	Silicon-on-insulator
SWG	Subwavelength grating
TE	Transverse electric
TM	Transverse magnetic

1 INTRODUCTION

This thesis covers the PhD work carried out on subwavelength gratings (SWGs) engineered silicon photonics devices which were fabricated using immersion lithography. This doctoral work resulted from a collaboration between the CEA-Leti in Grenoble (France), and the C2N, in Paris-Saclay (France).

This first chapter is outlined as follows. A brief overview of silicon photonics is given, followed by an overview of its fabless ecosystem, which enables the silicon photonics users with limited budgets (laboratories, small companies or start-ups) to have access to industrial or pre-industrial fabrication lines at reasonable cost. The motivations of the doctoral work are then given, followed by the general outline of the manuscript.

1.1 A BRIEF OVERVIEW OF SILICON PHOTONICS

Silicon photonics enables the on-chip integration of photonic integrated circuits (PICs) with two major advantages [1–3]. First, the high refractive index contrast of the material platform at telecom wavelengths allows for a high-density integration of optical devices. Second, silicon photonics leverages the existing complementary metal oxide semiconductor (CMOS) infrastructure and allows the large volume, low cost and robust production of optoelectronic devices.

Some examples of the silicon photonics material platforms include silicon-on-insulator (SOI) [3], silicon nitride-on-insulator (SiN) [4] and germanium-on-silicon [5]. Our work has been focused on the SOI platform (see Fig. 1.1).

The SOI platform consists of a silicon core layer, which is usually encapsulated with SiO_2, and is above an SiO_2 buried oxide (BOX) layer which is itself on a Si substrate. The Si substrate usually has no optical function and gives mechanical support.

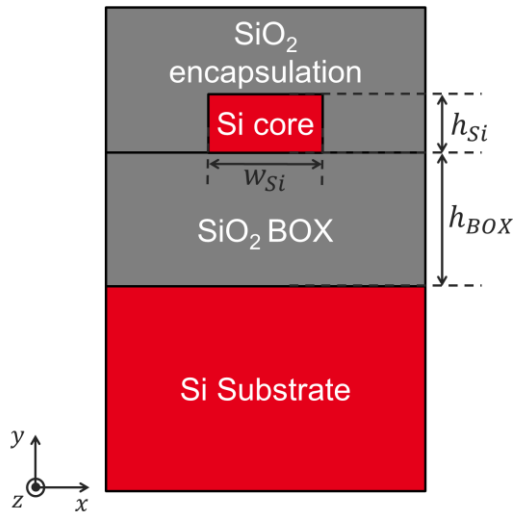

Fig. 1.1: Silicon-on-Insulator (SOI) platform. The Si waveguide is usually encapsulated with an SiO_2 cladding. The Si waveguide is above an SiO_2 buried oxide (BOX) layer, which is itself on an Si substrate.

At telecom wavelengths, $\lambda \sim 1.55$ µm, Si has a refractive index of $n_{Si} \sim 3.48$ and SiO_2 has an index of $n_{SiO_2} \sim 1.44$, giving a high refractive contrast of $\Delta n \sim 2$. Light is confined in the Si core along the x - and y - axis by total internal reflection, following similar waveguiding principles as in optical fibers. The waveguide can support single or multiple optical modes depending on its geometry. The mode is said to have transverse electric (TE) polarization if the dominant electric field component is parallel to the plane of the chip (along the x-axis) and transverse magnetic (TM) polarization if the dominant electric field component is perpendicular to the plane of the chip (along the y-axis).

The usual values for the SOI thicknesses proposed by silicon photonics fabrication facilities, referred to as silicon photonics foundries, are usually 180 nm ≤ h_{Si} ≤ 400 nm [2]. The BOX thicknesses are usually 680 nm ≤ h_{BOX} ≤ 3000 nm.

Considering the fundamental TE polarization at a wavelength $\lambda \sim 1.55$ µm, and a silicon thickness of $h_{Si} \sim 300$ nm, which is typically used at CEA-Leti, a single mode waveguide usually has a width of $w_{Si} \sim 400$ nm. Such small sub-micron dimensions result from the high index contrast $\Delta n \sim 2$ of the SOI platform. This therefore enables a high integration density of optical components on the photonic chip.

For comparison, optical fibers exhibit an index contrast at $\lambda \sim 1.55$ µm of only $\Delta n_{fiber} \sim 0.004$, with a core diameter of 10 µm.

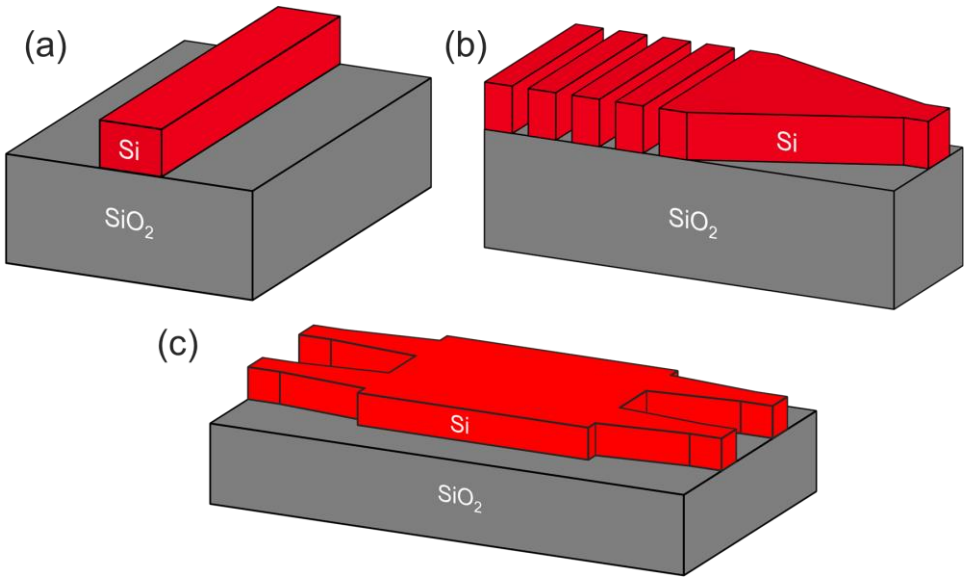

Fig. 1.2: Examples of photonic passive devices on the SOI platform. (a) Photonic waveguide which is used to guide the light. (b) Surface grating coupler which is used to couple light between the chip and an external optical fiber. (c) Multimode interferometer (MMI) coupler which is often used for power splitting and combining. The SiO_2 encapsulation and Si substrate are not shown for clarity.

The SOI platform can provide both passive and active functions. Passive components do not interact with an external electrical circuit. Some examples include optical beam propagation using waveguides (see Fig. 1.2(a)), coupling light off the chip to an external optical fiber using grating couplers (see Fig. 1.2(b)), and optical beam splitting and recombination using multimode interferometer (MMI) couplers (see Fig. 1.2(c)).

Conversely, active components interact with an external electrical circuit. Active functions include phase modulation, photodetection (usually germanium-based [6]) and light generation (through laser integration with III-V materials [7,8], as silicon is a poor light emitter due to its indirect bandgap).

In this work, only passive devices have been studied. More information about silicon photonics devices can be found in exhaustive reviews [9–16].

When assembled, the silicon photonics devices make up a photonic circuit, and provide more complex functionalities (see Fig. 1.3). For example, optical transceivers [17] convert optical signals into electrical signals (and vice-versa) to transmit and receive data (see Fig. 1.3(a)). The data in the form of electrical signals can be processed by co-integrated electronic circuits (see Fig. 1.3(b)). Another example is a beam steering photonic circuit, which can be implemented for light detection and ranging (LiDAR) applications (see Fig. 1.3(c)).

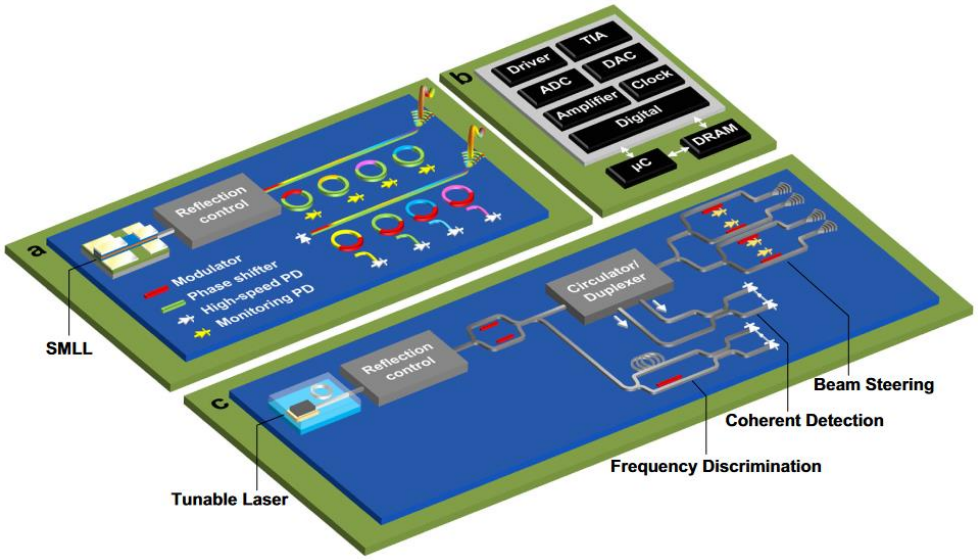

Fig. 1.3: Examples of photonic integrated circuits (PICs): (a) Optical transceiver, (b) Co-integration with electronic circuits, (c) Beam steering. Image from Shekhar et al. [1]

Fig. 1.4 shows the temporal evolution of the number of components integrated per PIC in the silicon photonics technology. The silicon photonics field started near 1985, with Soref et al. first demonstrating a phase modulator in silicon [18]. Today, the monolithic SOI platform is being deployed on a very-large-scale integration (with more than 10000 components per chip). The complexity of monolithic silicon photonic circuits is surpassing that of monolithic indium phosphide (InP). Silicon technologies based on the heterogenous integration of InP and or gallium arsenide (GaAs) platforms follow closely behind. The development of silicon photonics has been enabled by its CMOS compatibility, allowing for large volume production at low cost.

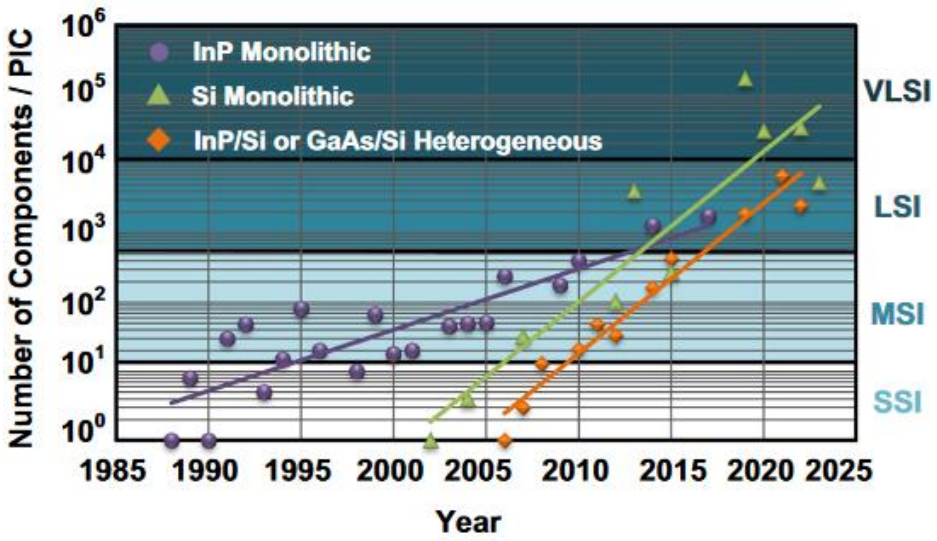

Fig. 1.4: Evolution of PIC platforms. The scale integrations range include small-scale, medium-scale, large-scale and very-large-scale integration (SSI, LSI, MSI and VLSI respectively). Image from Shekhar et al. [1].

The silicon photonics market has been mainly driven by the telecom and datacom applications, with industrial transceiver products, from companies such as Intel, Luxtera (now a subsidiary of Cisco Systems), Acacia and Lumemtum. Nowadays, the development roadmap includes new applications such as beam steering in free space [19], bio-sensing [20] and quantum computing [21].

1.2 THE SILICON PHOTONICS FABLESS ECOSYSTEM

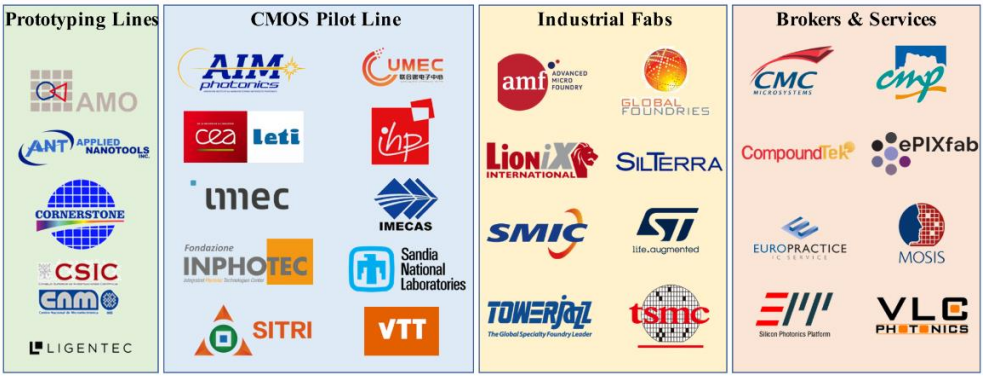

Fig. 1.5: Examples of silicon photonics foundries. Image from Siew et al. [2]

Building CMOS fabrication facilities is expensive. In the vast majority of cases, research laboratories, start-ups and small companies cannot afford to build their own. Therefore, silicon photonics foundries, which

use existing CMOS tools, provide fabrication services. These include prototyping lines, CMOS pilot lines, industrial fabs and brokers (see Fig. 1.5).

Silicon photonics foundries industrially produce silicon photonics chips on silicon wafers (see Fig. 1.6). A wafer is a silicon substrate onto which the chips have been repeatedly patterned. Today, many silicon photonics foundries are migrating from 200 mm to 300 mm diameter wafers [22–25] to be able to produce more chips and cope with the growing demand of the silicon photonics market.

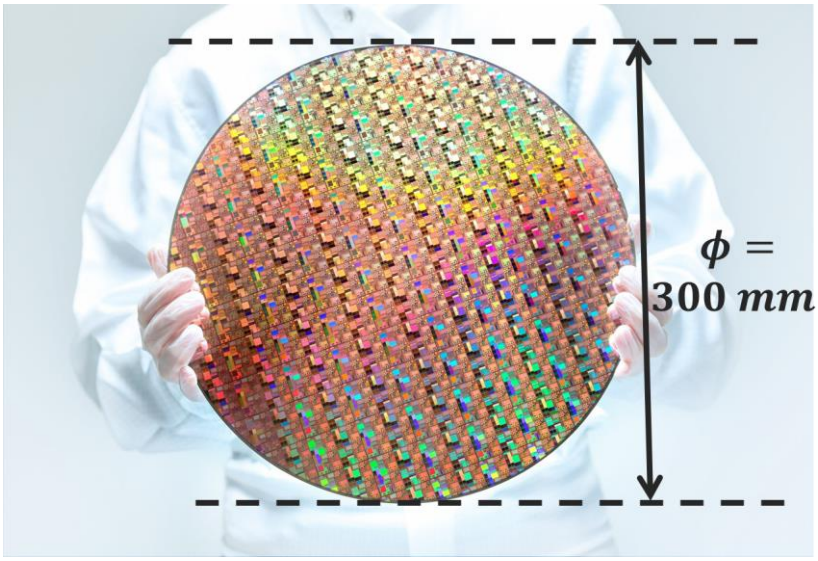

Fig. 1.6: 300 mm silicon photonic wafer

Silicon photonics foundries often propose multi-project wafer services (MPWs), allowing fabless users to access silicon photonics production lines, on small or large volumes, at reasonable costs [2,26,27]. The MPW service allows for the users to share the fabrication cost by sharing the same mask, which contains the photonic circuits to be patterned, and by using the same fabrication processes.

Foundries provide the users with process design kits (PDKs) which contain a library of standard and tested devices and circuits, design rules information and checking, and increasingly, circuit simulation tools.

Silicon photonics devices are usually designed using optical simulation software. In this doctoral work, optical simulations have been carried

out using software products from Ansys Lumerical, in particular, its finite difference time domain (FDTD) solver and its finite difference Eigenmode (FDE) solver. FDTD simulations involve solving an electromagnetic propagation problem by discretizing Maxwell equations into discrete grids of space and time. FDE simulations consists in solving for mode profiles supported by a waveguide geometry by discretizing space.

1.3 MOTIVATION OF THE DOCTORAL WORK

The optimization of the performance of SOI devices is usually limited to changing the geometry of the core Si, whose optical index is constant (n_{Si} ~ 3.48 at a wavelength λ = 1550 nm). To further expand the design space, the core Si can be periodically patterned with a so-called subwavelength grating (SWG), i.e., a grating with a period $\Lambda_{SWG} < \lambda/(2n_{eff})$, where n_{eff} is the effective index of the optical mode. For example, a typical period for the usual telecom wavelength of λ = 1550 nm is Λ_{SWG} < 300 nm, considering n_{eff} ~ 2.5. In the subwavelength regime, diffraction and reflection effects are suppressed, and the SWGs behave as metamaterials that allow refractive index engineering of the core waveguide material. This enables control over device performance parameters, such as polarization or spectral bandwidth, that are unattainable otherwise [28]. The incorporation of SWGs has allowed for improved device performance and novel device functionalities in silicon photonics.

However, the minimum feature sizes of SWGs are usually very small. For a wavelength λ = 1550 nm, the SWG period should be Λ_{SWG} < 300 nm, leading to feature sizes usually around 100 nm. Such small sizes are at the limit of most silicon photonics technologies, particularly that based on 200 mm wafers. Therefore, most reported SWG-engineered devices have been fabricated using electronic beam (e-beam) lithography, which can have a very high resolution (~ 30 nm), but is extremely slow and so, is not compatible with an industrial scale.

Immersion lithography is a more advanced and recent fabrication tool used in CMOS facilities that can define features ~ 70 nm with an optimized optical proximity correction (OPC) model, at an industrial scale. While this technology has been used in CMOS foundries for the

industry for over 10 years, it is currently being adopted by silicon photonics foundries and can potentially fabricate SWG-engineered silicon photonics devices on a large volume production.

The aim of this PhD work is to study the feasibility of immersion lithography for the realization of SWG-based silicon photonic devices. Such study, stands as an important step towards to bridging the gap between laboratory demonstrations of SWG-based devices and their large volume production. In this context, SWG-based silicon photonics devices have designed, fabricated using on the CEA-Leti pilot line, and characterized. Three different building blocks have been defined as case studies, as they imply different designs and technological challenges, namely:

- Power splitter: SWGs are used to engineer the anisotropy and dispersion of different optical modes to achieve an ultra-wideband response. Precise definition of fully etched nanometric-scale features, down to 70 nm, is required for the device operation.
- Fiber-chip grating coupler: SWGs allow the gradual modulation of the grating radiation strength along the device, while maintaining stringent phase-matching conditions, to maximize the power coupling efficiency with an optical fiber. SWGs with a minimum feature size of 70 nm have to be defined within L-shaped structures interleaving full and shallow etch steps.
- Optical antenna array: SWGs are implemented to yield a very weak grating radiation strength in an optical antenna, enabling a large aperture size, and thus minimizing the beam divergence. This antenna is implemented as a unitary antenna in a two-dimensional optical phased array for free-space optical communications. Shallowly etched diffraction gratings made of SWG-metamaterials with a minimum feature size of 100 nm have to be realized over a large area of 400 µm × 400 µm.

1.4 ORGANIZATION OF THE MANUSCRIPT

Chapter 2 gives the working principle and a corresponding literature review of SWG-based silicon photonics devices. Then, the working principle of immersion lithography as well as its advantages and

challenges for the fabrication of silicon photonics devices are also reviewed.

Chapter 3 covers the study of an ultrabroadband SWG-engineered 2x2 MMI 3-dB coupler. Its working principle is given, followed by its simulation, fabrication and characterization.

Chapter 4 covers the study of a high efficiency SWG-engineered L-shaped grating coupler. In this chapter, the motivations for using such a complex structure are given, followed by the simulation, fabrication and characterization procedures.

Chapter 5 covers the study of an SWG-engineered low divergence optical antenna for a two-dimensional optical phased array (2D-OPA), designed for free space optical communications. In this chapter, the motivations of implementing silicon photonics OPAs for free space communications are given, followed by the specifications of our OPA. The simulation, fabrication and characterization results of the optical antenna are then reported, followed by the characterization of the whole 2D-OPA.

Chapter 6 gives the overall conclusions of the PhD work based on the mentioned case studies.

2 LITERATURE REVIEW OF SUBWAVELENGTH GRATING (SWG) METAMATERIALS AND OF IMMERSION LITHOGRAPHY

The aim of this chapter is to provide an overview on the working principle of subwavelength gratings (SWGs) and to give the motivations for using immersion lithography for their fabrication.

The chapter outline is as follows. The different behaviors of a periodic waveguide grating are briefly presented, followed by a focus on the subwavelength regime. A brief review of literature, showing the benefits of SWG-metamaterials is then given. The motivations for the use of immersion lithography for the large volume production of SWG-engineered silicon photonics devices are then presented.

2.1 THE THREE OPERATION REGIMES OF A WAVEGUIDE GRATING

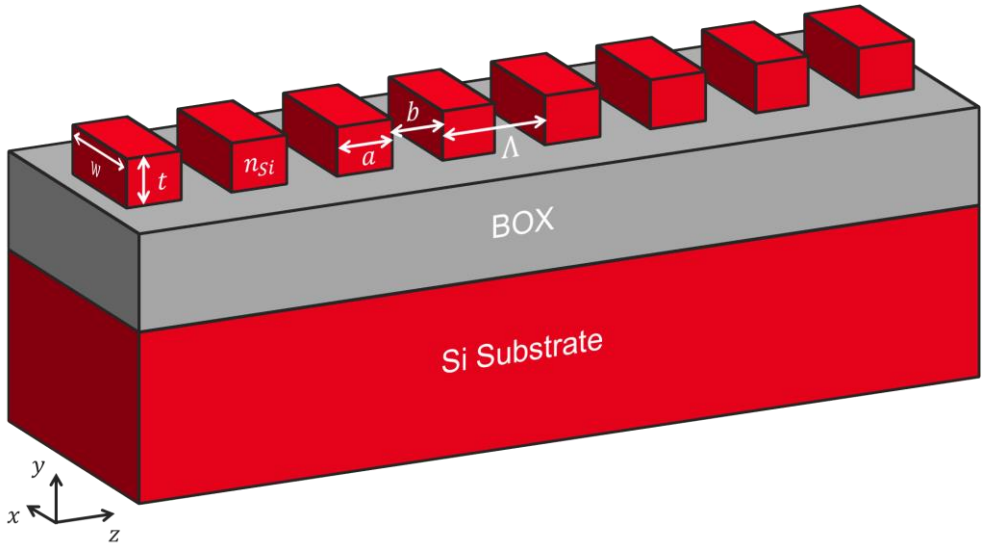

Fig. 2.1: A typical grating structure on the SOI platform. The upper cladding is not shown for clarity.

Fig. 2.1 shows a typical periodic grating structure on an SOI platform. The grating is made up of Si blocks, each of size $a \times w \times t$, embedded in a cladding material (which is usually SiO_2 or air). The grating period is Λ, with $\Lambda = a + b$, where b is the separation between two

consecutive Si blocks along the z-axis. The silicon duty cycle of the grating is defined as $DC_{Si} = a/\Lambda$.

Such periodic waveguide gratings can support periodic Floquet-Bloch modes [29]. Considering the propagation direction to be along the z-axis, the electric fields of the Floquet-Bloch modes, $E(x, y, z)$, can be expressed as in Eq. (2.1).

$$E(x, y, z + \Lambda) = E_B(x, y, z) \exp(-\gamma_B \Lambda) \qquad \text{Eq. (2.1)}$$

where $E_B(x, y, z)$ is the Bloch mode field distribution within a single period and γ_B its complex propagation constant. Usually, $\gamma_B = \alpha_B + jk_B = \alpha_B + j(2\pi/\lambda)n_B$ where α_B and k_B are the attenuation and propagation constants respectively, and n_B is the effective index of the Bloch mode.

The behavior of such a periodic waveguide grating is represented by its dispersion diagram, also referred as photonic-band diagram, as schematically shown in Fig. 2.2(a). In this figure, the vertical axis represents the angular frequency, $\omega = 2\pi c/\lambda$, where c is the speed of light in a vacuum and λ is the wavelength. As shown by the diagram, the periodic waveguide can operate under 3 distinctive regimes, depending on the size of the grating period, Λ, as compared to the propagating wavelength, λ and the Bloch effective index, n_B.

- When $\Lambda = \lambda/2n_B$, the waveguide operates in the **Bragg reflection regime**. Light cannot propagate through the structure and is gradually reflected by successive interference of the back-reflections at the index interfaces. In this regime, k_B is constant for $\omega_1 < \omega < \omega_2$. This range is called the photonic bandgap. Photonic crystal waveguides operate in this regime and are created by introducing line defects in a periodic lattice [30]. Spectral filters using Bragg gratings also operate in this regime [31].
- When $\Lambda > \lambda/2n_B$, (frequencies above the bandgap, $\omega > \omega_2$), the waveguide operates in the **diffractive regime**. The Bloch mode becomes leaky, and light is mainly radiated into the cladding and into the substrate. Grating couplers [13] operate in this regime.

- When $\Lambda < \lambda/2n_B$, (frequencies below the bandgap, $\omega < \omega_1$), the waveguide operates in the **subwavelength regime**. Diffraction effects are suppressed, and light propagates through the periodic waveguide in a similar way to that of an index-equivalent homogeneous waveguide. Such structures are referred to as subwavelength grating (SWG) metamaterials. They are very interesting as they enable refractive index engineering, using only two materials that can be defined using the usual silicon photonics lithographic fabrication processes. Hence, they enable higher degrees of freedom in the design of silicon photonics devices.

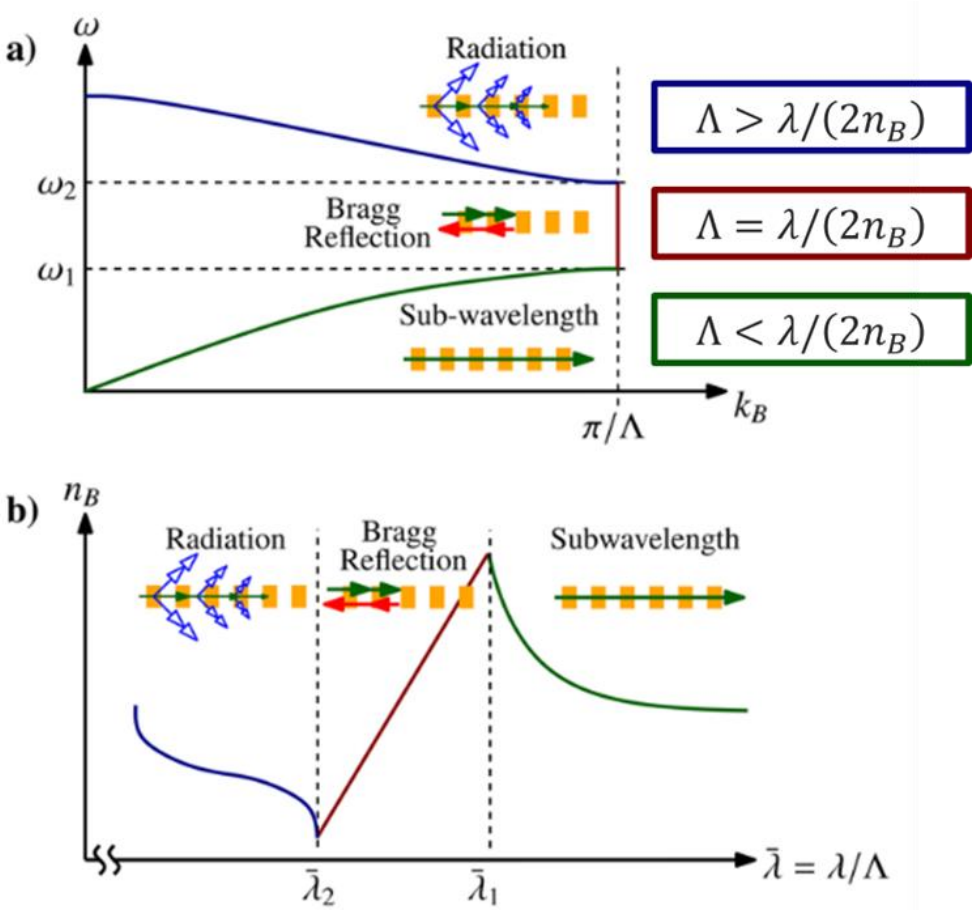

Fig. 2.2: (a) Dispersion diagram of a periodic waveguide grating in the $\omega - k_B$ space, where ω is the angular frequency and k_B is the propagation constant. (b) Equivalent representation of the diagram in the $n_B - \overline{\lambda}$ space, where n_B is the Bloch effective index and $\overline{\lambda}$ is the normalized wavelength. Higher order diffraction and reflection bands are not shown. Images from Halir et al. [32]

2.2 HOMOGENIZATION OF SWG-METAMATERIALS

Homogenization (or effective medium theory) consists in considering the SWGs as an equivalent homogeneous medium and finding its corresponding equivalent refractive index tensor (see Fig. 2.3). Determining the optical properties of an equivalent homogenized medium is advantageous in terms of simulation time and resources compared to full 3D-FDTD simulations of whole devices. Homogenization can also give physical insights when designing SWG devices.

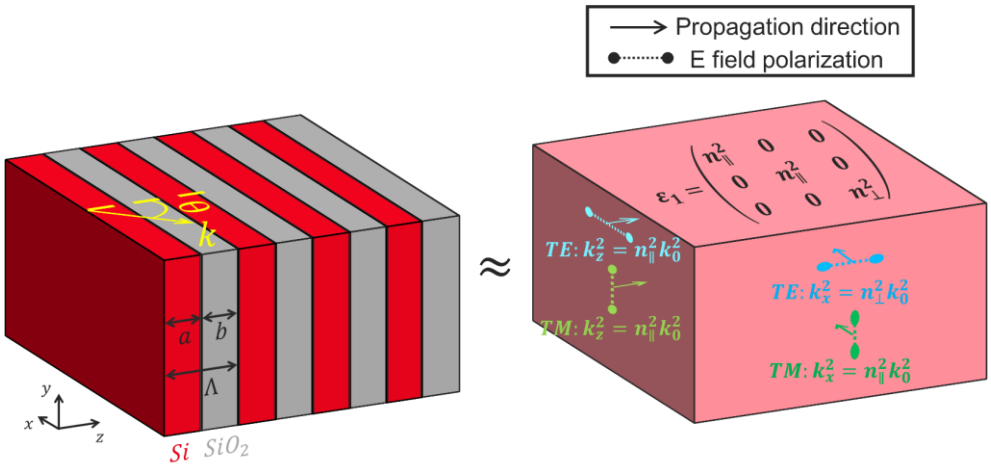

Fig. 2.3: Homogenization of a SWG as an equivalent uniaxial anisotropic crystal, with its diagonal permittivity tensor, ε_1

To create an equivalent homogenous medium, the SWG is initially considered as an infinite series of alternate layers (laminae) of two different media. Si and SiO_2 are here taken as examples. In the subwavelength regime ($\Lambda \ll \lambda$), the dispersion relations of a plane wave, with a wave vector $\hat{k}$ propagating in the x-z plane and forming an angle θ with respect to the normal of the laminar interfaces (along the z-axis), can be simplified to Eq. (2.2) for transverse electric (TE) and transverse magnetic (TM) polarizations [28,33].

$$TE: \frac{k_x^2}{n_\perp^2} + \frac{k_z^2}{n_\parallel^2} = k_0^2 \qquad \text{Eq. (2.2)}$$

$$TM: \frac{k_x^2}{n_\parallel^2} + \frac{k_z^2}{n_\parallel^2} = k_0^2 \qquad \text{Eq. (2.3)}$$

where k_x and k_z are the magnitudes of the wave vector propagating in the SWG, $\hat{k}$, along the x- and z- axis respectively, $k_x = |\hat{k}| \sin\theta$ and $k_z = |\hat{k}| \cos\theta$ where θ is the angle between $\hat{k}$ and the normal to the SWG interfaces, which is along the z-axis. The magnitude of the free space wave vector is $k_0 = 2\pi/\lambda$, where λ is the free space wavelength. $n_{\parallel}$ and $n_{\perp}$ are the equivalent SWG indices when the electric field is polarized parallel and perpendicular to the SWG interfaces

These equations show that the SWG behaves as a birefringent uniaxial anisotropic crystal, where $n_{\parallel}$ and $n_{\perp}$ are the ordinary and extraordinary indices of refractions respectively. In such a material, light experiences different refractive indices depending on its polarization state and its propagation direction. When the electric field polarization is parallel to the material interfaces (in the x-y plane), light experiences the $n_{\parallel}$ index. Conversely, when the electric field is polarized perpendicular to the material interfaces (along the z -axis), light experiences the $n_{\perp}$ index. This is schematically shown in Fig. 2.3.

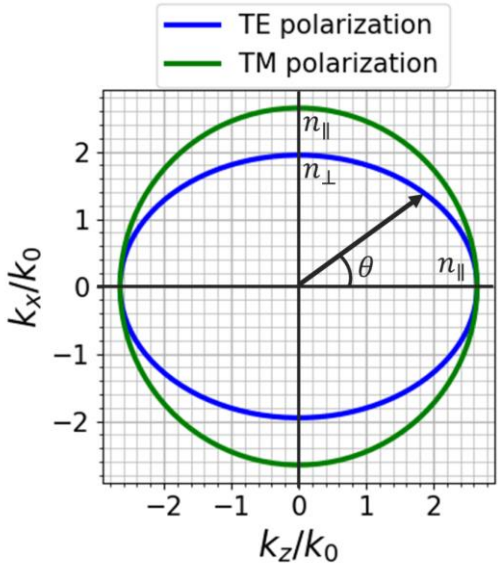

Fig. 2.4: Representation of the dispersion relations (see Eq. (2.2)and Eq. (2.3)) of a plane wave propagating in the SWG. The SWG behaves as a uniaxial anisotropic crystal, where $n_{\parallel}$ and $n_{\perp}$ are the ordinary and extraordinary refractive indices respectively. Also, $n_{\parallel}$ and $n_{\perp}$ are the equivalent SWG indices when the electric field is polarized parallel and perpendicular to the SWG interfaces. θ is the angle defined with respect to the normal of the plane of the SWG interfaces.

The dispersion relations given in Eq. (2.2) and Eq. (2.3) are represented in Fig. 2.4. The TE equation corresponds to an ellipse while the TM equation corresponds to a circle. As the TM polarization is always along the y- axis, it is always parallel to the material interfaces, whatever the propagation direction. It therefore always experiences the $n_{\parallel}$ index and has a circular dispersion relation. The direction of the TE polarization, changes with the propagation direction. For example, when the TE mode is propagating along the z-axis, it is polarized along the x-axis and experiences the $n_{\parallel}$ index, but when propagating along the x-axis, it is then polarized along the z-axis and experiences the $n_{\perp}$ index. The dispersion relation of the TE mode is therefore elliptical.

The homogenized SWG material is defined by a diagonal permittivity tensor ε_1 (see Fig. 2.4) as in a uniaxial anisotropic material. n_{ii} is the refractive index experienced when the electric field is polarized along the i-axis. As mentioned earlier, $n_{xx} = n_{yy} = n_{\parallel}$ as the electric field is parallel to the material interfaces. $n_{zz} = n_{\perp}$ as the electric field is polarized perpendicular to the interfaces.

$$\varepsilon_1 = \begin{pmatrix} n_{xx}^2 & 0 & 0 \\ 0 & n_{yy}^2 & 0 \\ 0 & 0 & n_{zz}^2 \end{pmatrix} = \begin{pmatrix} n_{\parallel}^2 & 0 & 0 \\ 0 & n_{\parallel}^2 & 0 \\ 0 & 0 & n_{\perp}^2 \end{pmatrix} \qquad \text{Eq. (2.4)}$$

The $n_{\parallel}$ and $n_{\perp}$ indices can be found analytically using the laminar model, which was proposed by Luque-González et al [33]. The method consists of solving for k_x and k_z in Eq. (2.5) and Eq. (2.6) and injecting them in Eq. (2.2) and Eq. (2.3) to find $n_{\parallel}$ and $n_{\perp}$. Matlab and Python implementations have been provided to calculate these indices in [33].

$$\cos(k_z\Lambda) = \cos(k_{1z}a)\cos(k_{2z}b) - \Delta_{TE}\sin(k_{1z}a)\sin(k_{2z}b) \qquad \text{Eq. (2.5)}$$

$$\cos(k_z\Lambda) = \cos(k_{1z}a)\cos(k_{2z}b) - \Delta_{TM}\sin(k_{1z}a)\sin(k_{2z}b) \qquad \text{Eq. (2.6)}$$

where $k_{iz} = \sqrt{(k_0 n_i)^2 - k_x^2}$ is the k_z part in the material i. When $i = 1$, the material is Si and when $i = 2$, the material is SiO_2. n_i is the refractive index of the material i. a is the length of Si and b is the length of SiO_2 in a single SWG period. Δ is a polarization-dependent factor as defined in Eq. (2.7) and Eq. (2.8).

$$\Delta_{TE} = \frac{1}{2}\left(\frac{n_2^2}{n_1^2}\frac{k_{1z}}{k_{2z}} + \frac{n_1^2}{n_2^2}\frac{k_{2z}}{k_{1z}}\right) \quad \text{Eq. (2.7)}$$

$$\Delta_{TM} = \frac{1}{2}\left(\frac{k_{1z}}{k_{2z}} + \frac{k_{2z}}{k_{1z}}\right) \quad \text{Eq. (2.8)}$$

As an illustration, $n_{\parallel}$ and $n_{\perp}$ have been evaluated for a free space wavelength of λ = 1550 nm as a function of the Si duty cycle in the SWG, $DC_{Si} = a/\Lambda$ (see Fig. 2.1), and for two different SWG pitch Λ = 200 nm and Λ = 50 nm (see Fig. 2.5). This graph shows that different values of $n_{\parallel}$ and $n_{\perp}$ can be synthetized using different DC_{Si}. For low values of DC_{Si}, the equivalent refractive indices tend to n_{SiO_2} and when DC_{Si} tends to 1, the equivalent indices tend to n_{Si}. In other words, by controlling their geometrical parameters such as the duty cycle, DC_{Si} and the period, Λ, SWGs enable refractive index engineering, without requiring the integration of supplementary materials, and can therefore give more degrees of freedom in the design of silicon photonics devices.

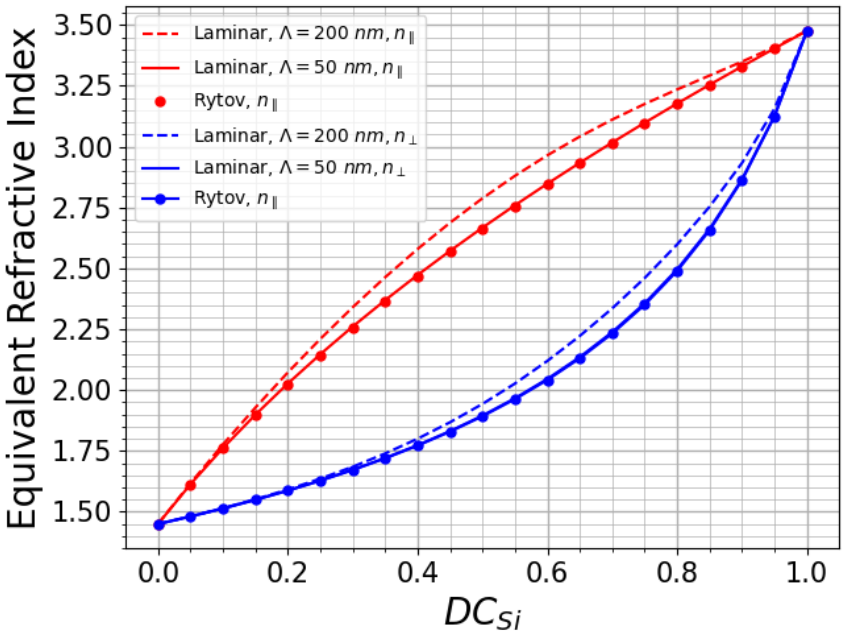

Fig. 2.5: Equivalent SWG refractive indices using the laminar model and Rytov equations

In the deep subwavelength regime, $n_{\parallel}$ and $n_{\perp}$ can be approximated using Rytov equations [34] (see Eq. (2.9) and Eq. (2.10)). As shown in Fig. 2.5, Rytov equations are consistent with the laminar model for a pitch Λ = 50 nm at a wavelength of λ = 1550 nm.

$$n_{\parallel}^2 = DC_{Si} n_{Si}^2 + (1 - DC_{Si}) n_{SiO_2}^2 \qquad \text{Eq. (2.9)}$$

$$\frac{1}{n_{\perp}^2} = DC_{Si} \frac{1}{n_{Si}^2} + (1 - DC_{Si}) \frac{1}{n_{SiO2}^2} \qquad \text{Eq. (2.10)}$$

where $n_{\parallel}$ and $n_{\perp}$ are the SWG-equivalent refractive indices parallel and perpendicular to the SWG indices respectively, DC_{Si} is the silicon duty cycle, n_{Si} and n_{SiO_2} are the refractive indices of Si and SiO_2 respectively.

Rytov equations and the laminar model can both provide a good approximation of the permittivity tensor of homogenized SWGs. They help to reduce the computational time and resources by simulating the homogenized SWGs instead of the full 3D geometry. This can provide a good starting point in the design of devices and give physical insights. However, 3D-FDTD simulations should still be carried out for further device optimization. Also, the thickness is supposed to be infinite in the Rytov equations and in the laminar model, which is not a real practical case. The depth dependence of the equivalent refractive indices in SWG materials has been studied, for example, by Lalanne et al. [35].

2.3 REFRACTIVE INDEX ENGINEERING IN SWG-ENGINEERED SILICON PHOTONICS DEVICES AND ASSOCIATED FABRICATION CHALLENGES

As seen previously, $n_{\parallel}$ and $n_{\perp}$ can be tailored by choosing the SWG period and duty cycle. In other words, SWG-metamaterials enable control over birefringence and refractive index, which gives to the designer additional degrees of freedom.

In this section, a few examples of SWG-engineering in silicon photonics devices are presented to give an overview of the new design possibilities offered by SWGs. These include SWG core waveguides, SWG edge couplers and some other passive devices. A thorough

description of the state of the art can be found in the numerous review articles [28,33,36–41].

2.3.1 SWG core waveguide

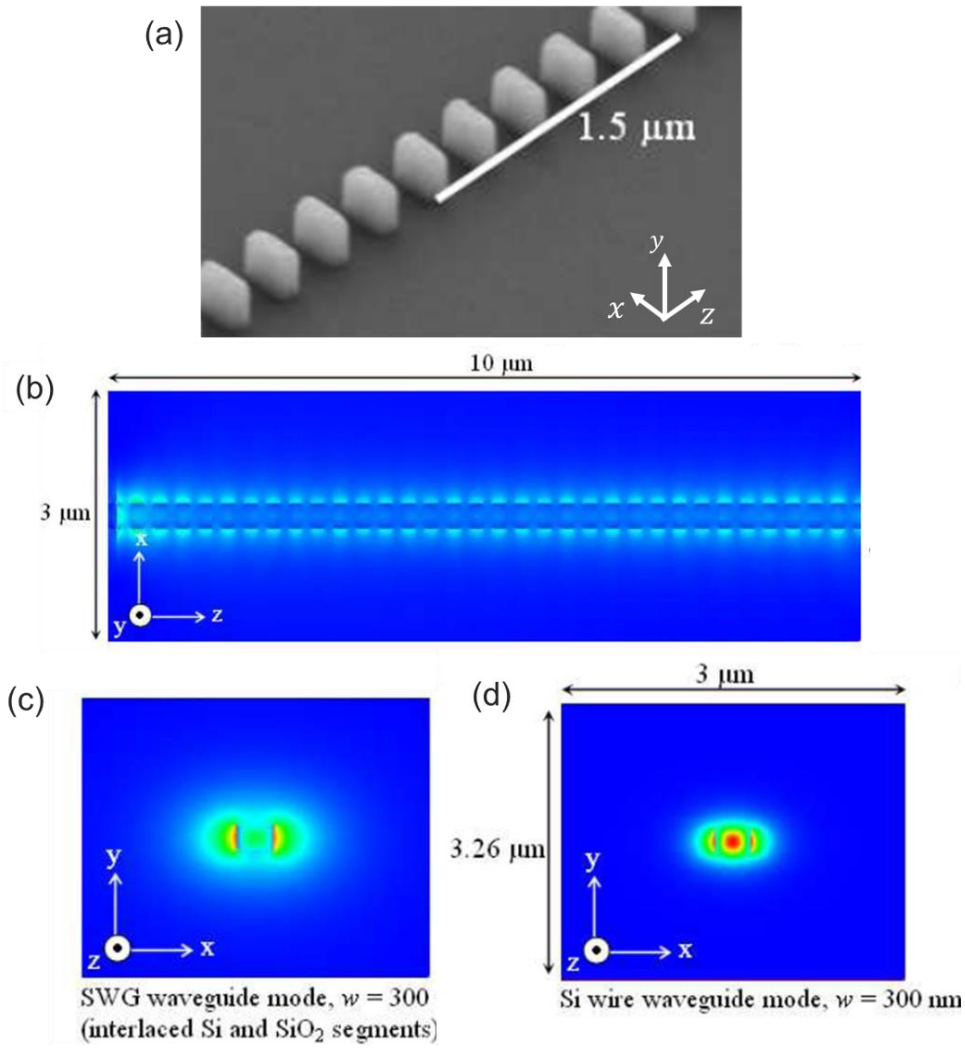

Fig. 2.6: (a) SEM image of the first waveguide with an SWG core on an SOI platform [42]. (b) Top view: Simulated TE Floquet-Bloch modes propagating along the SWG waveguide (c) Side view: SWG TE mode (d) Side view: conventional waveguide TE mode (same width as the SWG waveguide) which is more confined than the SWG core waveguide. Images from Bock et al. [42].

Fig. 2.6(a) shows a scanning electron (SEM) image of the first waveguide with an SWG core, realized on an SOI platform by Bock et al. [42] at the National Research Council Canada (NRC). The periodic SWG waveguide supports Floquet-Bloch modes, that propagate

without any theoretical loss despite the large number of optical interfaces (see Fig. 2.6(b)).

As the equivalent refractive index of the SWG core is lower than that of a conventional Si strip waveguide, its effective index is lower. As shown in Fig. 2.6(c) and (d), this lower effective index yields a field which is more delocalized in the SWG waveguide, compared to the strip waveguide.

In this first demonstration, waveguide losses of ~ 2.1 dB/cm were reported at a wavelength near 1550 nm, with a low polarization dependence. As the mode is more delocalized, the interaction with the sidewall roughness is reduced, thereby reducing backscattering and potentially, waveguide losses. Peng et al. reported < – 50 dB/mm of backscattering in SWG waveguides fabricated in a CMOS silicon photonics production process [43].

In addition to the control over effective index and modal confinement, SWGs can also give control over the evanescent tails of guided optical modes [44,45], waveguide dispersion [46,47], polarization [48] and reduced temperature sensitivities [49,50]. SWGs have also been implemented for the control reflectivity in waveguide facets [51].

2.3.2 SWG edge coupler

This ability to control the effective index and mode delocalization in a waveguide has been exploited to design SWG mode converters to implement high-efficiency fiber-chip edge couplers (see Fig. 2.7) [52].

By gradually modifying the duty cycle of the SWGs, the mode size is gradually expanded from 450 nm in a silicon waveguide to a Gaussian beam waist of 2 μm, matching the spot size of a lensed fiber. This was the first demonstration of an SWG-engineered device on an SOI platform. The measured fiber-waveguide coupling efficiency was – 0.9 dB for TE polarization and – 1.2 dB for TM polarization at a wavelength near 1500 nm. This device was further optimized, achieving a very high efficiency of – 0.32 dB, with a lensed fiber of Gaussian waist of 3.2 μm, with negligible polarization dependence loss, over a 100 nm bandwidth with a central wavelength of 1550 nm [53]. In addition, the

SWGs help to relax the fabrication tolerance as the waveguide tip is wider than that of a conventional inverse-tapered edge coupler.

A similar SWG edge coupler is today proposed as a fiber-coupling solution in the process design kit (PDK) offered by Global Foundries (see Fig. 2.16(a)) [54].

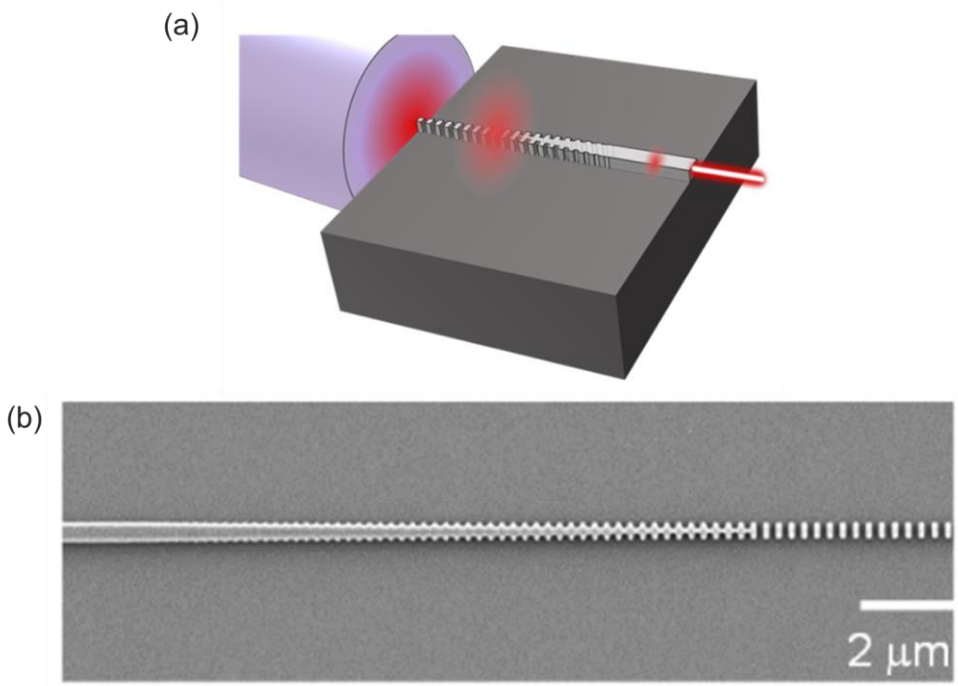

Fig. 2.7: SWG edge coupler (a) schematic (b) SEM image. Images from Cheben et al. [28]

2.3.3 Examples of other SWG passive devices

A silicon photonics foundry usually proposes a list of basic silicon photonics devices that can be implemented together in a circuit to perform complex optical functions. These include passive devices such as waveguides, fiber-waveguide coupling solutions (edge couplers and surface grating couplers), power splitters (MMIs, DC couplers) and wavelength filtering devices (ring resonators) among many others.

The performance of such passive devices can be enhanced using SWG-engineering. For instance, SWGs have helped in increasing coupling efficiency in surface fiber-chip grating couplers [55], in increasing the bandwidth of MMI [56] and directional couplers [57,58],

and in implementing ring resonators with small bending radii of ~10 μm, with a reasonable Q-factor of 45000 [59].

Table 2.1 summarizes the key performance parameters of some relevant SWG-based devices. They all have been demonstrated on an SOI platform and fabricated using e-beam lithography.

SWG Device	Experimental Performance	λ (nm)	Λ (nm)	MFS (nm)	Reference
SWG core waveguide	Propagation losses ~ 2.3 dB/cm (TE and TM)	1550	300	100	2010 Bock et al. [42]
SWG chirped edge coupler	Coupling efficiency ~ -0.30 dB (TE and TM)	1500-1600	300-400	100	2015 Cheben et al. [53]
SWG grating coupler	Coupling efficiency ~ -2 dB (TE)	~ 1540	450	100	2014 Benedikovic et al. [55]
3-dB 2x2 SWG MMI coupler	Excess loss < 1 dB (TE) Broadband	1375-1700	190	95	2016 Halir et al. [56]
SWG DC coupler	Excess Loss < 0.24 dB (TE) Broadband	1505-1675	260	120	2023 Vilas et al. [57]
SWG ring resonator	Q-factor ~ 45000 Radius ~ 10 μm	~ 1550	300	140	2016 Wang et al. [59]

Table 2.1: Examples of SWG-engineered devices whose conventional (non-SWG) counterparts are usually available in a foundry's process design kit (PDK). λ is the operational wavelength, Λ is the SWG period, MFS is the minimum feature size.

2.3.4 Challenges of SWG fabrication

Although SWG-metamaterials enable additional degrees of freedom in device design and help to boost the performance of the device, they often require features of small dimensions that are challenging to fabricate.

At telecom wavelengths, the SWG period is usually less than 300 nm and the SWG minimum feature sizes are usually close to 100 nm (see Table 2.1). For this reason, most of the devices have been fabricated using electronic beam (e-beam) lithography as the latter can define such small features. However, e-beam lithography is a serial and slow process [60], which is therefore not compatible with large-volume industrial production. Immersion lithography on the other hand, can define features around 70 nm in silicon photonics devices. Also, it is an industrial tool commonly used in manufacturing electronic chips, and is today being deployed in silicon photonics foundries. Immersion lithography has therefore the potential for producing SWG-based devices at a large scale,

2.4 IMMERSION LITHOGRAPHY

In this section, the working principle of immersion lithography is introduced, followed by a literature review of silicon photonics devices fabricated with this technique.

2.4.1 Photolithography working principle

Photolithography, also called optical lithography, is a widely adopted high volume fabrication process for manufacturing integrated circuits. Its working principle is outlined in Fig. 2.8.

A collimated light source of wavelength λ is used to image a pattern from a photomask, containing the shapes of the desired circuits, onto a photoresist which has been previously deposited on the silicon wafer. The photoresist is photosensitive, that is, its chemical properties change upon exposure to the light. Usually, the solubility of the exposed areas is changed. The exposed areas can be selectively removed using a developing solvent. The pattern is then transferred into the silicon wafer by etching, with the remaining photoresist acting as a protective layer. The remaining photoresist is finally removed in a so-called stripping process.

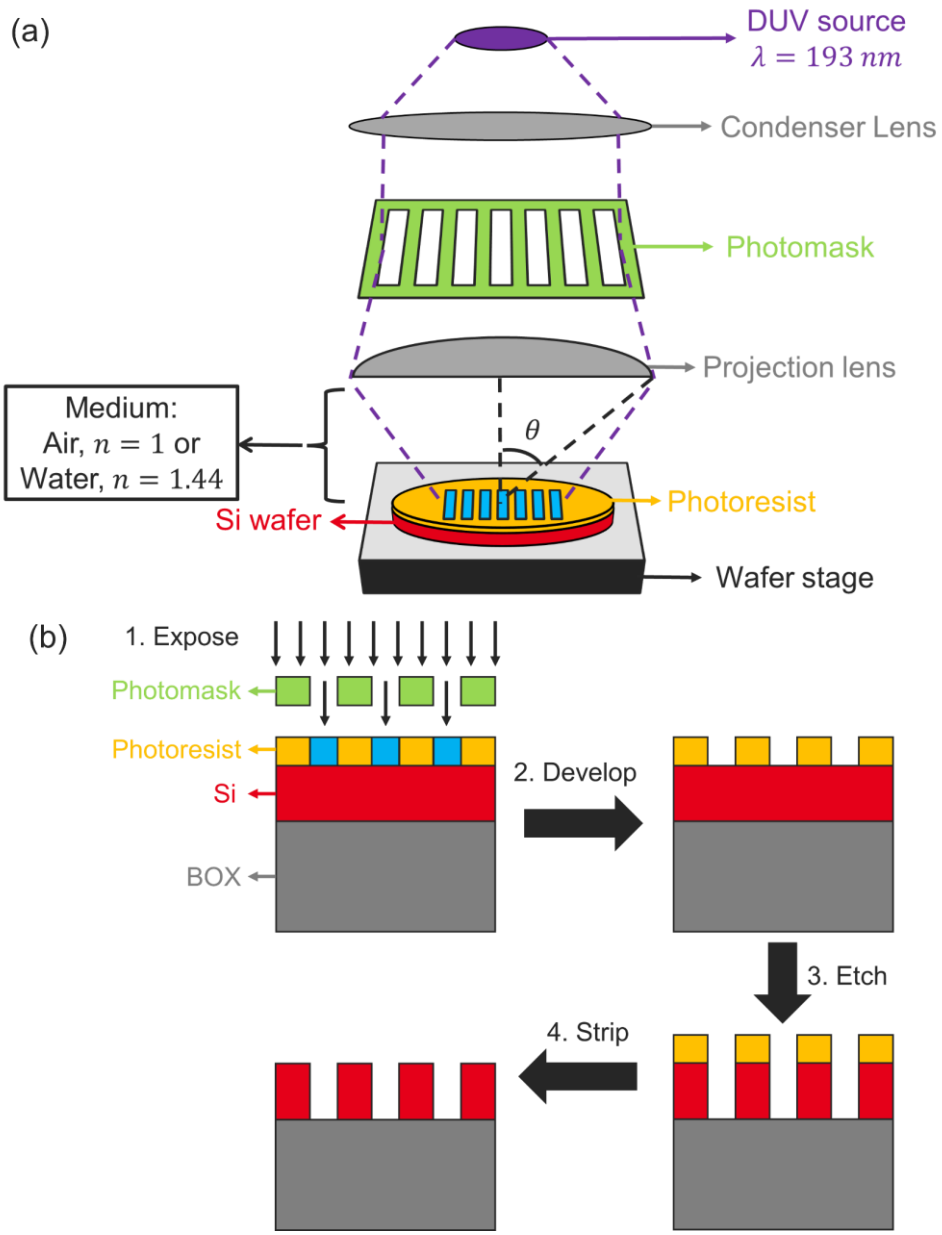

Fig. 2.8: Schematic of the working principle of photolithography, DUV = Deep-ultraviolet, θ = half angular aperture, n is the refractive index of the corresponding medium (a) Imaging system used to expose the photoresist (b) Lithographic process

2.4.2 Immersion lithography for resolution enhancement

The resolution of a photolithography system is defined as the smallest feature size that can be patterned. The resolution is also called critical dimension or half pitch. Its theoretical value is given by the Rayleigh equation as:

$$R = k_1 \frac{\lambda}{n \sin \theta} = k_1 \frac{\lambda}{NA} \qquad \text{Eq. (2.11)}$$

where R is the resolution, k_1 is a process-related factor (depending on illumination conditions, mask technology, photoresist, etc.), λ is the illumination wavelength, n is the refractive index of the medium between the projection lens and the photoresist, θ is half the angular aperture of the imaging system. The angle θ, defined in Fig. 2.8(a), represents half the maximum angle of acceptance. The product $n \sin \theta$ is equal to the numerical aperture, NA, of the imaging system.

Following Eq. (2.11), the resolution R is enhanced by reducing k_1, by reducing λ and by increasing NA. Several techniques have been implemented to optimize these values towards finer resolution to enable fabrication of smaller microelectronics devices and chips with denser circuits.

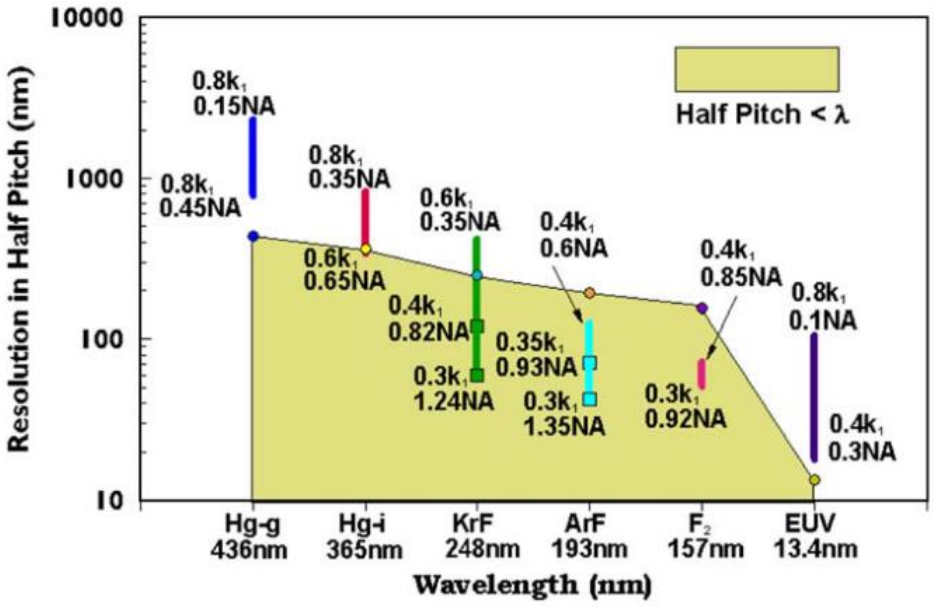

Fig. 2.9: Evolution of lithographic systems. The vertical bars indicate resolution enhancement by engineering k_1 and NA. The shaded area indicates subwavelength imaging (resolution < λ). Image from Lin et al. [61].

The evolution of the resolution and wavelength of lithographic systems is shown in Fig. 2.9. The general trend was to reduce the wavelength, from 436 nm down to 193 nm. The 193 nm wavelength is

produced by an argon fluoride (ArF) excimer laser source and is in the deep ultra-violet (DUV) range. To further enhance the resolution, the initial strategy was to further reduce the wavelength down to 157 nm. However, its development was impeded by various technological difficulties such as the development of affordable high quality lenses and high quality resists, among others [61].

Also, at the same time, an alternative solution was found to further enhance the resolution while keeping the 193 nm wavelength. It consists of adding a fluid (typically water) between the lens and the photoresist (see Fig. 2.10) and is called immersion lithography.

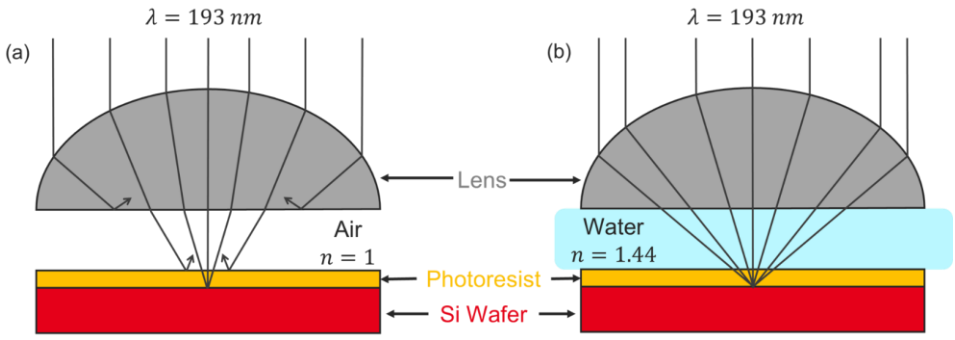

Fig. 2.10: (a) Dry lithography (b) Immersion lithography, in which the numerical aperture (NA) is increased thanks to the addition of water (which has a higher refractive index than air), thereby enhancing the resolution.

Adding water improves the numerical aperture, $NA = n \sin\theta$ of the system in two ways. First, water (n = 1.44) has a higher refractive index than air (n = 1) [62]. Second, water increases the angular aperture of the system, θ. Then, light at larger incident angles can contribute to the image formation in an immersion system. In a dry system, these rays would have been lost by total internal reflection. The resolution of immersion lithography is therefore enhanced as the NA is increased (see Eq. (2.11)). For silicon photonics devices, the nominal resolution of an immersion lithography system is around 70 nm, which is better than its dry counterpart offering a nominal resolution of 110 nm [63] (see Fig. 2.11).

The resolution for CMOS fabrication is better than for silicon photonics as the k_1 values are different. Indeed, the illumination conditions are different and silicon photonics devices are more susceptible to optical proximity effects.

Lithography	λ (nm)	NA	For CMOS		For silicon photonics	
			Illumination condition	Resolution (nm)	Illumination condition	Resolution (nm)
KrF	248	0.8	Dipole* (line) C-quad* (hole)	120	Annular*	150
ArF	193	0.9		65		110
ArF-I	193	1.35		40		70

* The figures to the right schematically illustrate the dipole, C-quad, and annular illumination conditions.

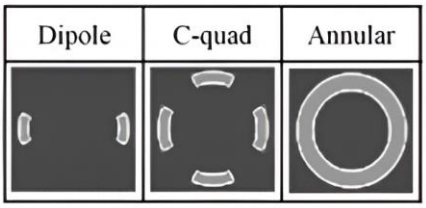

Fig. 2.11: Comparison of lithography tools used in CMOS and silicon photonics fabrication. ArF-I stands for argon fluoride-immersion lithography. Image from Horikawa et al. [63].

Another advantage of immersion lithography over dry lithography is its increased depth of focus (DOF), which is the tolerance to the focal error, at a given resolution [61]. However, the addition of water can induce some defectivity issues due to air bubbles, particles or stains [60,64]. Despite these issues, the development of λ = 193 nm immersion lithography was greatly favored over the λ = 157 nm lithography system as it leveraged the technological advancements brought by its dry counterpart (similar imaging system and resist) [65].

To further improve resolution, extreme UV (EUV) lithographic systems are proposed as an alternative to immersion lithography. However, EUV lithography is a relatively new technology and has some critical challenges yet to be solved, such as mask defects, high line edge roughness and resist outgassing [60].

Immersion lithography is a more mature technology. For example, commercial systems were available from around 2003 with Nikon, followed by ASML [60]. It is currently being used by several silicon photonics foundries such as AIM photonics [66], Global Foundries [23], IMEC [25], PETRA [22] and CEA-Leti [24] on 300 mm silicon photonics platforms [2].

2.4.3 Optical Proximity Correction (OPC)

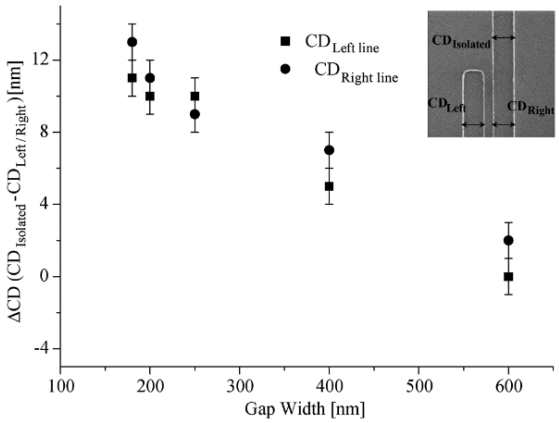

Fig. 2.12: Optical proximity effects result in different linewidths between an isolated and arrayed waveguides (ΔCD). ΔCD varies with the gap width, i.e., with the proximity of the waveguides. Image from Selvaraja et al. [67]

Although immersion lithography for silicon photonics could in principle provide a high resolution with the fabrication of minimum feature sizes of 70 nm, the actual resolution of the system is still limited by optical proximity effects (OPEs). OPEs are caused by optical interactions with nearby features and result in morphological and dimensional variations from the intended design [68]. For example, Selvaraja et al. have compared the linewidths obtained when dry lithography is used to define the same waveguide width in an isolated waveguide and in a dense array configuration [67] (see Fig. 2.12). The effective width has a difference of ΔCD, that changes a function of the proximity between the waveguides (gap width) in the array. Similarly, they have observed different hole diameters in photonic crystals according to their surrounding features.

Although immersion lithography exhibits weaker OPEs than dry lithography [63,69], this effect can still be significant and needs to be compensated as dimensional variations can negatively impact the performance of silicon photonics devices [70,71]. Controlling these dimensional variations could be especially critical for wide (multimode) SWG waveguides as significant performance degradation can result from very small fabrication deviations [72]. In addition, OPEs become more complex and difficult to compensate as the feature sizes get smaller [68,73,74]. A way to compensate these OPEs consists in changing the nominal layout on the photomask by moving the edges

or adding extra polygons so that the patterned shapes and dimensions are as close as possible to the intended ones [75,76]. Such resolution enhancement technique is called optical proximity correction (OPC).

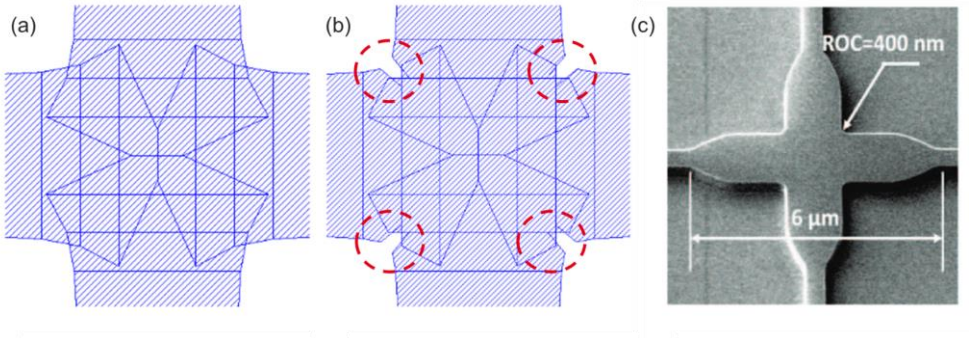

Fig. 2.13: (a) Intended waveguide crossing layout (b) OPC layout; the red dotted circles indicate the serifs, which are features which have been changed from the nominal design (c) SEM image. Images from Celo et al. [77]

Fig. 2.13 gives an example of how OPC has changed the initial design of a waveguide crossing and the corresponding SEM image by Celo et al. [77]. The authors have demonstrated lower insertion losses when OPC was applied.

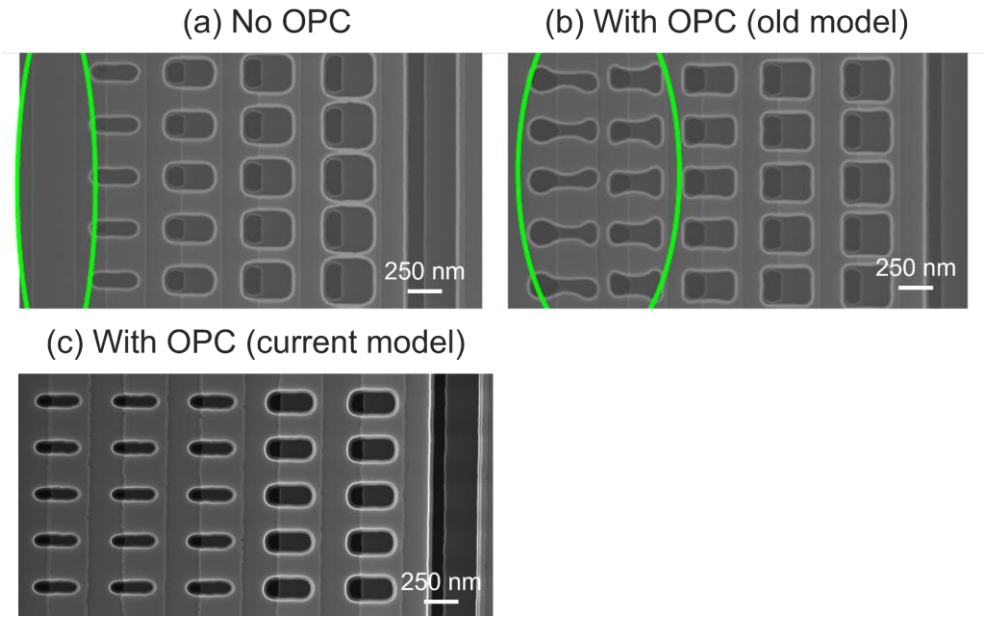

Fig. 2.14: Attempts at patterning SWG rectangular holes with immersion lithography at CEA-Leti. Feature sizes of 60 nm (a) could not be patterned without OPC (2021) and (b) were unsuccessfully patterned with an old OPC model (2021) (c) Similar SWG rectangular holes were defined using the new OPC model (2023). Feature sizes of 60 nm were more successfully patterned

At CEA-Leti, the OPC technology has been optimized to be able to define feature sizes as small as 60 nm. Fig. 2.14 shows SEM images of the same pattern, defined without OPC (Fig. 2.14(a)), using initial OPC models (Fig. 2.14(b)) and optimized OPC models (Fig. 2.14(c)). The optimized model, developed in 2023, enabled the patterning of 60 nm feature sizes. Other examples of realization of SWG devices with OPC are given in the manuscript (see Fig. 3.8, Fig. 4.19, Fig. 5.30).

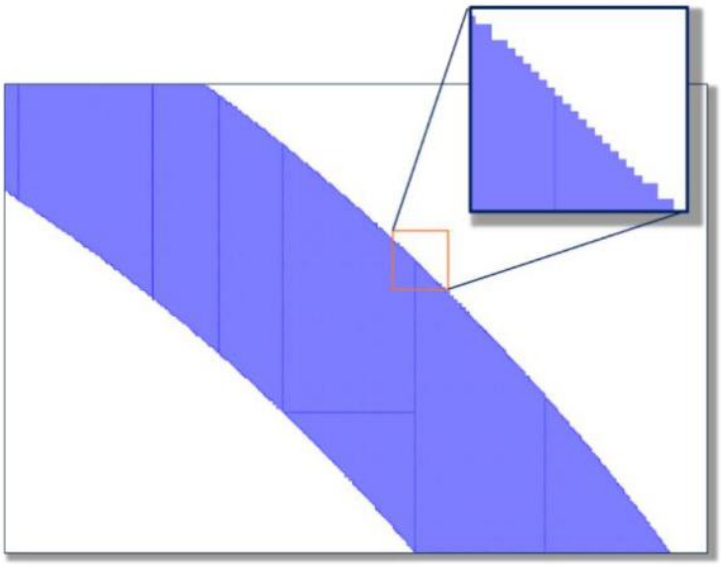

Fig. 2.15: Manhattanization process which consists in approximating the curves by small stair steps. Image from Giewont et al. [23]

For curvilinear silicon photonics devices such as waveguide bends or directional couplers, a Manhattanization is process is required before applying OPC [23,76,78,79]. This process consists in approximating the curves by using small stair-steps (see Fig. 2.15). The reason is that OPC models have been developed for Manhattan-like (orthogonal) CMOS structures. The resolution of the Manhattan grid used by silicon photonics foundries is usually 1 nm [80].

Also, OPC models for silicon photonics have to be optimized for a wider range of dimensional targets (typically 100 nm - 1 µm), compared to traditional CMOS devices [81]. The Manhattanization process and wider dimensional target range make OPC models for silicon photonics more challenging.

2.4.4 Silicon photonics devices fabricated using immersion lithography

This section aims at giving an overview of the silicon photonics that have been patterned using immersion lithography and the associated performance advantages.

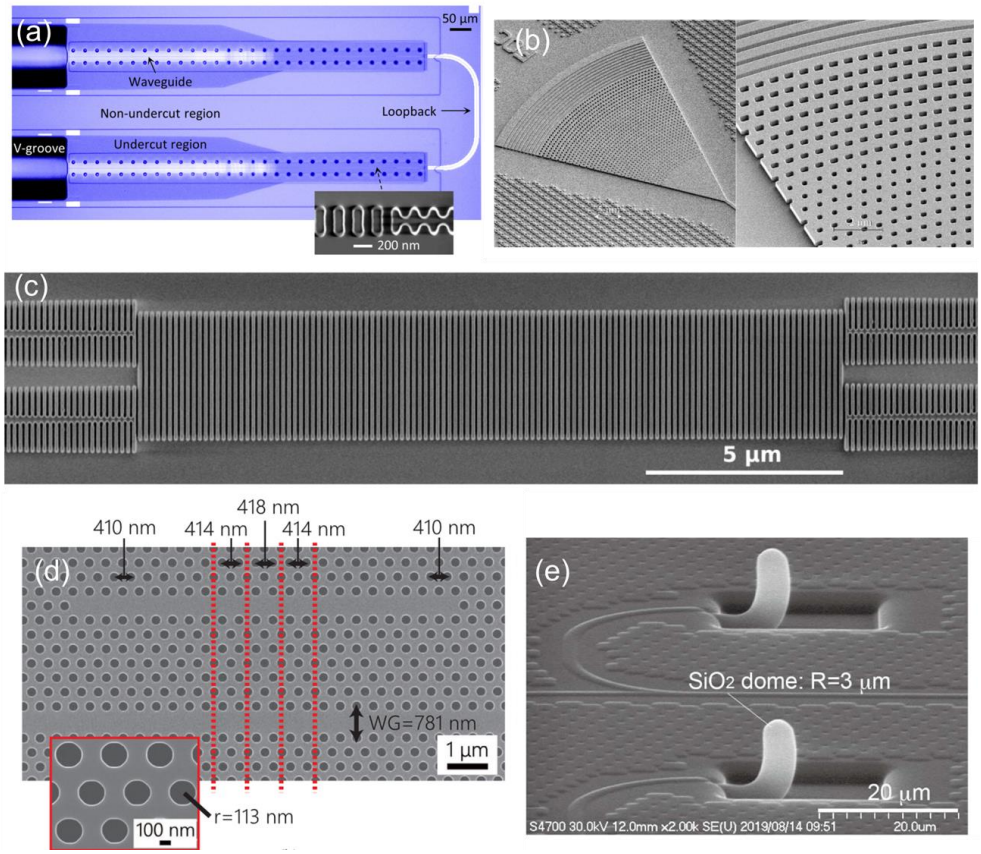

Fig. 2.16: Examples of reported devices with small feature sizes fabricated with immersion lithography: (a) SWG-engineered fiber-edge coupler (image from Barwicz et al. [54]) (b) SWG-engineered grating coupler (image from Ong et al. [82]), (c) SWG-engineered MMI (image from Vakarin et al. [83]) (d) Photonic crystal nano-cavities (image from Ashida et al. [84]), (e) Elephant coupler (image from Yoshida et al. [85]).

Some examples of silicon photonics devices with small feature sizes fabricated with immersion lithography are given in Fig. 2.16. Fig. 2.16(a) shows a high efficiency SWG-engineered fiber-edge coupler, with a minimum feature size (MFS) of 100 nm. This kind of coupler is available in the process design kit (PDK) of Global Foundries. Fig.

2.16(b) shows an SWG-engineered grating coupler for high fiber-positional freedom. Fig. 2.16(c) shows a broadband SWG-engineered MMI. Fig. 2.16(d) shows a high Q factor photonic crystal. Fig. 2.16(e) shows an 'elephant' mode converter, coupling a waveguide with a lensed single mode fiber with low coupling losses of 1.5 dB and low polarization dependency.

The performance of the presented devices in Fig. 2.16 has been summarized in Table 2.2, together with some other examples of silicon photonics devices with small feature sizes. Table 2.2 also gives their minimum feature sizes (MFS) and the foundry in which they were fabricated.

Device	**MFS (nm)**	**Performance**	**Foundry**	**Reference**
SWG fiber-chip edge coupler (available in commercial PDK)	100	TE coupling efficiency = – 0.7 dB TM coupling efficiency = – 1.4 dB	GF	[54] 2019 Barwicz et al. (see Fig. 2.16(a))
SWG grating coupler with very large tolerance to misalignment	100	Efficiency = -7.50 dB, Tolerance = 21.4 µm × 10.1 µm for 1 dB penalty loss	AIM Photonics	2018 Ong [82] (see Fig. 2.16(b))
SWG MMI	60	Broadband 1 dB bandwidth of 1460 – 1680 nm (220 nm)	ST	[83] 2021 Vakarin (see Fig. 2.16(c))
1D photonic crystal cavity	80	High Q factor = 0.84 million	IMEC	[86] 2021 Xie

Photonic crystal nanocavities	100	Average Q factor of 1.9 million (highest = 2.5 million)	PETRA	[84] 2018 Ashida (see Fig. 2.16(d))
Anti-Slot Photonic Crystals	70	1 dB loss	GF	[87] 2023 Allen
Si grating coupler	60	Perfectly vertical emission, 1.82 dB median losses	CEA-Leti	[88] 2021 Van Vaerenbergh
Hybrid Si/SiN grating coupler	60	Perfectly vertical emission 1.30 dB median insertion loss	CEA-LETI	[89] 2022 Van Vaerenbergh
Elephant coupler	70	1.5 dB insertion loss Polarization dependent loss = 0.25 dB	PETRA	[85] 2020 Yoshida (see Fig. 2.16(e))

Table 2.2: Some examples of Si photonic devices fabricated by immersion lithography with low minimum feature sizes, MFS. GF = Global Foundries (US), AIM Photonics= American Institute for Manufacturing Integrated Photonics (US), PETRA = Photonics Electronics Technology Research Association (Japan), IMEC = Interuniversity Microelectronics Center, Belgium, ST = STMicroelectronics (France), CEA-LETI (France)

Other reported demonstrations of silicon photonics devices fabricated using immersion lithography include an array waveguide grating, with less than 1.6 nm wavelength difference between the simulated and measured response [90], an SiN distributed Bragg reflector for laser cavities with maximum output powers of 2.5 mW, 5.1 mW and 0.5 mW at 1536 nm, 1561 nm and 1596 nm wavelengths respectively [91], color display metasurfaces with MFS of around 100 nm [92], high efficiency

SiN grating couplers for visible wavelengths with MFS = 85 nm [93] and 3D integration of a photonics/CMOS platform for a single-chip optical phased array (OPA) [94].

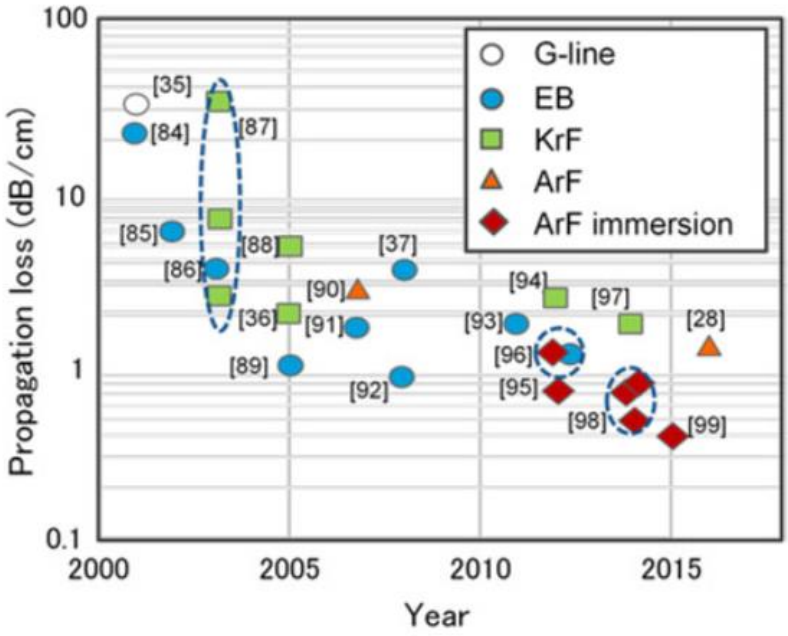

Fig. 2.17: Immersion lithography enabled very low propagation losses, EB stands for e-beam lithography, G-line has an illumination wavelength of λ = 436 nm, KrF has λ = 248 nm and ArF has λ = 193 nm. Image from from Horikawa et al. [22].

In addition to the enhanced resolution, immersion lithography and OPC also enable lower waveguide propagation losses [22,23,95,96] through line edge roughness reduction (see Fig. 2.17). Immersion lithography also provides reduced chip-to-chip dimensional variations on the wafer-scale, resulting into better uniformity in device performance [69,71,97]. Also, immersion lithography has enabled excellent mask alignments between SiN and Si layers in a hybrid grating coupler [89]. These alignments can be critical for the grating coupler efficiency.

2.5 CONCLUSION OF THE REVIEW

SWGs are periodic structures for which the period Λ is much smaller than the propagation wavelength λ. $\Lambda < \lambda/2n_{eff}$ where n_{eff} is the Bloch effective index. Typically, Λ < 300 nm for the usual telecom wavelength λ = 1550 nm. In this subwavelength regime, diffraction

and reflection effects are suppressed and the SWGs behave as a homogeneous anisotropic metamaterial.

The properties of the SWG-metamaterial can be modified by changing its geometrical parameters such as its period or its duty cycle. This has led to additional degrees of freedom for silicon photonics device design, thereby enhancing the performance of devices [28].

However, the required dimensions are small, and most demonstrations of SWG-based devices have been made at the laboratory level using e-beam lithography. Immersion lithography, which is today being deployed by silicon photonics foundries, can be used to fabricate the small dimensions required by SWGs with a process compatible with large-volume production.

By adding water between the imaging system and the silicon wafer, the resolution, R, of the system is enhanced. For a 193 nm wavelength lithography system, $R \sim 70$ nm for an immersion system, while $R \sim 110$ nm for a dry system. An OPC model should also be applied to correct for proximity effects. In addition to enhanced resolution, the use of immersion lithography has led to lower waveguide propagation losses and more uniform device performance at wafer scale.

3 ULTRA-BROADBAND SWG-ENGINEERED 2X2 MULTIMODE INTERFEROMETER (MMI) COUPLER

Multimode interferometers (MMIs) are multiport couplers which are one of the fundamental building blocks in silicon photonics circuits. They are often used for power splitting or combining functions. This chapter is dedicated to the study of an SWG-engineered MMI, fabricated by immersion lithography and OPC, with an enhanced bandwidth compared to a standard design without SWG-elements.

The outline of this chapter is as follows. First, the self-imaging principle, which is at the heart of MMI operation, is presented. The working principle of a conventional and a SWG-MMI with enhanced bandwidth are then given. This is followed by a literature review of SWG-MMIs. Next, our simulation, fabrication and characterization results are reported. Finally, our conclusions and perspectives are drawn.

3.1 THE SELF-IMAGING PRINCIPLE

A typical $N \times M$ MMI consists of a central multimode waveguide section, with N input waveguides and M output waveguides. For example, a 2 x 2 MMI is shown in Fig. 3.1(a). The access input and output single-mode waveguides are tapered to a multimode width near the MMI.

The operation of an MMI is governed by the self-imaging principle (also known as Talbot effect) [98]. When light is injected in one of the input waveguides, the multiple guided modes (Φ_ν, where ν is the mode number) are excited in the multimode region (see Fig. 3.1(b)), which then mutually interfere, creating periodically reproduced single or multiple images at periodic intervals along the direction of propagation (see Fig. 3.2). Hence the term "multimode interferometer".

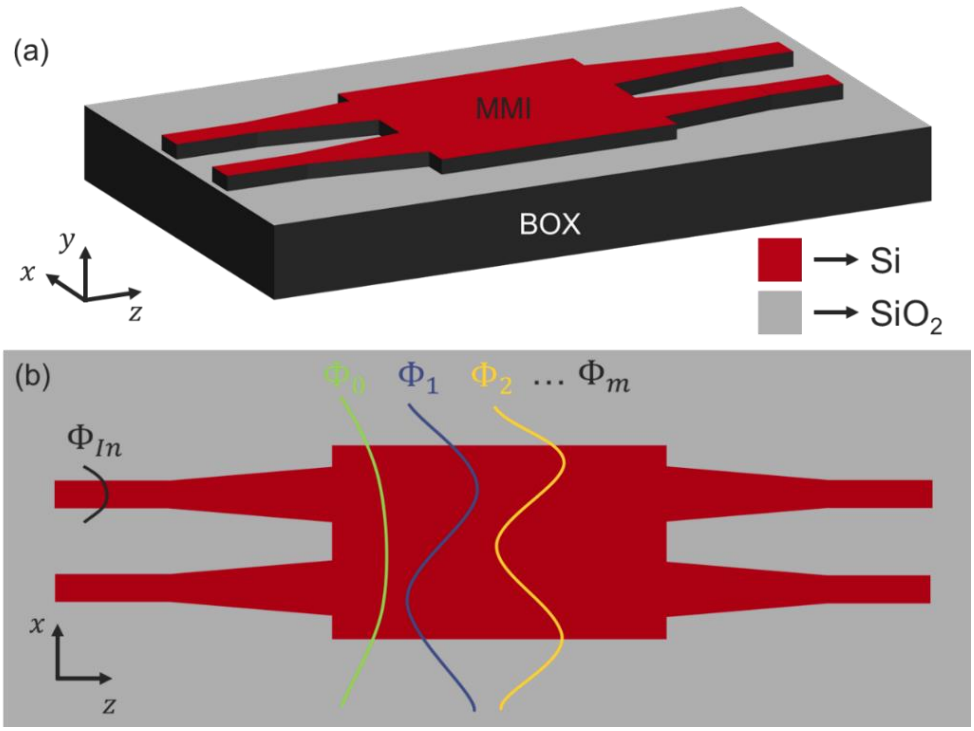

Fig. 3.1: (a) Perspective view of a 2x2 MMI. (b)Top view of the MMI. The input mode Φ_{In} excites multiple guided modes $(\Phi_0, \Phi_1, \ldots, \Phi_m)$ which then mutually interfere, creating optical field nodes at the entrance to the output waveguides. The cladding and Si substrate are not represented for clarity

The positions of the reproduced images are related to the beat length of the two lowest-order modes, L_π, as:

$$L_\pi = \frac{\pi}{\beta_0 - \beta_1} \qquad \text{Eq. (3.1)}$$

where β_ν is the propagation constant of the mode number ν.

Single images are formed at distances $z = L_{single}$:

$$L_{single} = p(3L_\pi) \text{ with } p = 0,1,2, \ldots \qquad \text{Eq. (3.2)}$$

where p is an integer and L_π is the beat length of the MMI.

When all the excited guided modes interfere in phase, a single direct image of the input field is formed at distances $x = L_{single}$ where p is an even integer in Eq. (3.2). For example, the first direct image is formed at $z = 6L_\pi$ in Fig. 3.2.

When the even modes interfere in phase and when the odd modes interfere in antiphase, a single mirrored image (with respect to the plane x = 0) of the input field is formed at positions $z = L_{single}$ where p is an odd integer in Eq. (3.2). The first mirrored image is formed at $z = 3L_\pi$ in Fig. 3.2.

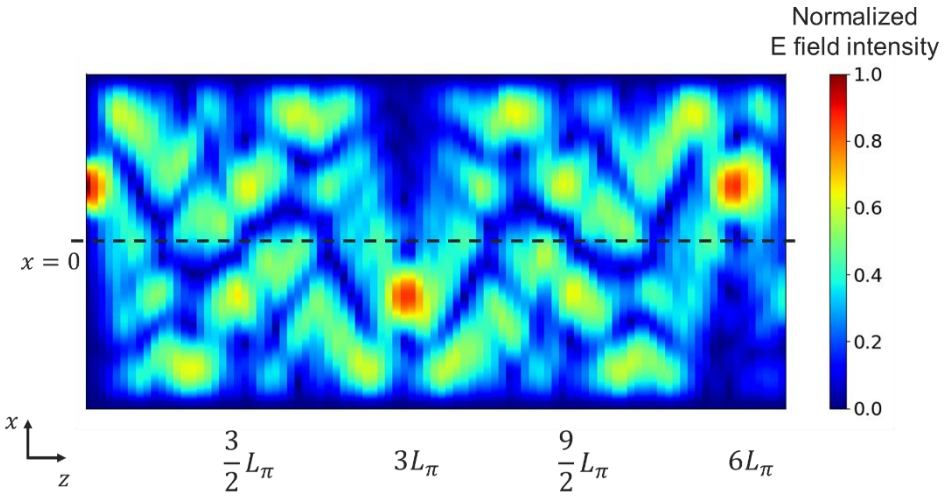

Fig. 3.2: Self-imaging principle: images of the input electric field (E field) are periodically repeated along the multimode section

3.2 THE CONVENTIONAL 2 X 2 MMI 3-DB COUPLER

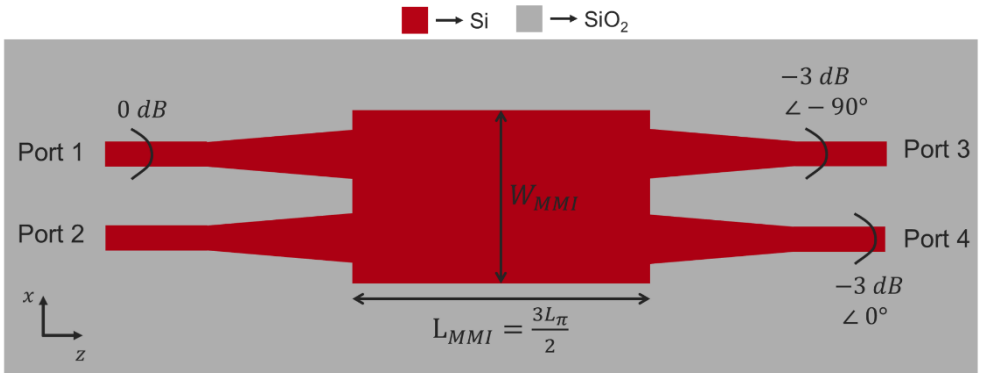

Fig. 3.3: Conventional design of a 2x2 3-dB MMI coupler, without SWGs.

In addition to the single images, multiple images can also be formed. For example, dual images are formed at distances $z = L_{dual}$:

$$L_{dual} = \frac{p}{2}(3L_\pi) \text{ with } p = 1,3,5,\ldots \qquad \text{Eq. (3.3)}$$

where p is an odd integer and L_π is the beat length.

The first dual images are formed at a distance $L = 3/2\ L_\pi$. By placing the output waveguides at the position $z = 3/2\ L_\pi$, the input beam can be split into two. The optical power in each of the output waveguides is half (-3 dB) of that of the input waveguide. The output electric fields are also in quadrature phase, with a 90° phase difference between them. Fig. 3.3 shows a 2 x 2 3-dB MMI coupler realized with this configuration.

The figures of merit of such a 2x2 MMI are defined using scattering parameters (s-parameters), which are complex amplitude transmission or reflection coefficients. For example, s_{31} is the transmission coefficient in port 3 from injection in port 1. The electric fields of the output port 3 and input port 1 are related by $E_3 = s_{31}E_1$ where E_i is the electric field in port i. Similarly, s_{11} is the reflection coefficient in port 1. The square of the s-parameters is proportional to optical power transmission or reflection. The total MMI transmission, η, is:

$$\eta = |s_{31}|^2 + |s_{41}|^2 \qquad \text{Eq. (3.4)}$$

where s_{31} and s_{41} are the complex transmission in output ports 3 and 4 respectively, from the input port 1.

Considering light injection in port 1, an ideal 2×2 3-dB MMI coupler should give $|s_{31}|^2 = |s_{41}|^2 = 0.50$ and a phase difference of -90° between ports 3 and 4, $\angle(s_{31}/s_{41}) = -90°$. However, depending on the MMI design, the obtained values will deviate from these ideal values.

Three commonly used figures of merits are:

1. Excess loss (EL), in dB, which is 10 times the negative log of the total transmission in ports 3 and 4, η. Ideally, η = 1 and EL = 0 dB. A lossy MMI has $\eta < 1$ and EL > 0 dB.

$$EL(dB) = -10\log(\eta) \qquad \text{Eq. (3.5)}$$

2. Power imbalance (IB), in dB, which is the 10 times the negative log of the optical power ratio between ports 3 and 4. Ideally, IB = 0 dB as $|s_{31}|^2 = |s_{41}|^2$. An unbalanced MMI has IB > 0 dB.

$$IB(dB) = 10\log\left(\frac{|s_{31}|^2}{|s_{41}|^2}\right) \quad \text{Eq. (3.6)}$$

3. Phase errors (PE) which are the deviation from the expected -90° phase difference between ports 3 and 4. In ideal MMI has PE = 0° and a non-ideal one has $PE \neq 0°$.

$$PE\ (°) = \angle\left(\frac{s_{31}}{s_{41}}\right) - (-90°) \quad \text{Eq. (3.7)}$$

Using these figures of merit, conventional MMIs based on Si waveguides are usually designed for use at a specific wavelength. The 1-dB bandwidth (wavelength range for which the excess losses are ≤ 1 dB) is around 100 nm at telecom wavelengths, limiting its use for broadband applications.

3.3 SWGs FOR ENHANCED MMI BANDWIDTH

Since the MMI length is fixed, only the images formed at the output port positions will be effectively outcoupled. Hence, for the MMI to have a large operational bandwidth, the images should be formed at the same position independently of the wavelength. In other words, the beat length of the MMI should be independent of the wavelength.

For a conventional MMI, the beat length L_π^{conv} can be approximated by re-writing Eq. (3.1) as:

$$L_\pi^{conv} \approx \frac{4W_e^2}{3\lambda} n_{eff,MMI} \quad \text{Eq. (3.8)}$$

where λ is the wavelength, $n_{eff,MMI}$ is the effective index of the multimode region and W_e is the effective waveguide width, which takes into account the lateral penetration depth of each mode [98]. On high index contrast platforms, such the SOI platform, the penetration depth is very small and $W_e \approx W_{MMI}$, where W_{MMI} is the width of the multimode region. L_π^{conv} is proportional to $1/\lambda$.

A typical design for an MMI for TE polarized light and SOI thickness of 220 nm is considered. The waveguide width is 3.25 μm. The beat length

is determined by calculating the effective indices, n_{eff}, of the two lowest order modes (using Ansys Lumerical mode-solver) and using Eq. (3.1). As shown in Fig. 3.4, L_π varies from 23 – 33 μm on the 1300 – 1700 nm wavelength range. The images at different wavelengths are formed over a wide range of positions, limiting the bandwidth of the conventional MMI to around 100 nm.

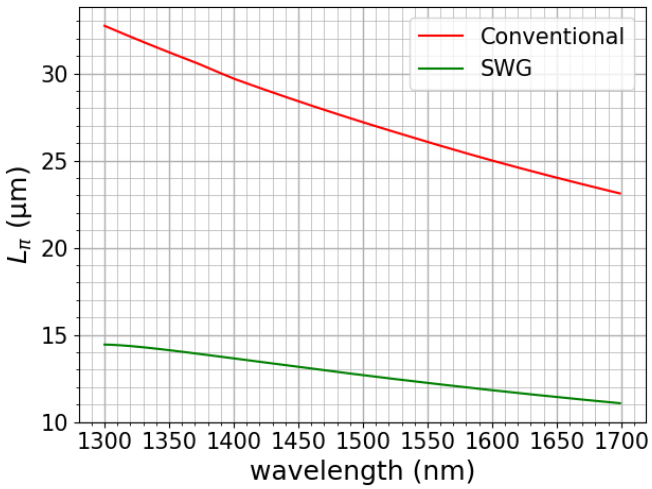

Fig. 3.4: Beat length (L_π) of a conventional and of a SWG-MMI

This variation in beat length can be mitigated by segmenting the central multimode region and tapering the access waveguides with SWGs [56,99], as shown in Fig. 3.5.

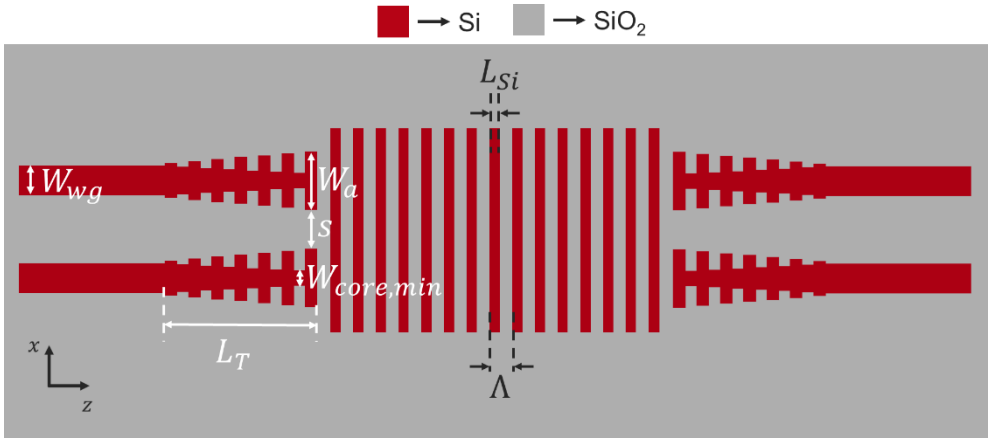

Fig. 3.5: Schematic of a 2x2 SWG-MMI

The SWG multimode region acts as an anisotropic metamaterial with a diagonal index tensor $diag(n_\parallel, n_\parallel, n_\perp)$ which can be estimated using the laminar material model [33]. $n_\parallel$ and $n_\perp$ are the equivalent SWG

refractive indices when the electric field is parallel or perpendicular to the SWG interfaces, which are parallel to the x-y plane. The beat length of the SWG-MMI, L_π^{SWG} can then approximated as [56]:

$$L_\pi^{SWG} \approx \frac{4W_e^2}{3\lambda}\frac{n_\perp^2}{n_\parallel} \qquad \text{Eq. (3.9)}$$

where W_e is the effective SWG waveguide width, λ is the wavelength, $n_\perp$ and $n_\parallel$ are the SWG-equivalent indices parallel and perpendicular to the SWG interfaces.

By varying the SWG period Λ and the duty cycle DC, the $n_\perp^2/n_\parallel$ term (SWG anisotropy) can be engineered to compensate for the wavelength dependence of $1/\lambda$ and reduce the variation in the beat length. Fig. 3.4 shows the calculated beat length for an MMI based on the design for the 220 nm-thick SOI platform given by Halir et al. in [56]. The MMI geometrical parameters are defined in Fig. 3.5. The following SWG parameters have been chosen as illustration: $\Lambda = 190$ nm, L_{Si} = 120 nm, giving $DC \sim 0.63$. The SWG MMI width is 3.25 μm, like the conventional design, and the injected light is TE polarized. Using the laminar model, $n_\parallel \approx 2.99, n_\perp = 2.17$ are obtained at λ = 1550 nm. This anisotropic material is added into Lumerical's mode solver and L_π was then determined from the effective indices of the two lowest order modes and Eq. (3.1).

As shown in Fig. 3.4, the beat length, L_π, varied from 11 – 14.5 μm for the SWG-MMI over the 1300 – 1700 nm wavelength range, which is a smaller variation than that of the conventional MMI. By reducing the variation of L_π, the MMI exhibits a greater bandwidth. Moreover, the L_π of the SWG-MMI is about half of that of the conventional design, making the SWG MMI shorter, as the MMI length is proportional to the beat length.

In addition to calculating the L_π based on the laminar model, the SWG-MMI is simulated using 3D-FDTD to determine its figures of merit. To inject light into the SWG multimode region, SWG tapers are implemented to provide a smooth index transition from the strip single-mode waveguide to the SWG multimode region [100]. A multi-mode waveguide is used at the MMI input to control the number

of excited modes and reduce losses due to radiation [101]. The SWG period and duty cycle are the same as in the multimode region. The core silicon was linearly varied from w_{wg} to $w_{core,min}$. The SWG width was also linearly varied from w_{wg} to W_a. The minimum separation between the access waveguides was s = 300 nm.

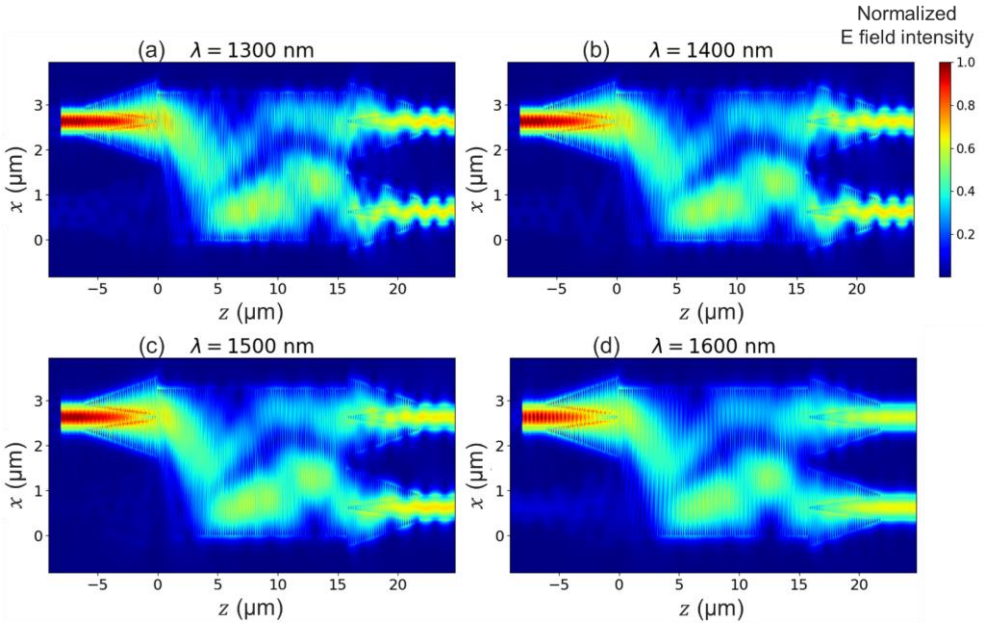

Fig. 3.6: Electric field intensity in a 2x2 SWG-MMI at different wavelengths: (a) λ = 1300 nm, (b) λ = 1400 nm, (c) λ = 1500 nm (d) λ = 1600 nm, illustrating its broadband operation. The SWG period was $\Lambda = 190$ nm, the duty cycle was $DC \approx 0.63$. The MMI length was $L_{MMI} \approx 15.86$ μm and the MMI width was $W_{MMI} \approx 3.25$ μm.

The optimized MMI parameters are given in Table 3.1 for Λ = 190 nm, L_{Si} = 120 nm (giving $DC \approx 0.63$) and $L_{MMI} \approx 15.86$ μm. The resulting electric field intensity of the 2x2 SWG MMI at different wavelengths are shown in Fig. 3.6. The optimized device yields calculated excess losses, EL < 1 dB, a power imbalance, IB < 1 dB, and phase errors, PE < ± 5° on a large wavelength range of 1250 – 1650 nm, resulting in a nominal useable bandwidth of at least 400 nm.

Parameter	Symbol	Value
SWG Period	Λ	190 nm
Length of Si in 1 SWG Period	L_{Si}	120 nm
SWG Duty Cycle	DC	0.63
Number of SWG Periods in the multimode region	N_{SWG}	83
MMI Length	L_{MMI}	15.86 µm
MMI Width	W_{MMI}	3.25 µm
Access width	W_a	1.70 µm
Access separation	s	300 nm
Taper Length	L_T	6.08 µm
Waveguide width	W_{wg}	500 nm
Minimum Si core width in SWG taper	$w_{core,min}$	74 nm

Table 3.1: 2x2 SWG-MMI parameters

3.4 LITERATURE REVIEW OF SWG-MMIS

The aim of this section is to illustrate how SWGs have been implemented in MMIs for performance enhancing. It is divided into two parts: bandwidth expansion and polarization control.

3.4.1 Bandwidth expansion

The broadband 2x2 SWG-MMI, consisting of a simple binary Si/SiO_2 grating as shown in Fig. 3.5, was first proposed by Maese Novo et al. [99]. This design was experimentally characterized after e-beam fabrication on a 220 nm-thick SOI platform [56]. A 1-dB bandwidth of 325 nm was measured on a wavelength range of 1375 – 1700 nm. In a joint work between C2N, CEA-Leti and ST-Microelectronics, a similar 2x2 SWG-MMI was fabricated using immersion lithography, but on a 300 nm-thick SOI platform [83]. The measured 1-dB bandwidth was 1480 – 1680 nm (200 nm). A summary is given in Table 3.2.

Type of MMI and its fabrication	**L_{MMI} x W_{MMI} (µm x µm)**	**MFS**	**1-dB bandwidth (nm)**	**Reference**
Conventional MMI	38.5 x 3.25	500 nm (input waveguide)	1500-1600 $\Delta\lambda = 100$	2016 Halir et al. [56]
SWG MMI 220 nm SOI e-beam	14 x 3.25	95 nm	1375-1700 $\Delta\lambda = 325$	2016 Halir et al. [56]
SWG MMI 300 nm SOI Imm. litho	19 x 3.25	75 nm	1480-1680 $\Delta\lambda = 200$	2021 Vakarin et al. [83]
SWG MMI 220 nm SOI Imm. litho	15.86 x 3.25	95 nm or 70 nm	1330-1680 $\Delta\lambda = 350$	Our work

Table 3.2: Reported 2x2 SWG-MMIs, with a comparison to a conventional design, Imm. Litho = immersion lithography, L_{MMI} and W_{MMI} are the MMI lengths and widths respectively. The minimum feature size (MFS) and experimental 1-dB bandwidths are given.

These types of broadband SWG-MMIs, made of simple binary gratings (as shown in Fig. 3.5), are garnering increasing interest. For instance, they have been implemented for broadband mode multiplexing [102,103] and for heterodyne mixing in optical hybrids [104] at telecom wavelengths. They have also been studied for sensing applications at mid-infrared wavelengths [105]. Such SWG-based MMI were also demonstrated in an angled-cut MMI with an arbitrary splitting ratio to increase the bandwidth from 40 nm (without SWGs) to 100 nm (with SWGs) [106].

Other broadband MMIs include sidewall SWG-MMIs [107,108], and other structures [109,110]. An ultrabroadband and polarization independent 1x2 SWG-MMI (see Fig. 3.7(a)) was proposed by Han et al. [111]. They have measured a 1-dB bandwidth over a wavelength range of 1260 – 1680 nm for both TE and TM input polarizations.

3.4.2 Polarization control

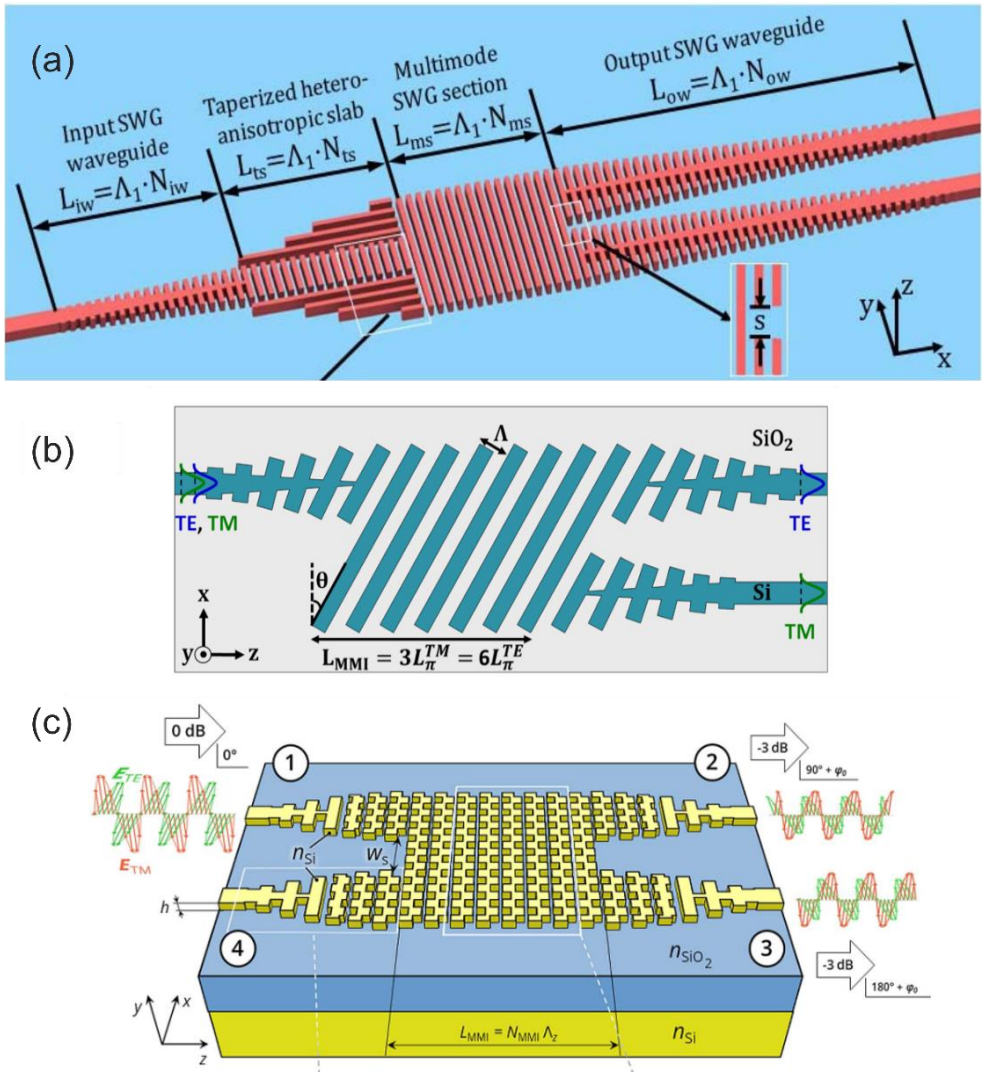

Fig. 3.7: (a) Polarization independent and ultra-broadband 1x2 SWG-MMI, image from Han et al. [111] (b) Tilted SWG-MMI for polarization splitting, image from Herrero-Bermello et al. [112] (c) Bricked SWG-MMI for polarization independence, image from Pérez-Armenta et al. [113]

The simple SWG structure as shown in Fig. 3.5, has also been used for a polarization management function to implement a polarization splitting MMI [114]. Polarization splitting was also achieved using tilted SWGs [112], depicted in Fig. 3.7(b), and other SWG structures [115,116]. By engineering the anisotropy of the SWGs, polarization independence was achieved using a bricked structure [117] (see Fig. 3.7(c)) or a central SWG slot [118]. Dual mode (TE_0 and TE_1) broadband SWG-MMIs have also been

proposed in [119,120]. Higher order mode conversion from TE_0 to TE_1 was also proposed using an SWG MMI [121].

3.4.3 Aim of our work

Our literature review showed that various SWG structures have been implemented in MMIs, improving their performance in terms of spectral bandwidth or polarization management. Most of them have been fabricated using e-beam lithography, except for the one reported by Vakarin et al. [83], in which a 2x2 broadband SWG MMI was fabricated using immersion lithography at ST-Microelectronics facilities. Our literature review also indicated that this type of broadband SWG MMI is gaining significant interest for telecom and sensing applications. It would therefore be advantageous to implement such an SWG-MMI in CEA-LETI's process design kit (PDK).

The aim of our work is to design and fabricate a similar 2x2 SWG-MMI, using immersion lithography and OPC at the CEA-LETI pilot line, and to validate its performance as part of an effort to make SWG-engineered devices available on an industrial scale.

3.5 Methodology and results

This section covers the design of experiment, in which the varied SWG-MMI parameters are presented, followed by the fabrication steps, and the experimental characterization.

3.5.1 Design of experiment

The SWG MMI is designed on a 220 nm-thick SOI platform for use with light in the fundamental TE polarization state. The BOX thickness was 2 µm. As shown in section 3.3, our simulations indicate that an SWG period of Λ = 190 nm, with a duty cycle of $DC \approx 0.63$, and a length of $L_{MMI} \approx 15.86$ µm, can give the SWG-MMI an ultra-broad bandwidth of 400 nm over the 1250 – 1650 nm wavelength range.

Our design of experiment consisted of: i) three different devices with fixed $L_{MMI} \approx 15.86$ µm, and duty cycles of $DC \approx 0.37$, 0.50, 0.63, and ii) three different devices with a fixed DC = 0.50 and lengths of $L_{MMI} \approx 14.81$ µm, 15.86 µm, 16.81 µm. These lengths corresponded to

different a number of SWG periods of N_{SWG} = 78, 83 and 88 respectively. All the MMIs in the design of experiment have a width of W_{MMI} = 3.25 µm. The following sections describe their fabrication and experimental characterization.

3.5.2 Fabrication

The SWG-MMI was fabricated using immersion lithography, with a single full-etch step. An upper SiO_2 encapsulation was then added. The nominal and OPC layouts of an SWG-MMI with an SWG period Λ = 190 nm and DC = 0.63 are shown in Fig. 3.8(a)-(c). After OPC, the lines are narrower, with modified edges. The smallest feature is the SiO_2 length, L_{SiO2} = 70 nm. An SEM image of the SWGs before cladding deposition is shown in Fig. 3.8(d).

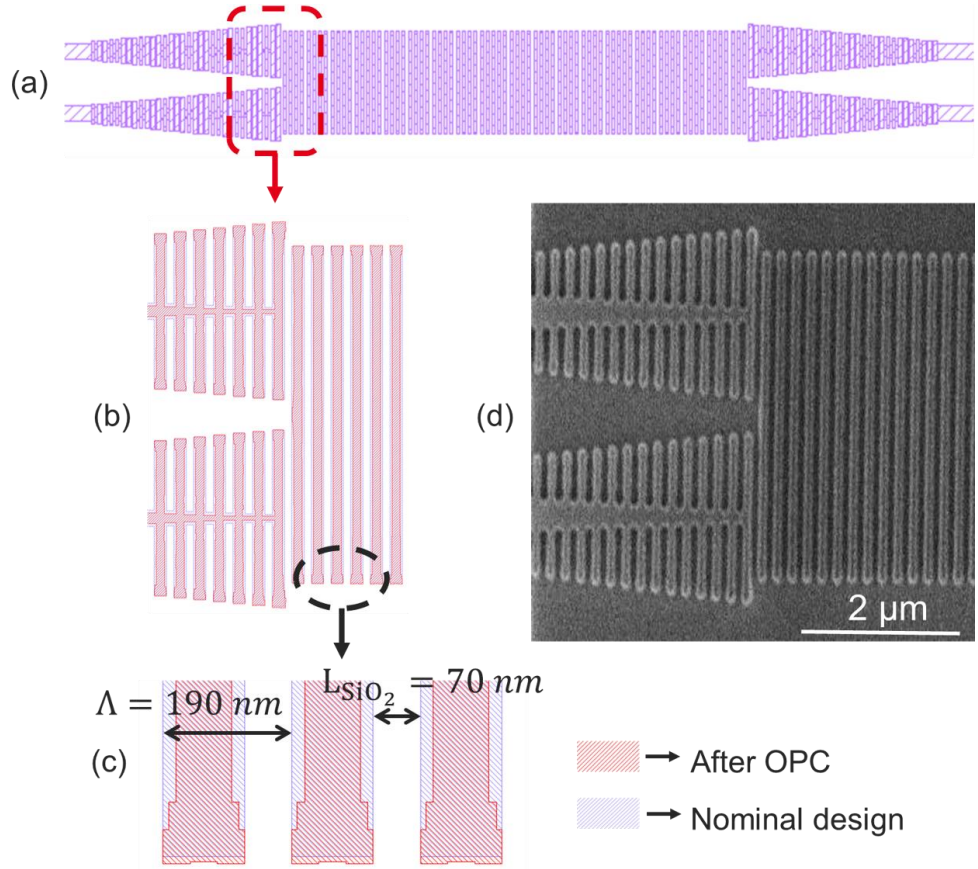

Fig. 3.8: (a)-(c) Nominal and OPC layouts of the SWG-MMI. The OPC model made the Si lines in the SWG narrower and modified the SWG edges. (d) Corresponding SEM image before the SiO_2 cladding deposition

Fig. 3.9 shows SEM images of SWG-MMI multimode sections with the three different duty cycles considered in our design of experiment, $DC \approx 0.37, 0.50, 0.63$. The measured SiO_2 lengths, L_{SiO_2}, were relatively close to the nominal values. The maximum deviation between the measured and nominal L_{SiO_2} was 8 nm in the SWG MMI with $DC = 0.37$. These results demonstrate that the OPC calibration is good, but further optimization is possible.

(a) DC ≈ 37 %

$L_{SiO_2}(measured) \approx 112\ nm$

$L_{SiO_2}(nominal) = 120\ nm$

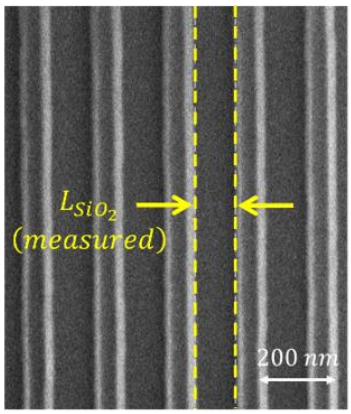

(b) DC ≈ 50 %

$L_{SiO_2}(measured) \approx 92\ nm$

$L_{SiO_2}(nominal) = 95\ nm$

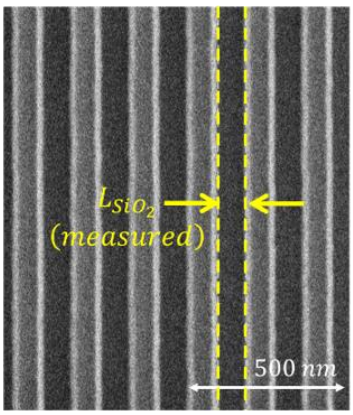

(c) DC ≈ 63 %

$L_{SiO_2}(measured) \approx 73\ nm$

$L_{SiO_2}(nominal) = 70\ nm$

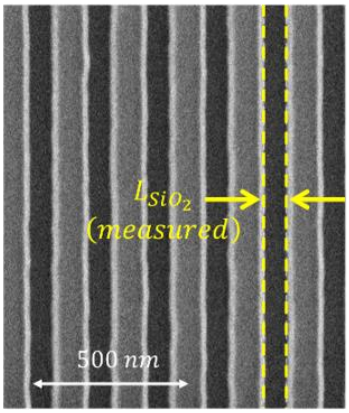

Fig. 3.9: SEM images of SWG MMI sections with different duty cycles, DC. (a) DC ≈ 0.37, (b) DC ≈ 0.50, (c) DC ≈ 0.63.

3.5.3 Experimental characterization protocol

Experimental characterizations were carried out at the C2N facilities. The characterization bench is schematically represented in Fig. 3.10. A tunable laser source is connected to a CT400 passive component tester. The laser output of the CT400 is connected to a polarization controller which is adjusted to inject TE-polarized light into the chip, using a cleaved SMF-28 single mode fiber. The same kind of fiber is used to collect the light from the output grating coupler. The transmission is characterized as a function of the wavelength using the CT400.

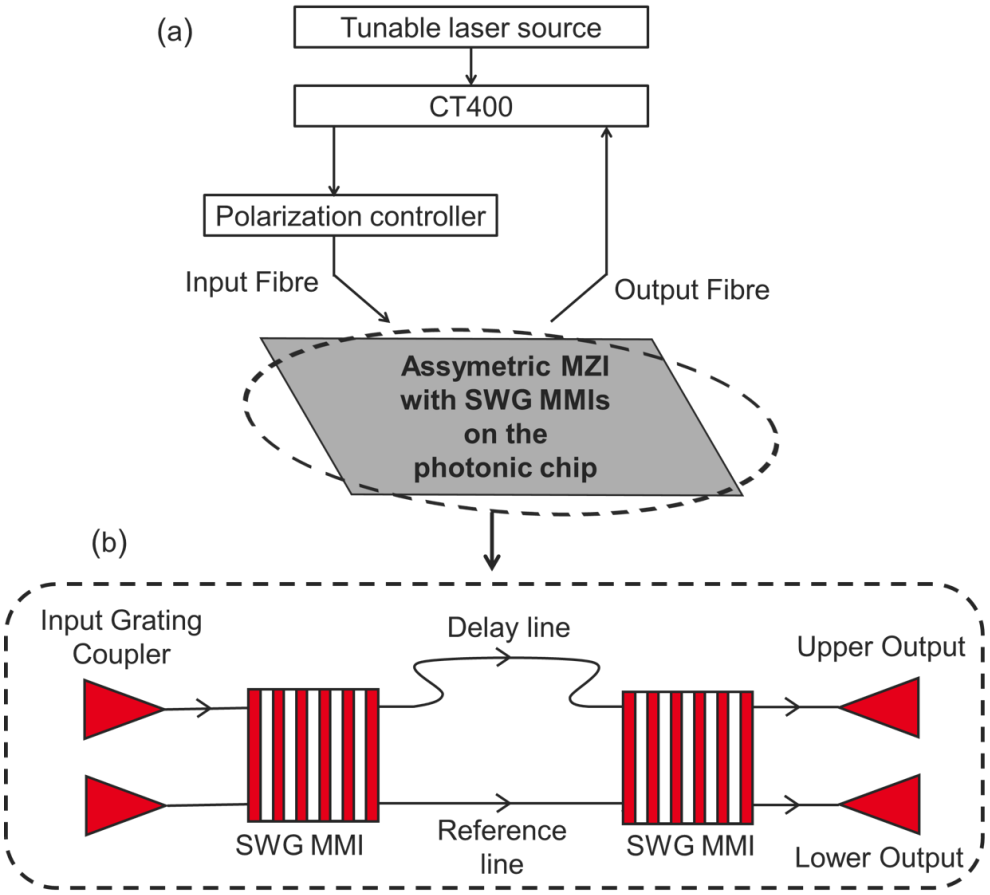

Fig. 3.10: (a) Characterization bench (b) Photonic circuit based on an asymmetric Mach-Zehnder interferometer (MZI) containing two nominally identical SWG-MMIs.

Fig. 3.10(b) describes the asymmetric Mach-Zender interferometer (MZI) configuration used to experimentally characterize the three key figures of merit, insertion loss, imbalance and phase errors [122]. The

asymmetric MZI comprises two nominally identical SWG-MMIs. The first SWG-MMI splits the input optical beam into the delay and reference lines, which are then recombined by the second SWG-MMI. The delay and reference lines are similar single mode waveguides, with different lengths. This difference in length between the delay and reference lines, ΔL, causes the signals to recombine with a phase difference, $\Delta\Phi(\lambda) = \frac{2\pi\, n_{eff}}{\lambda}\, \Delta L$, where n_{eff} is the effective index of the delay or reference line and λ is the wavelength. Due to this phase difference, $\Delta\Phi$, constructive and destructive interference occur, depending on the wavelength, forming an interference pattern (see Fig. 3.11).

The interference pattern consists of a series of maxima and minima. The separation between two consecutive maxima or minima is referred to as the free spectral range, FSR, and is given by $FSR = \frac{\lambda^2}{\Delta L\, n_g(\lambda)}$ where n_g is the group index of the delay or reference waveguide. In our MZI circuit, $\Delta L \approx$ 515 µm and $n_g \approx 4$, resulting in a $FSR \approx$ 1 nm at $\lambda \approx$ 1550 nm.

The experimental protocol essentially consists of aligning the input and output fibers above the grating couplers, adjusting the polarization and varying the wavelength using the CT400 which piloted the tunable laser source. The transmission spectra from both the upper and lower outputs are recorded and subtracted from a previously measured transmission spectrum of a reference circuit consisting solely of the input grating and output grating couplers (without the SWG-MMIs) measured with the same fiber angles. The normalized up and down transmission spectra, which are the MZI interference patterns, are shown in Fig. 3.11. From the measured transmission spectra, the three figures of merit are determined using similar procedures as in [122–125].

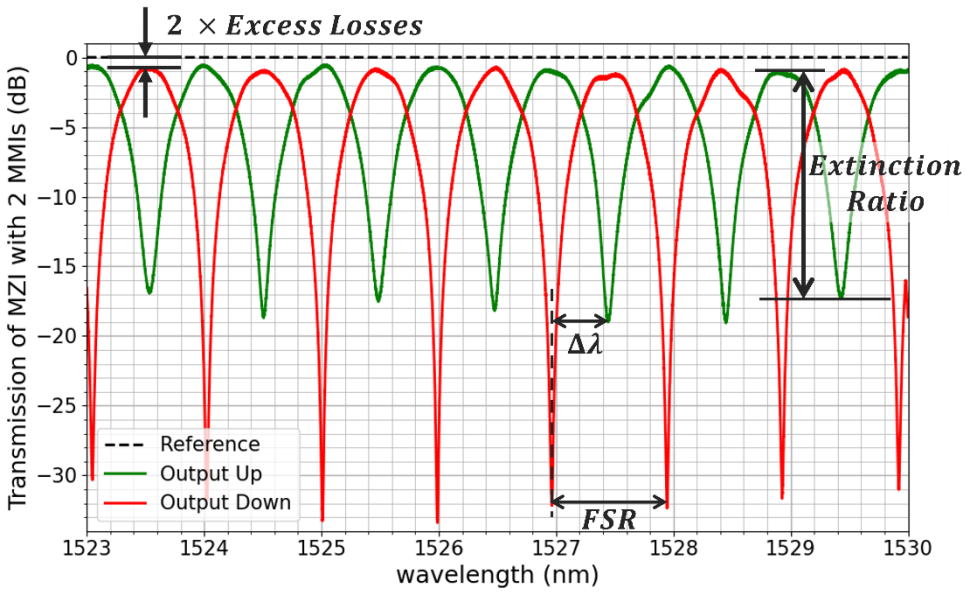

Fig. 3.11: MZI transmission from the upper and lower outputs. The response of the input and output grating couplers (from the reference circuit) were removed.

Excess losses (EL) for 1 SWG-MMI are obtained from the difference between the 0-dB reference line and the maxima of either the upwards or downwards transmissions, divided by 2. Ideally, the maxima are on the 0-dB line.

The power imbalance (IB) is determined by calculating the extinction ratios in the upper output transmission (green curve in Fig. 3.11). In dB, the extinction ratio (ER) is the difference in transmission between two adjacent maximum and minimum points. If the MMI is perfectly balanced, complete constructive and destructive interference would occur and the extinction ratio would be infinite. For an unbalanced lossless MMI, the power coupling coefficient κ can be determined from the extinction ratio as in Eq. (3.10) (see [123] for the derivation of the equation).

$$\kappa = \frac{1}{2} \pm \frac{1}{2}\sqrt{\frac{1}{10^{\frac{ER(dB)}{10}}}} \qquad \text{Eq. (3.10)}$$

where $ER(dB)$ is the extinction ratio in dB.

The power coupling coefficients of a lossy MMI in the two MMI output arms are $\eta\kappa$ and $\eta(1-\kappa)$ where η is the total transmission of the MMI:

$\eta = 10^{-\frac{EL\,(dB)}{10}}$. The magnitude of the power imbalance (IB) is given by the ratio of these coefficients and is invariant of the transmission, as per Eq. (3.11):

$$IB = \left|10\log\left(\frac{\kappa}{1-\kappa}\right)\right| \qquad \text{Eq. (3.11)}$$

where κ is the power coupling coefficient in the output waveguide of the MMI. For a perfectly balanced MMI, with κ = 0.5, the extinction ratio, ER, tends to infinity and the power imbalance, IB, tends to 0 dB.

It is important to note that the imbalance can only be determined from the upper output port, for light injection in the upper port. As shown in Fig. 3.12, the minimum transmission is always null in the lower output port of the MZI, regardless the value of κ, causing the extinction ratio to be larger in this port, giving an incorrect value of the imbalance.

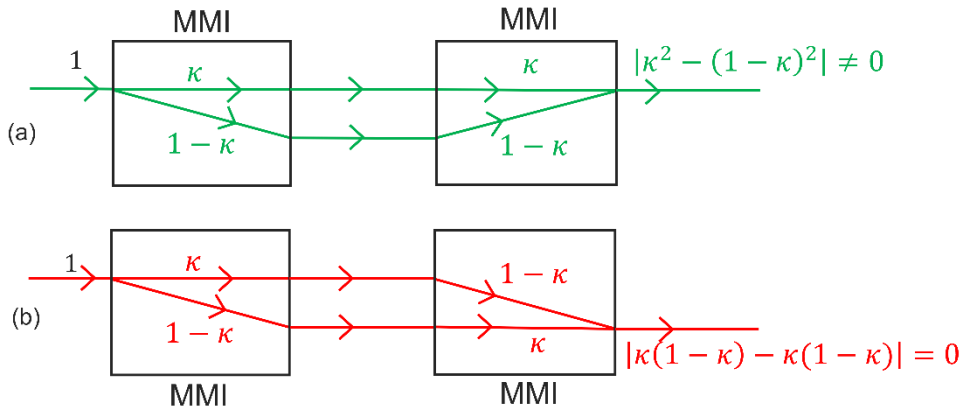

Fig. 3.12: Minimum transmission of the MZI in the (a) upper output port is non-null while (b) in the lower port is always null. In (b), the extinction ratio is infinite and cannot be used to calculate the power imbalance

The phase errors (PE) in radians are determined as:

$$PE\ (rad) = \pi\frac{\Delta\lambda}{FSR} + \frac{\pi}{2} \qquad \text{Eq. (3.12)}$$

where $\Delta\lambda$ is the difference in wavelength between a minimum in the lower output transmission and an adjacent minimum in the upper output transmission, FSR is the free spectral range (see Fig. 3.11).

Broadband characterization is carried out using 4 different tunable laser sources, each covering a specific wavelength range. Also, 2 different MZI circuits, with nominally identical SWG-MMIs, and 2 different grating couplers (GC_1 and GC_2) have been characterized. GC_1 enabled characterization in the wavelength range from 1300 – 1400 nm with fiber angles $\sim +18°$, and from 1500 – 1680 nm with fiber angles $\sim -18°$. Characterization over the remaining 1400 – 1500 nm range was enabled by GC_2 with fiber angles $\sim +18°$. In addition, due to the limited bandwidth of the grating coupler ($\sim$ 50 nm at -3 dB coupling efficiency), several measurements were made for a given laser source and MZI circuit, with slightly different fiber angles to cover smaller complementary wavelength ranges. These were then stitched together.

The resolution of the wavelength scan of the CT400 was set to 1 pm for accurate phase error measurement. The output power of each laser source was set to 2 mW, which was the maximum power delivered by one of the tunable laser sources. A higher laser power increases the chance for the minimum transmission to be greater than detector noise floor.

3.5.4 Results and discussion

This section is divided into two parts. In the first part, the measured figures of merit of the SWG MMI with a fixed MMI length, L_{MMI} = 15.86 µm, and varied duty cycles $DC \approx$ 0.37, 0.50, 0.63 are presented. Fig. 3.13, Fig. 3.14 and Fig. 3.15 show the measured excess loss, EL, power imbalance, IB, and phase errors, PE, respectively.

The different colors indicate different measurement windows with different fiber angles on the different MZI circuits (with different grating couplers) and different laser sources. They were smoothed using a moving average to give the black curve. The corresponding simulations were shown with a red dotted curve. For EL and IB, the grey dotted lines indicate the 1-dB level. For PE, they indicated the $\pm$ 5° levels.

The measured excess losses present marked discontinuities at the boundaries between different spectral windows measured with

different grating coupler angles and laser sources. In principle, the normalization with a reference waveguide should cancel out these effects. However, discrepancies appear, mainly at the band edges, far from the maximum of the peak coupling efficiency of the grating couplers. This problem could be solved in future realizations using edge couplers.

At wavelengths below 1400 nm, resonance effects are observed which result in noisier measurements in the EL, IB and PE. These resonance effects have also been observed in [56,105]. This increase in noise level could come from undesired reflections caused by an "internal resonance" between simultaneously occurring general and symmetric self-imaging mechanisms [98]. Another reason could be reflections at the sidelobes of the SWG metamaterial bandgap at these smaller wavelengths [54], which could be mitigated by reducing the SWG period.

The best results were obtained for a DC = 0.50. Considering the central wavelength per measurement window, where the measurement error is lowest, EL < 1 dB, IB < 1 dB and PE < $\pm$ 5° were obtained on the wavelength range λ = 1330 – 1680 nm. They agreed well with the simulations on this wavelength range.

Reasonably good results were obtained for a $DC \approx 0.63$. Similar results were obtained as with the DC = 0.50 on the same large wavelength range λ = 1330 – 1680 nm, but the measured imbalance was slightly higher, $IB \approx 1$ dB. The measured IB was also higher than simulated.
For $DC \approx 0.37$, the IB > 1 dB on the whole wavelength range and the PE < $\pm$ 5° on a smaller wavelength range λ = 1450 – 1680 nm. This performance was worse than simulated. This may be attributed to the OPC model being non-optimal for this duty cycle, resulting in higher deviations between fabricated and nominal dimensions (see Fig. 3.9(a)).

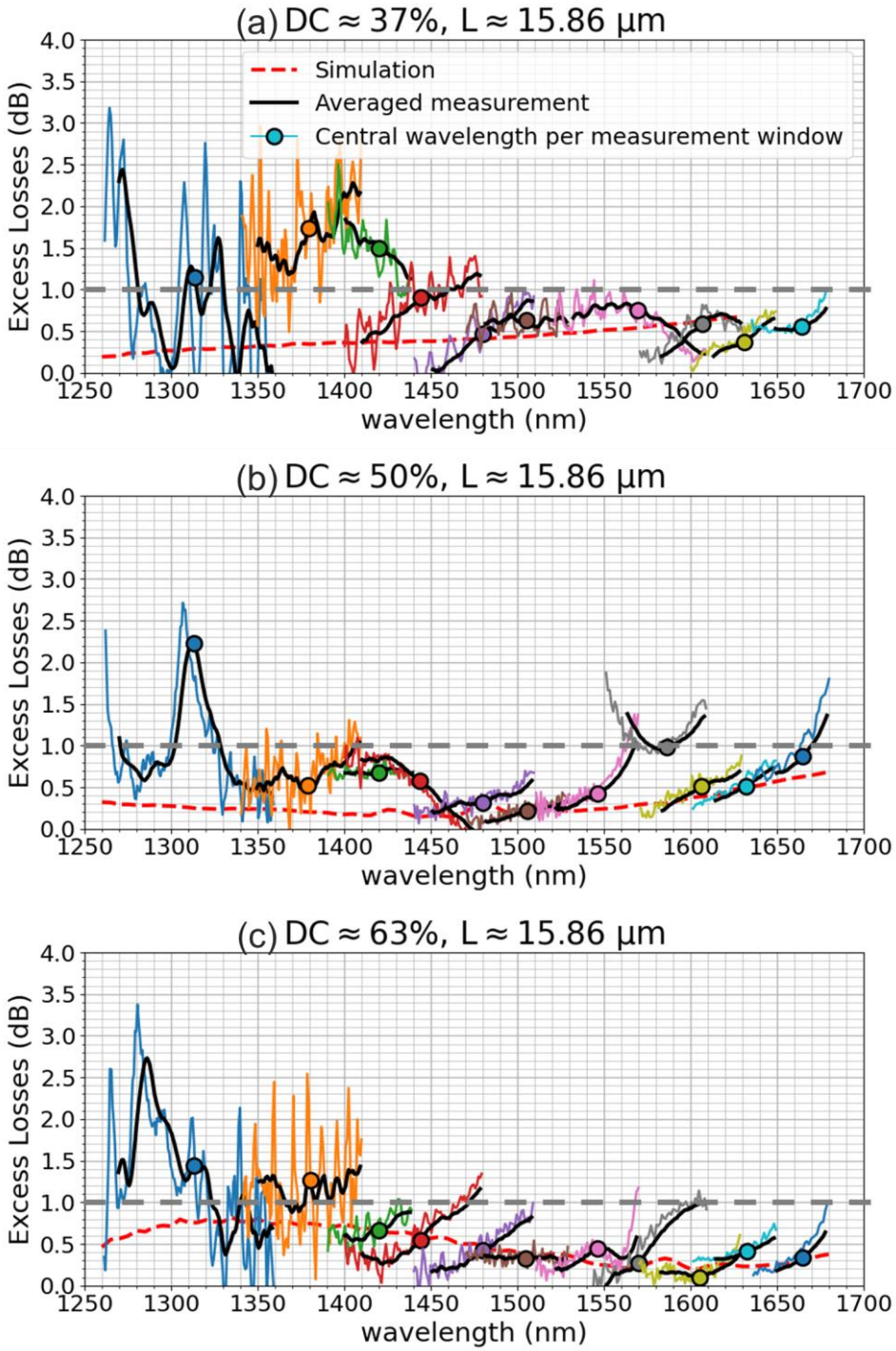

Fig. 3.13: Measured and simulated excess losses for a SWG-MMI length fixed at L_{MMI} = 15.86 µm and the duty cycles of (a) DC ≈ 0.37, (b) DC ≈ 0.50 and (c) DC ≈ 0.67. The different colors indicate the different discrete measurement windows. Black curves are the averaged measurements. The dotted red line shows the simulation results. The dotted grey line indicates the 1-dB level.

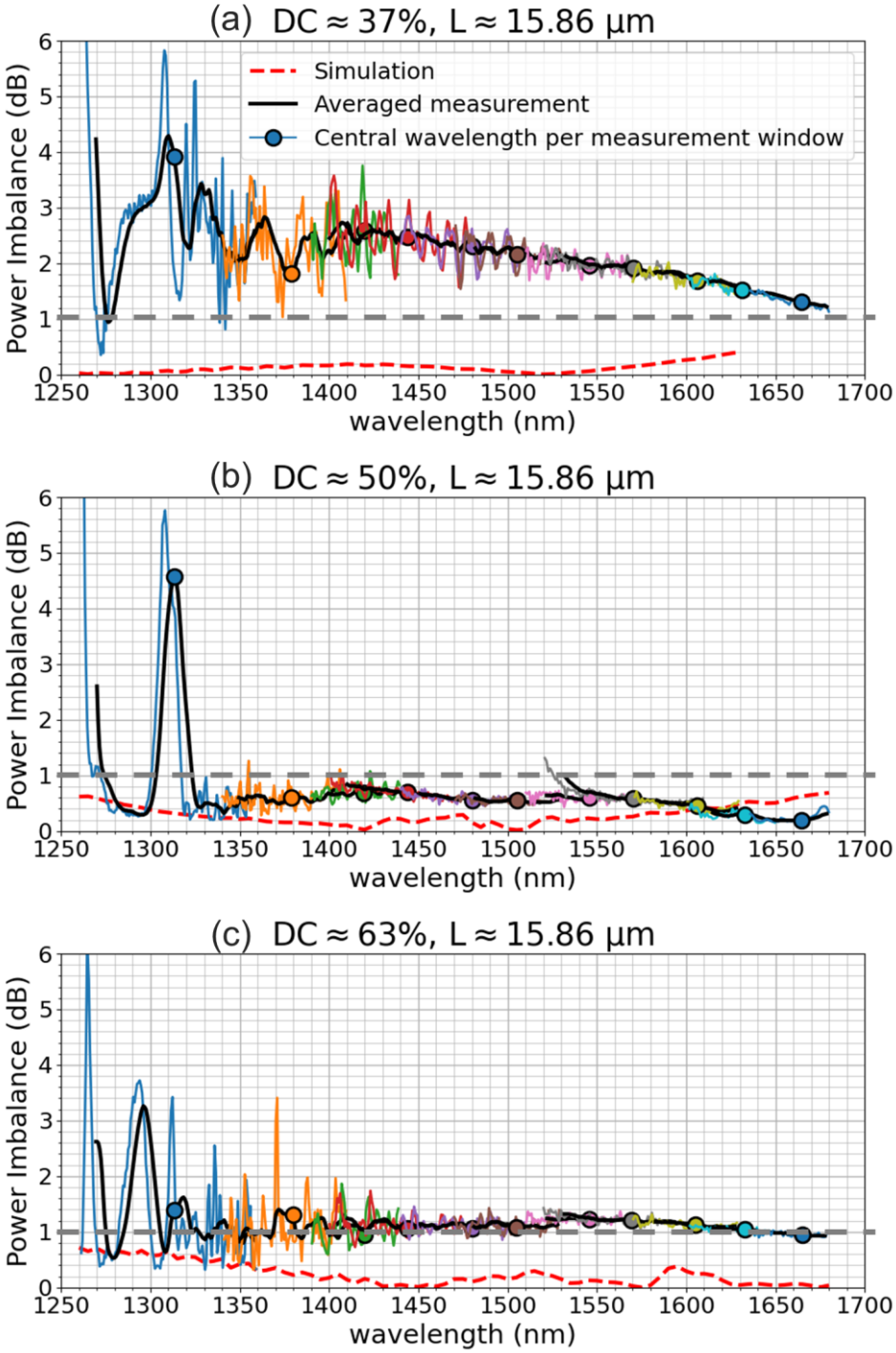

Fig. 3.14: Measured and simulated power imbalance for a SWG-MMI length fixed at L_{MMI} = 15.86 µm and the duty cycles of (a) DC ≈ 0.37, (b) DC ≈ 0.50 and (c) DC ≈ 0.67.

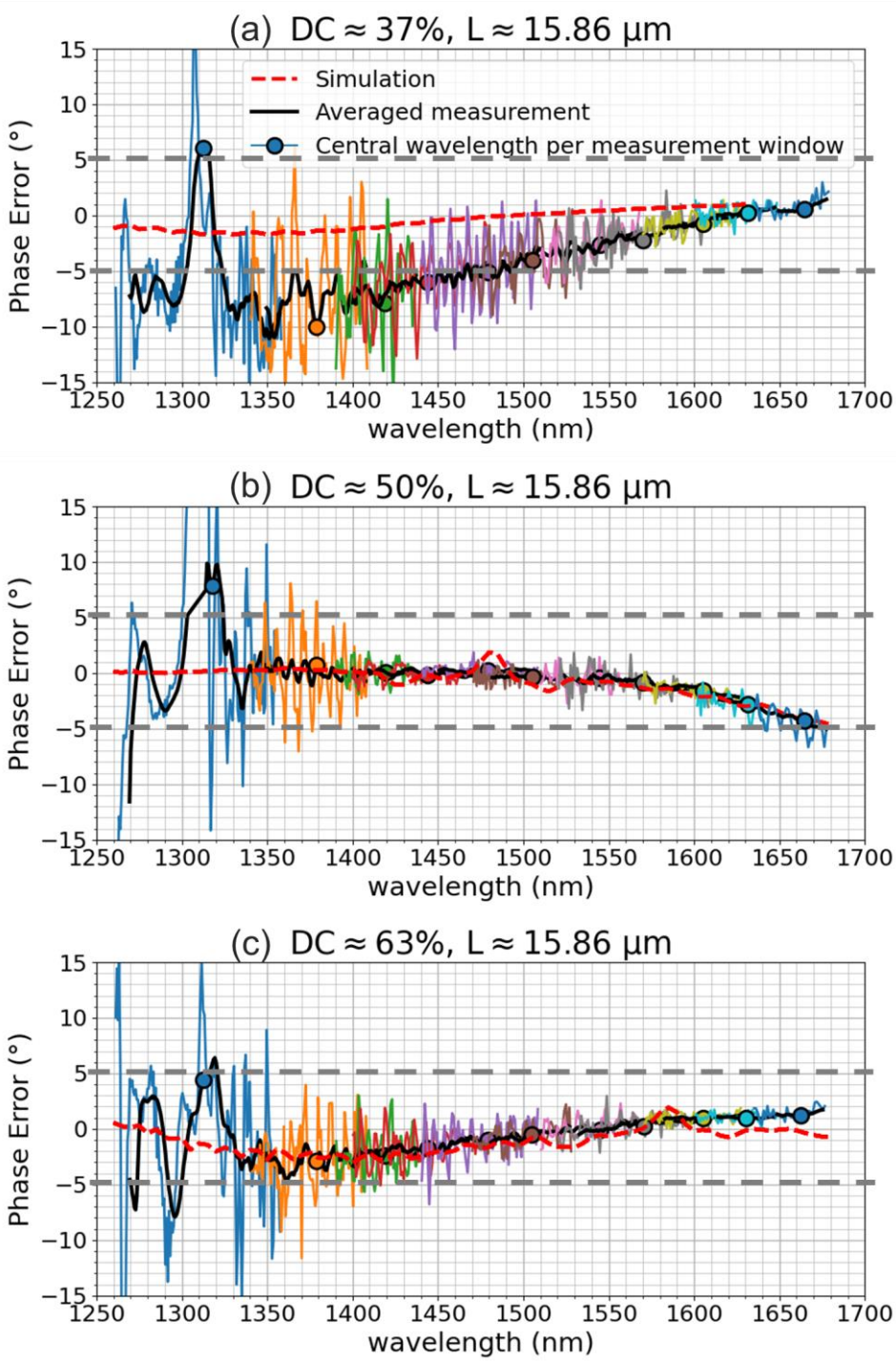

Fig. 3.15: Measured and simulated power errors for a SWG-MMI length fixed at L_{MMI} = 15.86 µm and the duty cycles of (a) DC ≈ 0.37, (b) DC ≈ 0.50 and (c) DC ≈ 0.67.

In the second part of this section, the measured figures of merit of the SWG-MMI with a fixed duty cycle, DC = 0.50, and varied MMI lengths, L_{MMI} = 14.81 µm, 15.86 µm and 16.81 µm are presented. The measured EL, IB, PE are shown in Fig. 3.16, Fig. 3.17 and Fig. 3.18 respectively.

L_{MMI} = 15.86 µm showed the best results. As mentioned earlier, the measured EL < 1 dB, IB < 1 dB and PE < $\pm$ 5° were obtained on the wavelength range λ = 1330 – 1680 nm and agreed with the simulations. If L_{MMI} = 14.81 µm, the performance is degraded, with EL < 1 dB on a smaller wavelength range λ = 1550 – 1680 nm. However, $IB \approx$ 1 dB and PE < $\pm$ 5° on a large wavelength range of λ = 1330 – 1680 nm. As for L_{MMI} = 16.81 µm, the worst performance was obtained with EL > 1 dB on almost the whole wavelength range and PE < $\pm$ 5° only on a small wavelength range λ = 1350 – 1570 nm. An IB < 1 dB was obtained on a larger wavelength range though. These results show that a deviation of $\pm$ 1 µm in the MMI length could be detrimental to the broadband operation of the SWG-MMI.

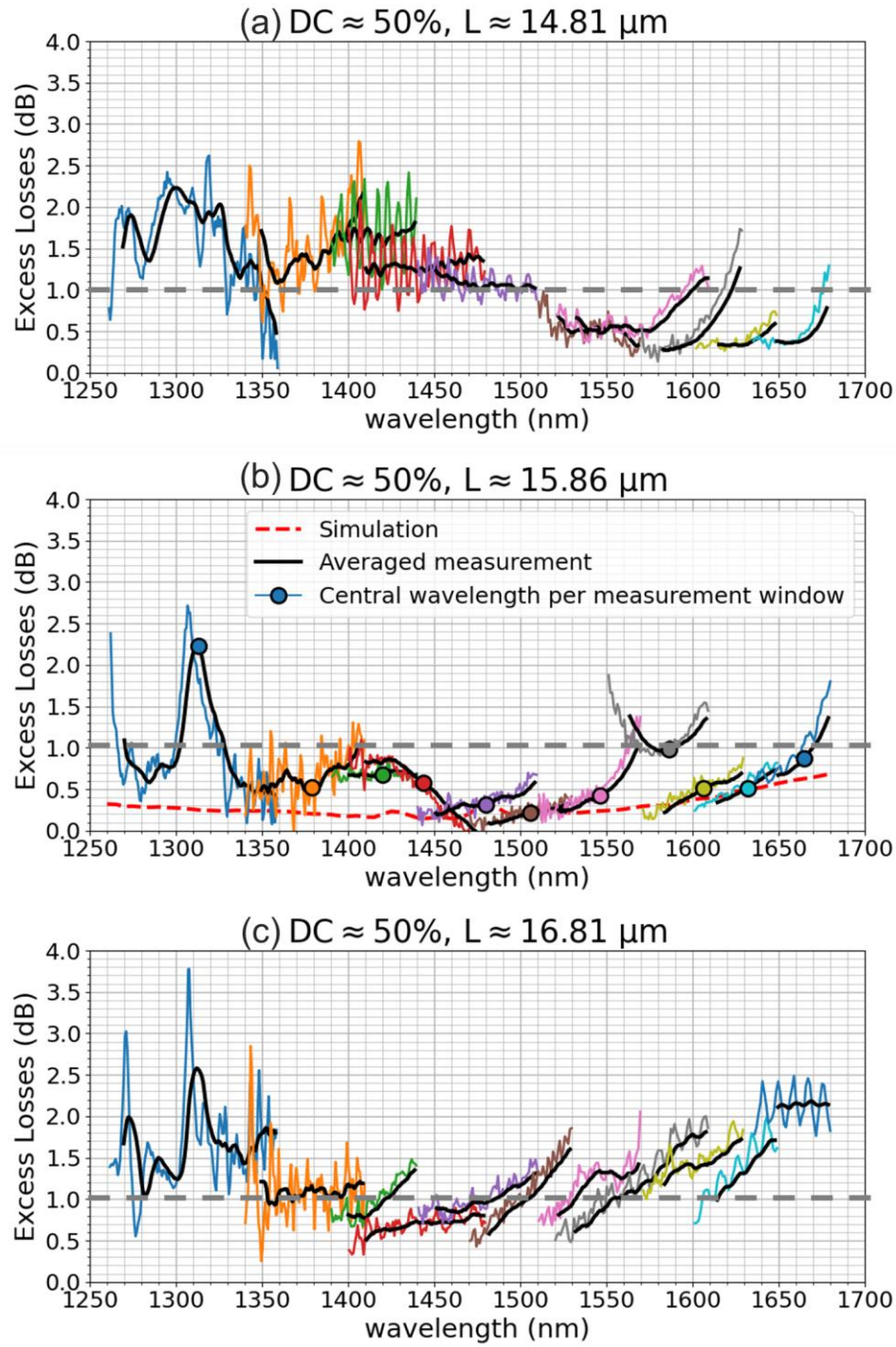

Fig. 3.16: Measured excess losses with fixed duty cycle, $DC = 0.50$ and varied MMI lengths, L_{MMI}. In (a) $L_{MMI} \approx 14.81$ µm, (b) $L_{MMI} \approx 15.86$ µm, (c) $L_{MMI} \approx 16.81$ µm.

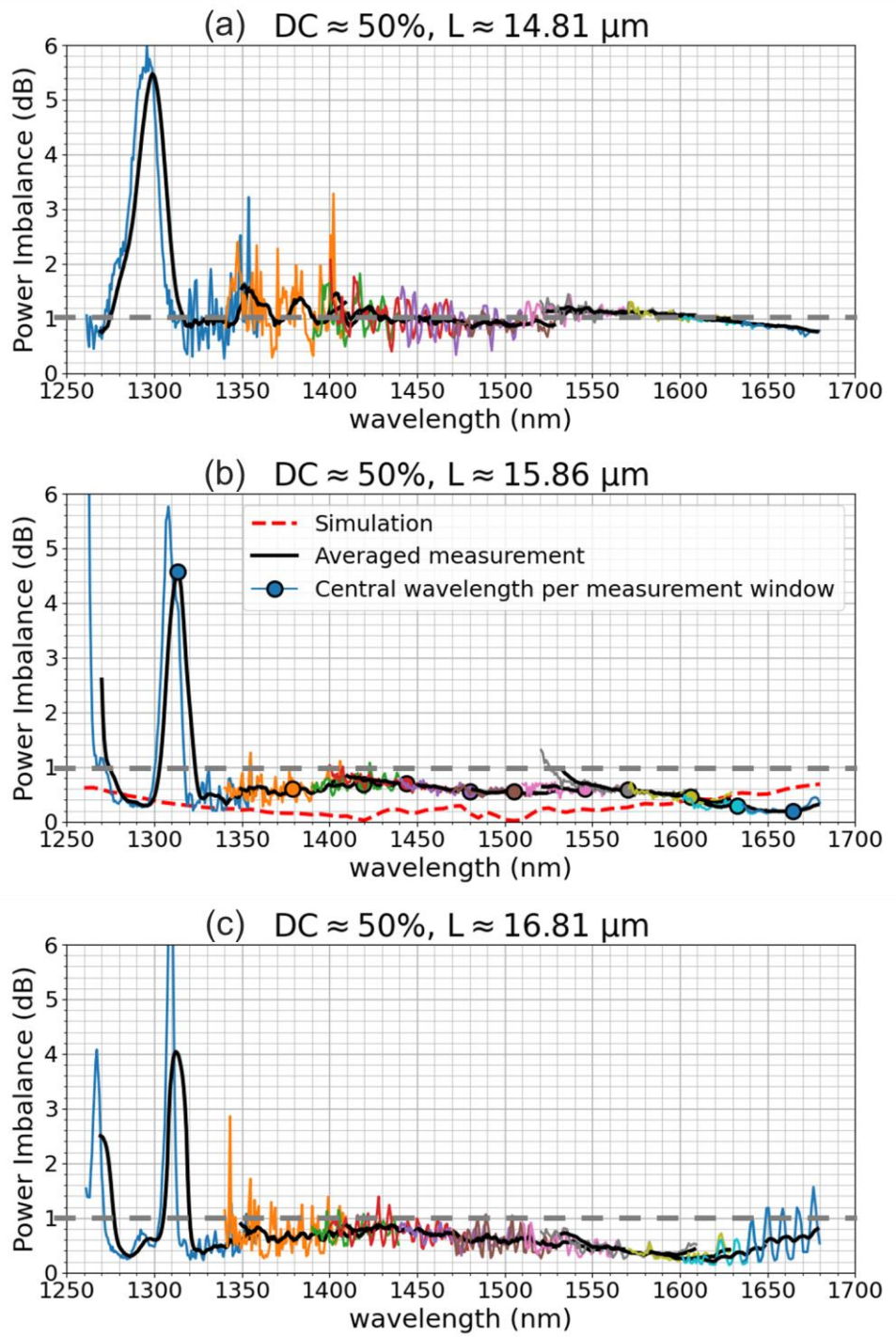

Fig. 3.17: Measured power imbalance with fixed duty cycle, $DC = 0.50$ and varied MMI lengths, L_{MMI}. In (a) $L_{MMI} \approx 14.81$ µm, (b) $L_{MMI} \approx 15.86$ µm, (c) $L_{MMI} \approx 16.81$ µm.

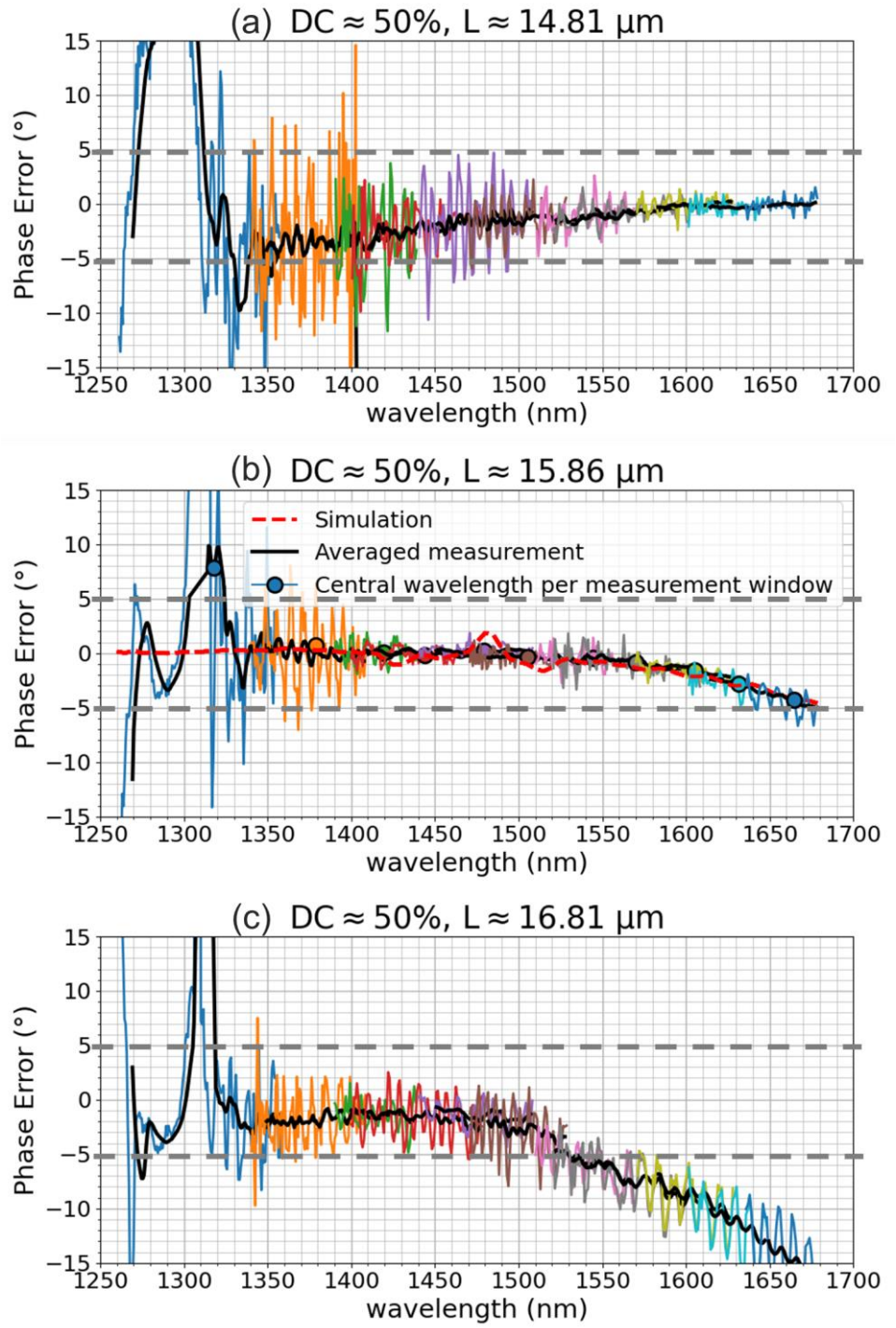

Fig. 3.18: Measured phase errors with fixed duty cycle, $DC = 0.50$ and varied MMI lengths, L_{MMI}. In (a) $L_{MMI} \approx 14.81$ µm, (b) $L_{MMI} \approx 15.86$ µm, (c) $L_{MMI} \approx 16.81$ µm.

3.6 CONCLUSION AND PERSPECTIVES

An ultra-broadband 2x2 3-dB SWG-MMI coupler, fabricated by immersion lithography at the CEA-Leti facilities, has been experimentally characterized. Excess losses, EL < 1 dB, a power imbalance, IB < 1 dB, and phase errors, PE < $\pm$ 5° have been measured over a wavelength range of λ = 1330 – 1680 nm, corresponding to a bandwidth of 350 nm, for the fundamental TE polarization. This bandwidth largely surpasses that of a conventional MMI without SWG elements (~ 100 nm). The SWG-MMI length was also half that of a conventional design.

Such a large bandwidth and reduced MMI length have been obtained by engineering the SWG modal dispersion such that the MMI beat length remained constant over a large wavelength range.

In the SWG-MMI, only a single full etch step was required. The best results were obtained with an SWG period Λ = 190 nm, and a duty cycle, DC = 0.50 (resulting into a minimum feature size of 95 nm). Reasonably good performance was also obtained with the same Λ = 190 nm and a DC = 0.63 (with a minimum feature size of 70 nm), except that the power imbalance was slightly higher (around 1 dB) on the same wavelength range of 1330 – 1680 nm. These results were presented at the Photonics North Conference in Canada in June 2023 [126].

The reported MMIs reached similar performance to another SWG-MMI with comparable dimensions but fabricated by e-beam lithography [56], indicating the feasibility of using SWG-engineered MMIs as part of industrial photonic design kits. Our demonstration also showed a larger bandwidth than another SWG-MMI fabricated using immersion lithography that was designed with a different SOI thickness [83]. However, resonance effects were observed at smaller wavelengths $\lambda \leq$ 1400 nm. The origin of this resonance must be further investigated.

4 SWG-ENGINEERED L-SHAPED GRATING COUPLER WITH HIGH COUPLING EFFICIENCY

Grating couplers are passive silicon photonics devices used to couple light between the on-chip waveguide and an external optical fiber placed above the chip surface. This chapter is dedicated to the study of a non-conventional grating coupler based on SWG metamaterials implemented on an L-shaped geometry that interleaves full and shallow etch steps. The gratings have been fabricated using immersion lithography and OPC. A high coupling efficiency with a standard optical fiber of -1.70 dB (68 %) has been measured at a wavelength of 1550 nm.

The outline of this chapter is as follows. First, the most widespread solutions to the fiber-chip coupling problem, which are edge couplers and surface grating couplers, are presented. As grating couplers allow for wafer-level testing, our work was focused on grating couplers. Their working principles and a corresponding literature review are then given. From the review, a promising high efficiency grating coupler concept, proposed by Benedikovic et al. [127], and compatible with CEA-LETI's pilot line was identified. This design uses L-shaped grating teeth combined with SWG elements. Such a grating coupler was redesigned to match CEA-LETI's fabrication specifications. Our corresponding design methodology and simulation results are then presented, followed by the fabrication and experimental characterization of the grating coupler. Finally, our conclusions and perspectives are drawn.

4.1 THE FIBER-CHIP COUPLING PROBLEM AND ITS MAIN SOLUTIONS

Efficiently interfacing an on-chip photonic waveguide with the external world (usually with optical fibers) is a key functionality for photonic integrated chips. However, efficient coupling is challenging since the modal size of the photonic waveguide (~ 500 nm) is much smaller than the mode field diameter of an optical fiber ($MFD \sim 10$ µm) [13,128,129]. Nowadays, there exists two main solutions: edge couplers (ECs) and grating couplers (GCs).

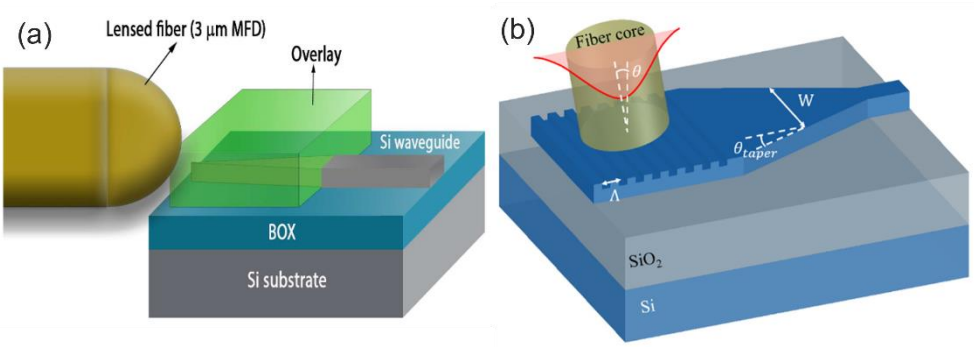

Fig. 4.1: (a) Typical edge coupler (EC). Image from Nambiar et al. [129] (b) Typical surface grating coupler (GC). Image from Cheng et al. [13]

Edge couplers, also referred to as butt, end-fire, or in-plane couplers, couple light horizontally at the lateral edges (facets) of a photonic chip to or from an optical fiber which is usually lensed. Fig. 4.1(a) schematically shows a basic EC, that consists of an inversely tapered waveguide in which the width is progressively reduced, deconfining the optical mode such that the modal size at the chip edge approaches that of the fiber. Using ECs, the typical coupling efficiency between a silicon waveguide and a single mode fiber at a wavelength of 1550 nm is around -2 dB [130]. Edge couplers have also low polarization dependent loss (< 1 dB) and can be considered broadband with typical 1-dB bandwidth exceeding 200 nm [129]. However, ECs have relatively low fiber-alignment tolerance, resulting in ~1 dB penalty for 500 nm misalignment [131]. They also suffer from a large footprint and are generally not compatible with wafer-level testing [13]. SWG-metamaterials have also been successfully used for the realization of ECs. Examples include SWGs as anti-reflective structures at the facets [132], SWGs for ultra-high coupling efficiency, bandwidth and polarization independence [53] and SWGs as metamaterial mode-size converters [133].

Grating couplers, also referred as surface or vertical or off-plane couplers, couple light by diffraction to or from an optical fiber, which is placed near-vertically above the chip surface (see Fig. 4.1(b)). More details on the working principles are given in section 4.2. Compared to ECs, GCs usually have smaller bandwidth and are highly polarization sensitive due to their diffractive nature. However, they enable practical wafer level-testing as they can be placed anywhere on the chip. Unlike ECs, GCs usually are used to couple light with standard non-lensed

fibers and have thus more relaxed fiber-alignment tolerance, with 1 dB penalty for 2 µm misalignment [131]. Achieving high coupling efficiency on a standard SOI platform, however, is challenging. Currently, grating couplers provided in CEA-Leti's PDK have coupling efficiencies of around -2 dB (63 %) at telecom wavelengths.

4.2 FIBER-CHIP GRATING COUPLER WORKING PRINCIPLE

The purpose of a GC is to couple light between a photonic waveguide on the chip and an external optical fiber. The fiber is placed near-vertically above the chip surface (see Fig. 4.2). GCs can be used as input, coupling light from the fiber into the chip waveguide, or as output, coupling light from the chip waveguide to the fiber. In both cases, the operation principles are the same.

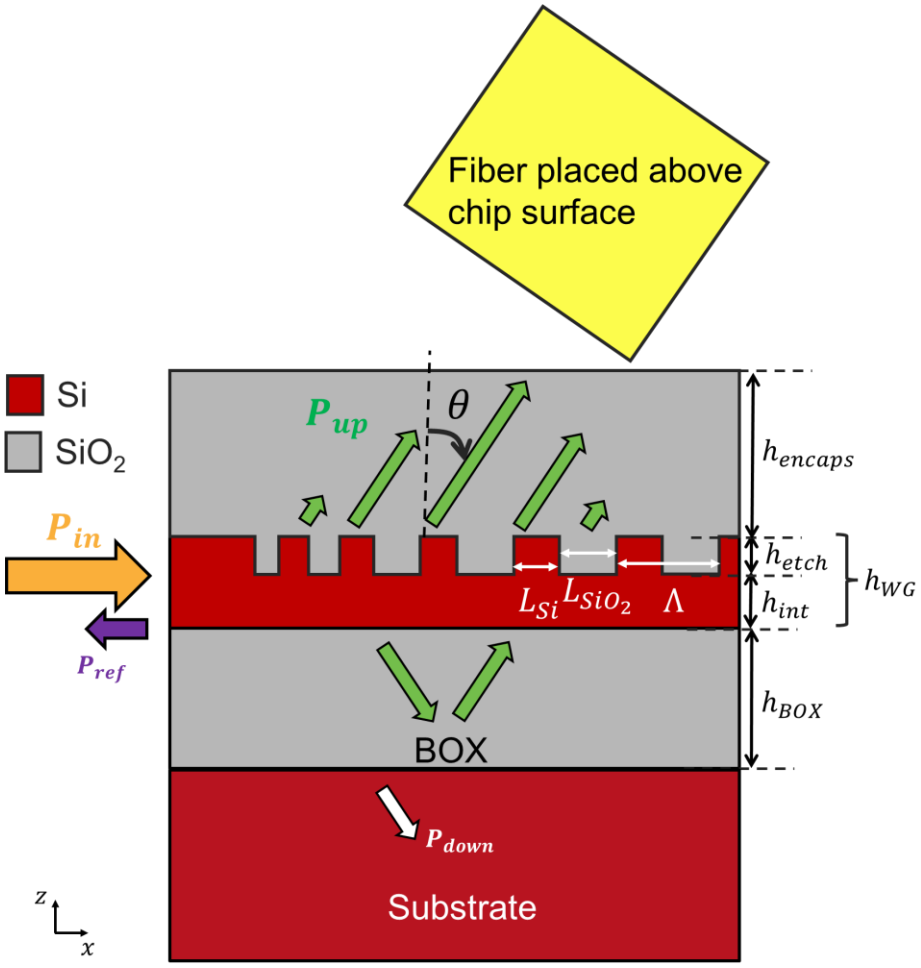

Fig. 4.2: 2D cross-section schematic of a conventional grating coupler.

To facilitate the explanation, the output GC case is considered. To simplify the problem, a 2D cross-section in the x-z plane is considered, considering an infinite size along the y-axis.

A GC is made up of periodic variations of the index profile in a waveguide. In conventional GCs, a single partial, or single full etch is usually performed to create this index profile. Each grating period, Λ, consists of an etched part of length, L_{SiO_2}, and of a silicon unetched part of length, L_{Si}. The grating period is defined as $\Lambda = L_{si} + L_{SiO_2}$. The duty cycle in each period is $DC = L_{Si}/\Lambda$.

4.2.1 Phase matching condition

As the period Λ is greater than half of the effective wavelength $\lambda/2n_{eff}$, where λ is the free space wavelength and n_{eff} the effective index of the mode supported by the grating, the GC works in the diffractive regime. Light is then diffracted following the phase matching condition:

$$n_c \sin\theta = n_B + m\frac{\lambda}{\Lambda} \qquad \text{Eq. (4.1)}$$

where n_c is the index of the upper cladding, θ is the diffraction angle in the upper cladding with respect to the vertical z-axis, m is the diffraction order, n_B is the effective index of the Bloch-Floquet mode in the grating. For an initial grating design, n_B can be approximated by an average of the effective indices in the unetched silicon regions, $n_{eff}(Si)$, and the etched regions, $n_{eff}(SiO_2)$:

$$n_B \approx DC \times n_{eff}(Si) + (1 - DC) \times n_{eff}(SiO_2) \qquad \text{Eq. (4.2)}$$

Solutions of the phase matching condition can be represented by wave vector diagrams [128]. Fig. 4.3 shows a wave vector diagram for perfectly vertical coupling. Although this configuration is desirable to facilitate packaging, it is often avoided as the grating operates in the Bragg reflection regime, causing high reflections into the waveguide via the m = 2 diffraction order. This Bragg reflection is usually avoided by designing the grating to emit the first order at a small angle from the vertical, typically ~ 8° in the SiO_2 encapsulation.

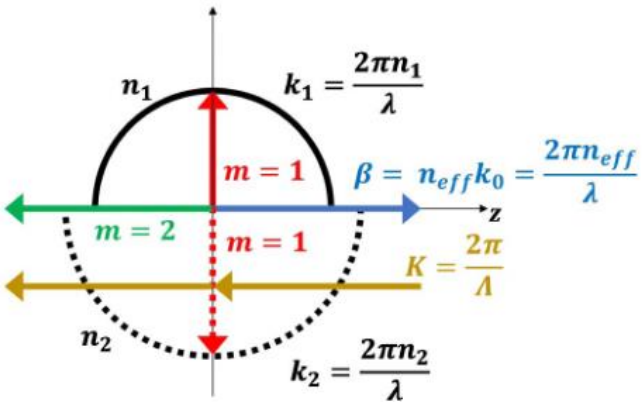

Fig. 4.3: Wave vector diagram for perfect vertical coupling, limited by high second order Bragg-reflections. Image from Marchetti et al. [128].

4.2.2 Coupling efficiency

Upon incidence on the grating, light incoming from the input waveguide is scattered in all directions (see Fig. 4.2). The following optical powers are defined:

- P_{in} is the input optical power injected by the waveguide.
- P_{up} is the power emitted upwards.
- P_{down} is the power diffracted downwards and lost into the substrate.
- P_{ref} is the power reflected into the waveguide.

The grating is long enough such that the residual optical power at the end of the grating is negligible.

By conservation of energy, $P_{in} = P_{up} + P_{down} + P_{ref}$. By normalizing with P_{in}, the following expression is obtained:

$$\eta_{up} + \eta_{down} + \eta_{ref} = 1 \qquad \text{Eq. (4.3)}$$

where $\eta_{up,down,ref}$ are the corresponding power fractions in the corresponding directions. For the optimization of the grating coupling efficiency, all the optical power that is not diffracted upwards towards the fiber is considered lost. In addition, to be efficiently coupled to the fiber, the profile of the upwards emitted field should match with the Gaussian fiber mode with the corresponding mode field diameter (MFD). The coupling efficiency, η_{CE}, which is the ratio of the optical

power coupled to the fiber to the optical power in the waveguide, is therefore defined as:

$$\eta_{CE} = \eta_{up} \times \eta_{OL} \qquad \text{Eq. (4.4)}$$

where η_{OL} is the modal overlap, which is essentially a convolution mathematical operation between the emitted field, $F(x)$, and the Gaussian fiber mode, $G(x)$:

$$\eta_{OL} = \frac{|\int F(x).G^*(x)\,dx|^2}{\int |F(x)|^2\,dx \int |G(x)|^2 dx} \qquad \text{Eq. (4.5)}$$

A figure of merit generally used to evaluate the performance of GCs is the directionality, η_{dir}, defined as:

$$\eta_{dir} = \frac{\eta_{up}}{\eta_{up} + \eta_{down}} \qquad \text{Eq. (4.6)}$$

where η_{up} and η_{down} are the optical power fractions going up (towards the fiber) and going down (lost in the substrate) respectively.

Using Eq. (4.3) and Eq. (4.6), the power fraction radiated upwards can be expressed as $\eta_{up} = \eta_{dir} \times (1 - \eta_{ref})$. Then, the coupling efficiency, η_{CE}, can be calculated as:

$$\eta_{CE} = \eta_{dir} \times \left(1 - \eta_{ref}\right) \times \eta_{OL} \qquad \text{Eq. (4.7)}$$

where η_{dir} is the directionality, η_{ref} is the reflected power fraction and η_{OL} is the modal overlap.

Eq. (4.7) and Eq. (4.4) are equivalent definitions of the coupling efficiency, but Eq. (4.7) gives more insight by separating the grating directionality, η_{dir}, and the reflections, η_{ref}.

An ideal GC should have a high directionality, η_{dir} = 1, low back-reflections, η_{ref} = 0, and high modal overlap, η_{OL} = 1, such that the coupling efficiency is η_{CE} = 1 = 100 % = 0 dB.

So far, a 2D-cross section of the grating coupler has been considered. However, the real problem is in 3D and the diffracted mode should also match the fiber mode along the transverse y-axis. To do so, the

usual method consists of using a linear adiabatic taper to expand the waveguide width from 500 nm to 15 µm, yielding a mode size matching that of a typical fiber mode ~ 10 µm. However, adiabatic tapers generally have a considerable length between 300 µm and 500 µm. Focusing grating couplers have been proposed to reduce the length to less than 20 µm [134]. In such GCs, the grating lines are curved to focus light into the optical fiber (see Fig. 4.4).

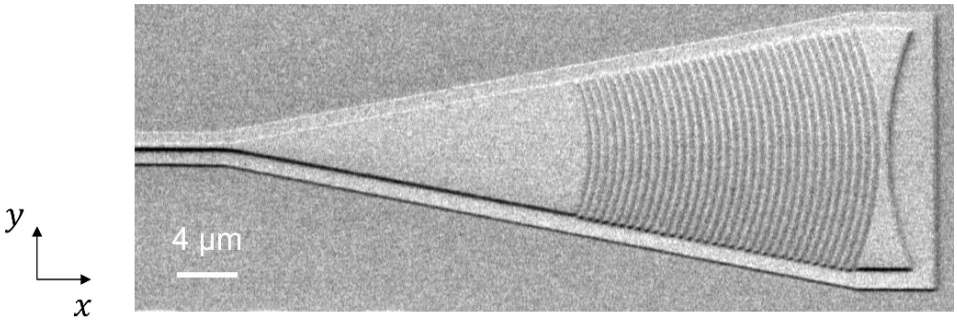

Fig. 4.4: SEM image of the focusing grating coupler at CEA-Leti.

4.3 GRATING COUPLER LITERATURE REVIEW

This section has been divided into three sub-sections, each summarizing reported techniques to optimize one key parameter, namely directionality, back reflections and modal overlap.

4.3.1 Enhancing directionality

In single-layer SOI stacks, the directionality is 50 % for fully etched gratings, due to the vertical symmetry. This vertical symmetry can be broken by partial etching and optimizing the etch depth to increase directionality (see Fig. 4.5(a)). To further increase directionality, the BOX thickness can be optimized [135,136] to maximize constructive interference between the upward diffracted light and the reflected light at the BOX-substrate interface (see Fig. 4.5(b)). Chen et al. experimentally demonstrated a high coupling efficiency of -1.20 dB (76 %) by optimizing the shallow etched grating on a 340 nm-thick SOI [137]. However, for 220 nm-thick SOI with a single partial etch, coupling efficiency is capped to -1.88 dB (65 %) in the telecom bands due to directionality limitations [131].

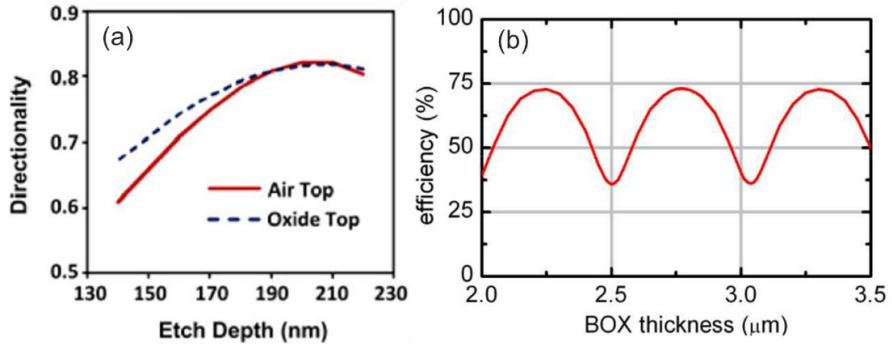

Fig. 4.5: Directionality optimization based on: (a) Etch depth optimization. Image from Chen et al. [137] (b) BOX thickness optimization. Image from Schmid et al. [135]

Additional materials can be used to improve directionality (see Fig. 4.6) and obtain coupling efficiencies > -1 dB. For example, a mirror can be added at the BOX-substrate interface to reflect light towards the fiber and interfere constructively with the upward diffracted light. The mirror can be a metal [138] or a distributed Bragg reflector. Another example consists of adding a Si-overlay [139] which induces constructive interference in the upwards direction by adding a π phase shift between two scatter centers (which are the etched and unetched parts) [129]. However, these solutions add fabrication complexity and increase the fabrication costs.

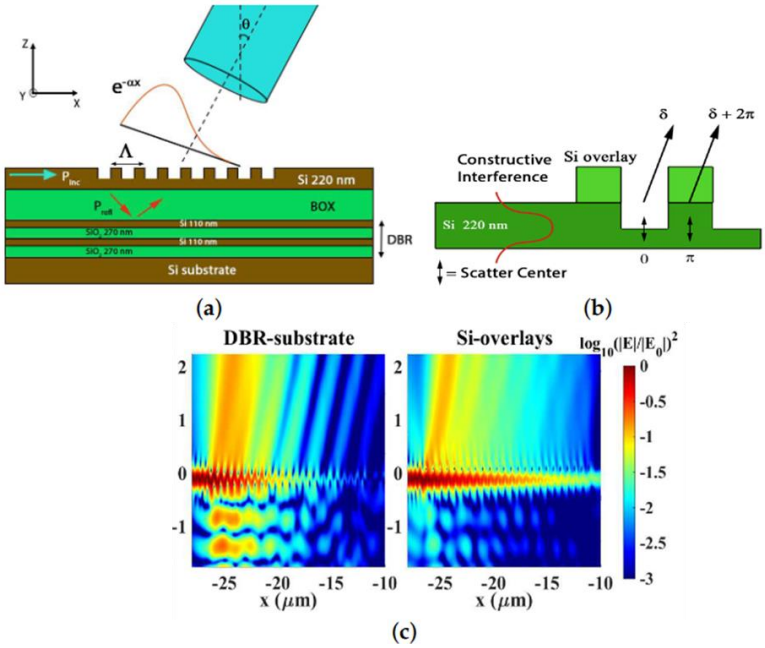

Fig. 4.6: Directionality enhancement strategies using additional materials: (a) Bottom mirrors with Distributed Bragg Reflectors (DBRs), (b) Si-overlay, (c) Simulated Electric fields. Images from Nambiar et al. [129]

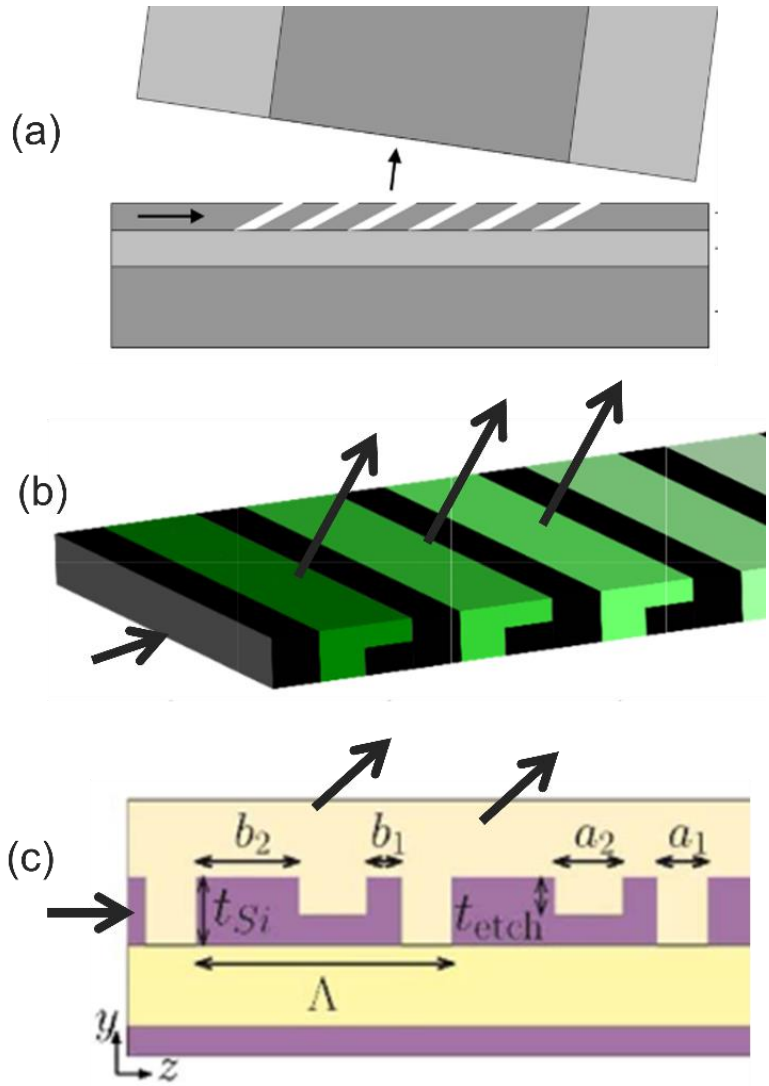

Fig. 4.7: Examples of blazed gratings. (a) Slanted grating. Image from Schrauwen et al. [140]. (b) L-shaped grating. Image from Benedikovic et al. [127]. (c) U-shaped grating. Image from Benedikovic et al. [141].

Another way of breaking the vertical symmetry is by implementing blazed gratings (see Fig. 4.7) that favor constructive interference in the upwards direction by acting as micro-prisms [142]. Their directionality is intrinsic and is independent of the BOX thickness. Several slanted gratings have been proposed, but the continuous slope is complicated to fabricate [140,143–145]. Alternatively, slanted gratings can be discretized into multilevel step gratings. Their fabrication is possible with multiple etch steps and controlled alignment. Such gratings are found in the literature in the form of L-shaped profiles [127,146–153] or U-shaped profiles, also referred to as interleaved structures,

[154,155,141,156]. These structures can achieve directionalities as high as 95 %. Michaels et al. proposed another dual-layer grating, with a simulated coupling efficiency of -0.035 dB (99 %), but this design would require very complex fabrication steps [157].

Table 4.1 gives a comparison of shallow etched gratings and some of the reported blazed gratings on SOI platforms.

Reference	**Technique**	η_{dir} (%) **(Sim.)**	η_{CE} (dB)
2010 Chen et al. [137]	Shallow etch (e-beam fab.)	90	Sim. = -0.75 Exp. = -1.20
2011 Mekis et al. [158]	Shallow etch (CMOS line fab.)	Not available	Exp. = -1.25
2007 Schrauwen et al. [140]	Slanted GC (focus ion beam fab.)	90	Sim. = -1.94 Exp. = -3.32
2017 Benedikovic et al. [147]	L-shapes with SWGs (DUV fab.)	98	Sim. = -2.20 Exp. = -2.70
2017 Chen et al. [149]	L-shapes with SWGs (e-beam fab.)	95	Sim. = - 0.70 Exp. = -1.90
2023 Vitali et al. [152]	L-shapes without SWGs (e-beam fab.)	97	Sim. = -0.28 Exp. = -0.80
This work	**L-shapes with SWGs (immersion DUV fab.)**	**99**	**Sim. = - 0.80** **Exp. = -1.70**
2015 Benedikovic et al. [141]	U-shapes with SWGs (e-beam fab.)	95	Sim. = -1.05 Exp. = -1.30
2015 Benedikovic et al. [156]	U-shapes with SWGs (DUV fab.)	95	Sim. = -1.10 Exp. = -2.00

Table 4.1: Examples of SOI grating couplers, fab. = fabrication, Sim. = simulated, Exp. = experimentally measured

4.3.2 Reducing back-reflections

Back-reflections in GCs mainly come from two sources: Bragg reflections and Fresnel reflections.

As discussed in section 4.2.1, Bragg reflections are usually avoided by designing the grating to emit/receive at a small angle from the vertical. However, if a vertical radiation angle is desired, an additional etched slit can be added (see Fig. 4.8(a)), acting as a partially reflecting mirror causing destructive interference of this Bragg reflection [159]. In this case, the reflections are reduced from 55 % without the slit, to 1 % with the slit.

Fresnel reflections arise from the index mismatch between the waveguide and grating region. For instance, shallow etched gratings have lower index mismatch and hence have lower back-reflections, of ~0.6 % in a Si/SiO2 grating. On the other hand, fully etched gratings exhibit strong back reflections of ~17 % [160,161].

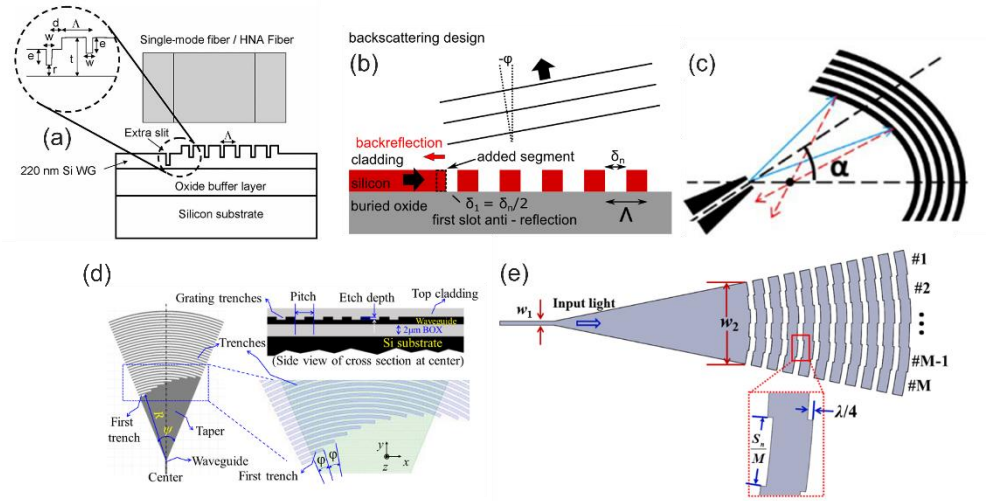

Fig. 4.8: Techniques to reduce back-reflections: (a) Additional slit. Image from Roelkens et al. [159]. (b) Additional slot. Image from Hoffmann et al. [161]. (c) Re-focusing grating lines. Image from Li et al. [162]. (d) Asymmetric grating trenches. Image from Song et al. [163]. (e) Sub-teeth with a λ/4 offset. Image from Zou et al. [164]

Other strategies to reduce back-reflections are shown in Fig. 4.8. To destructively interfere the back-reflections, Hoffmann et al. proposed an additional silicon slot which fills half the first etch [161]. Although

back-reflections were reduced to 4 %, this only works for GCs for which the diffraction angle $\theta < 0$. Another way to reduce back-reflections into the waveguide is to re-focus them away by curving the grating lines [162,165,166]. This, however, does not increase coupling efficiency, as energy in the reflections has not been re-directed towards the fiber. Similarly, asymmetric grating trenches were proposed to re-direct away the reflections but caused a 0.3 dB penalty in coupling efficiency [163,167]. Another strategy is to implement multiple sub-teeth with a $\lambda/4$ offset per grating line, where λ is the wavelength, to cause destructive interference of back reflected light. Although back-reflections were reduced to -25 dB, they come at the expense of an extra coupling loss of 0.8 dB due to an extra phase difference induced by this $\lambda/4$ offset.

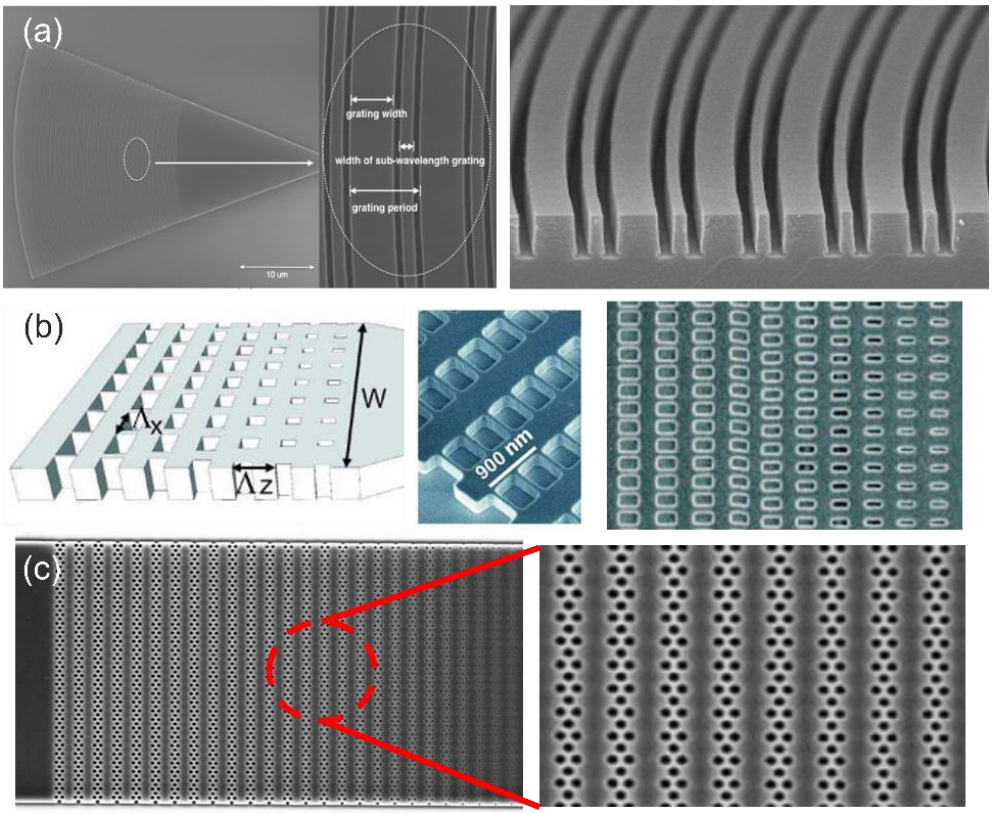

Fig. 4.9: Reducing back-reflections using SWGS. (a) SWG minor grating teeth, Image from Wang et al. [160] (b) Transversal SWGs. Image from Halir et al. [168] (c) Photonic crystal triangular lattice of nanoholes. Image from Ding et al. [169]

Most of the previously described strategies do not efficiently convert the back-reflections into power radiated towards the fiber and hence,

do not contribute to increasing the coupling efficiency. SWGs on the other hand, were able to do so by reducing the index contrast between the waveguide and grating regions (see Fig. 4.9). They have been implemented as SWG minor grating teeth (see Fig. 4.9(a)). In [160], the SWG minor teeth reduced back-reflections from -7.7 dB (17 %) down to -20 dB (0.01 %) in gratings with a constant period, also known as uniform gratings. SWGs have also been implemented as transversal rectangular SWGs in the first grating period [147,155] and along the other grating periods (see Fig. 4.9(b)) [127,151,168,170,55,171]. In the first demonstration of these rectangular SWG-engineered GCs by Halir et al., back-reflections were reduced down to 1 % in uniform gratings [168]. SWGs made up of circular nanoholes (see Fig. 4.9(c)) [169,172,173] have also reduced back-reflections to ~ 1 %.

Reducing beck-reflections can be done by apodization, in which the grating period and duty cycle are varied (see section 4.3.3). For example, Antelius et al. reduced back-reflections in completely-etched gratings from 21 % to 0.1 % through apodization [136]. Halir et al. reduced back-reflections from 1 % to 0.1 % through apodization using transversal SWG rectangles [168].

4.3.3 Increasing modal overlap

In a uniform GC (same period and duty cycle along the grating), the radiated field has an exponentially-decaying profile, $P(x) = P_0 \exp(-2\alpha x)$, where P_0 is the power in the waveguide and α is the grating radiation strength, which is the power diffracted upwards per grating period [13] . The maximum theoretical overlap between this decreasing exponential profile and the Gaussian fiber mode, $G(x)$, is ~ 80 %, and thus limits the coupling efficiency [174]. To increase the modal overlap, α can be varied along the grating, such that the diffracted field matches better with the Gaussian profile (see Fig. 4.10). Such gratings with varied α are said to be apodized (or chirped).

The grating radiation strength, α, can be controlled by varying the duty cycle [131,137,136,174–178] or the etch depth [179,180]. However, the etch depth is difficult to control and varying the duty cycle is generally the preferred solution. When apodizing the GC, the local grating index n_B changes, which also changes the diffraction angle θ, as described

by Eq. (4.1). The grating period Λ should therefore be adapted accordingly to maintain a fixed radiation angle along the grating.

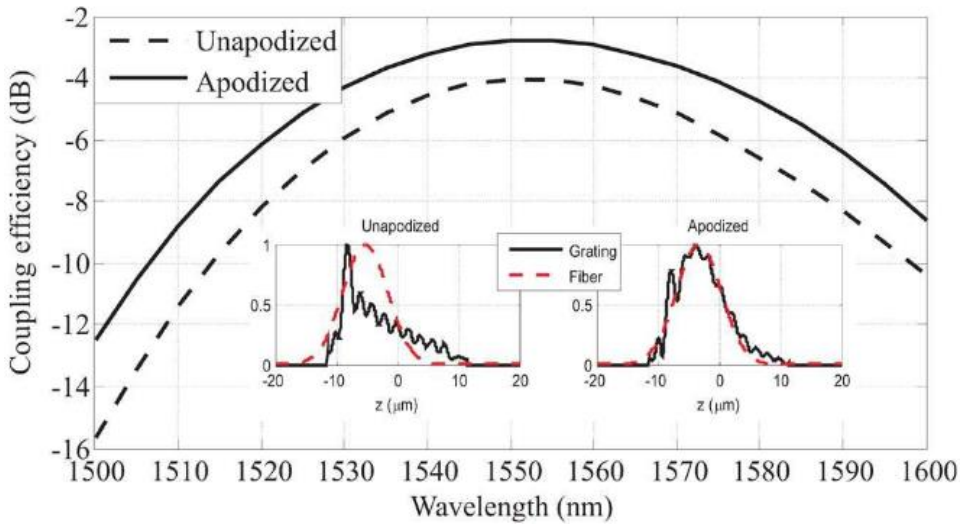

Fig. 4.10: Apodization increases modal overlap and hence coupling efficiency. Image from Halir et al. [168].

To produce a Gaussian mode, the grating strength should be low at the beginning and increase progressively along the grating. Hence, the ability to correctly apodize a GC is given by the minimum grating strength available, which is set by the minimum fabricable duty cycle, which is itself set by the minimum critical dimension of the lithography process (CD_{min}). By using SWGs, the minimum grating strength can be lowered for a given CD_{min}, yielding a better overlap with the desired Gaussian (see Fig. 4.11). By doing so, the record grating coupler efficiency at CEA-Leti has been established at -1.35 dB for a single etch grating with SWG-elements [181]. Other apodized SWG-engineered GCs are reported in [55,168,170,182].

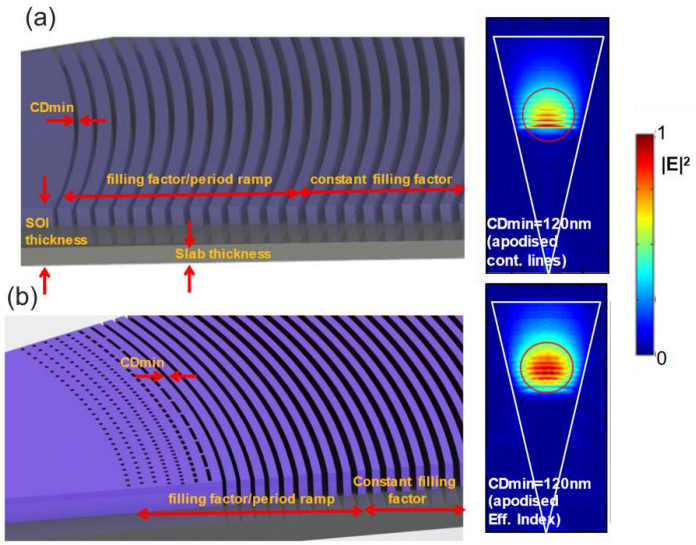

Fig. 4.11: Apodised (a) non-SWGs, (b) SWGs GC and their simulated electric fields. In both cases, CD_{min} = 120 nm, but the SWGs enabled a lower grating strength and increased the modal overlap. Images from Fowler et al. [181]

4.3.4 Summary of the literature review and aim of our work

Conventional shallowly etched gratings have shown efficiencies as high as -1.20 dB through the optimization of the etch depth, BOX thickness and apodization in both, laboratory demonstrations [137] and industrial CMOS fabrication lines [158]. However, some energy is still lost into the substrate. To mitigate such losses, very high directionality blazed gratings have been proposed [127,147,156]. They can be readily fabricated in a photonic CMOS line through the available multiple etch steps and controlled alignment. To further enhance the coupling efficiency, back-reflections need to be reduced and modal overlap needs to be increased through apodization. These can be simultaneously achieved using SWGs, which offer higher control on the index contrast and grating strength [168].

A promising high efficiency blazed L-shaped and SWG-engineered grating coupler, was proposed by Benedikovic et al. [127], achieving a simulated coupling efficiency of ~ - 0.25 dB (94 %). This design is compatible with CEA-LETI's CMOS pilot line, not requiring any additional material, or a modified process, and could potentially be fabricated at industrial scale. It is however more complicated to fabricate than the conventional shallow etched grating due to the two etch steps and small feature sizes of the SWGs. A similar grating,

fabricated by e-beam lithography, showed a measured coupling efficiency of -1.90 dB instead of a simulated value of - 0.70 dB [149].

The aim of our works is therefore to design a SWG-engineered L-shaped grating coupler on CEA-LETI's platform, fabricate it using immersion lithography, and experimentally characterize it, to study the industrial feasibility of this grating design approach.

4.4 METHODOLOGY AND RESULTS

This section presents the design, fabrication and experimental characterization of our SWG-engineered L-shaped grating coupler.

4.4.1 Design

Our aim is to maximize the coupling efficiency of a grating coupler at a wavelength of λ = 1550 nm, which couples the fundamental transverse-electric (TE) polarized mode from the photonic waveguide to a single mode fiber, SMF-28, which has a mode field diameter of MFD = 10.4 µm, at λ = 1550 nm (Corning [183]).

Fig. 4.12(a) shows a schematic 3D-view of the SWG-engineered L-shaped grating coupler. The grating is apodised using SWG-metamaterials on the first five periods. On the remaining periods, the grating has a uniform period without any SWGs. Fig. 4.12(b) shows a 2D cross-section along the x-z plane of the L-shaped grating. The SWG-metamaterials are indicated by their equivalent index $n_{SWG,i}$ with $i = 1,2,3,4,5$ being the number of the considered period.

The design constraints given by CEA-LETI on its 300 nm-thick SOI platform are:

- Silicon full thickness of h_{Si} = 300 nm.
- Silicon shallow thickness of h_{int} = 165 nm.
- BOX thickness of h_{BOX} = 720 nm.
- The critical dimension (minimum feature size) of CD_{min} = 70 nm.
- Top encapsulation with SiO_2.
- Grating diffraction angle at the 1550 nm wavelength should be θ_{SiO_2} = 8° in the silica encapsulation.

The radiation angle constraint, θ_{SiO_2} = 8°, comes from the need to be compatible with standard for fiber connectors (see Corning's APC Connectors and Adapters datasheet [184]). This corresponds to a radiation angle in air θ_{air} = 11.5°, as per Snell's refraction law: $n_{air}\sin(\theta_{air}) = n_{SiO_2}\sin(\theta_{SiO_2})$, where n_{air} = 1 and n_{SiO_2} = 1.44 are the refractive indices of air and SiO_2 respectively.

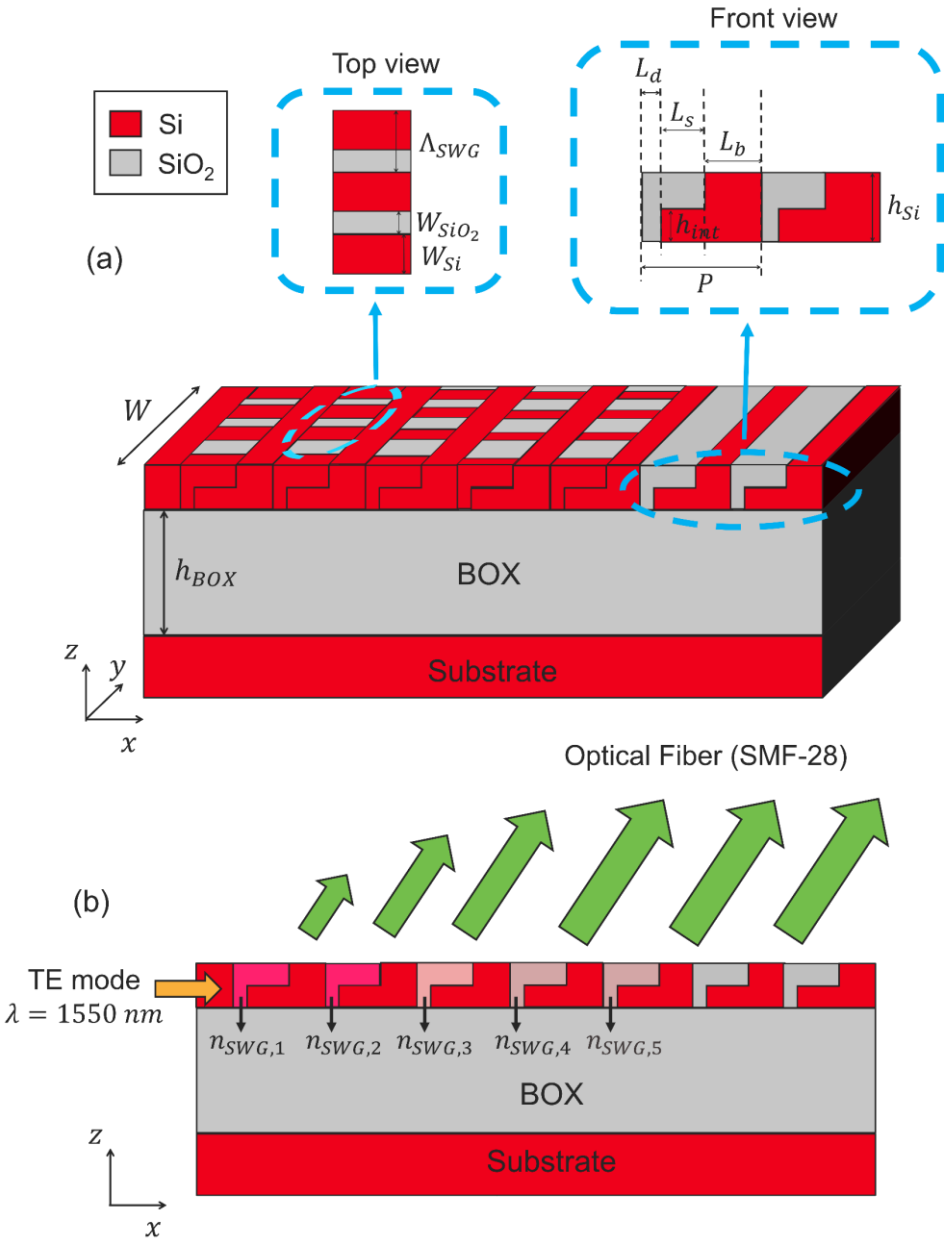

Fig. 4.12: Schematic view of the SWG-engineered L-Shaped grating coupler (a) in 3D. (b) in 2D with the equivalent SWG indices, n_{SWG}. The gradual color change indicates the gradual change in n_{SWG}. The SiO_2 encapsulation is not shown for clarity.

Our design procedure consists of three main steps:

Step 1: Finding the L-shaped parameters in the uniform part (without SWGs)

The first step is to find the required dimensions of the L-shaped profile (without SWGs) respecting the phase matching equation, Eq. (4.1), to achieve a radiation angle of θ_{SiO_2} = 8° at λ = 1550 nm, while maximizing the grating directionality. As the heights are fixed, our design parameters in the L-shaped profile are L_d, L_s and L_b, as shown in the front-view of Fig. 4.12(a). L_d is the length of the fully etched part (d stands for $deep$), L_s is the length of the partially etched part (s is for $shallow$), and L_B is the non-etched part (b is for $block$). The period of the grating is $P = L_d + L_s + L_B$.

To do so, 2D-FDTD simulations of a uniform L-shaped grating without SWGs are performed. In 2D-simulations, the y-dimension is considered infinite, resulting in the geometry shown in Fig. 4.12(b). The background material is set to SiO_2. The refractive indices are n_{SiO2} = 1.44 and n_{Si} = 3.48 at a wavelength λ = 1550 nm. The FDTD grid dimensions are $\delta_x = \delta_z$ = 25 nm.

In our simulations, the grating is implemented to outcouple the light from the waveguide towards the fiber, as shown in Fig. 4.12(b). The total number of periods in the uniform L-shaped grating, without SWGs, is N = 30 such that negligible power is left in the waveguide after diffraction by the grating.

Based on the design given in [127] and after optimization, the following parameters have been obtained: L_d = 105 nm, L_s = 265 nm and L_b = 295 nm, giving P = 665 nm. The radiation angle is θ_{SiO2} = 8° at λ = 1550 nm. These parameters have also been implemented in 3D-FDTD simulations to verify the validity of the 2D simulations.

In 3D, the grating has a width of W = 15 µm (see Fig. 4.12(a)) such that the diffracted mode has a mode diameter of ~ 10.4 µm along the y-dimension and hence, optimizing the modal overlap along this direction. The FDTD grid is $\delta_x = \delta_y = \delta_z$ = 25 nm. To simplify our simulations, the taper between the 400 nm wide waveguide to the

W = 15 µm wide grating is not simulated. Instead, the TE-mode source was injected into a 15 µm wide waveguide ahead of the grating.

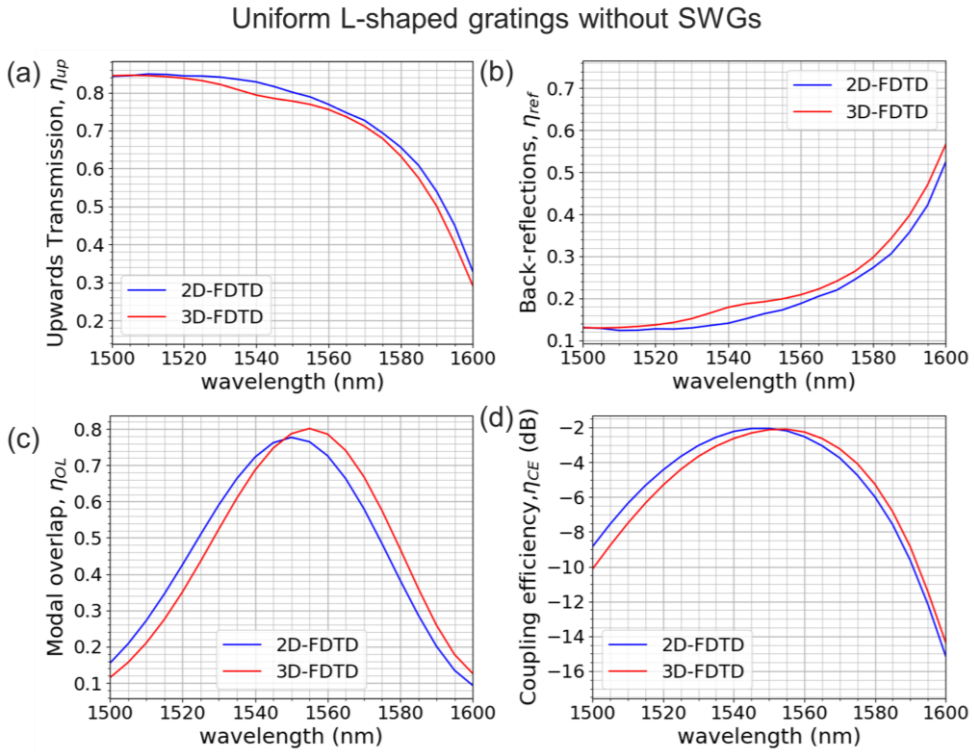

Fig. 4.13: Comparison of 2D and 3D-FDTD simulation results of a uniform L-shaped grating without SWGs with the following parameters: L_d = 105 nm, L_s = 265 nm, L_b = 295 nm and P = 665 nm. (a) Upwards transmission. (b) Back-reflections. (c) Modal Overlap. (d) Coupling efficiency.

Fig. 4.13 shows a comparison of the 2D- and 3D-simulation results, which are in a relatively good agreement. At λ = 1550 nm, the difference in the 2D and 3D simulation results are around 2 – 4 % in the upwards transmission, η_{up}, the back-reflections, η_{ref}, and in the modal overlap, η_{OL}. Also, the same peak coupling efficiency, η_{CE}, is obtained but with a minor difference of 5 nm in the peak wavelength. This shows that the 2D-FDTD simulations of the L-shaped grating couplers without SWGs can provide good approximations. They are advantageous as they are faster and consume less computational resources.

As for the performance of the uniform L-shaped grating without SWGs, the 3D-FDTD simulations show that at λ = 1550 nm, the grating has a high upwards transmission, $\eta_{up} \sim 0.78$, and a very low downwards

transmission (power lost into the substrate), $\eta_{down} \sim$ 0.01. The L-shaped grating has thus a very high directionality, $\eta_{dir} = \eta_{up}/(\eta_{up} + \eta_{down}) \sim$ 0.99. However, the L-shaped grating has relatively large back-reflections, $\eta_{ref} \sim$ 0.20. The modal overlap with the SMF-28 fiber mode is around $\eta_{OL} \sim$ 0.80 and the coupling efficiency was $\eta_{CE} = \eta_{up} \times \eta_{OL} \sim$ 0.62, which gives, $\eta_{CE} \sim$ -2.00 dB.

Step 2: Apodization by using SWGs equivalent indices in 2D- simulations

Apodization was used to reduce back-reflections and increase modal overlap, simultaneously. As shown in Fig. 4.12(a), the grating is divided two sections: i) an apodized section implementing SWGs with varying n_{SWG} and P, comprising N_a periods, and ii) a uniform section without SWG and fixed P, comprising N_u periods. We chose N_a = 5 and N_u = 25 following the work of a Benedikovic et al. [127].

The SWG-engineered L-shaped grating periods are simulated in 2D using their equivalent refractive indices, n_{SWG} (see Fig. 4.12(b)). The n_{SWG} are obtained by the multilayer slab model [185]. In this model, the SWGs structures are considered as a multilayer slab and n_{SWG} is obtained by finding the effective index of the fundamental TE mode propagating perpendicularly to the direction of periodicity of the multilayer slab. The SWG period is Λ_{SWG} and the width of the silicon segments is W_{si} (see the top view of Fig. 4.12(a)). Fig. 4.14(a) shows the n_{SWG} equivalent indices obtained as a function of W_{Si} for Λ_{SWG} = 350 nm at a wavelength of λ = 1550 nm.

When apodizing the L-shaped gratings with SWG-metamaterials, the grating pitch, P, should be changed to respect the phase matching condition, as per Eq. (4.1), such that the radiation angle is always θ_{SiO_2} = 8° for different values of n_{SWG}. If P is not changed, different values of n_{SWG} result in different Bloch effective indices in the grating, n_B, and result in different diffraction angles. To find the value of P which yields θ_{SiO_2} = 8°, various 2D-simulations of uniform L-shaped gratings with a given n_{SWG} have been performed. In these simulations, the L-shaped parameter L_b has been changed, and L_s and L_d were fixed, to change P (as $P = L_d + L_s + L_b$). Fig. 4.14(b) shows the values of L_B to be used for different n_{SWG} such that θ_{SiO_2} = 8°.

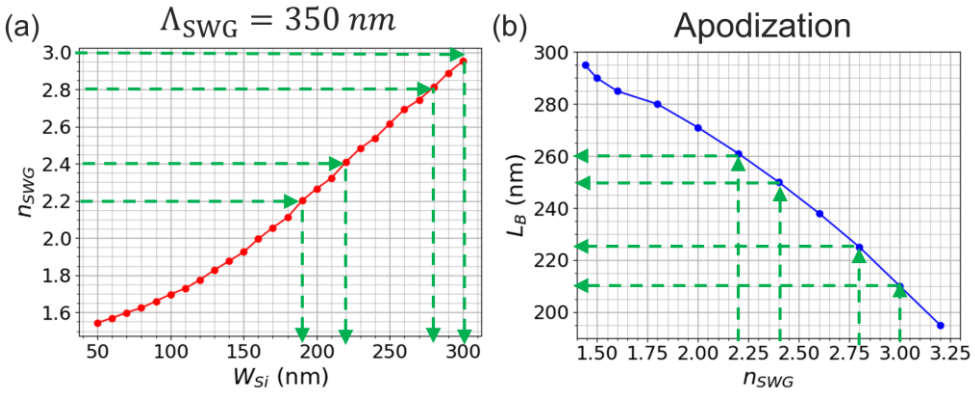

Fig. 4.14: (a) Multilayer slab simulation giving equivalent SWG indices, n_{SWG}, as a function of W_{Si} for Λ_{SWG} = 350 nm at λ = 1550 nm. (b) Finding the corresponding L_B for a given n_{SWG} such that the phase matching condition is respected when apodizing the grating. The green arrows indicate the n_{SWG} values used in the optimized structure in the 3D simulations.

As a starting point for designing our apodised L-shaped grating coupler, a linear variation in the n_{SWG} equivalent indices for the first five periods with $n_{SWG,lin\,var} = [3.00, 2.80, 2.60, 2.40, 2.20]$ has been chosen. For each of these n_{SWG} values, L_B was adjusted to keep a constant angle of θ_{SiO_2} = 8°. The remaining periods N_u = 25 are uniform.

The 2D-simulation results of the linearly varied n_{SWG} apodised structure are shown in Fig. 4.15. The SWGs provide a gradual change in the index contrast in the first five periods, reducing back-reflections from ~ 0.20 in a uniform L-shaped grating without SWGs, down to ~ 0.01 at λ = 1550 nm. This increases the power diffracted upwards from ~ 0.80 without SWGs, to ~ 0.96 with SWGs. The modal overlap slightly increases from ~ 0.78 to ~ 0.83. Overall, the coupling efficiency increases from ~ -2.00 dB (60 %) without SWGs to ~ -1.00 dB (80 %) with SWGs. The L-shaped grating coupler with SWGs is further optimized by varying n_{SWG} and adapting L_B around the initial design point. Finally, the optimized n_{SWG} values are $n_{SWG,opt} = [3.00, 3.00, 2.80, 2.40, 2.20]$. These values are indicated by the green dotted arrows in Fig. 4.14. The modal overlap of 0.86 is higher than the grating with the linear variation in n_{SWG}, yielding a slight increase in the coupling efficiency from ~ -1.00 dB (80 %) with a linear variation in SWG index to ~ -0.83 dB (83 %) at λ = 1550 nm (see Fig. 4.15(d)).

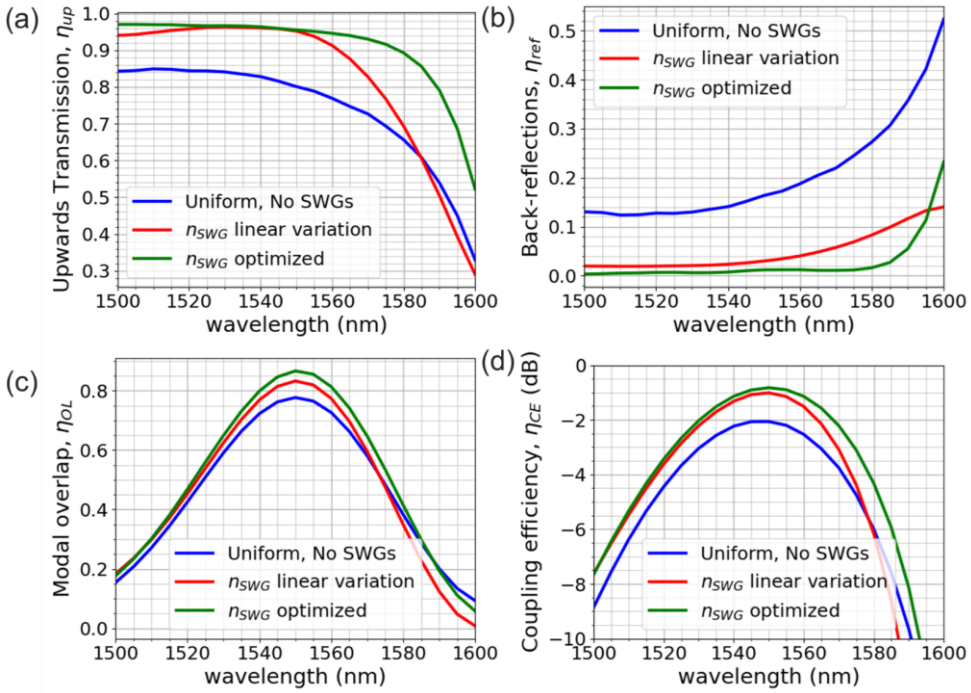

Fig. 4.15: 2D-optimization. The equivalent SWG indices used as starting point follow a linear variation of $n_{SWG,lin\ var}$ = [3.00, 2.80, 2.60, 2.40, 2.20]. The optimized values are $n_{SWG,opt}$ = [3.00, 3.00, 2.80, 2.40, 2.20].

Step 3: Optimizing in 3D-simulations

As a final step, the grating geometry is optimized using the 3D-model shown in Fig. 4.12(a)). The SWG transversal period is Λ = 350 nm. The values of W_{Si} corresponding to each n_{SWG} are chosen using the simulations in Fig. 4.14(a). The initial parameters for the 3D-geometry coming from the 2D design are: $W_{Si,opt\ 2D} = [300, 300, 280, 220, 190]$ nm for the corresponding $L_{b,opt\ 2D} = [210, 210, 225, 250, 260]$ nm.

The results of the 3D-simulations differ from the 2D-simulations, as shown in Fig. 4.16. For the 2D-simulations at λ = 1550 nm, $\eta_{up} \sim 0.96$ $\eta_{ref} \sim$ 0.01 and $\eta_{CE} \sim$ 0.83 dB were obtained, while in the 3D-simulations $\eta_{up} \sim$ 0.88, $\eta_{ref} \sim$ 0.10 and $\eta_{CE} \sim$ -1.25 dB were obtained. The modal overlap is very similar with $\eta_{OL} \sim$ 0.87 and $\eta_{OL} \sim$ 0.85 for 2D- and 3D- simulations, respectively. The differences in the simulation results can be attributed to differences between the n_{SWG} values obtained with the multilayer slab model and the values actually achieved in the 3D-structure.

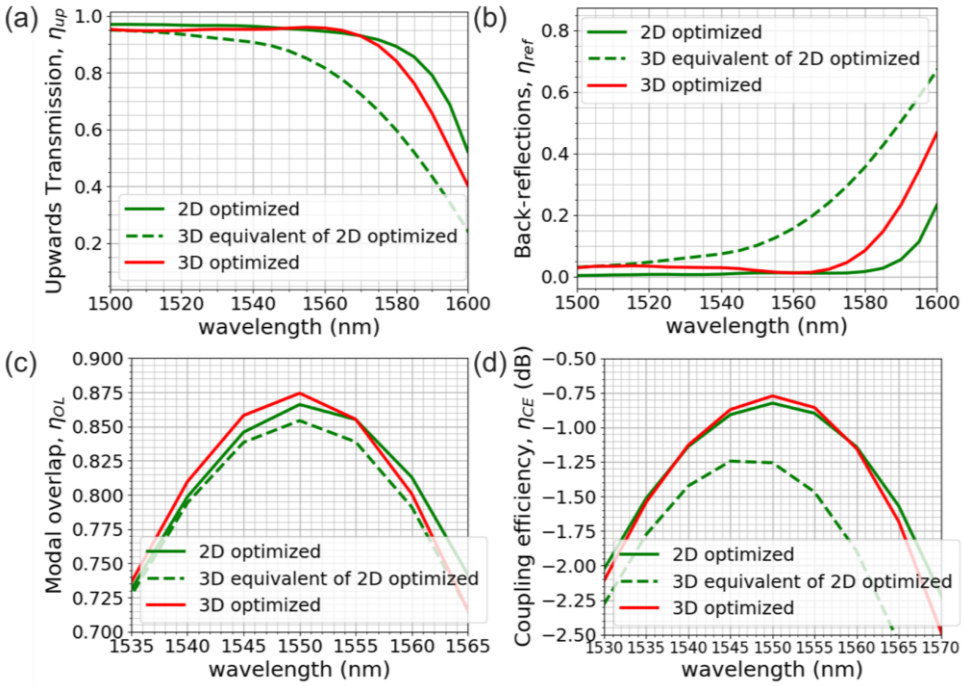

Fig. 4.16: Comparison of 2D- and 3D-simulations: (a) upwards transmission, (b) back-reflections, (c) modal overlap and (d) coupling efficiency. Results from 2D-simulations are shown with green solid lines. 3D simulations of the geometry optimized with the 2D-model are shown with green dotted lines. Red solid lines correspond to the geometry optimized in 3D. Discrepancies between 2D- and 3D-simulations are attributed to the inaccuracy of the multilayer slab model in predicting the equivalent SWG refractive index, n_{SWG}.

The values of W_{Si} are re-optimized, based on 3D-simulations starting from the values from the multilayer slab model. The W_{Si} values are varied around this initial design point, and L_B values are adapted for to yield a radiation angle of θ_{SiO_2} = 8°. Finally, the optimized design in 3D has the following parameters in the SWG part: $W_{Si,opt\,3D} = [280, 280, 260, 180, 160]$ nm and $L_{b,opt\,3D} = [220, 220, 230, 260, 265]$ nm. The parameters of the L-shaped SWG-engineered grating coupler optimized in 3D-simulations are given in Table 4.2.

The minimum feature size of the optimized design is W_{SiO_2} = 70 nm, for $W_{Si,opt\,3D}$ = 280 nm, respecting the CD_{min} = 70 nm. The calculated figures of merit for the optimized 3D-geometry are presented in Fig. 4.16, showing a η_{CE} ~ -0.77 dB (84 %) at λ = 1550 nm. In this case, the

values obtained by 3D-optimization are closer to those obtained with the 2D-model.

Parameter	Symbol	Value
Partial silicon height	h_{int}	165 nm
Full silicon height	h_{Si}	300 nm
BOX thickness	h_{BOX}	2 µm
Number of apodized periods	N_a	5
Number of uniform periods	N_u	25
Total number of periods	N	30
Grating length	L	~ 19.7 µm
Grating width	W	15 µm
Uniform part		
Length of the fully etched part	L_d	105 nm
Length of the partially etched part	L_s	265 nm
Length of the non-etched part	L_b	295 nm
Grating period	P	665 nm
Apodized part		
Length of the non-etched part	$L_{b,apo}$	$[220, 220, 230, 260, 265]$ nm
Grating Period	P_{apo}	$[590, 590, 600, 630, 635]$ nm
Si width per SWG period	W_{Si}	$[280, 280, 260, 180, 160]$ nm
SiO_2 per SWG period	W_{SiO_2}	$[70, 70, 90, 170, 190]$ nm
SWG period	Λ_{SWG}	$[350, 350, 350, 350, 350]$ nm

Table 4.2: L-shaped grating with SWGs parameters (optimized in 3D-FDTD). In the apodised part, L_d and L_s were the same as in the uniform part.

Comparison of the L-shaped gratings with and without SWGs

Fig. 4.17 and Table 4.3 compare the 3D-optimized L-shaped gratings apodised with SWGs with the uniform L-shaped gratings without SWGs. The SWGs apodization increases the power radiated upwards, reduces the back-reflections and increases the modal overlap, yielding a coupling efficiency of $\eta_{CE} \sim 0.84$ = -0.77 dB with θ_{SiO2} = 8° at a wavelength of 1550 nm.

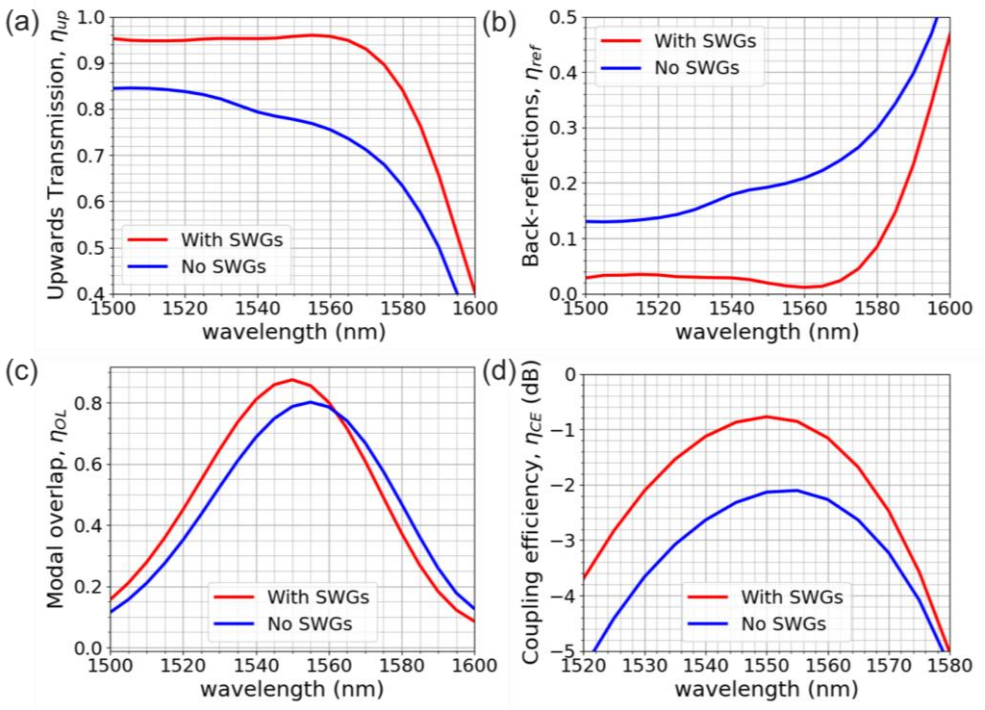

Fig. 4.17: 3D-simulation results of the L-shaped grating couplers with and without SWGs: (a) upwards transmission, (b) back-reflections, (c) modal overlap and (d) coupling efficiency.

Performance parameter	Symbol	With SWGs	Without SWGs
Central wavelength	λ	1550 nm	1550 nm
Polarization	–	TE	TE
Radiation angle in SiO_2	θ_{SiO_2}	8°	8°
Power fraction radiated upwards	η_{up}	0.96	0.78
Power fraction radiated downwards	η_{down}	0.01	0.01
Directionality	η_{dir}	0.99	0.99
Power fraction reflected	η_{ref}	0.02	0.20
Modal Overlap	η_{OL}	0.87	0.80
Coupling efficiency	η_{CE}	0.84 = - 0.77 dB	0.62 = -2.00 dB

Table 4.3: Comparison of performance parameters between apodised L-shaped gratings with SWGs and uniform L-shaped gratings without SWGs at the central wavelength λ = 1550 nm.

4.4.2 Fabrication

The fabrication process used to define the L-shaped profiles is depicted in Fig. 4.18 (a)-(c). Silicon nitride is used as a hard mask for the etching. Two lithographic masks are used to define the non-etched (300 nm-thick) and the shallow etched (165 nm-thick) regions. The first mask level is used define the non-etched Si regions, with a thickness of 300 nm. The unprotected areas by the first mask are etched down till their thickness is 165 nm. Then the second mask level is used to define the partially etched features, which are 165 nm-thick. The areas protected by the second mask or the SiN hard mask are not etched, while the unprotected areas are fully etched.

The second mask overlays the first mask by ~ 50 nm. This ensures that the L-shaped profile is preserved in case of a small misalignment to the right, as shown in Fig. 4.18 (d)-(e). If the misalignment is smaller than the overlay, the length of the unetched part (300 nm-thick) is unaffected. However, the length of the partially etched part (165 nm-thick) changes with the misalignment.

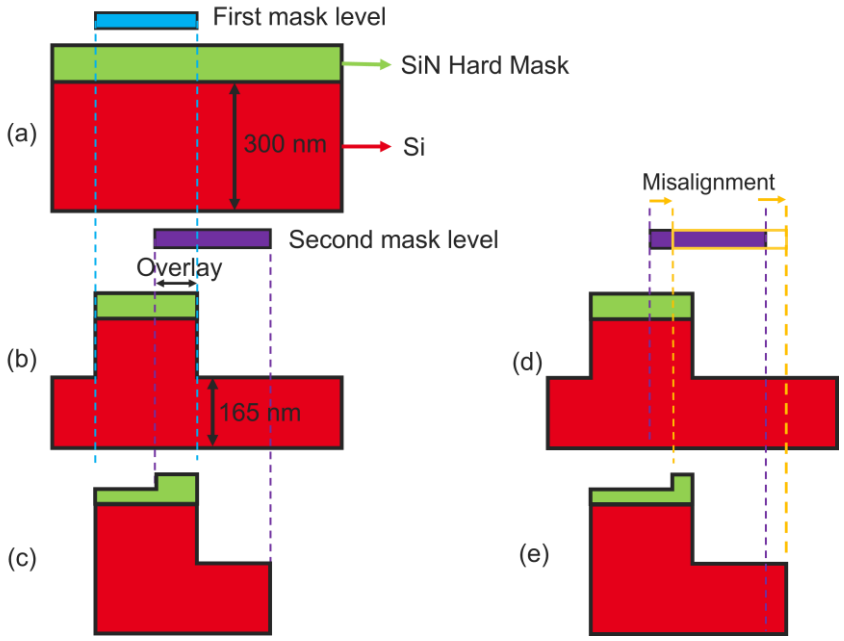

Fig. 4.18: Process flow used to fabricate the L-shaped profile. (a) The first mask level is used to define the 300 nm-thick features. After the first etch step, the areas which are not protected by the first mask have a height of 165 nm. (b) The second mask level is used to define the 165 nm-thick features. It has an overlay of around 50 nm with the first mask level. The role of the overlay is to give an L-shaped profile, in case of a small misalignment. After the second etch step, the areas which were not protected by the second mask or the SiN hard mask are fully etched. (c) The resulting L-shaped profile with nominal dimensions. (d) The second mask level is slightly misaligned to the right, with a misalignment smaller than the overlay of 50 nm. The misaligned position is indicated by the yellow lines and the nominal position by the purple lines. (e) The L-shaped profile has been preserved despite the misalignment. The length of the 300 nm-thick part is unaffected, but the length of the 165 nm-thick part is slightly longer than the nominal dimension.

The fabrication process of interleaving full and shallow etch steps is mainly affected by two kinds of errors: the misalignment in between the two masks levels, and the over/under etching in the shallow step. The nominal mask misalignment error is in a range of $\delta_x = \pm 30$ nm, while the nominal error in the thickness of the shallowly etched areas is $\delta h_{int} = \pm 10$ nm.

The effects of the mask misalignment on the peak coupling efficiency and on the peak wavelength are shown in Table 4.4. Changes in δ_x cause changes in the grating effective index n_B, and therefore lead to shifts in the peak transmission wavelength, as per Eq. (4.1). The worst coupling efficiency of -1.50 dB is predicted for δ_x = -30 nm.

The effects of the thickness errors in the shallow etched areas are shown in Table 4.5. The optimum wavelength is shifted, but the peak coupling efficiency is almost unaffected.

δ_x (nm)	-30	0	+30
Peak η_{CE} (dB)	-1.50	-0.78	-0.78
Peak wavelength (nm)	1510	1550	1590

Table 4.4: Tolerance analysis as a function of masks misalignment, δ_x

δh_{int} (nm)	-10	0	+10
Peak η_{CE} (dB)	-0.76	-0.78	-0.82
Peak wavelength (nm)	1540	1550	1560

Table 4.5: Tolerance analysis as a function of deviations in the partial height, δh_{int}

The L-shaped GC with SWGs was fabricated using immersion lithography and an OPC model. Fig. 4.19 shows the original layout dimensions in red and the dimensions after OPC in blue. For small holes the OPC model increases the width at the center, while for larger holes it is mainly the corners that are corrected.

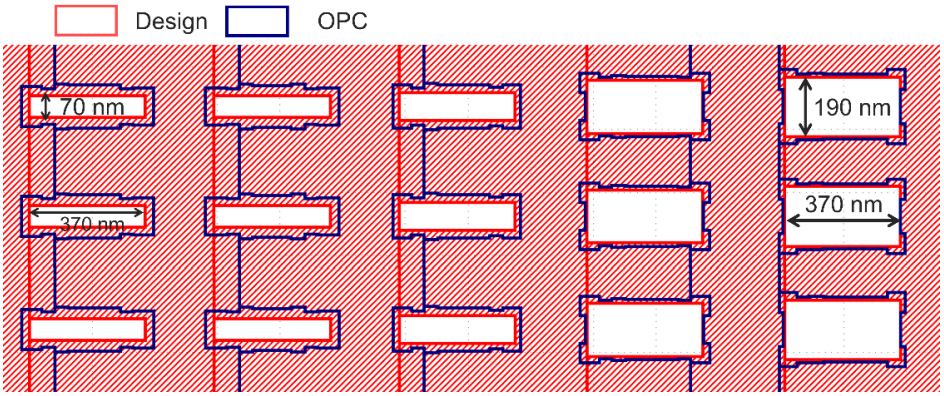

Fig. 4.19: Comparison of layout before and after applying the OPC model. The original design layout is marked in red. The corrected layout is plot in blue.

Fig. 4.20 and Fig. 4.21(a) show SEM images of one L-shaped grating after the two etching steps, before SiO_2 encapsulation. The SWG rectangular holes have rounded corners, which have not been considered in our simulations. Fig. 4.21(b) shows an SEM image of the transversal section of the grating. The edges of the L-shaped holes are not perfectly vertical and the hard SiN mask etch has not been removed. These two effects have not been considered in the simulations for device optimization. The transversal section cut is

obtained by focus ion beam (FIB) etching along the red line in Fig. 4.21(a). The chip is cladded with metal to improve the contrast.

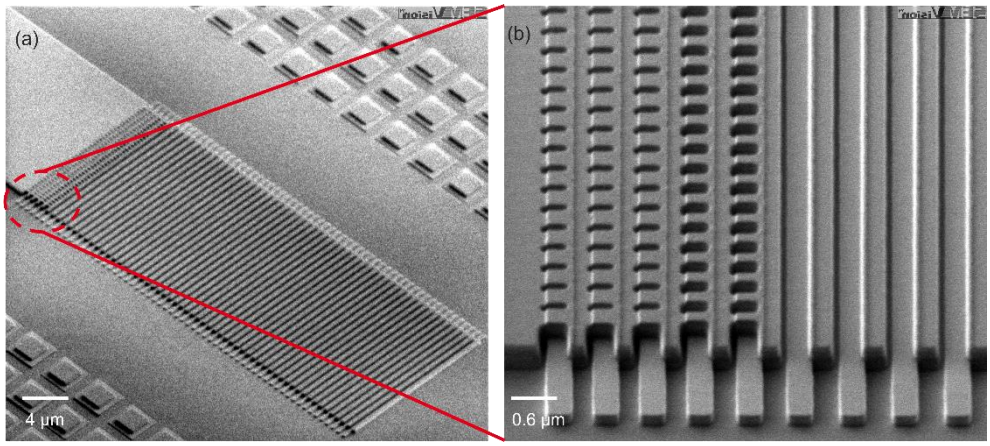

Fig. 4.20: (a) SEM image of the L-shaped GC with SWGs fabricated by immersion lithography (b) zoomed in image

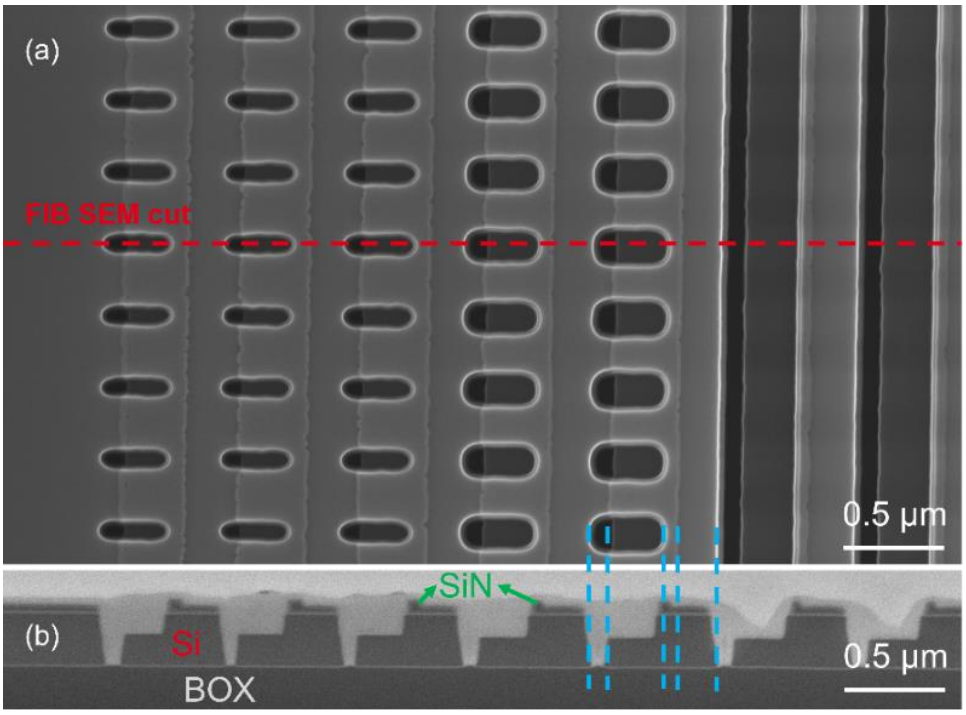

Fig. 4.21: (a) Top view SEM image (b) FIBSEM image, taken in the middle of the SWGs holes, metal was deposited in the holes for better contrast

4.4.3 Experimental characterization

Fig. 4.22 shows a schematic representation of the characterization bench used to measure the grating coupler efficiency. A tunable laser

source is connected to a polarization maintaining (PM) fiber (Fiber 1). Fiber 1 is then connected to an 8° angle polished PM fiber (Fiber 2) via the fiber connector 1. The polished face of the fiber is parallel to the chip surface (see Fig. 7.1(a) in Appendix 7.1). Fiber 2 produces a Gaussian beam, propagating in air at an angle of 11.5°, which is then coupled to the on-chip waveguide via the input grating coupler. After propagation in the waveguide, the light is outcoupled to air via the output grating coupler. The gratings have been put in back-to-back configuration. The outcoupled light is then collected by an 8° angle polished single mode fiber (SMF), referred here as Fiber 3, which is then connected to another SMF fiber (Fiber 4) via the fiber connector 2. Fiber 4 is finally connected to a power meter.

The input laser power P_{in} (dBm) and measured output power are recorded P_{out} (dBm). The heights of the fibers above the chip surface are $h \sim 20$ µm, which is within the Rayleigh range, z_R, of a Gaussian beam with a mode field diameter of MFD = 10.4 µm. $z_R = \pi w_0^2/\lambda \sim$ 55 µm, where w_0 is the beam radius at the waist, $w_0 = MFD/2$, and λ is the wavelength, $\lambda = 1.55$ µm. At this height, a 0.20 dB penalty in coupling efficiency per grating coupler can be induced as compared to when the fiber is in contact with the surface of the chip [181].

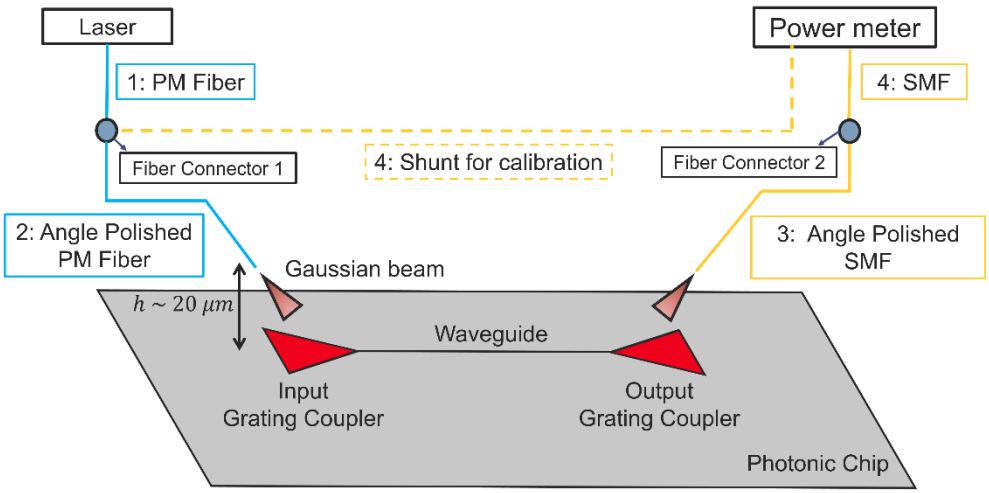

Fig. 4.22: Characterization bench, PM = Polarization Maintaining, SMF = Single mode Fiber.

Before measuring the coupling efficiency of the grating coupler, the bench intrinsic losses are calibrated by measuring the transmission

when the laser is directly connected to the power meter, that is, connecting Fiber 4 to Connector 1. In this configuration, the Fibers 2 and 3, the grating couplers and the interconnecting waveguide are not included in the calibration circuit. The set-up losses, P_{set-up} (dBm), are then recorded. The calibrated input power, $P_{in,calib}$, is therefore given by:

$$P_{in,calib}\ (\text{dBm}) = P_{in}\ (\text{dBm}) - P_{set-up}\ (\text{dBm}) \qquad \text{Eq. (4.8)}$$

where P_{in} is the input laser power and P_{set-up} are the set-up intrinsic losses.

The coupling efficiency of the grating, η_{CE}, is extracted from the measured output power, P_{out} (dBm) as:

$$\eta_{CE}(dB) = \frac{P_{out}(dBm) - P_{in,calib}(dBm) - P_{wg}(dB)}{2} \qquad \text{Eq. (4.9)}$$

where P_{wg} is the loss in the waveguide interconnecting the two gratings. Note that we are considering that the input and output grating couplers have the same coupling efficiency.

The interconnection waveguides have a measured propagation loss of ~ 1 dB/cm. This value has been extracted from additional test structures included in the chip. The waveguide connecting the two grating has a length of 1.3 mm, resulting in a loss of P_{wg} ~ 0.13 dB.

The change of fiber connectors during the calibration and measurement steps induced an estimated measurement error of ± 0.20 dB per connector. As two connectors are changed, the measurement error in coupling efficiency is estimated to be $\Delta\eta_{CE}$ = ± 0.40 dB.

The measured coupling efficiency of a uniform L-shaped GC without SWGs, and an apodised L-shaped GC with SWGs are shown in Fig. 4.23. Without SWGs, the measured peak coupling efficiency is $\eta_{CE}\ (No\ SWGs)$ = -2.70 ± 0.40 dB and is centered at around a wavelength of 1550 nm. For comparison, the simulated coupling efficiency is -2.10 dB. The difference between the simulated and measured coupling efficiency is 0.60 dB. Part of this difference (0.30 dB)

come from the Fresnel reflections at the air-SiO_2 encapsulation interface, which was not considered in our simulations (see Appendix 7.1). Part of the difference between the measured and simulated values of coupling efficiency might come from fabrication imperfections, such as the side wall angles in the L-shaped profile, which have not been considered in simulations. Also, part of this difference lies within the measurement uncertainties.

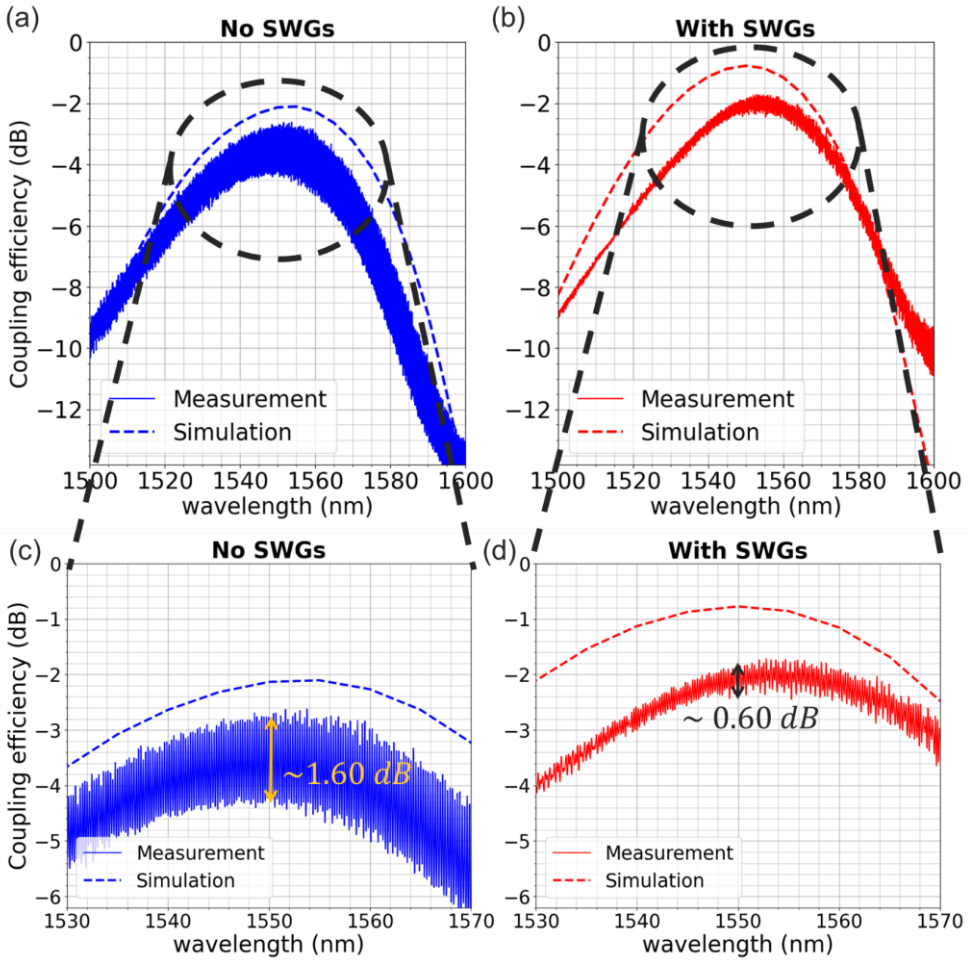

Fig. 4.23: Measured coupling efficiency per grating, η_{CE}, of L-shaped GCs (a) without and (b) with SWGs. (c) and (d) are the corresponding zoomed in graphs.

With SWGs, the measured peak coupling efficiency is $\eta_{CE}\,(With\,SWGs)$ = -1.70 dB ± 0.40 dB and is centered around a wavelength of 1555 nm. This is 1 dB improvement compared with the case without SWGs. The simulated coupling efficiency is -0.77 dB at a peak wavelength of 1550 nm. The difference between the simulated

and measured coupling efficiencies is 0.93 dB, which included 0.30 dB losses due to the Fresnel reflections at the air-encapsulation interface. The remaining part of the difference can be attributed to the simplified simulation scheme, in which the sidewall angles, the SiN hard mask, the rounded corners of the SWGs and fabrication imperfections have not been considered.

The oscillation ripples in the measured transmission spectrum come from the back-reflections in the input and output grating couplers that from a Fabry-Perot cavity. The measured free spectral range (FSR) of the oscillations near a wavelength λ = 1550 nm is $FSR_{measured} \sim 250$ nm for the grating with and without SWGs. The FSR can be calculated as:

$$FSR_{cavity} = \frac{\lambda^2}{n_g \times 2L_{wg}} \qquad \text{Eq. (4.10)}$$

where n_g is the group index, and L_{wg} is the waveguide length connecting the two gratings. For $L_{wg} \sim$ 1300 µm and a simulated group index of $n_g \sim$ 4, the calculated free spectral range is FSR_{cavity} = 230 nm, in good agreement with the measured value.

The amplitude of the oscillations in the transmission spectrum of a Fabry-Perot cavity, A_{cavity}, is proportional to the back-reflections, R, of a grating coupler as: $A_{cavity} = \frac{4R}{(1+R)^2}$. The higher the reflections, the bigger the amplitude of the oscillations.

Without SWGs, the amplitude of the oscillations in the transmission spectrum of a single grating coupler is $A_{GC}\ (No\ SWGs) \sim$ 1.60 dB at a wavelength of λ = 1550 nm. This value corresponds to reflections of $\eta_{ref}\ (No\ SWGs) \sim$ 0.18. Detailed description of the mathematical determination of η_{ref} from the amplitude of the oscillations is given in Appendix 7.2. This value is close to the simulated value of 0.20. With SWGs, the amplitude in the single grating coupler spectrum is reduced to $A_{GC}\ (With\ SWGs) \sim$ 0.60 dB, and the reflections corresponds to $\eta_{ref}\ (With\ SWGs) \sim$ 0.07. These measured reflections are higher than the simulated value of 0.02 and partially accounts for the lower measured coupling efficiency. The difference between the measured

and simulated reflectance might come the structural differences between the fabricated and simulated shapes (rounded corners of SWGs, sidewall angles in the L-shapes, …).

The simulated and experimental results for the gratings with and without SWG are summarized in Table 4.6.

	No SWGs		**With SWGs**	
	Simu.	Exp.	Simu.	Exp.
η_{CE} (dB)	-2.10	-2.70	-0.80	-1.70
η_{ref}	0.20	0.18	0.02	0.07

Table 4.6: L-shaped grating coupler simulation (Simu.) and experimental (Exp.) results with or without SWGs at a wavelength λ = 1550 nm. η_{CE} is the coupling efficiency of a single grating and η_{ref} are the back-reflections.

4.5 CONCLUSION AND PERSPECTIVES

The simulation of the L-shaped grating couplers without SWG predict a high directionality $\eta_{dir} \sim$ 0.99, with strong back-reflections $\eta_{ref} \sim$ 0.20, limiting the coupling efficiency to $\eta_{CE} \sim$ -2.00 dB near a wavelength of 1550 nm. To reduce back-reflections and increase the modal overlap simultaneously while maintaining a high directionality, the L-shaped grating couplers has been apodized with SWG-metamaterials. The optimized SWG-based design yields a very high simulated coupling efficiency $\eta_{CE} \sim$ -0.80 dB. The experimental coupling efficiency is η_{CE} = -1.70 $\pm$ 0.40 dB, which is the highest measured efficiency for an L-shaped grating fabricated without e-beam lithography. The difference between the simulated and measured values may be attributed to fabrication imperfections which have not been considered in the simulations, including rounded corners in the SWGs, side wall angles in the L-shaped profile and the SiN hard mask.

As a comparison, SWG-engineered grating coupler from CEA-Leti [181] exhibits a higher coupling efficiency of -1.35 dB at a central wavelength of λ = 1310 nm. In this case, only a single shallow-etch step is required to fabricate the grating. Our work shows that although the simulated efficiency of SWG-engineered L-shaped grating coupler can be better than -1 dB, the experimental values are closer to – 2 dB. The L-shaped geometry requires interleaving shallow and full etch steps,

complicating the fabrication process and adding additional uncertainties, like the misalignment between the two masks. This complexity, together with the tight fabrication tolerances of the design may be the cause to the limited experimental efficiency.

For a next fabrication run, the L-shaped grating should be further optimized, considering the fabrication imperfections observed in this run. For example, corner rounding is unavoidable [186] and can be compensated in design by properly choosing the duty cycles in the SWGs. The side wall angles in the L-shaped profiles should be measured and the dimensions in the L-shaped could re-adapted if needed. The SiN hard mask should also be accounted in the simulations. The Fresnel losses at the air-encapsulation interface can be reduced by using an index matching liquid, which is generally the case in packaged devices [187].

5 SWG-ENGINEERED LOW DIVERGENCE ANTENNA FOR TWO DIMENSIONAL (2D) OPTICAL PHASED ARRAYS (OPAS) FOR FREE SPACE OPTICAL COMMUNICATIONS

This chapter is dedicated to the design fabrication and experimental characterization of a novel optical antenna architecture providing low radiation divergence, which is a key parameter in integrated two-dimensional optical phased arrays (2D-OPAs) for applications in point-to-point free space optical (FSO) communications, also referred as long range optical wireless communications (OWCs) [188]. SWG engineering is used to control the radiation strength of gratings in the optical antenna, achieving a large aperture size and low radiation divergence. SWGs are also exploited to realize a compact transition between single-mode input waveguide and the large-area antenna.

The outline of the chapter is as follows. First, an overview of FSO communications is given, describing the working principles, motivations and challenges. Then, the motivation for implementing OPAs for FSO communications is discussed. This is followed by the working principles of an integrated OPA and a corresponding literature review. The specifications of the designed OPA and of the designed low divergence SWG-engineered antenna are then given. Next, the simulation, fabrication and characterization results are reported, showing results of the single antenna and the 2D-OPA. Finally, we present the conclusions and perspectives.

5.1 FREE SPACE OPTICAL (FSO) COMMUNICATIONS

In FSO communications, data is carried by a laser beam typically in the near-infrared, 750 - 1600 nm wavelengths, through the atmosphere (also referred to as free space) between a transmitter and a receiver (see Fig. 5.1). The transmitter consists of an optical source (typically a laser) to produce an optical beam, a modulator to encode data onto the optical carrier signal, an optical amplifier to increase the amplitude of the signal and beam forming optics to transmit the output beam into the atmosphere. The beam then propagates through the atmosphere and is collected by the receiver. The receiver consists of

beam collecting optics which then send the light onto a photodetector which converts the optical signal into an electrical signal for processing.

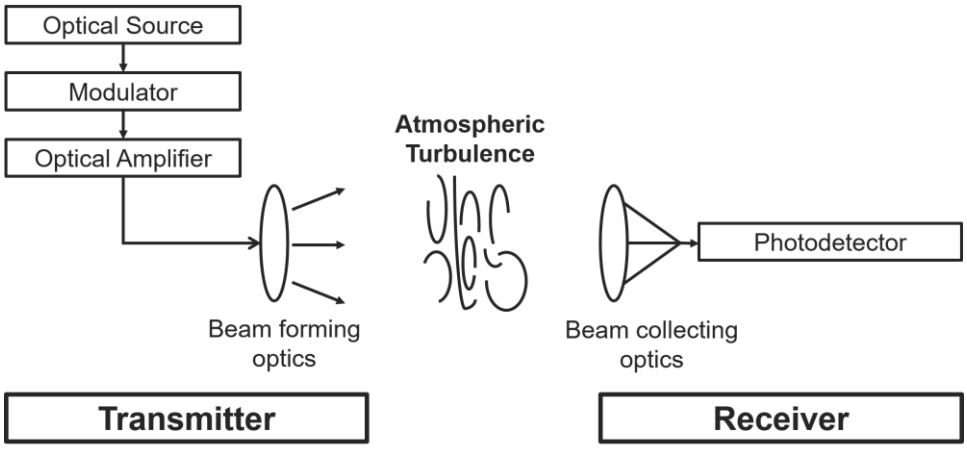

Fig. 5.1: Typical block diagram of a free space optical (FSO) communication link

FSO communications are gaining significant interest as they have the following advantages [188–190]:

1. They do not require licensing by regulatory authorities as opposed to the radio frequency (RF) communications, whose frequency bands are increasingly congested.
2. High optical frequencies can provide high modulation bandwidths, that is, high information carrying capacity. For instance, optical frequencies could allow bandwidths of the order of hundreds of THz, which is 10^5 times the typical bandwidth using a RF carrier [189].
3. The optical wavelengths are small and enable narrow beam divergence, which is proportional to λ/D where λ is the wavelength and D is the aperture diameter. For example, a typical optical divergence is around 0.34 μrad (with λ_{opt} = 1.55 μm and D_{opt} = 10 cm), while the typical RF divergence is around 67.2 mrad (with λ_{RF} = 3 cm, D_{RF} = 1 m) [191]. The optical beam is therefore more directive for a given aperture size and can allow for long range data transmission with a major part of the emitted power being collected by the receiver [192]. Beams with narrower divergence are also less prone to interference with other links thanks to their spatial selectivity [190].

A significant and largely unsolved problem that hampers the performance of FSO communications is the atmospheric turbulence along the transmission path [193,194]. This turbulence results from local variations in air temperature and pressure, causing local changes in the refractive index of air and hence, scintillation. Scintillation is the temporal variation in the intensity and phase of the propagating beam. The received signal quality is then degraded (see Fig. 5.2) [190]. This random intensity pattern is also known as intensity speckle.

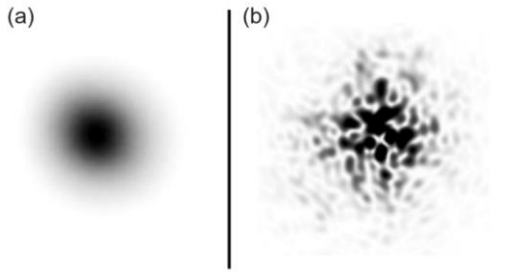

Fig. 5.2: (a) Transmitted Gaussian signal (b) Received signal, distorted due to atmospheric turbulence. Images from Henniger et al. [190].

In addition, atmospheric turbulence also causes spatial beam deviations, also referred to as beam wander, and hence, misalignment between the transmitter and the receiver [195]. Losses due to atmospheric turbulence, also referred to as fading losses, can be as high as 10.7 dB on a 20 km link at a wavelength of 1.55 µm [190] (see Fig. 5.3, which also gives some other characteristics of such a link).

OLiBuT - Optical Link Budget Tool

Version 1.3

Transmit power (mean)	P_{Tx}			**23,0 dBm**
	θ	**1,00**	**mrad** full 1/e2 div.	
	L	**20,0**	**km** link distance	
	λ	**1550**	**nm** wavelength	
System loss	A_{system}	**0,5**		**-3,0 dB**
Rx antenna	D	**11,00**	**cm** ant. diameter	
Received Power	P_{Rx}			**-22,2 dBm** **6036 nW**
Atmos. extinction *[Kruse-Mie, ITU-R P.1814]*	A_e	**25** **0,2**	**km** visibility **dB/km**	**3,5 dB**
Fading loss	A_{fade}	**1,5** **1,00E-02**	pow.scintillatin index frac. fade time	**10,7 dB**
Receiver sensitivity (mean)	S_r	**1,0E-07**	BER	**-36 dBm** **251 nW**
Margin of the link	M_{link}			**0 dB**

Fig. 5.3: Typical FSO communication system parameters. Image from Henniger et al. [190].

One technique to compensate for atmospheric turbulence effects is to use an adaptive optics system. Fig. 5.4 shows such a system on the receiver side. A wavefront sensor analyses the received distorted wavefront and sends a signal to a deformable mirror to correct the wavefront [189].

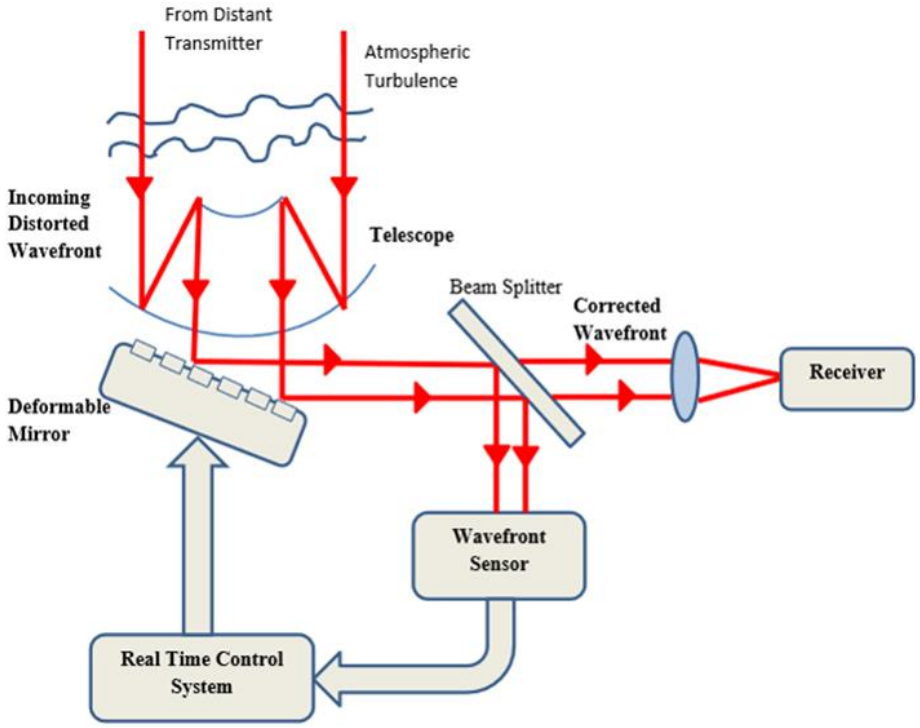

Fig. 5.4: Typical adaptative optics system to compensate for phase front distortions induced by atmospheric turbulence. Image form Kaushal et al.[189].

Other issues related to FSO communications are the building sway, produced by misalignment due to mechanical vibrations or the reduction of signal-to-noise ratio due to solar background radiation. A common mitigation technique is using a diversity scheme [196] in which the same signal is sent through multiple channels with different characteristics. Other mitigation techniques are discussed in [188,189].

5.2 OPAs FOR FREE SPACE OPTICAL COMMUNICATIONS

Optical phased arrays are non-mechanical, solid-state, beam shaping and steering devices [197,198]. There are various subcategories of OPAs [199]: micro-electromechanical system (MEMS) OPAs [200,201], liquid crystal OPAs [202] and photonic integrated chip (PIC) OPAs

among others. In PIC-OPAs, all key components can be integrated on a single chip, reducing size and weight as compared to relatively bulky non-integrated beam forming systems. PIC-OPAs also have higher tuning speeds as compared to MEMS and liquid crystal OPAs [198]. Also, PIC-OPAs have been demonstrated on various material platforms, including III-V [203–205], SiN [206–208] and SOI [209–218]. However, the SOI platform offers potentially cheaper costs as it leverages standard CMOS fabrication processes. From now on in the manuscript, OPAs are referred as PIC-OPAs unless specified otherwise.

OPAs have mainly been studied for beam steering in automotive light detection and ranging (LiDAR) applications [19,219,220], but are also well suited for point-to-point communications in free space [221–223]. In this case, OPAs can act within compact integrated optical beam transceivers [224–226], to compensate phase-front distortions caused by atmospheric turbulence through active phase tuning.

Reference	Speed	Link Distance	Performance
2018 Poulton et al. [227]	10 Gbps	50 m	First lens-free OPA-OPA link
2020 Rhee et al. [228]	32 Gbps	3 m	46° x 10° steering range
2023 Li et al. [229]	32 Gbps	54 m	100° x 2° steering range
2018 Wang et al. [230]	12.5 Gbps	140 cm	Indoor wireless communications

Table 5.1: Reported optical phased arrays (OPAs) used for communications in free space.

Table 5.1 gives a summary of the reported OPAs used for FSO communications. In [227], the first OPA-OPA link was demonstrated. In [228–230], the transmitter was an OPA and the receiver consisted of free space optics, fiber collimators and photodiodes.

5.2.1 Working principles of a photonic integrated chip (PIC) OPA

A typical OPA configuration is illustrated in Fig. 5.5. Light is first injected into the chip either by an integrated laser or externally via fiber coupling. The input beam is then divided into various channels by a

power splitting tree, which can be made up of several binary splitting stages. Each channel contains a phase modulator, placed ahead of an optical antenna. Each optical antenna then emits light into free space. Through constructive interference of the emitted fields, an optical beam is formed. By controlling the phase of the individually emitted fields with the phase modulators, the optical beam can be shaped or steered.

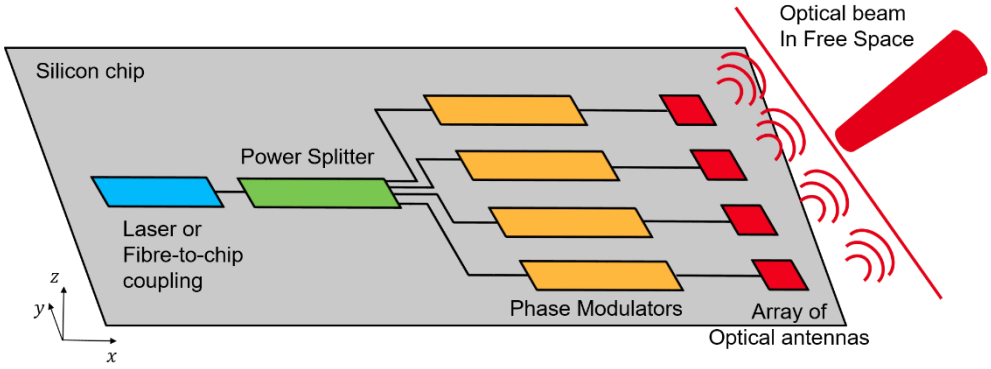

Fig. 5.5. Working principles of a typical silicon photonics OPA.

The optical antennas can be of two types. First, they can consist of surface diffractive structures, such as grating couplers [210], which diffract light out of the chip surface into free space. Surface-emitting OPAs are the most popular type. The other type of optical antenna consists of edge couplers, which emit light from the chip facet into free space. This type of OPA is known as an end-fire (EF) OPA [216,231]. Our work focuses on the more popular surface-emitting OPA.

5.2.2 Far field emission profile of an OPA

The far field emission of the OPA is determined by the sum of the emitted optical fields from each individual antenna. Mutual interference produces an optical beam in the far field region. The far field region is said to be fully formed beyond the Fraunhofer distance, d_F:

$$d_F = \frac{2D^2}{\lambda} \qquad \text{Eq. (5.1)}$$

where λ is the wavelength and D is the aperture size, that is, the surface over which all the antennas of the OPA emit. According to

Fresnel diffraction theory, the far field profile is given by the spatial Fourier transform of the near field [199].

For illustration purposes, the 1D-array presented in Fig. 5.6 is considered. It is composed of square antennas of length l, separated by a constant array period Λ. The square antennas each emit a uniform electric field, at the same wavelength, λ in free space. So, the size of the emitted field is l. The 1D-array fill factor, FF_{1D}, is defined as the ratio between the antenna size, l, and the array period Λ, as $FF_{1D} = l/\Lambda$.

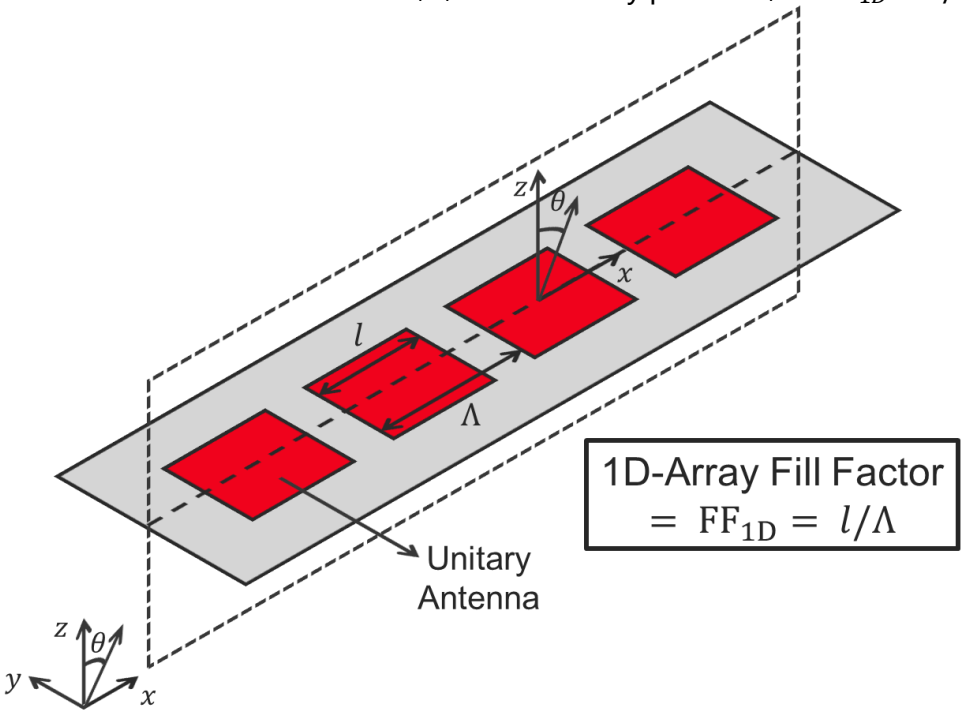

Fig. 5.6: 1D-array of square apertures. l is the antenna size, Λ is the array period and λ is the wavelength. The 1D-array fill factor is $FF_{1D} = l/\Lambda$. θ is the circular coordinate angle in the far field pattern in the x-z plane

The normalized angular distribution of the far field intensity , $I(\theta)$, in the x-z plane along the antenna array, marked with dashed lines in Fig. 5.6, can be described as follows [223,232,233]:

$$I(\theta) = |EF(\theta) \times AF(\theta)|^2 \qquad \text{Eq. (5.2)}$$

where θ is the circular coordinate angle in the far field profile, defined as in Fig. 5.6, $EF(\theta)$ is the element factor and is $AF(\theta)$ is the array factor.

The element factor, $EF(\theta)$, is given by the far field pattern of the unitary antenna composing the array. For a rectangular aperture of length l, and uniform electric field, the element factor is a $sinc$ function:

$$EF(\theta) = \frac{\sin\left(k_0 \frac{l}{2} \sin\theta\right)}{k_0 \frac{l}{2} \sin\theta} \qquad \text{Eq. (5.3)}$$

where $k_0 = 2\pi/\lambda$ is the free-space wave vector

$AF(\theta)$ is the array factor and describes the interference effects of the fields emitted by the antennas in the array as:

$$AF(\theta) = \frac{\sin(\frac{N}{2} k_0 \Lambda \sin\theta)}{\sin(\frac{1}{2} k_0 \Lambda \sin\theta)} \qquad \text{Eq. (5.4)}$$

where k_0 is the free-space wave vector, N is the number of antennas and Λ is the array period.

Examples of far field profiles, calculated using Eq. (5.2), are presented in Fig. 5.7. The considered array has N = 4 square apertures and operates at a wavelength of λ = 1550 nm. Two different regimes arise depending on the size of Λ relative to $\lambda/2$.

Fig. 5.7(a)-(c) show the $EF(\theta)$, $AF(\theta)$ and far field profiles, calculated for a fixed period $\Lambda = 600\ \text{nm} < \lambda/2$, and increasing l, yielding filling factors of $FF_{1D} = 0.5$, 0.75 and 1. In all the three cases, only a single lobe (peak) is present. Increasing l reduces the angular width of the $EF(\theta)$, as they are related by a Fourier Transform. However, this has little effect on the overall far field profile. This $\Lambda < \lambda/2$ configuration, providing a single radiation lobe, is ideal for point-to-point communications. However, implementing such a small period is challenging as it would require very small antenna gratings, capable of diffracting all the optical power on a distance $< \lambda/2$ = 775 nm. For comparison, a single period in a typical grating coupler is near 600 nm.

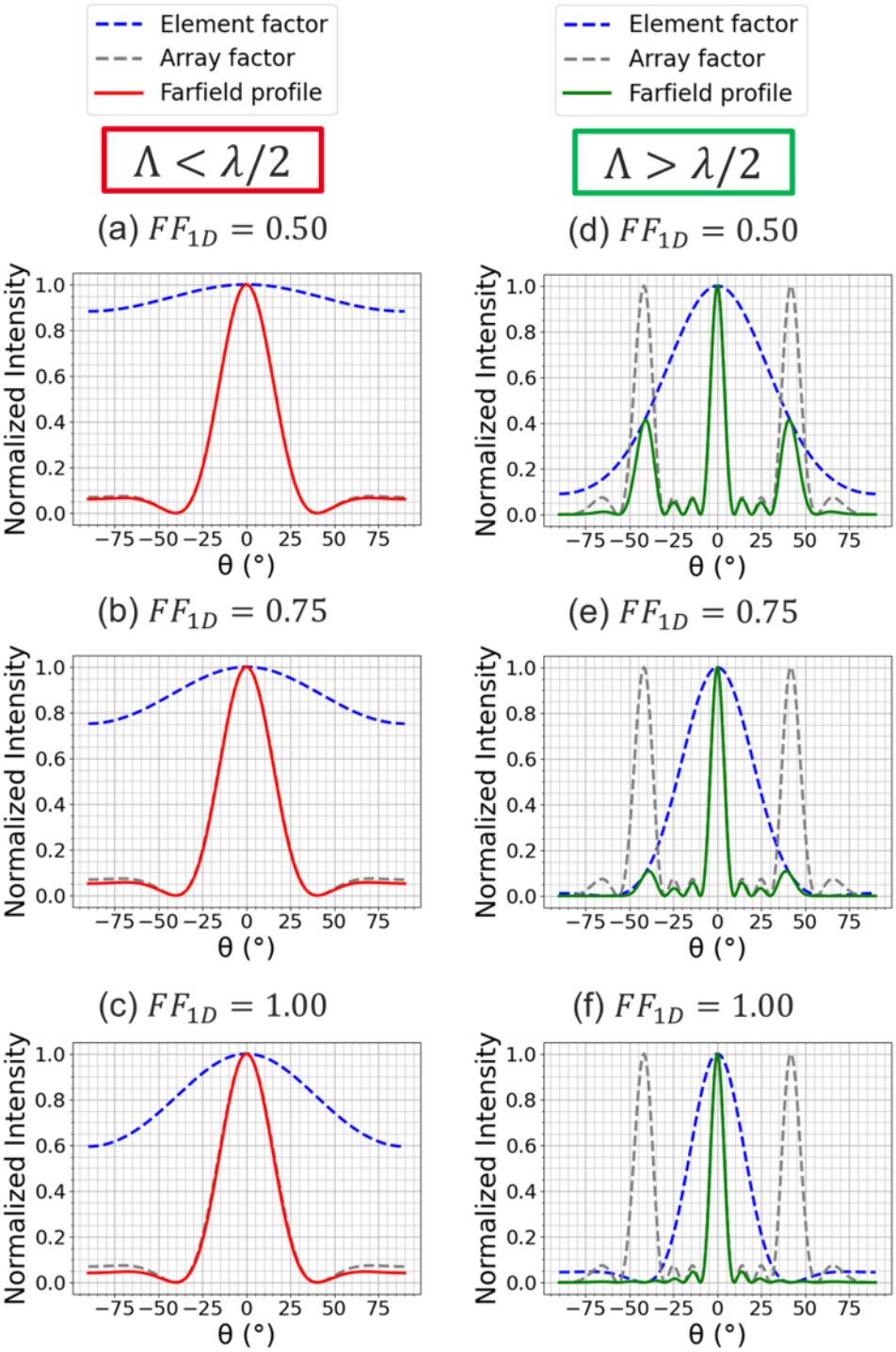

Fig. 5.7: Far field intensity profiles with $N = 4$ antennas, separated by a period Λ, operating at a wavelength $\lambda = 1.55$ µm. Two configurations are shown, with different 1D-array fill factors, FF_{1D}: (a) – (c) $\Lambda = 0.600$ µm $< \lambda/2$, resulting in an $AF(\theta)$ with a single radiation, and (d) – (f) $\Lambda = 3.325$ µm $> \lambda/2$ in yielding three radiation lobes in the $AF(\theta)$. The side lobe level in the far field is reduced by increasing the FF_{1D}.

Fig. 5.7(d)-(f) present the $EF(\theta)$, $AF(\theta)$ and far field profiles calculated for a fixed period $\Lambda = 1.5\lambda = 2325$ nm. The antenna length, l, is set to achieve filling factors of $FF_{1D} = 0.5$, 0.75 and 1. The $AF(\theta)$ exhibits three lobes with equal amplitude. For small angles, the separation between side lobes, $\delta\theta$, can be approximated as:

$$\delta\theta \approx \frac{\lambda}{\Lambda} \qquad \text{Eq. (5.5)}$$

where λ is the wavelength and Λ is the array period.

The full width at half maximum (FWHM) of the peaks, $\delta\theta_{FWHM}$ in radians, can be approximated for small steering angles by:

$$\delta\theta_{FWHM} \approx \frac{\lambda}{N\Lambda} \qquad \text{Eq. (5.6)}$$

where λ is the wavelength, N is the number of antennas and Λ is the array period

For $\Lambda = 3\lambda/2 = 2.325$ µm, the side lobes are separated by $\delta\theta \approx 40°$ and the beamwidth is $\delta\theta_{FWHM} \approx 10°$ in accordance with Eq. (5.5) and Eq. (5.6).

The side lobe level relative to the maximum intensity in the far field profile, SLL, is defined as:

$$SLL\ (dB) = 10 \times \log_{10}\left(\frac{I_{side\ lobe}}{I_{max}}\right) \qquad \text{Eq. (5.7)}$$

where $I_{side\ lobe}$ is the intensity of the side lobe and I_{max} is the maximum intensity in the far field pattern.

The side lobes are not usually used in communications links and lead to a reduced energy efficiency [198]. To reduce the side lobe level, SLL, the angular width of the modulating $EF(\theta)$ should be reduced. As the angular width of the $EF(\theta)$ is inversely proportional to the size of the unitary emitter, l, the latter should be increased. For a given pitch Λ, an increase in l leads to an increase in the array fill factor $FF_{1D} = l/\Lambda$. Hence, in the $\Lambda > \lambda/2$ regime, the SLL can be reduced by increasing the FF_{1D} (see Fig. 5.7(d)-(e)).

A particular case arises when $FF_{1D} = 1$, that is, when $l = \Lambda$. The whole array behaves as a large single antenna and a single beam is obtained. The suppression of the side lobes arises from the coincidence of the zeros in the element factor with the higher orders of the array factor (see Fig. 5.7(c)). However, this case is unfeasible in practice as some space must be dedicated to route light to the antennas.

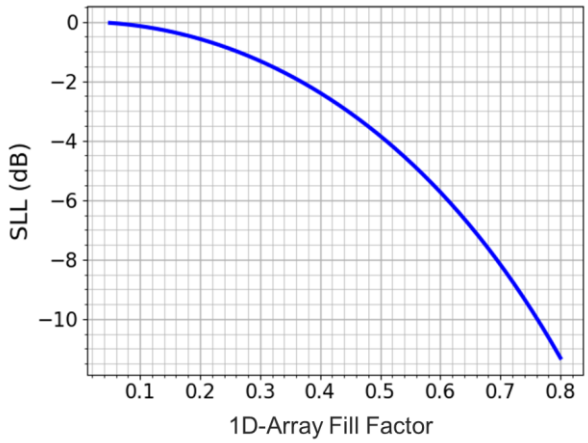

Fig. 5.8: Side lobe level, SLL, as a function of the 1D-array fill factor, FF_{1D}, with $\Lambda = 3\lambda/2$, where Λ is the pitch and λ is the wavelength.

A compromise should therefore be found between a high FF for low side lobe level, and practical implementations by leaving sufficient space for feeding the antennas. Fig. 5.8 shows the side lobe level as a function of the array fill factor for $\Lambda = 3\lambda/2$. A relevant target value for the FF_{1D} is 0.76 which gives an SLL of -10 dB (10 %).

To illustrate the effects of beam steering on the SLL, the array configuration with pitch $\Lambda = 3\lambda/2$ and array fill factor FF_{1D} = 0.76 has been considered (see Fig. 5.9). To steer the beam, a phase gradient is applied between the fields emitted by the unitary antennas, causing an angular shift, $\Delta\theta$ in the far field pattern as shown in Fig. 5.9(a). When steered, the intensity in the main lobe decreases and the intensity of the side lobe increases, causing an increase in the side lobe level, SLL (see Fig. 5.9(b)-(c)). Thus, the considered array configuration, with $\Lambda > \lambda/2$ and FF_{1D} = 0.76 yields a good $SLL \sim$ -10 dB for θ = 0°, but yields a narrow steering range. Yet, such small steering range is sufficient for the point-to-point communications envisioned in this work.

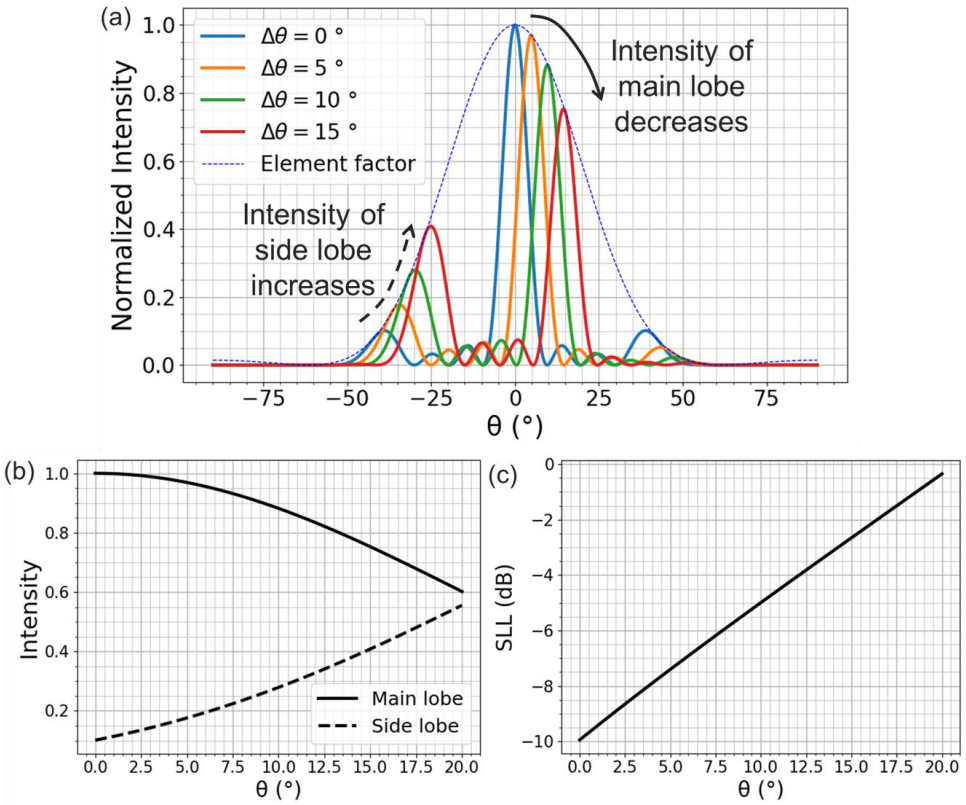

Fig. 5.9: Beam steering for an array with $\Lambda = 3\lambda/2$ and $FF_{1D} = 0.76$. (a) Far field distribution, (b) the intensity of the main lobe and the side lobe, (c) side lobe level, SLL, decreases as the beam steering angle $\Delta\theta$ increases.

The 1D-array example illustrates the general principles governing side-lobe formation. The same general physical principles apply for a 2D-array, which is the final objective of this work.

5.3 LITERATURE REVIEW OF 2D-OPAS

There are two main strategies to steer the optical beam in 2D. The first one consists of controlling the relative phase of the electric fields emitted by the antennas in 2D-arrays to control the radiation angles θ and φ, which along the x- and y-axis respectively. This is shown in Fig. 5.10(a) [19]. The second one, presented in Fig. 5.10(b), consists in using a 1D-array [229,234]. In this case, the relative phase among the antennas is tuned to steer the beam angle φ, along the y-axis, and wavelength tuning to scan the beam angle θ, along the x-axis, as the radiation angle of a diffractive grating changes with the wavelength. 2D-scanning using only wavelength tuning has also been

demonstrated using serpentine OPAs [235], but is an uncommon approach.

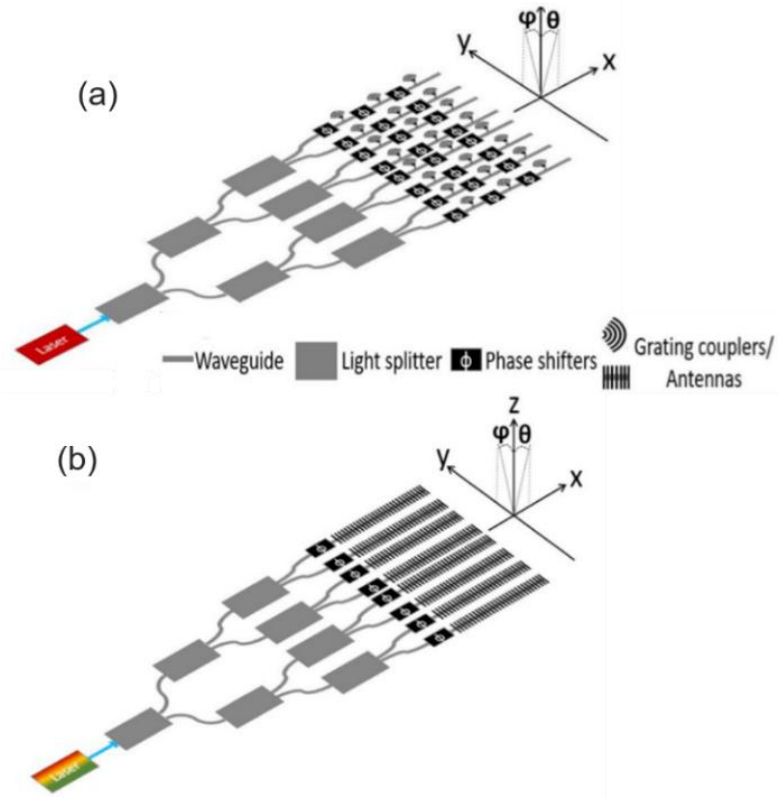

Fig. 5.10: (a) 2D-array achieving 2D-beam steering by controlling the relative phase emitted by the antennas. (b)1D-array achieving 2D-beam steering with relative phase control along one direction and wavelength tunning along the other one. Images from Hsu et al. [220].

While the two configurations provide 2D-beam steering, only the 2D-arrays allow the compensation of phase front errors due to atmospheric turbulences. Hence, the literature review is focused on 2D-arrays, which can be classified according to the shape into and rectangular and circular, or according to the periodicity into periodic or sparse.

5.3.1 Rectangular periodic arrays

Fig. 5.11 shows two examples of 2D-periodic arrays and their produced far field patterns [210,236]. In both cases, the array pitch is around 10 µm, which is greater than the operating wavelength of 1.55 µm. As the array fill factor is low, side lobes are present in the far field patterns.

Other periodic 2D-arrays can be found in [225,226,237–241], all with a pitch greater than the wavelength.

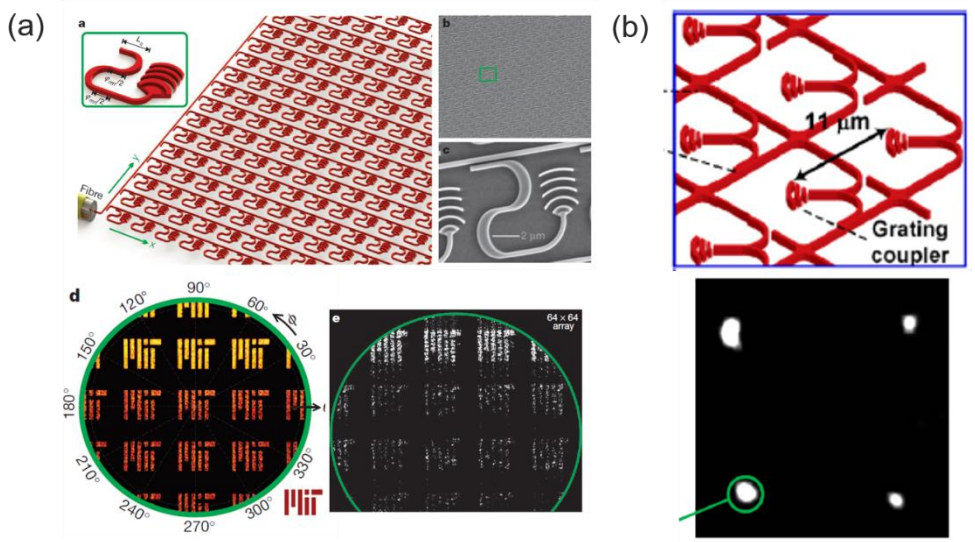

Fig. 5.11: Examples of 2D-rectangular periodic arrays with pitch greater than the half wavelength, $\Lambda > \lambda/2$. The array fill factor was low. Side lobes were visible. (a) 64x64 phased-array, pitch = 9 µm x 9 µm. Images from Sun et al. [210], (b) 2D-array with reduced number of phase shifters, pitch = 11 x 11 µm. Images from Ashtiani et al. [236]

The smallest pitch to date in a 2D-OPA was reported by Zhang et al. in 2023 (see Fig. 5.12(a)) [226]. Still, the pitch of 5.5 µm x 5.5 µm is larger than the wavelength of 1550 nm. Such small pitch was attained by reducing crosstalk using sinusoidal waveguides. The antenna size is 2.34 µm x 3 µm, giving a low array fill factor of 0.42 x 0.55. Side lobes are therefore present in the far field (Fig. 5.12(b)).

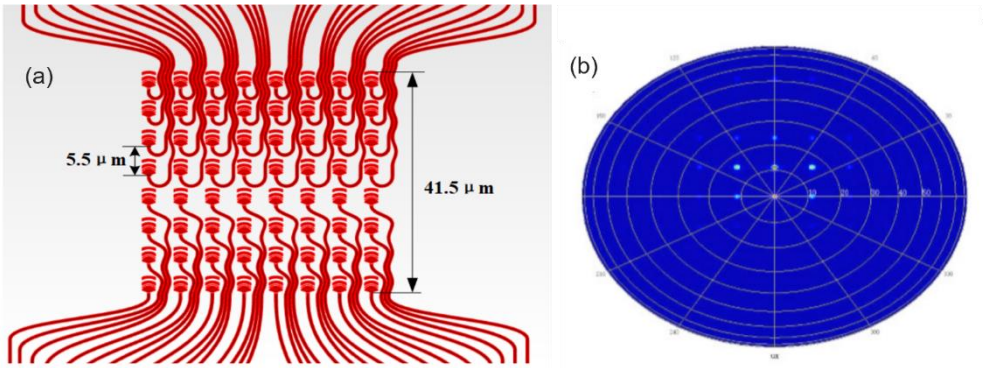

Fig. 5.12: (a) Smallest 2D-rectangular array pitch using sinusoidal waveguides to reduce crosstalk. (b) Its far field simulation. Images from Zhang et al. [226]

A pitch smaller than the half wavelength has only been demonstrated in 1D-arrays using dissimilar adjacent waveguides to limit crosstalk [216,218].

No 2D-arrays with pitch ($\Lambda \gg \lambda$) and high fill factor with attenuated side lobes have been found in the literature.

5.3.2 Rectangular sparse (aperiodic) arrays

These are non-uniform arrays in which the antennas are irregularly placed (see Fig. 5.13(A)), so as to smear the side lobe emissions into the noise floor [212,213,242,243]. The energy that was contained in the side lobes is now scattered in various angles (see Fig. 5.13(B)) and do not increase the power fraction in the main lobe.

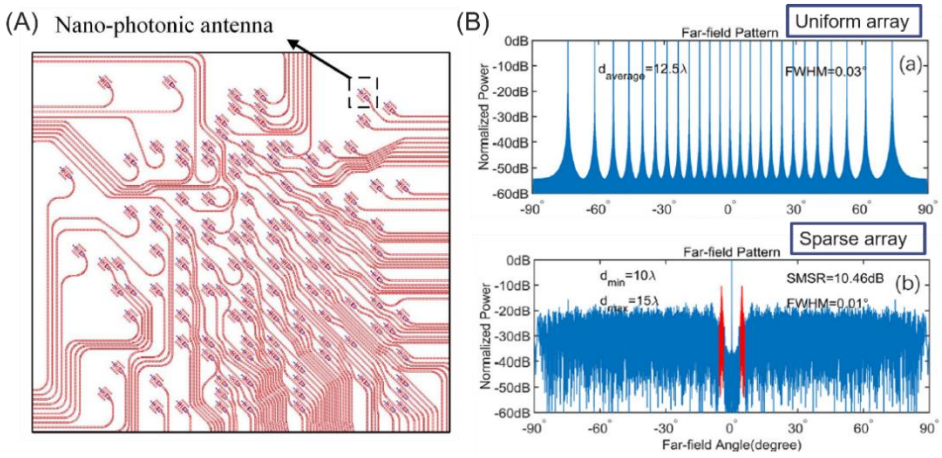

Fig. 5.13: (A) Sparse array. Image from Fateli et al. [213] (B) Comparison of far field profiles of (a) uniform and (b) sparse arrays. Images from Yang et al. [243].

5.3.3 Circular arrays

A few circular arrays have been reported in the literature [244–247]. Fig. 5.14 compares the far field patterns of a rectangular array and circular arrays (periodic and sparse) [244]. The considered emitted wavelength is 1 µm. A radial pattern is observed in the circular OPA and is still showing significant side lobes, which are reduced using a sparse configuration.

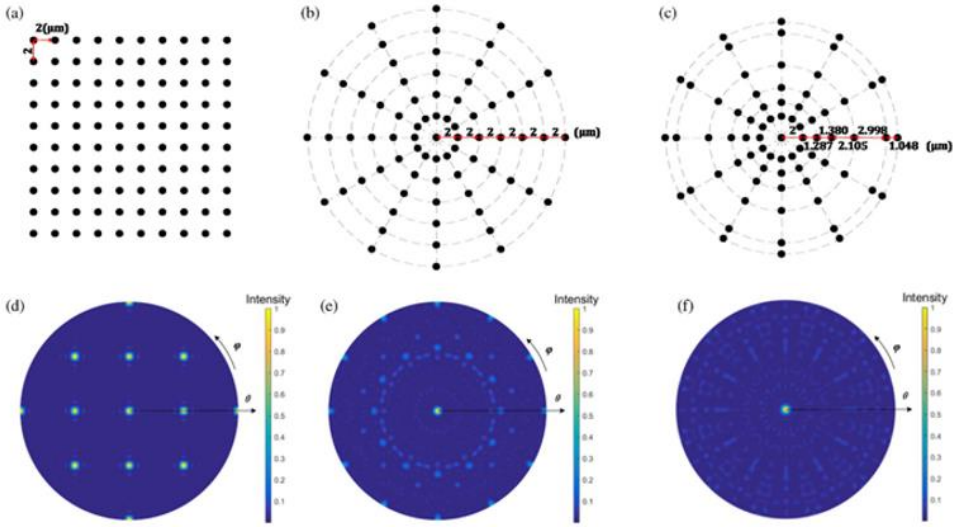

Fig. 5.14: (a) 10x10 Rectangular array, with pitch = 2λ, (b) 73-element circular array with periodic radial spacing = 2λ, and (c) with sparse spacing (range : 1λ to 3λ) (d)-(f) are the respective far field patterns. Images from Zhang et al. [244]

However, to date, circular arrays are difficult to implement due to complex waveguide routing systems. Benedikovic et al. proposed a central circular grating coupler (Fig. 5.15) to feed a circular OPA, but this resulted in a minimum optical intensity at the center of the far field pattern [246,247].

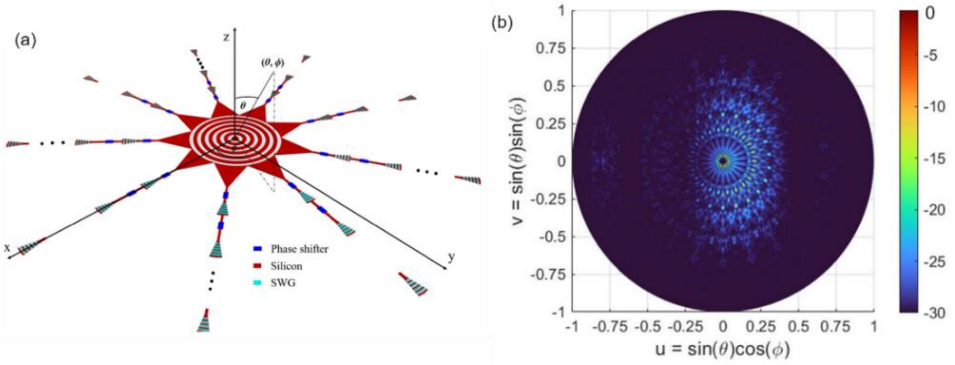

Fig. 5.15: (a) Circular OPA with central circular grating coupler as feeding system. (b) Corresponding far field profile. Images from Benedikovic et al [247].

5.4 AIM OF OUR WORK AND OPA DESIGN SPECIFICATIONS

An unexplored strategy for reducing side lobe levels while increasing the optical power in the main lobe is to implement a periodic rectangular 2D-array, with a large array pitch and high array fill factor, as described in section 5.2.2. This configuration, however, comes at the

expense of a reduced, but sufficient steering range for point-to-point communications. The aim of our work is therefore to implement such an array, whose specifications are given in this section.

The 2D-OPA schematic is shown in Fig. 5.16. The array period and antenna size are $\Lambda_{x,y}$ and $l_{x,y}$, along the x- and the y-axis, respectively. The linear fill factor corresponding to the x- or y-dimension is $FF_{x,y} = l_{x,y}/\Lambda_{x,y}$. A square OPA is considered with $l_x = l_y$ and $\Lambda_x = \Lambda_y$. The array fill factor, FF_{2D}, can be defined as the square of either one of the linear fill factors: $FF_{2D} = FF_x^2 = FF_y^2$.

The array is designed for CEA-Leti's 300 nm-thick SOI platform to operate at 1.55 µm wavelength and TE polarization. For a small-scale proof of concept, the following OPA specifications have been made as shown in Table 5.2.

N_x = N_y= 4 was chosen, giving 16 antennas in total. The array pitch was set to Λ_x = Λ_y = 90 µm, resulting in a lobe separation of $\delta\theta_x$ = $\delta\theta_y$ ≈ 1.0° in the far field as per Eq. (5.5). The full width at half maximum (FWHM) of the main lobe shall be around $\Delta\delta_{FWHM,x}$ = $\Delta\delta_{FWHM,y}$ ≈ 0.25° according to Eq. (5.6). Finally, the target value of the array fill factor has been set to FF_x = FF_y = 0.76, resulting in a side lobe level of SLL ≈ -10 dB (10 %), as shown in Fig. 5.8 and for leaving space for interconnecting waveguides. The optical mode produced by an antenna in the near field should have a mode size of at least l_x = l_y = 0.76 × 90 µm = 68.4 µm, to achieve the desired fill factor.

Thermo-optic phase shifters (heaters) are used to control the phase of the emitted field by each antenna [15]. The phase is controlled by passing a current through the resistive heater, changing the temperature of the adjacent waveguide, hence its effective index and the phase of the propagating mode. In our OPA, each antenna requires a phase shifter. The 16 heaters are driven simultaneously with a 16-channel electric probe [248].

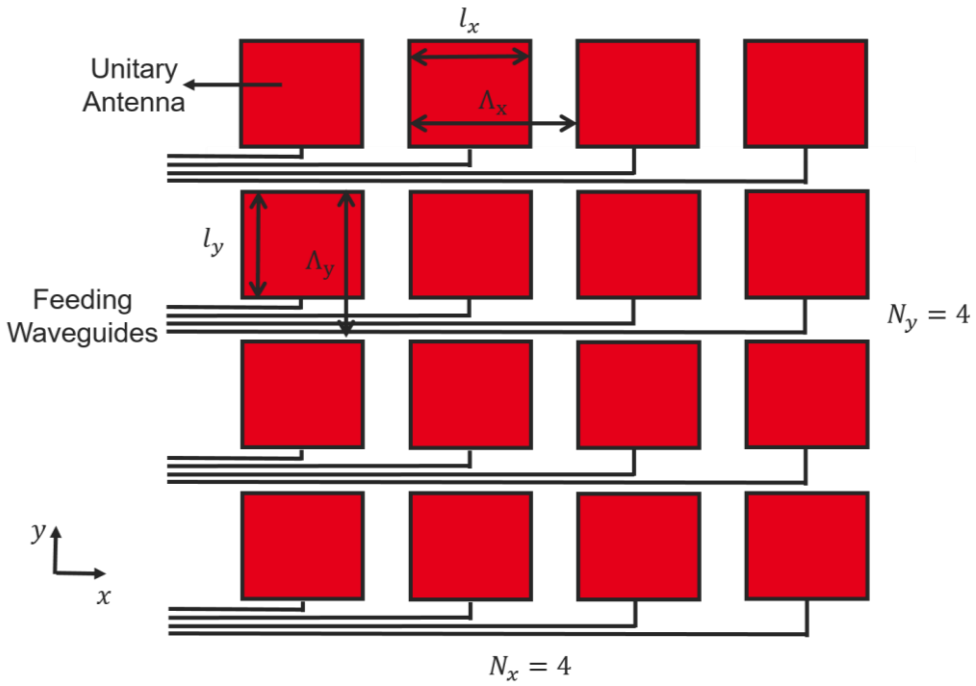

Fig. 5.16: Schematic of the proposed 4x4 OPA array. Phase shifters are not shown here for simplicity.

Parameter	**Symbol**	**Value**
Free space wavelength	λ	1.55 μm
Number of Antennas	$N_x = N_y$	4
Array Pitch	$\Lambda_x = \Lambda_y$	90 μm
Linear Fill Factor	$FF_x = FF_y$	0.76
Near field mode size	$l_x = l_y$	68.4 μm
Far field profile		
Lobe separation	$\Delta\theta_x = \Delta\theta_y$	1.00°
FWHM of main lobe	$\Delta\theta_{FWHM,x} = \Delta\theta_{FWHM,y}$	0.25°
Side Lobe Level	SLL	-10 dB (10 %)

Table 5.2: OPA specifications

Each antenna is fed by a single mode waveguide. Hence, an optical mode converter is required between the single mode waveguide, with a width of 500 nm, and the optical antenna with a width of 68.4 μm. The converter is required to be compact to maximize the array fill factor.

5.5 LITERATURE REVIEW OF BEAM EXPANSION SOLUTIONS

We consider here optical antennas implemented with diffractive gratings. The size of the radiated beam is determined by the grating width, in the direction perpendicular to the propagation, and its effective length, along the propagation axis. The effective length, l_e, refers to the length required to radiate all the power injected into the grating. In the subsequent literature review, we present solutions to laterally expand the optical mode from a narrow single-mode waveguide and a wide grating coupler, and strategies to increase the effective grating length.

2D-beam expansion is often performed in grating couplers, in which the beam diameter is typically expanded (in the near infrared wavelengths) from ~ 500 nm in a single mode waveguide to ~ 10 µm to match the mode field diameter of an optical fiber.

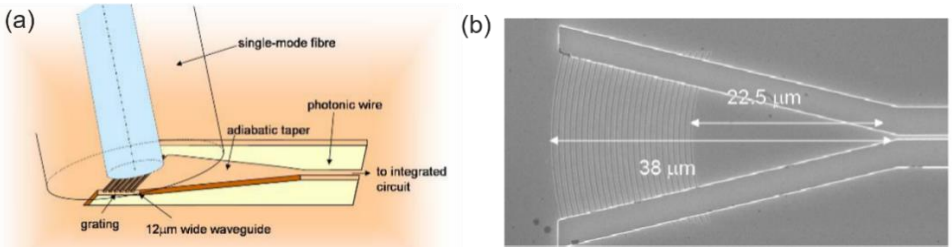

Fig. 5.17: (a) Straight 1D-grating coupler with 700 µm long taper, (b) Focusing grating coupler with 22.5 µm long taper. Images from Van Laere et at. [134].

Diffraction gratings are generally used to couple light to an optical fiber. Hence, they generally have a width of ~ 15 µm. The transition between single-mode waveguide, of ~ 0.5 µm width and the taper can be done using a straight adiabatic taper, as shown in Fig. 5.17(a). However, the required taper length is very long (> 200 µm) [134], and would yield a low array fill factor if implemented in an OPA. Non-adiabatic tapers, like the one shown in Fig. 5.17(b), allow low loss mode conversion on a length ~ 20 µm [134]. However, the tapers still occupy a footprint similar to that of the diffraction grating, limiting the achievable fill factor to less than 50 %. Demonstrated OPAs with non-adiabatic tapers have shown high side lobe levels in their far field patterns (see Fig. 5.11).

In 2018, Kim et al. reported a mode size converter to make the transition between a 500 nm-wide waveguide and a 140 µm-wide grating [249]. The converter, presented in Fig. 5.18, exploits evanescent coupling between the mode of the waveguide and the slab mode to achieve the size conversion. Due to the phase-matching conditions, the slab modes propagate with an angle of 28° with respect to the waveguide longitudinal axis, resulting in a large converter area that limits the potential array filling factor.

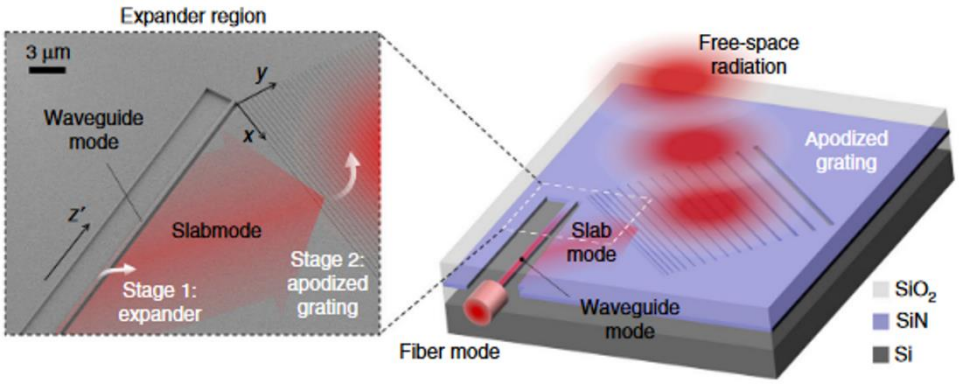

Fig. 5.18: Mode size converter based on evanescent coupling. Image from Kim et al. [249].

Other on-chip mode expanders include graded-index (GRIN) lenses [250], semi-lenses [251] and hollow tapers [252]. Still, no solution has been found in the literature providing array fill factors > 50 %.

In addition to on-chip mode expanders, several solutions have been proposed to implement weakly radiating gratings for beam expansion in free space. These solutions can achieve effective lengths of $l_e = 100\lambda - 10000\,\lambda$, where λ is the wavelength. For comparison, conventional fiber-chip grating couplers typically have an effective length of $l_e = 10\lambda$.

To implement such weak diffraction gratings, shallow etch steps can be used [257]. Other strategies include SWG nanoholes [253], as shown in Fig. 5.19(a), and corrugated sidewalls [254], as shown in Fig. 5.19(b), which help to lower the index contrast and hence, reduce the grating radiation strength. Another strategy consists of placing radiative elements laterally next to the waveguide core to diffract the evanescent field of the propagating mode [255], shown in Fig. 5.19(c). By using an SWG-waveguide instead of a conventional solid

waveguide core, as shown in Fig. 5.19(d), the delocalization of the evanescent field can be controlled, thus enabling control of the grating radiation strength [256]. These four design approaches have enabled mm-long antennas ($\sim 1000\lambda$).

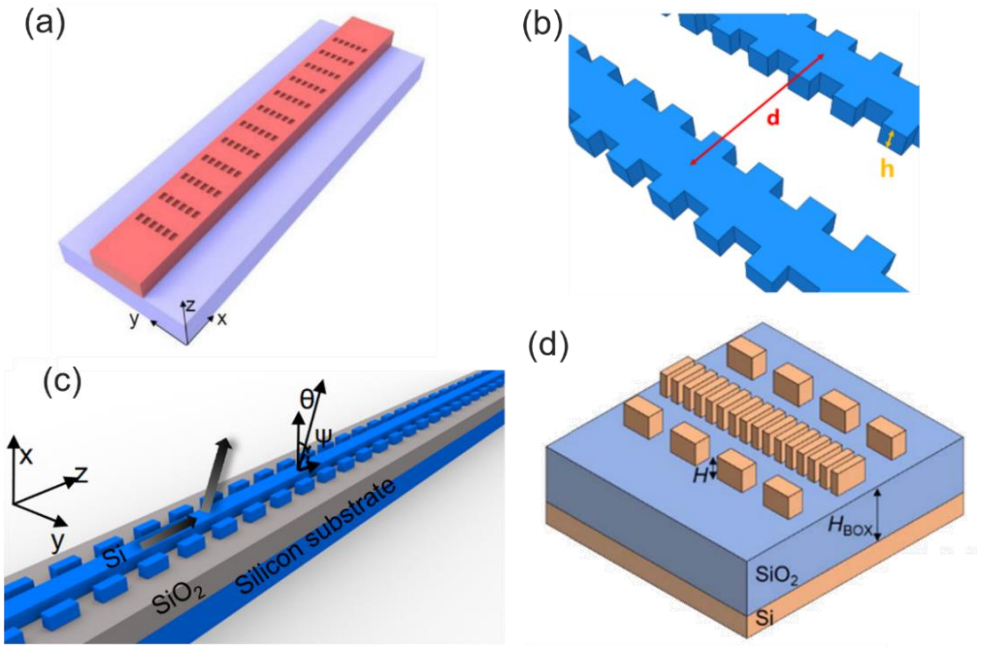

Fig. 5.19: Strategies for implementing weak gratings: (a) SWG nanoholes. Image from Li et al. [253], (b) Sidewall corrugations. Image from Yu et al. [254]. Laterally separated radiative elements with (c) solid waveguide core. Image from Chen et al. [255] (d) SWG waveguide. Image from Ginel-Moreno et al. [256].

5.6 ANTENNA STRUCTURE AND SIMULATION RESULTS

Fig. 5.20 and Fig. 5.21 schematically show the suggested OPA antenna geometry, allowing the expansion between a 500-nm-wide waveguide and a 50-µm-wide grating along both directions. The antenna comprises two separate diffraction stages: i) a waveguide-to-slab expansion grating and, ii) a free space radiation grating. The device is designed for the CEA-Leti's 300 nm-thick SOI platform at a wavelength λ = 1.55 µm and TE polarization. It was intended to maximize the array fill factor of a 2D-OPA.

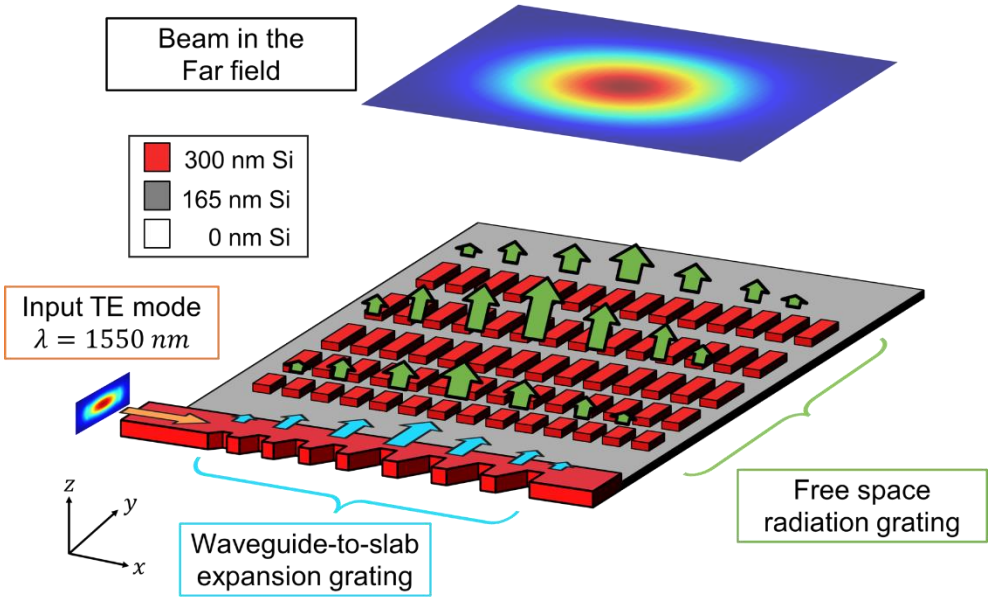

Fig. 5.20: 3D-view of the proposed OPA antenna, composed of a waveguide-to-slab expansion grating and of a free space radiation grating. The SiO_2 cladding and the BOX are not shown for the sake of clarity. The beam has a size of ~ 50 × 50 µm in the near field. The far field full width at half maximum divergence is around $\delta\theta_{FWHM}$ = 1.40° in both the x- and y-axis.

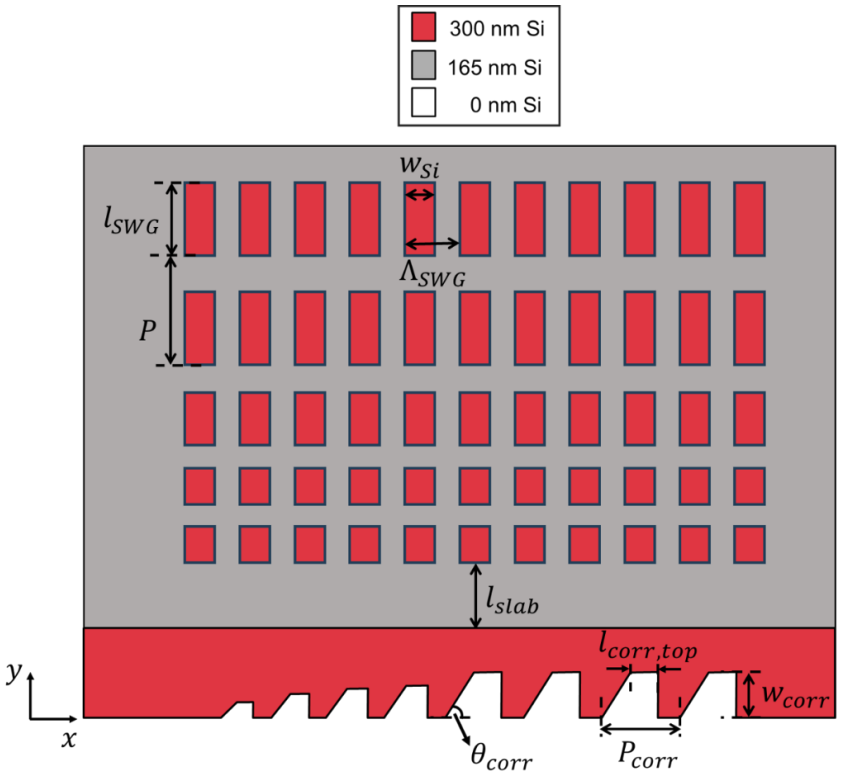

Fig. 5.21: Top view of the OPA antenna and its geometrical parameters

The waveguide-to-slab expansion grating is made up of single sided fully etched sidewall corrugations with a triangular shape. The grating period and apodization are optimized to create a Gaussian slab mode with a diameter of ~ 50 µm along the x-axis, propagating perpendicular to the waveguide, along the y-axis. This way the radiation grating can be placed near the waveguide, maximizing the array fill factor when implemented in an OPA.

The free-space radiation grating is implemented with shallow etched SWG-metamaterial ridges to minimize the grating radiation strength and maximize the effective grating length. The grating is apodized along the y-axis to yield a radiated field with a Gaussian profile. In the near field, the antenna radiates a Gaussian mode with a size of 50 µm × 50 µm. This corresponds to an angular divergence in the far field of 1.40° both along the x- and y-axis. This antenna structure, which enables a high array fill factor in a 2D-OPA, as shown in Fig. 5.16, has been patented by CEA-Leti [258].

In the next sections, the design methodologies of the waveguide-to-slab expansion grating and of the free space radiation grating are presented. The simulations are carried out using 3D-FDTD. The refractive indices used at λ = 1.55 µm are n_{Si} = 3.48 and n_{SiO_2} = 1.44.

5.6.1 Design of the waveguide-to-slab expansion grating

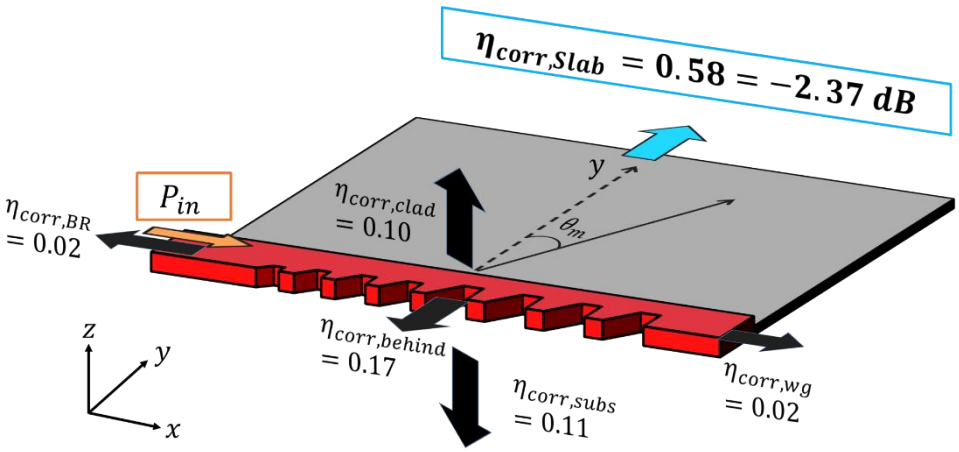

Fig. 5.22: Optical power distribution by the waveguide-to-slab expansion grating. Its power efficiency is $\eta_{Slab,corr}$.

The proposed waveguide-to-slab expansion grating geometry, as shown in Fig. 5.22, is inspired by the mode demultiplexer reported in [259,260]. A similar structure has been implemented as a compact light feeding circuit of a 1D-OPA [261] and is also referred to as a distributed Bragg deflector [262–265].

The sidewall corrugations act as blazed gratings and diffract the input light into the adjacent slab [259]. Their operation is governed by the grating equation:

$$n_{slab}\sin(\theta_m) = n_{WG} + m\frac{\lambda}{P_{corr}} \qquad \text{Eq. (5.8)}$$

where n_{slab} and n_{WG} are the effective indices of the slab and input waveguide modes respectively, θ_m is the radiation angle (with respect to the y-axis) for the diffraction order m, λ is the wavelength and P_{corr} is the period of the corrugation.

By controlling w_{corr}, the grating strength of the corrugation can be tuned. This gives control over the length over which the light is extracted. Also, by choosing the appropriate values of w_{corr} and P_{corr}, the emission angle θ_{corr} can be set to 0°, allowing the free space radiation grating to be placed close to the waveguide and hence, to maximize the array fill factor of an OPA.

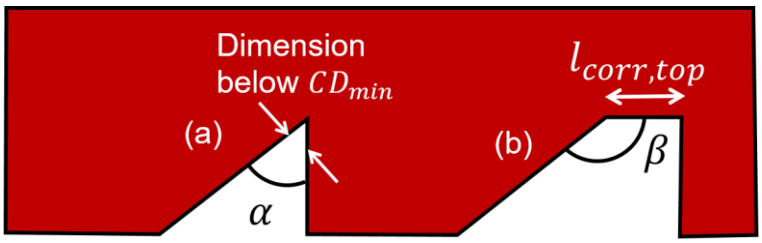

Fig. 5.23: (a) Triangular corrugation, α is acute and not allowed by fabrication design rules (b) β is obtuse thanks to the additional length $l_{corr,top}$.

For compatibility with the fabrication design rules of CEA-Leti, a section of length $l_{corr,top}$ = 80 nm is included in the blazed grating geometry (see Fig. 5.23), thereby avoiding an acute angle.

The waveguide width is $w_{WG} = 600\,nm$. The grating is designed to maximize diffraction into the m = -1 order, with a radiation angle of

$\theta_{m=-1} = 0°$. To further maximize the diffraction into the -1st order, the corrugations have been blazed using an angle $\theta_{corr} = 30°$.

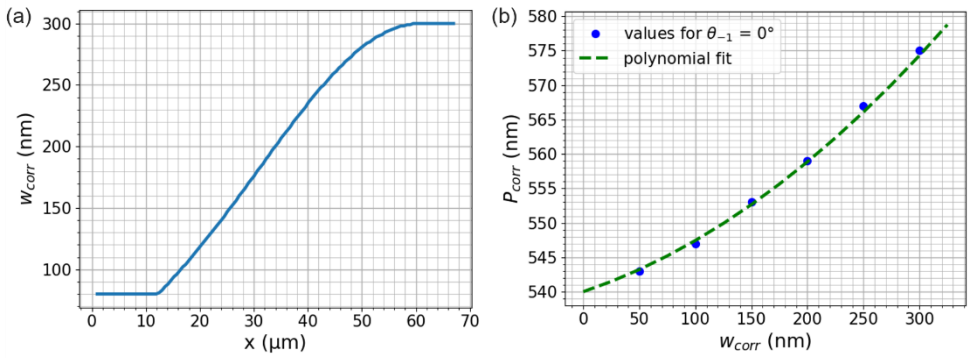

Fig. 5.24: Apodization of grating by (a) varying w_{corr}, the width in the corrugations along the x-axis and (b) setting the corresponding period in the corrugations, P_{corr}, such that each corrugation grating radiates at an angle of 0°

To obtain a Gaussian profile in the slab mode with a diameter of around 50 μm, the grating is apodised as shown in Fig. 5.24. To do so, a procedure similar to the one described in [259] is followed. The corrugation width, w_{corr}, is varied between $w_{corr,min}$ = 80 nm and $w_{corr,max}$ = 300 nm for x < 60 μm, where x is the position along the grating. The apodization function is a Gaussian: $w_{corr}(x) = w_{corr,max} e^{\frac{-x^2}{2\sigma_{corr}^2}}$, where σ = 60 μm is the standard deviation of the Gaussian function. If $w_{corr}(x) < w_{corr,min}$, then $w_{corr}(x)$ is set to $w_{corr,min}$ to respect fabrication design rules. For x > 60 μm, the grating is uniform with $w_{corr}(x) = w_{corr,max}$. However, different w_{corr} values with fixed period, P_{corr}, result into different radiation angles and non-parallel wavefronts. Several simulations have been run to determine the corresponding P_{corr} for various values of w_{corr} which give a diffraction angle of 0°. Then, the following has been fitted using a second order polynomial: $P_{corr} = 0.0002 w_{corr}^2 + 0.0543 w_{corr} + 540$. Following this polynomial, P_{corr} has been adapted along the grating for the various w_{corr}. The number of corrugations, N_{corr}, is set to 120.

The electric field intensity of the resulting slab mode is shown in Fig. 5.25, exhibiting a quasi-Gaussian profile along the x-axis. Its corresponding far field simulation pattern presented a propagation angle of θ_{Slab} = -0.30° in silicon, close to the targeted 0°.

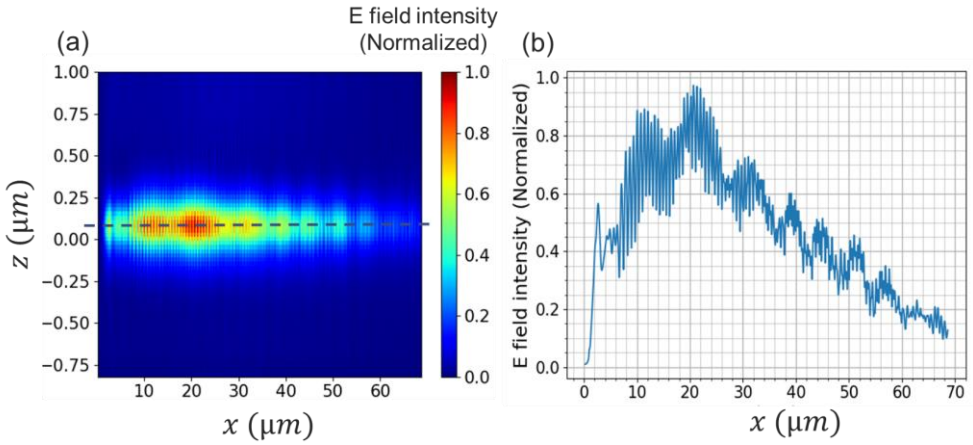

Fig. 5.25: (a) Electric field in the Si slab (b) 1D-profile taken at the point of maximum intensity (indicated along the dotted lines in (a)).

This waveguide-to-slab expansion grating, however, has a relatively low power efficiency, $\eta_{corr,Slab}$, which is defined as the ratio of the optical power transmitted to the slab to the optical power in the input waveguide (see Fig. 5.22). According to our simulations, the efficiency is $\eta_{corr,Slab}$ = 0.58 = -2.37 dB. Energy is mainly lost in radiative modes with $\eta_{corr,behind}$ = 0.17 (in the opposite direction of propagation of the slab mode), $\eta_{corr,subs}$ = 0.11 (towards the substrate), $\eta_{corr,clad}$ = 0.10 (towards the cladding). The residual transmission after propagation in the waveguide and the back-reflections were both negligible ($\eta_{corr,wg}$ = $\eta_{corr,BR}$ = 0.02). The energy efficiency of our waveguide-to-slab expansion grating can be improved with further optimization. Also, additional SWGs-metamaterials can be implemented for the waveguide-to-slab expansion grating to operate in the single beam condition [266].

The slab mode then travels a distance of $l_{Slab} = 5\ \mu m$ along the y-axis before being diffracted into free space by the free space radiation grating.

5.6.2 Design of the SWG-engineered free space radiation grating

The free space radiation grating (see Fig. 5.26) diffracts the slab mode, producing a 2D-Gaussian mode in free space. SWGs are used here to create an equivalent grating ridge with a lower index contrast as compared to a continuous Si grating ridge [253]. Light is therefore diffracted over a longer distance, producing a larger mode in the near

field along the y-axis and hence, a narrower angular divergence is obtained in the far field. The geometrical parameters of the radiation grating are shown in Fig. 5.21.

It is important to note that diffraction only occurs along the propagation y-axis. The SWG pitch is set to Λ_{SWG} = 350 nm and the silicon width is fixed to w_{Si} = 120 nm in every SWG-metamaterial ridge.

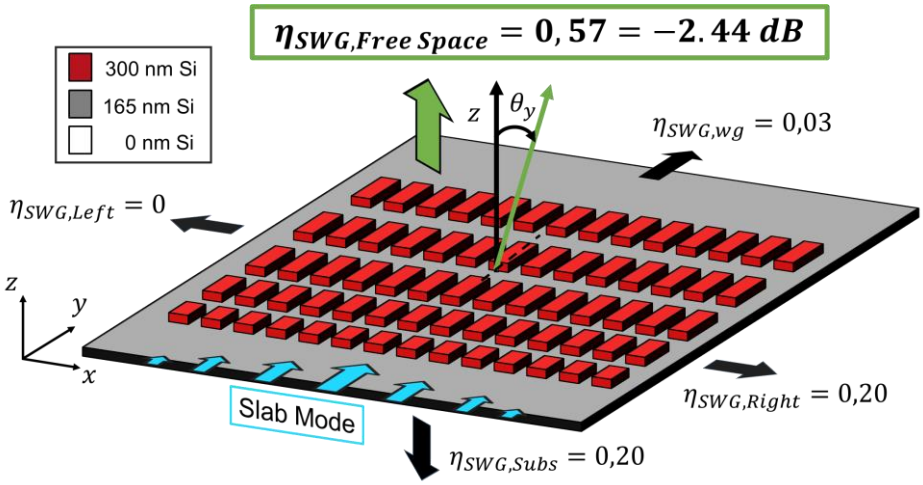

Fig. 5.26: Optical power distribution of the free space radiation grating. Its power efficiency is $\eta_{SWG,Free\ Space}$.

The working principle of this grating is also governed by Eq. (5.8), except that here, diffraction occurs into free space (instead of a silicon slab) at an angle θ_y (see Fig. 5.26). The apodization methodology is similar to the one used for the waveguide-to-slab expansion grating (see Fig. 5.27).

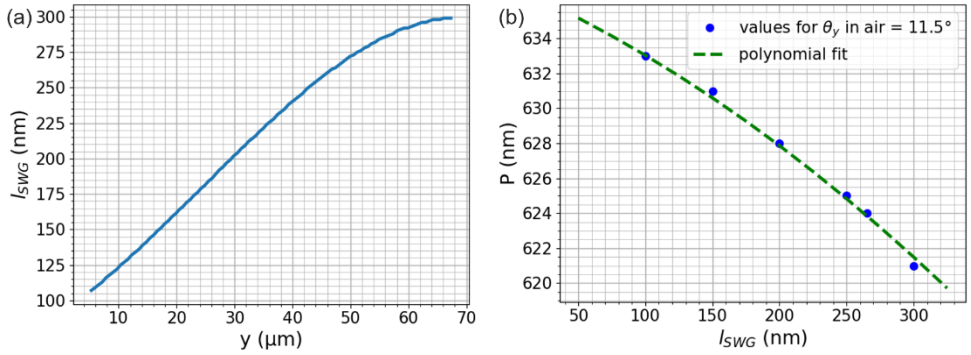

Fig. 5.27: (a) Apodization function (b) Corresponding period P such that the radiation angle is 11.5° in air for every SWG-equivalent grating ridge.

The grating strength is varied by varying the longitudinal length l_{SWG}. The apodization function is $l_{SWG}(y) = l_{SWG,max} e^{\frac{-(y-y_0)^2}{2\sigma_{SWG}^2}}$ where $l_{SWG,max}$ = 300 nm, y_0 = l_{slab} = 5 µm as the free space radiation grating starts after the slab, σ_{SWG} = 90 µm is the standard deviation of the Gaussian. The grating longitudinal period, P, is adapted such that each SWG-equivalent grating ridge radiates at an angle of θ_y = 11.5° in air and is given by the following polynomial: $P = -6 \times 10^{-5} l_{Si}^2 - 0.0337 l_{Si} - 637$. This diffraction angle was chosen to minimize back-reflections from the m = -2 grating diffraction order, which can be coupled back into the slab if θ_y = 0°. The number of SWG equivalent ridges, N_{SWG}, has been set to 100.

Fig. 5.28 shows the simulated emitted near field in free space, which is quasi-Gaussian along both the x and y axes. The mode field diameter (MFD) is around 50 µm in both directions.

Fig. 5.29 shows the far field simulation results. The beam is emitted at angles θ_x = -1.0° and θ_y = 12.2° in the air. These values are close to the targeted ones of $\theta_{x,target}$ = 0° and $\theta_{y,target}$ =11.5°. The far field profile is Gaussian with a full width at half maximum (FWHM) divergence of $\delta\theta_{FWHM}$ = 1.40° along x and y directions. This divergence corresponds to a beam waist of around w_0 = 24 µm at a wavelength λ = 1.55 µm, calculated from:

$$w_0 = \frac{\sqrt{2 \ln 2}}{\pi \, \delta\theta_{FWHM}} \lambda \qquad \text{Eq. (5.9)}$$

where $\delta\theta_{FWHM}$ is the FWHM divergence of the Gaussian beam and λ is the wavelength.

The beam diameter (or mode field diameter, MFD) is therefore MFD = $2 \times w_0$ = 48 µm. The emitted MFD is less than the targeted 68.4 µm (see Table 5.2) and is less than the geometric antenna dimensions, $L_{Ant} \times W_{ant} \approx$ 70 µm × 70 µm. If implemented in a 2D-array of pitch $\Lambda_x \times \Lambda_y$ = 90 µm × 90 µm as per our specifications, the array fill factor along the x and y-axes is $FF_x = FF_y$ = 48/90 = 0.53, resulting in an $SLL \approx$ - 5 dB instead of the targeted -10 dB.

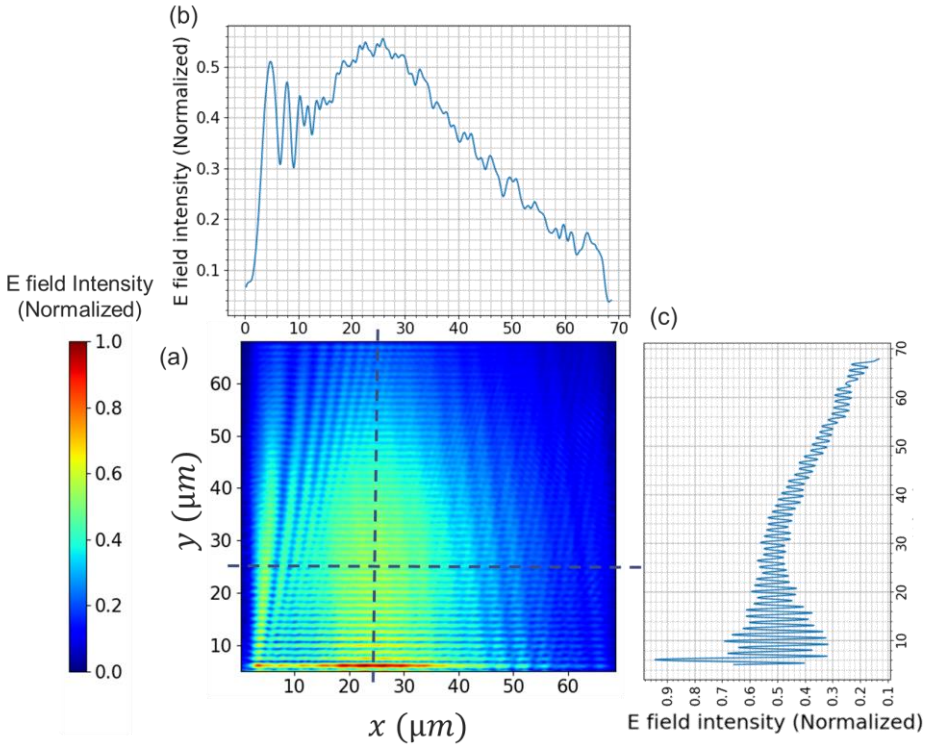

Fig. 5.28: (a) Near field in free space, with 1D-profiles (indicated by the dotted lines) (b) along the x-axis and (c) y-axis.

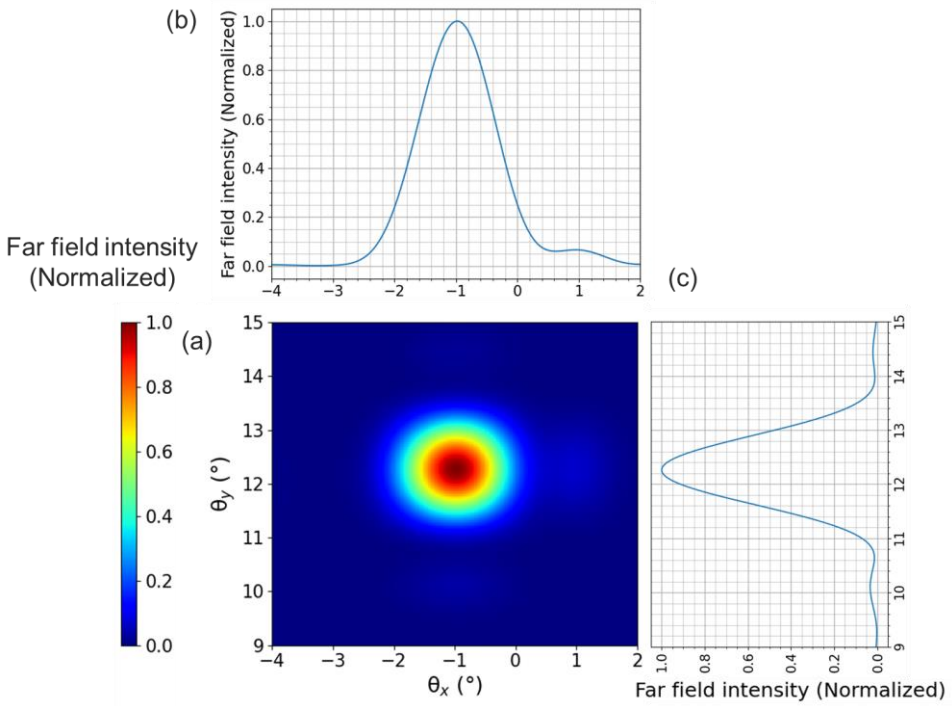

Fig. 5.29: (a) Far field profile of the emitted beam with associated 1D-profiles taken at the position of maximum intensity (b) along θ_x and (c) along θ_y.

The simulated transmission efficiency of the free space radiation grating, defined as the transmitted optical power into free space relative to the optical power injected into the slab is $\eta_{SWG,Free\ Space}$ = 0.57 = -2.53 dB. Power losses to the substrate are $\eta_{SWG,Subs}$ = 0.20. The directionality of the grating should be optimized. Another $\eta_{SWG,Right}$ = 0.20 was lost in the plane of the chip, towards the positive x-axis. These can be extracted into free space by increasing the number of SWG periods in each grating ridge which was set to 120. A negligible residual transmission $\eta_{SWG,wg}$ = 0.03 was left after diffraction by the gratings.

The overall simulated efficiency of the whole antenna is $\eta_{Ant} = \eta_{corr,Slab} \times \eta_{SWG,Free\ Space}$ = 0.33 = -4.81 dB and should be further optimized.

5.6.3 Summary of the design parameters of the antenna

Table 5.3 summarizes the OPA antenna parameters.

Corrugations	Value	SWGs	Value
w_{WG}	600 nm	Λ_{SWG}	350 nm
N_{corr}	120	w_{Si}	120 nm
θ_{corr}	30°	N_{SWG}	100
$l_{corr,top}$	80 nm	l_{SWG}	107 – 300 nm
w_{corr}	80 – 300 nm	P	621- 633 nm
P_{corr}	543 – 575 nm	θ_x	-1.00° in air
l_{slab}	5 µm	θ_y	12.24° in air
θ_{Slab}	-0.30° in Silicon	$\Delta\theta_{FWHM}$	1.40°
		MFD	48 µm
$\eta_{corr,Slab}$	0.58 (-2.32 dB)	$\eta_{SWG,Free\ Space}$	0.57 -2.53 dB)
$L_{Ant} \times W_{ant}$	~ 70 µm × 70 µm	η_{Ant}	0.33 (-4.81 dB)

Table 5.3: OPA antenna parameters

In our simulations, a 2D quasi-Gaussian beam is obtained in the near field. The far field radiation angles are θ_x = -1.0° and θ_y =12.2° in air. The far field FWHM divergence is 1.40°, along both directions. This corresponds to an MFD = 48 µm in the near field. If arrayed with a pitch of 90 µm × 90 µm in an OPA, the array fill factor would be

0.53 × 0.53 and the side lobe level would be ~ -5 dB. The antenna power efficiency is η_{Ant} = 0.33 ~ -5 dB.

5.7 ANTENNA FABRICATION

The antenna was fabricated using immersion lithography. Fig. 5.30 shows the design and OPC layouts of the structures (staircase fashion for side wall corrugations, bigger squares in SWGs). Fig. 5.30 also shows the associated SEM images before cladding deposition. The minimum feature sizes are 80 nm in the corrugations and 100 nm in the SWG elements.

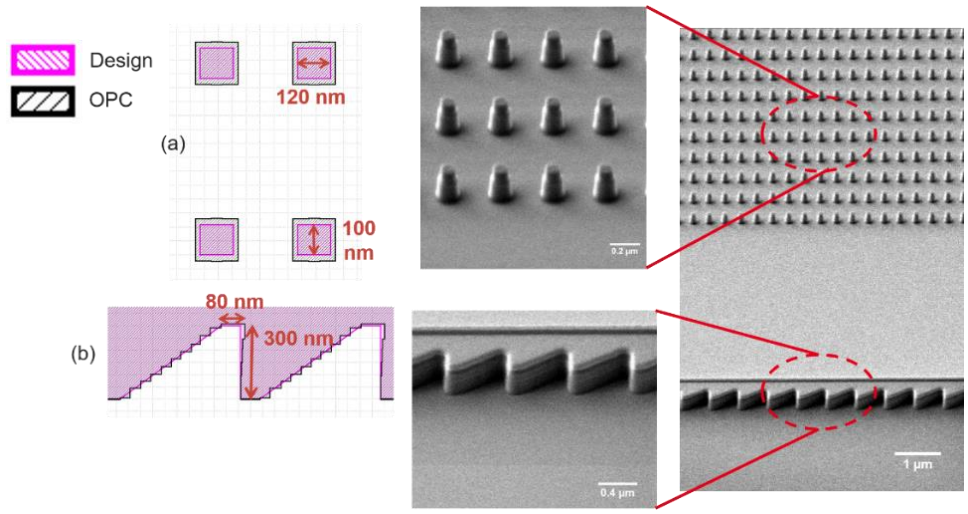

Fig. 5.30: Nominal design and OPC layouts with associated SEM images of (a) the free space radiation grating and (b) the waveguide-to-slab expansion grating.

5.8 ANTENNA CHARACTERIZATION

In the following sections, experimental determinations of the OPA antenna far field divergence, absolute emission angles and power efficiency of the fabricated antenna are described.

5.8.1 Divergence characterization set up

The characterization set up is schematically represented in Fig. 5.31. A laser with wavelength λ = 1550 nm is injected into a photonic waveguide via the input grating coupler. The light is then fed to the OPA antenna which diffracted the light into free space. The diffracted beam is imaged using an angularly calibrated camera (see section 5.8.2

for the calibration procedure). The camera is placed at a height $h \sim 40$ mm above the antenna surface. At this height, the camera is in the far field, beyond the expected Fraunhofer distance, given by Eq. (5.1): $d_F \sim 3$ mm considering an aperture size of $D \sim 50$ µm. The camera is then connected to a computer to save the images.

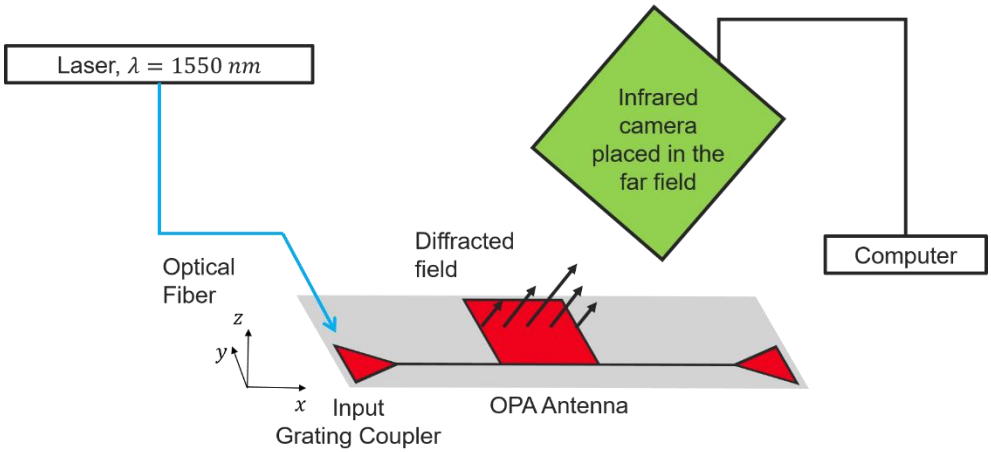

Fig. 5.31: Far field imaging set up.

The images are recorded in 8-bit format, meaning that the pixel intensities were in the range 0-255. Care is taken not to saturate the image by setting the exposure time of the camera such that the maximum pixel intensity was around 230 while taking the images. The background noise level is subtracted in the image and the pixel intensities are then normalized (by dividing by the maximum pixel intensity), which make the new range of pixel intensities from 0-1.

5.8.2 Angular calibration of the camera

The procedure (see Fig. 5.32) for calibrating the camera angularly (°/pixel) is as follows [248]:

1. A passive OPA is used as a reference structure. This OPA consists of antennas with a known array pitch, and results in an angular separation of 10° in the far field profile between two radiation lobes.
2. The distance between the two lobes is measured in pixels. To obtain the angular scale in °/pixel, the known angular separation of 10° is divided by the measured pixel distance, obtaining 0.02°/pixel.

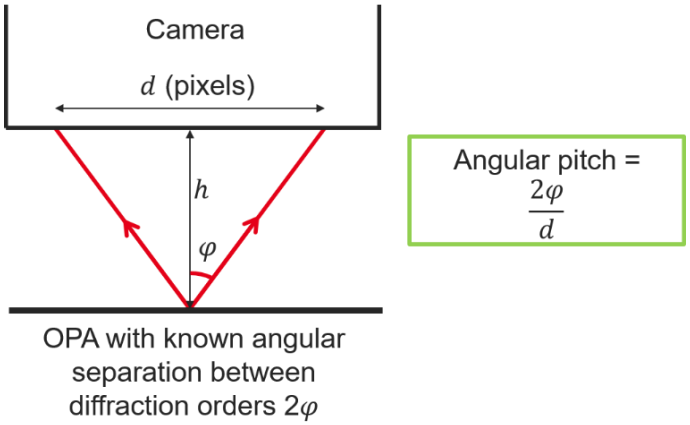

Fig. 5.32: Angular calibration of the camera.

5.8.3 Measurement protocol of the antenna emission angles

Fig. 5.33 shows the experimental protocol used to determine the absolute emission angle of the antenna, θ_x. Moving the camera vertically upwards by $\Delta h = h_2 - h_1$, the image of the beam is horizontally translated by $\Delta x = x_1 - x_2$. The angle θ_x can therefore be determined as $\theta_x = 90° - \frac{\Delta h}{\Delta x}$. The same procedure is also done to find the angle θ_y.

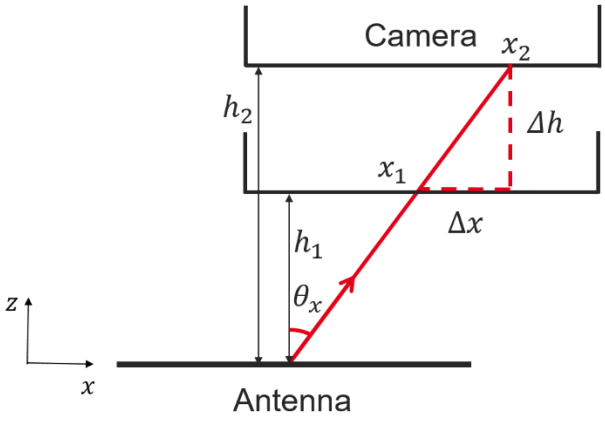

Fig. 5.33: Experimental protocol used to determine the absolute emission angle of the antenna.

This method gives an approximation of the absolute value of the emission angle. For higher accuracy, the axes of the camera should be perfectly aligned with the axes of the antenna.

5.8.4 Measured divergence and emission angles

Fig. 5.34(a) shows the far field image of the produced beam by the OPA antenna. θ_x and θ_y are the angular axes as defined in Fig. 5.20, with θ_x being along the direction of the input waveguide.

The measured emission angles are $\theta_x \approx 0.5°$ and $\theta_y \approx 8.1°$. These values are close to the simulated values of -1.0° and 12.2° respectively.

Fig. 5.34(b) and (c) show the experimental and simulated far field cross-sections which are taken at the point of maximum intensity. The simulated curves have been translated to superpose the experimental and simulated maxima. This operation does not change the angular divergence. Experimental and simulated results are in good agreement, showing that the FWHM divergence of the antenna is around 1.40°, corresponding to a MFD = 48 µm.

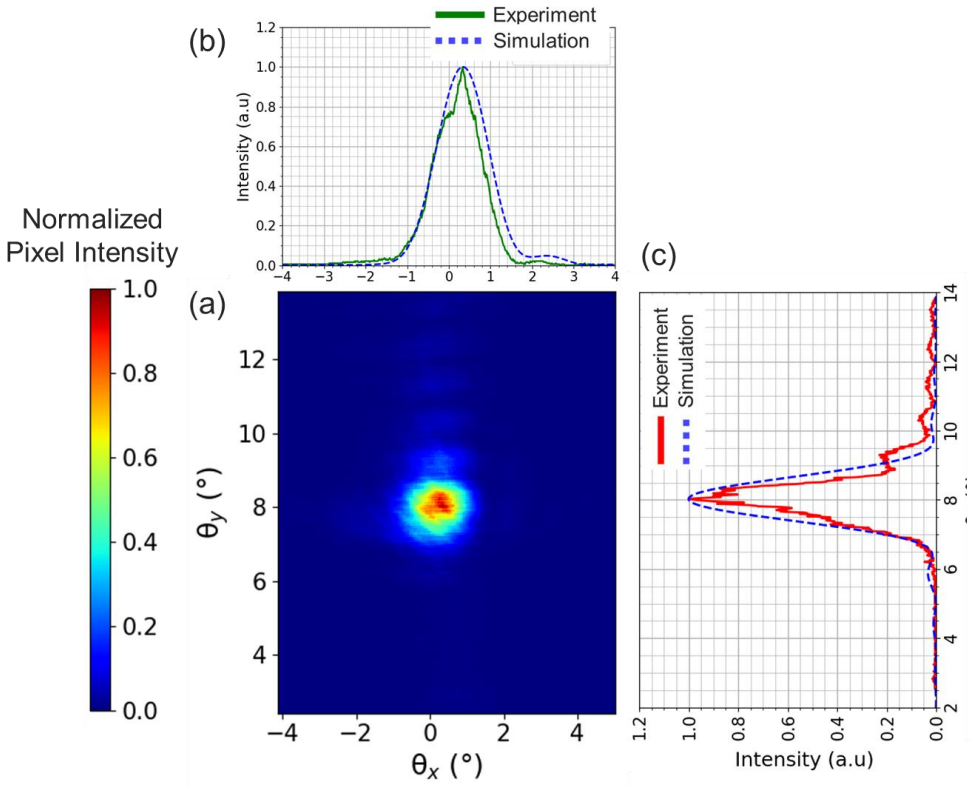

Fig. 5.34: (a) Experimental far field image of the OPA antenna. (b)-(c) Far field intensity 1D cross-sections taken at the point of maximum intensity. The simulation curves have been translated to superpose the curves at the same maximum.

5.8.5 Power measurement

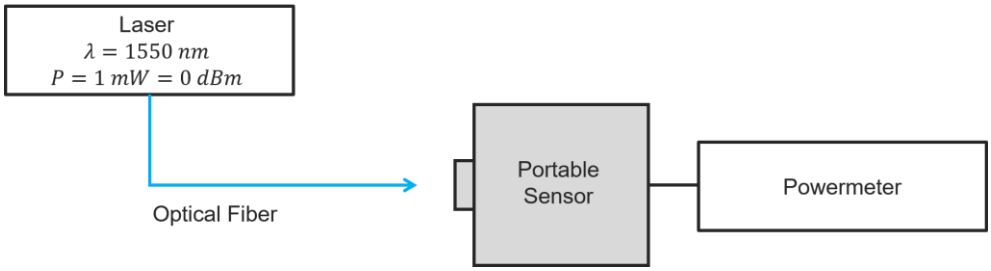

Fig. 5.35: Power-meter calibration setup.

To measure the optical power emitted by the antenna, a portable sensor connected to a power-meter is used. The power-meter is calibrated by directly measuring the output power of the laser, set to emit an optical power of 0 dBm =1 mW (see Fig. 5.35). The measured power is -0.012 dBm at a wavelength λ = 1.55 µm. These very close values indicate that the calibration of the power-meter is adequate.

The optical power emitted by the antenna is measured experimentally using a similar set up as in Fig. 5.31, but instead of using the camera, the portable sensor connected to the power-meter is used. The sensor is placed at an approximate height of 45 mm above the wafer surface (beyond the Fraunhofer distance) and is clamped to a stable support on a bench.

The power of the input laser is set to P_{las}= 0 dBm and the wavelength is set to λ = 1550 nm. The measured power is P_{meas} = -12.6 dBm. The transmission at λ = 1550 nm between the fiber and the input grating is T_{fib-GC} = -4.30 dB (obtained from a previous grating-fiber loss measurement). The power efficiency of the antenna, T_{Ant}, which is defined as the power transmission from the input waveguide to free space is therefore given by:

$$T_{Ant}(dB) = P_{meas}(dBm) - P_{las}(dBm) - T_{fib-GC}(dB)$$

We obtain $T_{Ant} \approx$ -8.30 dB. The simulated efficiency is η_{Ant} = -4.80 dB. The antenna is therefore more lossy than expected by 3.50 dB. These losses could come from either the waveguide-to-slab expansion grating, or the free space radiation grating.

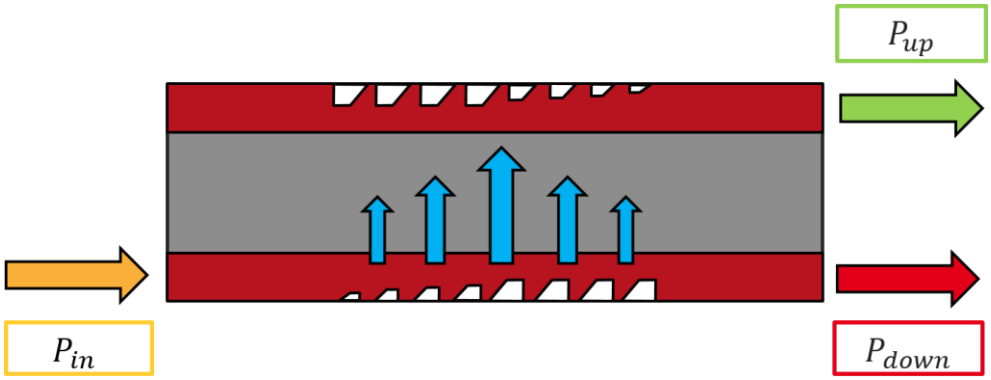

Fig. 5.36: Waveguide-to-slab expansion gratings placed in a back-to-back configuration to measure their power transmission.

The losses of the waveguide-to-slab expansion gratings are measured in a back-to-back configurations (see Fig. 5.36). Conventional fiber-chip grating couplers are used to couple light in and out of the chip. We measure the power of the outcoupled from the up and down output grating couplers, P_{up} and P_{down} respectively. These are given by:

$$P_{up}(dBm) = P_{in}(dBm) + 2 \times T_{fib-GC}(dB) + 2 \times T_{corr-slab}(dB)$$

$$P_{down}(dBm) = P_{in}(dBm) + 2 \times T_{fib-GC}(dB) + T_{corr-WG}$$

where P_{in} is the input power of the laser, P_{in} = 0 dBm, T_{fib-GC} is the transmission between fiber and grating coupler, $T_{corr-slab}$ is the transmission of the waveguide-to-slab expansion grating, $T_{corr-WG}$ is the residual transmission in the waveguide after diffraction by the corrugations.

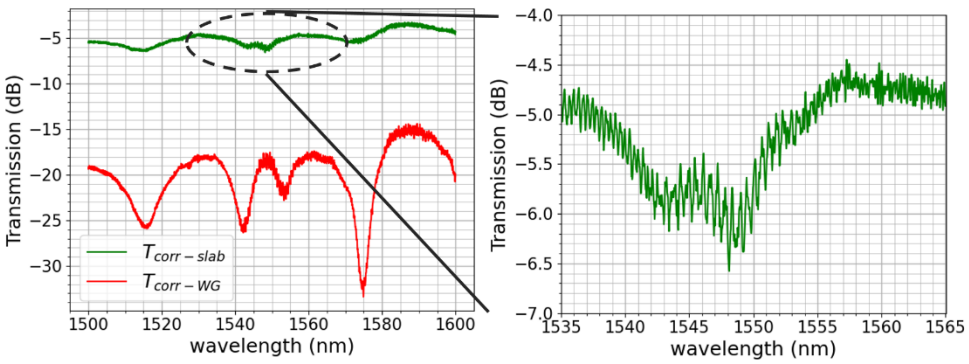

Fig. 5.37: Measured transmissions of the waveguide-to-slab expansion grating.

Fig. 5.37 shows the determined $T_{corr-slab}$ and $T_{corr-WG}$. $T_{corr-WG}$ is very low ≈ -17 dB, which shows that little power is left after the in-plane diffraction. At λ = 1550 nm, $T_{corr-slab}$ ≈ - 6.00 dB. The simulated value is $\eta_{corr,Slab}$ = -2.32 dB. The corrugations are more lossy than expected, by 3.68 dB. The difference between the simulated and measured overall antenna efficiency, of 3.50 dB, can be attributed to the additional loss in the waveguide-to-slab expansion grating.

5.8.6 Comparison of SWG and non-SWG antenna

Two other antennas with the same waveguide-to-slab expansion grating, with different free space radiation gratings have been designed and characterized. The free space radiation gratings are both unapodised, but one is made up of SWGs-ridges and the other one is made up of continuous silicon ridges (non-SWGs), as shown in Fig. 5.38(a), (b). The geometrical fill factors in the gratings are almost the same (l_{SWG}/P_{SWG} ≈ $l_{Si\ block}/P_{Si\ block}$).

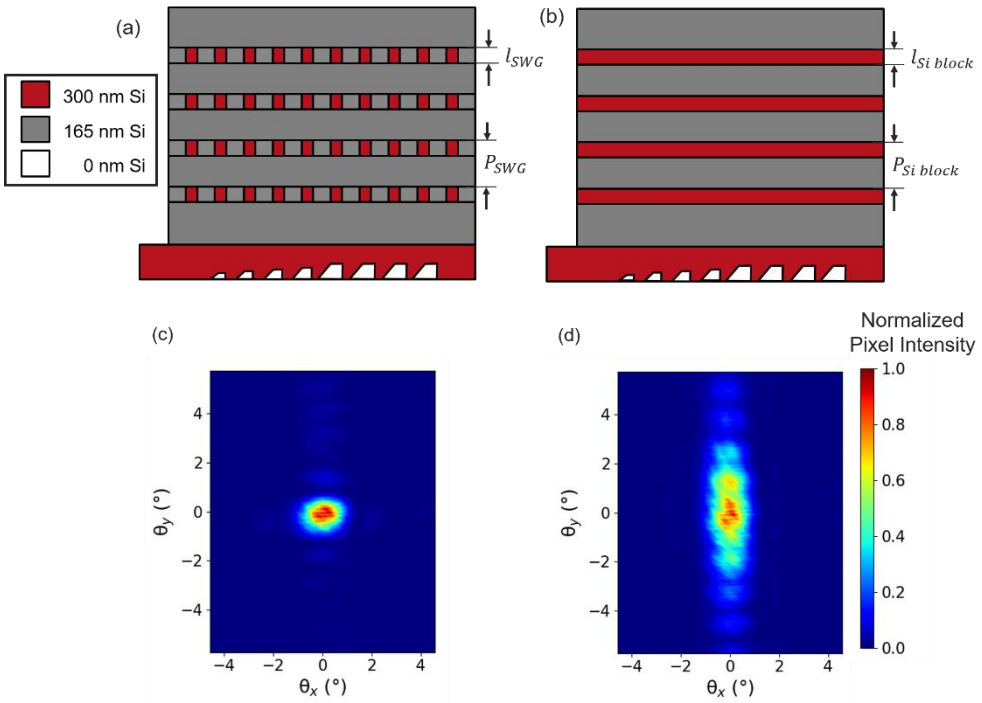

Fig. 5.38: (a) Schematic of SWG-ridge antenna and (b) non-SWG (Si ridge) antenna (c) Far field images of SWG and (d) non-SWG antennas. The measured divergence of the SWG antenna (~ 1.40°) was smaller than the measured divergence of the non-SWG antenna (~ 4.41°).

The respective imaged far fields are shown in Fig. 5.38(c) and (d). The divergence along θ_x is the almost the same for both the antennas, $\Delta\theta_{FWHM,x} \approx 1.40°$. This was expected since the waveguide-to-slab expansion gratings are the same in both the antennas. Along θ_y, the divergence was smaller for the SWGs-metamaterial free space radiation gratings as compared to the non-SWGs counterpart, $\Delta\theta_{FWHM,y}(SWGs) \approx 1.40° < \Delta\theta_{FWHM,y}(non-SWGs) \approx 4.41°$.

This indeed shows that the emitted near field mode size is larger with the SWGs–metamaterials, which have indeed reduced the index contrast and the grating radiation strength.

5.8.7 Antenna characterization summary

The experimentally angular divergence of our OPA antenna is $\Delta\theta_{FWHM} \approx 1.40°$ in both the x and y directions, and is in good agreement with our simulations. This divergence corresponds to an MFD = 48 μm in the near field. The MFD is lower than the targeted value, resulting in a lower array fill factor for the intended array with a pitch along both directions of 90 μm. This should result in a side lobe level of $SLL \sim$ -5 dB, which is worse than the targeted value of -10 dB.

The power efficiency of the antenna was measured to be $T_{Ant} \approx$ - 8.30 dB. The simulated transmission is η_{Ant} = -4.80 dB. The antenna is 3.50 dB more lossy than expected. Separate measurements determined that the origin of these differences mainly come from the waveguide-to-slab expansion grating.

Finally, the divergence of an antenna made up with SWG-equivalent ridge lines and the divergence of an antenna with continuous Si grating ridge lines were experimentally compared. Both gratings had the same geometric duty cycle. The beam produced by the SWG-equivalent ridges showed a smaller divergence than the full Si ridges, showing that the use of SWGs-metamaterials lead to a grating with reduced index contrast and enabled light emission over a longer distance.

5.9 OPA FABRICATION AND CHARACTERIZATION

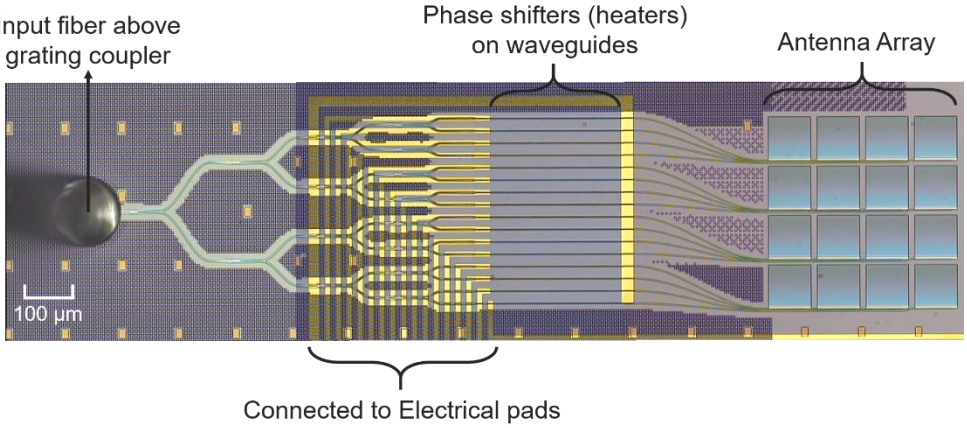

Fig. 5.39: OPA microscope image, with metal thermo-optic phase shifters and the 4×4 array of antennas. Light was injected into the OPA circuit from an external laser source at a wavelength λ = 1550 nm via an input grating coupler.

A passive OPA (without phase shifters) was fabricated on the same wafer as the previously studied antenna onto which thermo-optic phase shifters (metal heaters) were added at the C2N facilities. The heaters were defined using e-beam lithography, followed by a lift off process. A microscope image of the fabricated OPA with the metal heaters is shown in Fig. 5.39.

A similar set up, as shown in Fig. 5.31, is used to image the far field profile of the whole OPA. In addition, a multi-channel electrical probe was used to contact the 16 phase shifters simultaneously [248]. The phase shifters are operated individually using a series of digital-to-analog convertors (DACs). When no voltage is applied, the phase of the emitted fields of each of the antennas is random, owing to the random input waveguide lengths combined with fabrication-induced dimensional variations [226], and lead to a random pattern in the far field profile as shown in Fig. 5.40(a). The OPA is calibrated by tuning the phase of all 16 channels to maximize the optical power into the main lobe. The phase-calibrated far field profile is shown in Fig. 5.40(b). Similar phase correction was demonstrated in [267]. Using the relative amplitude of the secondary emission lobes, the unitary antenna far field profile, which is the element factor, can be distinguished.

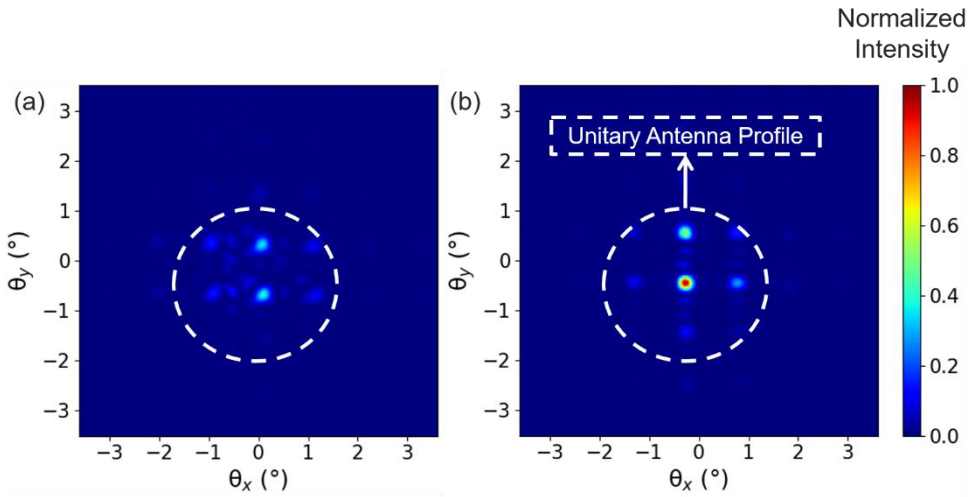

Fig. 5.40: (a) Phase-uncalibrated and (b) phase-calibrated OPA

The far field cross section of the phase-calibrated OPA is shown in Fig. 5.41. The lobes are separated by 1.00° and the FWHM divergence of the main lobe is around 0.25°, in good agreement with the design (see Table 5.2). The OPA is not perfectly calibrated as the intensity of the two side lobes is not the same (see Fig. 5.9). This is probably because 3 phase shifters out of the 16 have been damaged during the experiment, limiting the phase calibration.

The side lobe level, SLL, is determined using the highest side lobe intensity along both axes. The largest SLL appears along θ_y, $SLL(\theta_y)$ = -2.60 dB. Along θ_x, $SLL(\theta_x)$ = -5.22 dB is obtained. This value of θ_x is expected as the measured MFD = 48 µm of the near field of the unitary antenna leads to an array fill factor of 0.53 (see section 5.8.7).

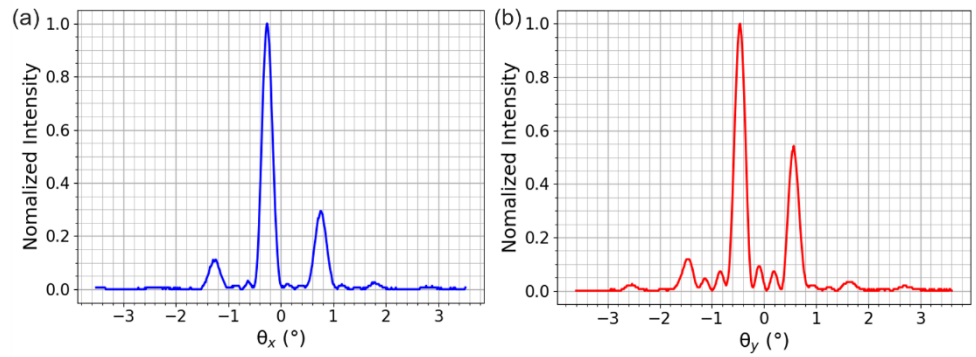

Fig. 5.41: Calibrated-OPA 1D-cuts along (a) θ_x (b) θ_y.

Hence, our work shows that it is indeed possible to attenuate side lobe levels in a 2D-periodic OPA with a large array period by maximizing the array fill factor. However, further studies should be carried out to further maximize the array fill factor to further attenuate the side lobe levels and to improve the efficiency of the unitary antenna.

5.10 CONCLUSIONS AND PERSPECTIVES

The aim of our study was to design a 2D-OPA with a novel antenna structure for FSO communications. In such systems, the OPAs act as integrated-on-chip beam phase front modulators, which can actively compensate phase front distortions induced by atmospheric turbulence.

However, if the array pitch in the OPAs is larger than half the wavelength, side lobes are present in the far field. These side lobes are not generally used in communication links and result in energy loss. To date, no 2D-OPA with a pitch smaller than half the wavelength has been demonstrated. Such small pitch is very challenging to implement due to the small wavelength size (very short antennas with high grating strengths will be required and optical crosstalk needs to be suppressed). Sparse arrays, with variable pitch greater than the wavelength, can be used to suppress side lobes, but the energy once contained in the side lobes is not transferred to the main lobe, but lost in noise instead.

In our work, a periodic 2D-OPA with a pitch larger than the wavelength and with a high array fill factor is studied. By maximizing the array fill factor, the side lobe levels can be reduced and the optical power in the main lobe can be increased, on a small, but sufficient angular steering range for point-to-point communications.

Such a high array fill factor can be achieved by using our compact antenna structure consisting of 2 separate diffraction stages: a wavelength-to-slab expansion grating and a free space radiation grating. The wavelength-to-slab expansion grating diffracts the input light at a right angle, allowing the free space radiation grating to be placed close to the waveguide and hence, allowing the maximization of the array fill factor of an OPA. The free space radiation grating

consists of SWG-equivalent grating ridges which lowered the index contrast and enabled diffraction on a longer distance. The angular far field divergence was thus lowered.

The antenna was fabricated using immersion lithography and OPC. Its measured far field FWHM divergence is $\theta_{FWHM} \approx 1.40°$ along both directions, in good agreement with simulations. The corresponding MFD is 48 µm, which yields a linear fill factor of 0.53 along both dimensions. The measured side lobe level in the OPA far field profile is around -5 dB, as expected from its determined array fill factor. However, the side lobe level still needs to be attenuated for practical implementation.

Our antenna suffers from large optical losses. The measured efficiency is around -7 dB, while the simulated efficiency is near - 4 dB. This 3 dB difference is induced by the waveguide-to-slab expansion grating, with measured additional 3 dB loss. The antenna power efficiency should be further be increased. For instance, the wavelength-to-slab expansion grating can be optimized to work in the single beam condition using SWGs-metamaterials. The directionality of the free space radiation grating needs to be further optimized.

In conclusion, our work shows that the proposed compact antenna can be used as a unitary emitter in an OPA. Two directions of improvement have been identified. First, the array fill factor still needs to be increased for further side lobe level reduction. Second, the power efficiency of the antenna should also be increased. The capability of the OPA to compensate phase front distortions induced by atmospheric turbulence should also be studied.

These results on the passive OPA antenna have been presented at the Optical Wireless Communications Conference in Eindhoven, Netherlands in December 2023 [268].

A scientific article presenting the work of this study is being written at the moment of writing the PhD manuscript.

6 CONCLUSION AND PERSPECTIVES OF THE PHD

Silicon photonics enables optical device integration at the chip-level, leveraging the maturity of the semi-conductor fabrication processes for high yield, large volume and low-cost production of complex optoelectronic circuits. SWG-metamaterials can be used to engineer silicon photonics devices by controlling key properties like light confinement and dispersion. These properties are tuned through the design of the grating geometrical parameters at the subwavelength scale. The SWG-metamaterials provide additional degrees of freedom when designing silicon photonics devices. At the usual telecom wavelength of λ = 1550 nm, SWGs have a period, Λ_{SWG} < 300 nm, and usually have feature sizes ~ 100 nm. Due to their small sizes, most SWG demonstrations relied on e-beam lithography. However, immersion lithography with OPC has recently emerged as a promising tool to pattern such small dimensions at an industrial scale.

The main goal of this PhD is to assess the feasibility of fabricating SWG-engineered silicon photonics devices on a large volume production line. Three representative SWG-based devices have been designed, fabricated using immersion lithography and OPC on the CEA-Leti pilot line, and have been characterized.

The first device is an ultrabroadband SWG-engineered 2x2 MMI 3-dB coupler. Broadband MMIs are one of the most successful demonstrations of SWGs for the engineering of passive devices. In this case, SWGs are used to tune modal dispersion to achieve a flat and broadband device response. Such device relies on a single full-etch step and periodic nanostructures with minimum feature size of 95 nm. We experimentally demonstrated excess losses < 1 dB, a power imbalance < 1 dB and phase errors < $\pm$ 5° on a 1330 – 1680 nm wavelength range, resulting in a bandwidth of 350 nm. These results are comparable with previous demonstrations using e-beam lithography [56]. These results illustrate the potential of immersion lithography for the realization of SWG devices requiring a single etch step. As shown in chapter 3, OPC plays a key role in achieving reasonably good agreement between the intended and realized

shapes. However, our 3D-FDTD simulations predicted that such performance should have been obtained on a larger wavelength range of 1250-1680 nm. For wavelengths λ < 1400 nm, resonance effects have been observed experimentally, limiting the bandwidth of the SWG-engineered MMI. The origins of these resonance effects are still unknown and should be investigated. Yet, the measured bandwidth of the SWG-engineered MMI was larger than the bandwidth that can be achieved using a conventional design without SWG-metamaterials, which is around 100 nm.

The second device is a high efficiency SWG-apodised L-shaped grating coupler. In this case, two etch steps are combined with longitudinal and transversal periodic structures to achieve destructive interference of the field radiated to the substrate and constructive interference of the field radiated to the air, key to maximizing fiber-chip coupling efficiency. In addition, SWGs are used to finely control the grating radiation strength to maximize the overlap between the light radiated upwards and the mode of an SMF-28 fiber. The experimental coupling efficiency between the TE polarized on-chip waveguide mode with an optical fiber mode of field diameter ~ 10.4 µm of a fiber placed at an angle of θ = 11.5° was $\eta_{CE,exp}(SWGs) \sim -1.70$ dB (68 %). This is the best experimental efficiency for an L-shaped grating fabricated without e-beam lithography. The simulated coupling efficiency is $\eta_{CE,sim}(SWGs) \sim -0.80$ dB (83 %) at a wavelength of λ = 1550 nm. 0.30 dB of this 0.90 dB difference between the simulated and measured values, comes from the Fresnel reflection losses at the air-encapsulation interface, which have not been considered in the simulations. The remaining 0.60 dB could come from fabrication imperfections, which have not been considered in our simulations, such as the rounded corners in the SWG-elements or the sidewall angles in the L-shaped profile after etching. The SWG-metamaterials were crucial in these L-shaped gratings as they have enhanced the coupling efficiency. Without SWGs, the measured coupling efficiency of the L-shaped grating coupler was $\eta_{CE,exp}(No\ SWGs) \sim -2.70$ dB (54 %) at a wavelength of λ = 1550 nm, which is 1.00 dB lower than the measured value with SWGs. By providing a gradual index contrast between the silicon waveguide and the L-shaped grating region, the SWG-metamaterials have reduced back-reflections. With SWGs, the

measured back-reflections at λ = 1550 nm were $\eta_{ref,exp}(SWGs) \sim 7$ %, which were smaller than the back-reflections measured without SWGs, $\eta_{ref,exp}(No\ SWGs) \sim 18$ %. Yet, the SWG-apodised L-shaped grating coupler shows a comparable efficiency to the SWG-apodised single-etch grating coupler from CEA-Leti [181], with an efficiency of ~ -1.35 dB at a wavelength of $\lambda \sim 1310$ nm. Our works have shown that although the SWGs-engineered L-shaped grating coupler could potentially exhibit a sub-decibel efficiency, its fabrication processes are still too complex, limiting its coupling efficiency to one which is comparable to a single-etched grating engineered with SWGs.

The third device is a new architecture for a SWG-engineered 2D-OPA antenna designed for free space optical communications. The antenna's architecture enabled a high array fill factor in both dimensions, which allowed for reducing the side lobe levels and for increasing the optical power in the main lobe. It consisted of a waveguide-to-slab expansion grating, with a closely placed free space radiation grating, for maximizing the array fill factor. The free space radiation grating was engineered using SWG-metamaterials which have helped in lowering the angular divergence of the antenna. The measured divergence of the optical antenna was $\Delta\theta_{FWHM} \sim 1.40°$ along both dimensions and agreed with the simulated values. However, the measured power efficiency of the antenna was – 8.30 dB, which was 3.50 dB less than its simulated value, η_{Ant} = – 4.80 dB. This difference was most probably caused by a more lossy waveguide-to-slab expansion grating, with a measured transmission being 3.68 dB lower than its simulated value. The side lobe level of the 2D-OPA was measured to be around -5 dB. This study has demonstrated a proof-of-concept of an antenna capable of maximizing the array fill factor in both dimensions of a uniform 2D-OPA for reduced side lobe levels. However, for practical free space optical communications, both its power efficiency and its array fill factor and should still be increased.

The three silicon photonic devices studied in this PhD showed high performance, illustrating the potential of immersion lithography for the large-volume fabrication of SWG-engineered devices. However, there is still a gap between simulated and measured results. For

example, the measured SWG-MMI bandwidth was 100 nm smaller than simulated, the measured coupling efficiency of the SWG-engineered L-shaped grating coupler was 0.90 dB less than simulated and the measured power efficiency of the SWG-engineered OPA antenna was 3.50 dB less than simulated. These differences might come from the lithographic and etching effects, such as rounded corners in the SWGs or side wall angles, which have not been considered in our simulations. Advanced SEM metrology techniques [269,270] could be implemented to accurately measure the fabricated dimensions and would enable the quantification of the fabrication effects on the performance of silicon photonics devices.

To enhance the performance of the designed SWG-engineered devices, the fabrication processes (lithography, OPC and etching for example) could be optimized to better match the fabricated shapes with the designed ones. However, there is a limit in these optimizations and some effects then become unavoidable. For example, it is almost impossible to obtain perfectly perpendicular corners, resulting in rounded corners to some extent [186]. Hence, it would be judicious to consider the lithographic effects during the simulation stage and to adapt the design to compensate such effects. As such, lithographic simulation tools [78] could become very insightful and useful tools.

7 APPENDIX

7.1 FRESNEL REFLECTIONS AT THE AIR INTERFACES DURING CHARACTERIZATION OF GRATING COUPLERS

The usual measurement configuration includes air between the fiber and the chip surface (SiO_2 encapsulation). Fresnel reflections occur at the fiber-air and air-chip surface interfaces (see Fig. 4.23(a)). These have not been considered in our simulations.

At one interface, the reflectance is $R = \left(\frac{n_{SiO2}\cos(\theta_{SiO2}) - n_{air}\cos(\theta_{air})}{n_{SiO2}\cos(\theta_{SiO2}) + n_{air}\cos(\theta_{air})}\right)^2 \approx 0.03$ with θ_{SiO2} = 8° and θ_{air} = 11.5°. The transmittance after the two interfaces is $T = (1-R)^2 \approx 0.94$. The Fresnel reflections at the two interfaces thus cause a loss of $-10\log(T) \sim 0.30$ dB.

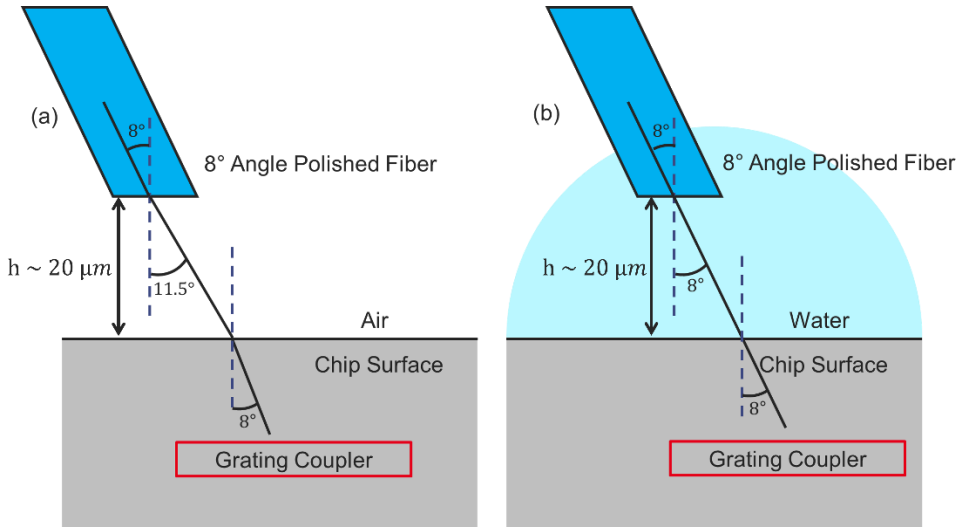

Fig. 7.1: (a) Usual characterization set up with air (b) water added to reduce Fresnel reflections at air-fiber and air-chip interfaces

To experimentally measure the losses caused by the Fresnel reflections at the air interfaces, the L-shaped grating with SWGs was characterized with water added in between fiber and chip surface (see Fig. 7.1(b)). Water acts as an index-matching liquid and mitigates to a certain extent, the Fresnel reflections. The results were compared to ones obtained in the usual configuration in which air is present instead of

water (see Fig. 7.2). A 0.25 dB gain in coupling efficiency was obtained using water, close to the theoretical gain of 0.30 dB.

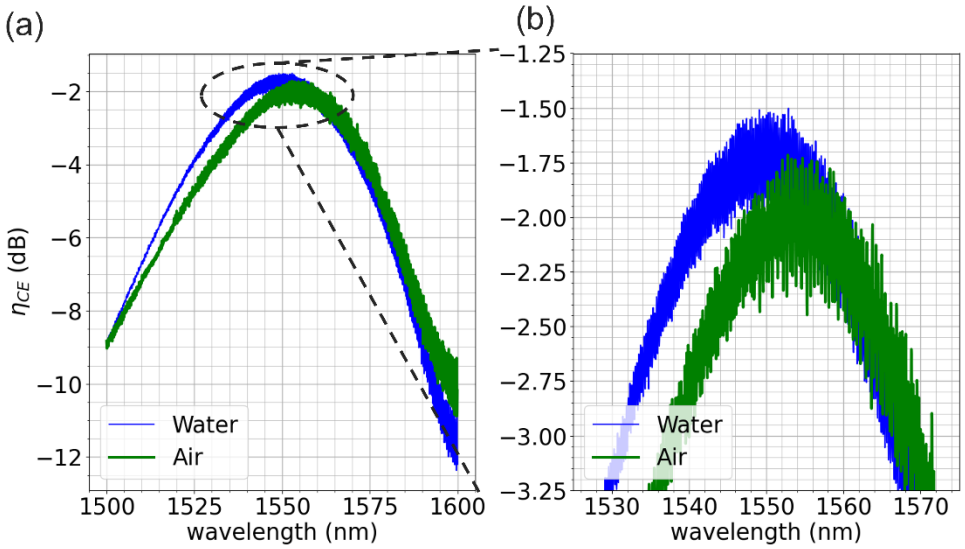

Fig. 7.2: (a) Coupling efficiency measurements with water or air in between the fiber and the chip surface. (b) Zoom on the graph.

7.2 DETERMINATION OF THE REFLECTION OF THE GRATING COUPLER FROM THE AMPLITUDE OF A FABRY-PEROT CAVITY

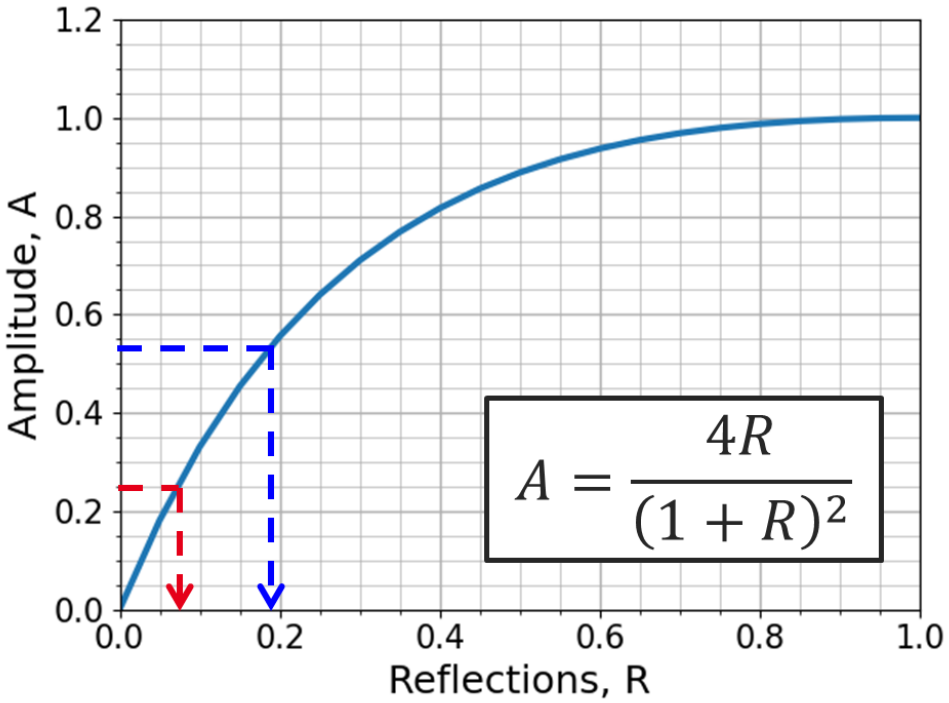

Fig. 7.3: Amplitude of the Fabry-Perot cavity, A, as a function of the grating coupler's reflection, R.

During the experimental characterization of the grating coupler's coupling efficiency, the input and output grating couplers act as partially reflecting mirrors, with reflection R, and created a Fabry-Perot cavity. The amplitude of the Fabry-Perot cavity made up of the two gratings, A, is well known and is given by $A = \frac{4R}{(1+R)^2}$, which is evaluated. in Fig. 7.3. The higher the reflection, R, the larger the amplitude, A. A and R are in linear units.

To obtain the value of R from the measured coupling efficiency of a single grating coupler, in dB, as the one shown in Fig. 4.23, the efficiency is multiplied by 2, to retrieve the transmission of two grating couplers. Then, the measured transmission is converted from dB to linear units and the normalized amplitude is calculated. The value of R is obtained from Fig. 7.3.

For example, let us consider the coupling efficiency curve for a grating couplers without SWGs shown Fig. 4.23(c). The maximum coupling efficiency for a single grating is η_{CE} = -2.70 dB and the minimum efficiency is η_{CE} = -4.30 dB. The transmission of 2 gratings is retrieved multiplying the coupling efficiency by two. Then, the maximum transmission for two gratings is $T_{max}(2\ GC)$ = -3.40 dB and the minimum transmission is $T_{min}(2\ GC)$ = -8.60 dB. In linear units, these correspond to $T_{max}(2\ GC)$ = 0.29 and $T_{min}(2\ GC)$ = 0.14. These values are normalized by dividing both values by $T_{max}(2\ GC)$, giving $T_{max,norm}(2\ GC)$ = 1 and $T_{min,norm}(2\ GC)$ = 0.14/0.29 = 0.48. The amplitude of the oscillations is A = $T_{max,norm}(2\ GC) - T_{min,norm}(2\ GC)$ = 1 - 0.48 = 0.52. From Fig. 7.3, this value of A = 0.52 corresponds to reflections, R = η_{ref} = 0.18, as indicated by the blue arrows.

The same steps are followed to find the reflections with SWGs. The normalized amplitude in linear units is A = 0.25, which corresponds to R = 0.07, as indicated by the red arrows in Fig. 7.3.

8 BIBLIOGRAPHY

1. Shekhar, S.; Bogaerts, W.; Chrostowski, L.; Bowers, J.E.; Hochberg, M.; Soref, R.; Shastri, B.J. Roadmapping the next Generation of Silicon Photonics. *Nat Commun* **2024**, *15*, 751, doi:10.1038/s41467-024-44750-0.
2. Siew, S.Y.; Li, B.; Gao, F.; Zheng, H.Y.; Zhang, W.; Guo, P.; Xie, S.W.; Song, A.; Dong, B.; Luo, L.W.; et al. Review of Silicon Photonics Technology and Platform Development. *J. Lightwave Technol.* **2021**, *39*, 4374–4389, doi:10.1109/JLT.2021.3066203.
3. Chen, X.; Milosevic, M.M.; Stankovic, S.; Reynolds, S.; Bucio, T.D.; Li, K.; Thomson, D.J.; Gardes, F.; Reed, G.T. The Emergence of Silicon Photonics as a Flexible Technology Platform. *Proc. IEEE* **2018**, *106*, 2101–2116, doi:10.1109/JPROC.2018.2854372.
4. Saseendran, S.S.; Kongnyuy, T.D.; Figeys, B.; Buja, F.; Troia, B.; Kerman, S.; Marinins, A.; Jansen, R.; Rottenberg, X.; Tezcan, D.S.; et al. A 300mm CMOS-Compatible PECVD Silicon Nitride Platform for Integrated Photonics with Low Loss and Low Process Induced Phase Variation. In Proceedings of the Optical Fiber Communication Conference (OFC) 2019; OSA: San Diego, California, 2019; p. M1C.4.
5. Soref, R. Mid-Infrared Photonics in Silicon and Germanium. *Nature Photon* **2010**, *4*, 495–497, doi:10.1038/nphoton.2010.171.
6. Vivien, L.; Osmond, J.; Fédéli, J.-M.; Marris-Morini, D.; Crozat, P.; Damlencourt, J.-F.; Cassan, E.; Lecunff, Y.; Laval, S. 42 GHz Pin Germanium Photodetector Integrated in a Silicon-on-Insulator Waveguide. *Opt. Express* **2009**, *17*, 6252, doi:10.1364/OE.17.006252.
7. Wang, Y.; Jiao, Y.; Williams, K. Scaling Photonic Integrated Circuits with InP Technology: A Perspective. *APL Photonics* **2024**, *9*, 050902, doi:10.1063/5.0200861.
8. Verrinder, P.; Wang, L.; Fridlander, J.; Sang, F.; Rosborough, V.; Nickerson, M.; Yang, G.; Stephen, M.; Coldren, L.; Klamkin, J. Gallium Arsenide Photonic Integrated Circuit Platform for Tunable Laser Applications. *IEEE J. Select. Topics Quantum Electron.* **2022**, *28*, 1–9, doi:10.1109/JSTQE.2021.3086074.

9. Wang, J.; Long, Y. On-Chip Silicon Photonic Signaling and Processing: A Review. *Science Bulletin* **2018**, *63*, 1267–1310, doi:10.1016/j.scib.2018.05.038.
10. Shawon, M.J.S.; Li, F. A Review of the Building Blocks of Silicon Photonics: From Fabrication Perspective. *semicond. sci. and inf. n.a.* **2019**, *1*, 29–35, doi:10.30564/ssid.v1i1.1282.
11. Wu, S.; Mu, X.; Cheng, L.; Mao, S.; Fu, H.Y. State-of-the-Art and Perspectives on Silicon Waveguide Crossings: A Review. *Micromachines* **2020**, *11*, 326, doi:10.3390/mi11030326.
12. Xu, Y.; Tian, Z.; Meng, X.; Chai, Z. Methods and Applications of On-Chip Beam Splitting: A Review. *Front. Phys.* **2022**, *10*, 985208, doi:10.3389/fphy.2022.985208.
13. Cheng, L.; Mao, S.; Li, Z.; Han, Y.; Fu, H. Grating Couplers on Silicon Photonics: Design Principles, Emerging Trends and Practical Issues. *Micromachines* **2020**, *11*, 666, doi:10.3390/mi11070666.
14. Bogaerts, W.; De Heyn, P.; Van Vaerenbergh, T.; De Vos, K.; Kumar Selvaraja, S.; Claes, T.; Dumon, P.; Bienstman, P.; Van Thourhout, D.; Baets, R. Silicon Microring Resonators. *Laser & Photonics Reviews* **2012**, *6*, 47–73, doi:10.1002/lpor.201100017.
15. Sun, H.; Qiao, Q.; Guan, Q.; Zhou, G. Silicon Photonic Phase Shifters and Their Applications: A Review. *Micromachines* **2022**, *13*, 1509, doi:10.3390/mi13091509.
16. Lipson, M. Guiding, Modulating, and Emitting Light on Silicon-Challenges and Opportunities. *J. Lightwave Technol.* **2005**, *23*, 4222–4238, doi:10.1109/JLT.2005.858225.
17. Liu, Y.; Wang, S.; Wang, J.; Li, X.; Yu, M.; Cai, Y. Silicon Photonic Transceivers in the Field of Optical Communication. *Nano Communication Networks* **2022**, *31*, 100379, doi:10.1016/j.nancom.2021.100379.
18. Soref, R.; Bennett, B. Electrooptical Effects in Silicon. *IEEE J. Quantum Electron.* **1987**, *23*, 123–129, doi:10.1109/JQE.1987.1073206.
19. Sun, X.; Zhang, L.; Zhang, Q.; Zhang, W. Si Photonics for Practical LiDAR Solutions. *Applied Sciences* **2019**, *9*, 4225, doi:10.3390/app9204225.
20. Shahbaz, M.; Butt, M.A.; Piramidowicz, R. Breakthrough in Silicon Photonics Technology in Telecommunications, Biosensing, and

Gas Sensing. *Micromachines* **2023**, *14*, 1637, doi:10.3390/mi14081637.
21. Silverstone, J.W.; Bonneau, D.; O'Brien, J.L.; Thompson, M.G. Silicon Quantum Photonics. *IEEE J. Select. Topics Quantum Electron.* **2016**, *22*, 390–402, doi:10.1109/JSTQE.2016.2573218.
22. Horikawa, T.; Shimura, D.; Okayama, H.; Jeong, S.-H.; Takahashi, H.; Ushida, J.; Sobu, Y.; Shiina, A.; Tokushima, M.; Kinoshita, K.; et al. A 300-Mm Silicon Photonics Platform for Large-Scale Device Integration. *IEEE J. Select. Topics Quantum Electron.* **2018**, *24*, 1–15, doi:10.1109/JSTQE.2018.2819893.
23. Giewont, K.; Hu, S.; Peng, B.; Rakowski, M.; Rauch, S.; Rosenberg, J.C.; Sahin, A.; Stobert, I.; Stricker, A.; Nummy, K.; et al. 300-Mm Monolithic Silicon Photonics Foundry Technology. *IEEE J. Select. Topics Quantum Electron.* **2019**, *25*, 1–11, doi:10.1109/JSTQE.2019.2908790.
24. Szelag, B.; Garcia, S.; Adelmini, L.; KazarMendes, M.; Guerber, S.; Congia, S.; Myko, A.; Grosse, P.; Virot, L.; Wilmart, Q. High Performance 300mm Silicon Photonics Platform for R&D and Product Prototyping. In Proceedings of the 2022 IEEE Photonics Conference (IPC); IEEE: Vancouver, BC, Canada, November 2022; pp. 1–2.
25. Ferraro, F.; De Heyn, P.; Kim, M.; Rajasekaran, N.; Berciano, M.; Muliuk, G.; Bode, D.; Lepage, G.; Janssen, S.; Magdziak, R.; et al. Imec Silicon Photonics Platforms: Performance Overview and Roadmap. In Proceedings of the Next-Generation Optical Communication: Components, Sub-Systems, and Systems XII; Li, G., Nakajima, K., Srivastava, A.K., Eds.; SPIE: San Francisco, United States, March 15 2023; p. 9.
26. Khan, M.U.; Xing, Y.; Ye, Y.; Bogaerts, W. Photonic Integrated Circuit Design in a Foundry+Fabless Ecosystem. *IEEE J. Select. Topics Quantum Electron.* **2019**, *25*, 1–14, doi:10.1109/JSTQE.2019.2918949.
27. Rahim, A.; Goyvaerts, J.; Szelag, B.; Fedeli, J.-M.; Absil, P.; Aalto, T.; Harjanne, M.; Littlejohns, C.; Reed, G.; Winzer, G.; et al. Open-Access Silicon Photonics Platforms in Europe. *IEEE J. Select. Topics Quantum Electron.* **2019**, *25*, 1–18, doi:10.1109/JSTQE.2019.2915949.

28. Cheben, P.; Schmid, J.H.; Halir, R.; Manuel Luque-González, J.; Gonzalo Wangüemert-Pérez, J.; Melati, D.; Alonso-Ramos, C. Recent Advances in Metamaterial Integrated Photonics. *Adv. Opt. Photon.* **2023**, *15*, 1033, doi:10.1364/AOP.495828.
29. Joannopoulos, J.D.; Johnson, S.G.; Winn, J.N.; Meade, R.D. *Photonic Crystals: Molding the Flow of Light*; 2nd edition.; Princeton University Press: Princeton Oxford, 2008; ISBN 978-0-691-12456-8.
30. Loncar, M.; Doll, T.; Vuckovic, J.; Scherer, A. Design and Fabrication of Silicon Photonic Crystal Optical Waveguides. *J. Lightwave Technol.* **2000**, *18*, 1402–1411, doi:10.1109/50.887192.
31. Wang, X.; Shi, W.; Yun, H.; Grist, S.; Jaeger, N.A.F.; Chrostowski, L. Narrow-Band Waveguide Bragg Gratings on SOI Wafers with CMOS-Compatible Fabrication Process. *Opt. Express* **2012**, *20*, 15547, doi:10.1364/OE.20.015547.
32. Halir, R.; Bock, P.J.; Cheben, P.; Ortega-Moñux, A.; Alonso-Ramos, C.; Schmid, J.H.; Lapointe, J.; Xu, D.; Wangüemert-Pérez, J.G.; Molina-Fernández, Í.; et al. Waveguide Sub-wavelength Structures: A Review of Principles and Applications. *Laser & Photonics Reviews* **2015**, *9*, 25–49, doi:10.1002/lpor.201400083.
33. Luque-González, J.M.; Sánchez-Postigo, A.; Hadij-ElHouati, A.; Ortega-Moñux, A.; Wangüemert-Pérez, J.G.; Schmid, J.H.; Cheben, P.; Molina-Fernández, Í.; Halir, R. A Review of Silicon Subwavelength Gratings: Building Break-through Devices with Anisotropic Metamaterials. *Nanophotonics* **2021**, *10*, 2765–2797, doi:10.1515/nanoph-2021-0110.
34. S.M.RYTOV Electromagnetic Properties of a Finely Stratified Medium.Pdf. *SOVIET PHYSICS JETP* **1956**, *2*.
35. Lalanne, P.; Lemercier-Lalanne, D. Depth Dependence of the Effective Properties of Subwavelength Gratings. *J. Opt. Soc. Am. A* **1997**, *14*, 450, doi:10.1364/JOSAA.14.000450.
36. Kazanskiy, N.L.; Butt, M.A.; Khonina, S.N. Silicon Photonic Devices Realized on Refractive Index Engineered Subwavelength Grating Waveguides-A Review. *Optics & Laser Technology* **2021**, *138*, 106863, doi:10.1016/j.optlastec.2020.106863.
37. Meng, Y.; Chen, Y.; Lu, L.; Ding, Y.; Cusano, A.; Fan, J.A.; Hu, Q.; Wang, K.; Xie, Z.; Liu, Z.; et al. Optical Meta-Waveguides for

Integrated Photonics and Beyond. *Light Sci Appl* **2021**, *10*, 235, doi:10.1038/s41377-021-00655-x.
38. Sun, L.; Zhang, Y.; He, Y.; Wang, H.; Su, Y. Subwavelength Structured Silicon Waveguides and Photonic Devices. *Nanophotonics* **2020**, *9*, 1321–1340, doi:10.1515/nanoph-2020-0070.
39. Halir, R.; Ortega-Monux, A.; Benedikovic, D.; Mashanovich, G.Z.; Wanguemert-Perez, J.G.; Schmid, J.H.; Molina-Fernandez, I.; Cheben, P. Subwavelength-Grating Metamaterial Structures for Silicon Photonic Devices. *Proc. IEEE* **2018**, *106*, 2144–2157, doi:10.1109/JPROC.2018.2851614.
40. Schmid, J.H.; Cheben, P.; Janz, S.; Lapointe, J.; Post, E.; Delâge, A.; Densmore, A.; Lamontagne, B.; Waldron, P.; Xu, D.-X. Subwavelength Grating Structures in Silicon-on-Insulator Waveguides. *Advances in Optical Technologies* **2008**, *2008*, 1–8, doi:10.1155/2008/685489.
41. Naraine, C.M.; Westwood-Bachman, J.N.; Horvath, C.; Aktary, M.; Knights, A.P.; Schmid, J.H.; Cheben, P.; Bradley, J.D.B. Subwavelength Grating Metamaterial Waveguides and Ring Resonators on a Silicon Nitride Platform. *Laser & Photonics Reviews* **2022**, 2200216, doi:10.1002/lpor.202200216.
42. Bock, P.J.; Cheben, P.; Schmid, J.H.; Lapointe, J.; Delâge, A.; Janz, S.; Aers, G.C.; Xu, D.-X.; Densmore, A.; Hall, T.J. Subwavelength Grating Periodic Structures in Silicon-on-Insulator: A New Type of Microphotonic Waveguide. *Opt. Express* **2010**, *18*, 20251, doi:10.1364/OE.18.020251.
43. Peng, B.; Xiong, C.; Khater, M.; Jensen, A.S.; Green, W.M.J.; Barwicz, T. Metamaterial Waveguides with Low Distributed Backscattering in Production O-Band Si Photonics. In Proceedings of the Optical Fiber Communication Conference; OSA: Los Angeles, California, 2017; p. Tu3K.3.
44. Jahani, S.; Jacob, Z. Breakthroughs in Photonics 2014: Relaxed Total Internal Reflection. *IEEE Photonics J.* **2015**, *7*, 1–5, doi:10.1109/JPHOT.2015.2418266.
45. Jahani, S.; Kim, S.; Atkinson, J.; Wirth, J.C.; Kalhor, F.; Noman, A.A.; Newman, W.D.; Shekhar, P.; Han, K.; Van, V.; et al. Controlling Evanescent Waves Using Silicon Photonic All-Dielectric

Metamaterials for Dense Integration. *Nat Commun* **2018**, *9*, 1893, doi:10.1038/s41467-018-04276-8.
46. Benedikovic, D.; Berciano, M.; Alonso-Ramos, C.; Le Roux, X.; Cassan, E.; Marris-Morini, D.; Vivien, L. Dispersion Control of Silicon Nanophotonic Waveguides Using Sub-Wavelength Grating Metamaterials in near- and Mid-IR Wavelengths. *Opt. Express* **2017**, *25*, 19468, doi:10.1364/OE.25.019468.
47. Jafari, Z.; Zarifkar, A. Dispersion Flattened Single Etch-Step Waveguide Based on Subwavelength Grating. *Optics Communications* **2017**, *393*, 219–223, doi:10.1016/j.optcom.2017.02.056.
48. Yu, Z.; Xu, H.; Liu, D.; Li, H.; Shi, Y.; Dai, D. Subwavelength-Structure-Assisted Ultracompact Polarization-Handling Components on Silicon. *J. Lightwave Technol.* **2022**, *40*, 1784–1801, doi:10.1109/JLT.2021.3134469.
49. Ibrahim, M.; Schmid, J.H.; Aleali, A.; Cheben, P.; Lapointe, J.; Janz, S.; Bock, P.J.; Densmore, A.; Lamontagne, B.; Ma, R.; et al. Athermal Silicon Waveguides with Bridged Subwavelength Gratings for TE and TM Polarizations. *Opt. Express* **2012**, *20*, 18356, doi:10.1364/OE.20.018356.
50. Zhang, J.; Xu, L.; Mao, D.; D'Mello, Y.; Wei, Z.; Li, W.; Plant, D.V. Temperature-Insensitive and Low-Loss Single-Mode Silicon Waveguide Crossing Covering All Optical Communication Bands Enabled by Curved Anisotropic Metamaterial. *Nanophotonics* **2023**, *12*, 4095–4107, doi:10.1515/nanoph-2023-0524.
51. Schmid, J.H.; Cheben, P.; Janz, S.; Lapointe, J.; Post, E.; Xu, D.-X. Gradient-Index Antireflective Subwavelength Structures for Planar Waveguide Facets. *Opt. Lett.* **2007**, *32*, 1794, doi:10.1364/OL.32.001794.
52. Cheben, P.; Bock, P.J.; Schmid, J.H.; Lapointe, J.; Janz, S.; Xu, D.-X.; Densmore, A.; Delâge, A.; Lamontagne, B.; Hall, T.J. Refractive Index Engineering with Subwavelength Gratings for Efficient Microphotonic Couplers and Planar Waveguide Multiplexers. *Opt. Lett.* **2010**, *35*, 2526, doi:10.1364/OL.35.002526.
53. Cheben, P.; Schmid, J.H.; Wang, S.; Xu, D.-X.; Vachon, M.; Janz, S.; Lapointe, J.; Painchaud, Y.; Picard, M.-J. Broadband Polarization Independent Nanophotonic Coupler for Silicon Waveguides with

Ultra-High Efficiency. *Opt. Express* **2015**, *23*, 22553, doi:10.1364/OE.23.022553.
54. Barwicz, T.; Peng, B.; Leidy, R.; Janta-Polczynski, A.; Houghton, T.; Khater, M.; Kamlapurkar, S.; Engelmann, S.; Fortier, P.; Boyer, N.; et al. Integrated Metamaterial Interfaces for Self-Aligned Fiber-to-Chip Coupling in Volume Manufacturing. *IEEE J. Select. Topics Quantum Electron.* **2019**, *25*, 1–13, doi:10.1109/JSTQE.2018.2879018.
55. Benedikovic, D.; Cheben, P.; Schmid, J.H.; Xu, D.; Lapointe, J.; Wang, S.; Halir, R.; Ortega-Moñux, A.; Janz, S.; Dado, M. High-efficiency Single Etch Step Apodized Surface Grating Coupler Using Subwavelength Structure. *Laser & Photonics Reviews* **2014**, *8*, doi:10.1002/lpor.201400113.
56. Halir, R.; Cheben, P.; Luque-González, J.M.; Sarmiento-Merenguel, J.D.; Schmid, J.H.; Wangüemert-Pérez, G.; Xu, D.; Wang, S.; Ortega-Moñux, A.; Molina-Fernández, Í. Ultra-broadband Nanophotonic Beamsplitter Using an Anisotropic Sub-wavelength Metamaterial. *Laser & Photonics Reviews* **2016**, *10*, 1039–1046, doi:10.1002/lpor.201600213.
57. Vilas, J.; Fernández De Cabo, R.; Olivares, I.; González-Andrade, D.; Velasco, A.V.; Dias-Ponte, A. Low-Loss Directional Coupler for the C, L and U Bands Based on Subwavelength Gratings. *IEEE Photon. Technol. Lett.* **2023**, *35*, 1331–1334, doi:10.1109/LPT.2023.3325660.
58. Halir, R.; Maese-Novo, A.; Ortega-Moñux, A.; Molina-Fernández, I.; Wangüemert-Pérez, J.G.; Cheben, P.; Xu, D.-X.; Schmid, J.H.; Janz, S. Colorless Directional Coupler with Dispersion Engineered Sub-Wavelength Structure. *Opt. Express* **2012**, *20*, 13470, doi:10.1364/OE.20.013470.
59. Wang, Z.; Xu, X.; Fan, D.; Wang, Y.; Chen, R.T. High Quality Factor Subwavelength Grating Waveguide Micro-Ring Resonator Based on Trapezoidal Silicon Pillars. *Opt. Lett.* **2016**, *41*, 3375, doi:10.1364/OL.41.003375.
60. Sharma, E.; Rathi, R.; Misharwal, J.; Sinhmar, B.; Kumari, S.; Dalal, J.; Kumar, A. Evolution in Lithography Techniques: Microlithography to Nanolithography. *Nanomaterials* **2022**, *12*, 2754, doi:10.3390/nano12162754.

61. Lin, B.J. The Ending of Optical Lithography and the Prospects of Its Successors. *Microelectronic Engineering* **2006**, *83*, 604–613, doi:10.1016/j.mee.2005.12.017.
62. Daimon, M.; Masumura, A. Measurement of the Refractive Index of Distilled Water from the Near-Infrared Region to the Ultraviolet Region. *Appl. Opt.* **2007**, *46*, 3811, doi:10.1364/AO.46.003811.
63. Horikawa, T.; Mogami, T. Ultra-Fme Si Photonics Fabrication Technology Based on 40-Nm-Node CMOS Process. In Proceedings of the 2015 IEEE 12th International Conference on Group IV Photonics (GFP); IEEE: Vancouver, BC, Canada, August 2015; pp. 157–158.
64. Sanders, D.P. Advances in Patterning Materials for 193 Nm Immersion Lithography. *Chem. Rev.* **2010**, *110*, 321–360, doi:10.1021/cr900244n.
65. Owa, S.; Nagasaka, H. Immersion Lithography; Its Potential Performance and Issues.; Yen, A., Ed.; Santa Clara, CA, June 25 2003; p. 724.
66. Fahrenkopf, N.M.; McDonough, C.; Leake, G.L.; Su, Z.; Timurdogan, E.; Coolbaugh, D.D. The AIM Photonics MPW: A Highly Accessible Cutting Edge Technology for Rapid Prototyping of Photonic Integrated Circuits. *IEEE J. Select. Topics Quantum Electron.* **2019**, *25*, 1–6, doi:10.1109/JSTQE.2019.2935698.
67. Selvaraja, S.K.; Jaenen, P.; Bogaerts, W.; Van Thourhout, D.; Dumon, P.; Baets, R. Fabrication of Photonic Wire and Crystal Circuits in Silicon-on-Insulator Using 193-Nm Optical Lithography. *J. Lightwave Technol.* **2009**, *27*, 4076–4083, doi:10.1109/JLT.2009.2022282.
68. Meyerhofer, D.; Lin, B.J. Resolution And Proximity Effect In Optical Lithography.; Santa Clara, CA, United States, January 1 1988; pp. 174–187.
69. Takahashi, H.; Toyama, M.; Seki, M.; Shimura, D.; Koshino, K.; Yokoyama, N.; Ohtsuka, M.; Sugiyama, A.; Ishitsuka, E.; Sano, T.; et al. The Impacts of ArF Excimer Immersion Lithography on Integrated Silicon Photonics Technology.
70. Pond, J.; Wang, X.; Flueckiger, J.; Reid, A.; Niegemann, J.; Liu, A.; Chrostowski, L. Design and Optimization of Photolithography Friendly Photonic Components.; He, S., Lee, E.-H., Eldada, L.A., Eds.; San Francisco, California, United States, March 3 2016; p. 97510V.

71. Horikawa, T.; Shimura, D.; Jeong, S.-H.; Tokushima, M.; Kinoshita, K.; Mogami, T. The Impacts of Fabrication Error in Si Wire-Waveguides on Spectral Variation of Coupled Resonator Optical Waveguides. *Microelectronic Engineering* **2016**, *156*, 46–49, doi:10.1016/j.mee.2015.11.015.
72. Ortega-Moñux, A.; Čtyroký, J.; Cheben, P.; Schmid, J.H.; Wang, S.; Molina-Fernández, Í.; Halir, R. Disorder Effects in Subwavelength Grating Metamaterial Waveguides. *Opt. Express* **2017**, *25*, 12222, doi:10.1364/OE.25.012222.
73. Azpiroz, J.T.; Rosenbluth, A.E.; Lai, K.; Fonseca, C.; Yang, D. Critical Impact of Mask Electromagnetic Effects on Optical Proximity Corrections Performance for 45nm and Beyond. *Journal of Vacuum Science & Technology B: Microelectronics and Nanometer Structures Processing, Measurement, and Phenomena* **2007**, *25*, 164–168, doi:10.1116/1.2429667.
74. Boutami, S.; Hassan, K.; Dupré, C.; Baud, L.; Fan, S. Experimental Demonstration of Silicon Photonic Devices Optimized by a Flexible and Deterministic Pixel-by-Pixel Technique. *Applied Physics Letters* **2020**, *117*, 071104, doi:10.1063/5.0013558.
75. Chou, D.; McAllister, K. Line End Optimization through Optical Proximity Correction (OPC): A Case Study.; Flagello, D.G., Ed.; San Jose, CA, March 10 2006; p. 61543A.
76. Orlando, B.; Farys, V.; Schneider, L.; Cremer, S.; Postnikov, S.V.; Millequant, M.; Dirrenberger, M.; Tiphine, C.; Bayle, S.; Tranquillin, C.; et al. OPC for Curved Designs in Application to Photonics on Silicon.; Erdmann, A., Kye, J., Eds.; San Jose, California, United States, March 15 2016; p. 97801U.
77. Celo, D.; Dumais, P.; Liu, W.; Zhang, C.; Goodwill, D.J.; Jiang, J.; Bernier, E. Optical Proximity Correction in Geometry Sensitive Silicon Photonics Waveguide Crossings. In Proceedings of the 2017 IEEE 14th International Conference on Group IV Photonics (GFP); IEEE: Berlin, Germany, August 2017; pp. 45–46.
78. Meagher, C.; Sowinski, Z.; Yu, C.; Hu, S.; Nummy, K.; Ghosal, M.M.; Viswanathan, R.; Abdo, A.; Wiltshire, T. Patterning Challenges for Monolithic Silicon Photonics: AP/DFM: Advanced Patterning / Design for Manufacturability. In Proceedings of the 2018 29th Annual SEMI Advanced Semiconductor Manufacturing

Conference (ASMC); IEEE: Saratoga Springs, NY, USA, April 2018; pp. 155–158.
79. Boeuf, F.; Vulliet, N.; Baudot, C.; Messaoudene, S.; Baylac, E.; Cremer, S. Challenges in Silicon Photonics Process Technology. In Proceedings of the 2017 European Conference on Optical Communication (ECOC); IEEE: Gothenburg, September 2017; pp. 1–3.
80. Alloatti, L.; Wade, M.; Stojanovic, V.; Popovic, M.; Ram, R.J. Photonics Design Tool for Advanced CMOS Nodes. *IET Optoelectronics* **2015**, *9*, 163–167, doi:10.1049/iet-opt.2015.0003.
81. Huang, Z.; Zheng, Z.; Chen, S.; Feng, J.; Huang, W.; Cao, G. Preliminary Round of OPC Development in 180nm Node Silicon Photonics MPW Platform. In Proceedings of the 2020 International Workshop on Advanced Patterning Solutions (IWAPS); IEEE: Chengdu, China, November 5 2020; pp. 1–3.
82. Ong, E.W.; Wallner, T.; Fahrenkopf, N.M.; Coolbaugh, D.D. High Positional Freedom SOI Subwavelength Grating Coupler (SWG) for 300 Mm Foundry Fabrication. *Opt. Express* **2018**, *26*, 28773, doi:10.1364/OE.26.028773.
83. Vakarin, V.; Melati, D.; Dinh, T.T.D.; Le Roux, X.; Kan, W.K.K.; Dupré, C.; Szelag, B.; Monfray, S.; Boeuf, F.; Cheben, P.; et al. Metamaterial-Engineered Silicon Beam Splitter Fabricated with Deep UV Immersion Lithography. *Nanomaterials* **2021**, *11*, 2949, doi:10.3390/nano11112949.
84. Ashida, K.; Okano, M.; Yasuda, T.; Ohtsuka, M.; Seki, M.; Yokoyama, N.; Koshino, K.; Yamada, K.; Takahashi, Y. Photonic Crystal Nanocavities With an Average Q Factor of 1.9 Million Fabricated on a 300-Mm-Wide SOI Wafer Using a CMOS-Compatible Process. *JOURNAL OF LIGHTWAVE TECHNOLOGY* **2018**, *36*, 9.
85. Yoshida, T.; Atsumi, Y.; Omoda, E.; Sakakibara, Y. Polarization-Insensitive Vertically Curved Si Surface Optical Coupler Bent by Ion Implantation. *IEEE Photon. Technol. Lett.* **2020**, *32*, 1319–1322, doi:10.1109/LPT.2020.3022354.
86. Xie, W.; Verheyen, P.; Pantouvaki, M.; Van Campenhout, J.; Van Thourhout, D. Efficient Resonance Management in Ultrahigh- *Q* 1D Photonic Crystal Nanocavities Fabricated on 300 Mm SOI CMOS Platform. *Laser & Photonics Reviews* **2021**, *15*, 2000317, doi:10.1002/lpor.202000317.

87. Allen, J.A.; Arnold, K.P.; Halimi, S.I.; Ryder, L.D.; Afzal, F.O.; Bian, Y.; Aboketaf, A.; Dezfulian, K.; Rakowski, M.; Augur, R.; et al. Deep Subwavelength Anti-Slot Photonic Crystals Fabricated in Monolithic Silicon Photonics Technology. *IEEE Photon. Technol. Lett.* **2023**, *35*, 461–464, doi:10.1109/LPT.2023.3255821.
88. Van Vaerenbergh, T.; Sun, P.; Hooten, S.; Jain, M.; Wilmart, Q.; Seyedi, A.; Huang, Z.; Fiorentino, M.; Beausoleil, R. Wafer-Level Testing of Inverse-Designed and Adjoint-Inspired Vertical Grating Coupler Designs Compatible with DUV Lithography. *Opt. Express* **2021**, *29*, 37021, doi:10.1364/OE.433744.
89. Van Vaerenbergh, T.; Hooten, S.; Jain, M.; Sun, P.; Wilmart, Q.; Seyedi, A.; Huang, Z.; Fiorentino, M.; Beausoleil, R. Wafer-Level Testing of Inverse-Designed and Adjoint-Inspired Dual Layer Si-SiN Vertical Grating Couplers. *J. Phys. Photonics* **2022**, *4*, 044001, doi:10.1088/2515-7647/ac943c.
90. Okayama, H.; Shimura, D.; Takahashi, H.; Seki, M.; Toyama, M.; Sano, T.; Koshino, K.; Yokoyama, N.; Ohtsuka, M.; Sugiyama, A.; et al. Si Wire Array Waveguide Grating with Parallel Star Coupler Configuration Fabricated by ArF Excimer Immersion Lithography. *Electron. lett.* **2013**, *49*, 410–412, doi:10.1049/el.2013.0206.
91. Purnawirman; Sun, J.; Adam, T.N.; Leake, G.; Coolbaugh, D.; Bradley, J.D.B.; Hosseini, E.S.; Watts, M.R. C- and L-Band Erbium-Doped Waveguide Lasers with Wafer-Scale Silicon Nitride Cavities. *Opt. Lett.* **2013**, *38*, 1760, doi:10.1364/OL.38.001760.
92. Hu, T.; Tseng, C.-K.; Fu, Y.H.; Xu, Z.; Dong, Y.; Wang, S.; Lai, K.H.; Bliznetsov, V.; Zhu, S.; Lin, Q.; et al. Demonstration of Color Display Metasurfaces via Immersion Lithography on a 12-Inch Silicon Wafer. *Opt. Express* **2018**, *26*, 19548, doi:10.1364/OE.26.019548.
93. Song, J.H.; Kongnyuy, T.D.; Troia, B.; Saseendran, S.S.; Soussan, P.; Jansen, R.; Rottenberg, X. Grating Devices on a Silicon Nitride Technology Platform for Visible Light Applications. *OSA Continuum* **2019**, *2*, 1155, doi:10.1364/OSAC.2.001155.
94. Kim, T.; Ngai, T.; Timalsina, Y.; Watts, M.R.; Stojanovic, V.; Bhargava, P.; Poulton, C.V.; Notaros, J.; Yaacobi, A.; Timurdogan, E.; et al. A Single-Chip Optical Phased Array in a Wafer-Scale Silicon Photonics/CMOS 3D-Integration Platform. *IEEE J. Solid-State Circuits* **2019**, *54*, 3061–3074, doi:10.1109/JSSC.2019.2934601.

95. Levi, S.; Tiec, R.L.; Dupre, C.; Vannuffel, C.; Dewolf, T.; Garcia, S.; Millard, K.; Meynard, B.; Lee, Y.; Colard, M.; et al. Characterization of Light Propagation Loss in Photonics Devices Using High-Resolution CDSEM Metrology. In Proceedings of the 2022 International Symposium on Semiconductor Manufacturing (ISSM); IEEE: Tokyo, Japan, December 12 2022; pp. 1–4.
96. Selvaraja, S.K.; De Heyn, P.; Winroth, G.; Ong, P.; Lepage, G.; Cailler, C.; Rigny, A.; Bourdelle, K.K.; Bogaerts, W.; Van Thourhout, D.; et al. Highly Uniform and Low-Loss Passive Silicon Photonics Devices Using a 300mm CMOS Platform. In Proceedings of the Optical Fiber Communication Conference; OSA: San Francisco, California, 2014; p. Th2A.33.
97. Jeong, S.-H.; Shimura, D.; Simoyama, T.; Seki, M.; Yokoyama, N.; Ohtsuka, M.; Koshino, K.; Horikawa, T.; Tanaka, Y.; Morito, K. Low-Loss, Flat-Topped and Spectrally Uniform Silicon-Nanowire-Based 5th-Order CROW Fabricated by ArF-Immersion Lithography Process on a 300-Mm SOI Wafer. *Opt. Express* **2013**, *21*, 30163, doi:10.1364/OE.21.030163.
98. Soldano, L.B.; Pennings, E.C.M. Optical Multi-Mode Interference Devices Based on Self-Imaging: Principles and Applications. *J. Lightwave Technol.* **1995**, *13*, 615–627, doi:10.1109/50.372474.
99. Maese-Novo, A.; Halir, R.; Romero-García, S.; Pérez-Galacho, D.; Zavargo-Peche, L.; Ortega-Moñux, A.; Molina-Fernández, I.; Wangüemert-Pérez, J.G.; Cheben, P. Wavelength Independent Multimode Interference Coupler. *Opt. Express* **2013**, *21*, 7033, doi:10.1364/OE.21.007033.
100. Pérez-Galacho, D.; Halir, R.; Francisco, L.; Wangüemert-Pérez, J.G.; Ortega-Moñux, A.; Molina-Fernández, Í.; Cheben, P. Adiabatic Transitions for Sub-Wavelength Grating Waveguides.
101. Halir, R.; Molina-Fernandez, I.; Ortega-Monux, A.; Wanguemert-Perez, J.G.; Xu, D.-X.; Cheben, P.; Janz, S. A Design Procedure for High-Performance, Rib-Waveguide-Based Multimode Interference Couplers in Silicon-on-Insulator. *J. Lightwave Technol.* **2008**, *26*, 2928–2936, doi:10.1109/JLT.2007.914511.
102. González-Andrade, D.; Dias, A.; Wangüemert-Pérez, J.G.; Ortega-Moñux, A.; Molina-Fernández, Í.; Halir, R.; Cheben, P.; V. Velasco, A. Experimental Demonstration of a Broadband Mode Converter and Multiplexer Based on Subwavelength Grating

Waveguides. *Optics & Laser Technology* **2020**, *129*, 106297, doi:10.1016/j.optlastec.2020.106297.
103. Hussain, Z.L.; Fyath, R.S. Design and Simulation of a Compact Three-Mode (de)Multiplexer Based on a Subwavelength Grating Multimode Interference Coupler. *Photonics and Nanostructures - Fundamentals and Applications* **2021**, *47*, 100966, doi:10.1016/j.photonics.2021.100966.
104. Xu, L.; Wang, Y.; Patel, D.; Morsy-Osman, M.; Li, R.; Parvizi, M.; Ben-Hamida, N.; Plant, D.V. Ultra-Broadband and Ultra-Compact Optical 90o Hybrid Based on 2x4 MMI Coupler with Subwavelength Gratings on Silicon-on-Insulator. **2018**.
105. Stirling, C.J.; Halir, R.; Sánchez-Postigo, A.; Qu, Z.; Penadés, J.S.; Murugan, G.S.; Wangüemert-Pérez, J.G.; Molina-Fernández, Í.; Nedeljkovic, M. A Broadband 2×2 Multimode Interference Coupler for Mid-Infrared Wavelengths. *Optics Letters* **2021**.
106. El-Fiky, E.; D'Mello, Y.; Wang, Y.; Skoric, J.; Saber, M.G.; Kumar, A.; Samani, A.; Xu, L.; Li, R.; Patel, D.; et al. Ultra-Broadband and Compact Asymmetrical Beam Splitter Enabled by Angled Sub-Wavelength Grating MMI. In Proceedings of the Conference on Lasers and Electro-Optics; OSA: San Jose, California, 2018; p. STh4A.7.
107. Ortega-Monux, A.; Zavargo-Peche, L.; Maese-Novo, A.; Molina-Fernandez, I.; Halir, R.; Wanguemert-Perez, J.G.; Cheben, P.; Schmid, J.H. High-Performance Multimode Interference Coupler in Silicon Waveguides With Subwavelength Structures. *IEEE Photon. Technol. Lett.* **2011**, *23*, 1406–1408, doi:10.1109/LPT.2011.2161866.
108. Föhn, T.; Vogel, W.; Schmidt, M.; Berroth, M.; Butschke, J.; Letzkus, F. Optimized 90° Hybrids with Sidewall Grating in Silicon on Insulator. In Proceedings of the Optical Fiber Communication Conference; OSA: San Francisco, California, 2014; p. Th3F.4.
109. Shi, Y.; Shao, B.; Zhang, Z.; Zhou, T.; Luo, F.; Xu, Y. Ultra-Broadband and Low-Loss Silicon-Based Power Splitter Based on Subwavelength Grating-Assisted Multimode Interference Structure. *Photonics* **2022**, *9*, 435, doi:10.3390/photonics9070435.
110. Hadij-ElHouati, A.; Halir, R.; Ortega-Monux, A.; Wanguemert-Perez, J.G.; Podmore, H.; Schmid, J.H.; Cheben, P.; Molina-Fernandez, I. Metamaterial Engineered C+L Band 90° Hybrid with

150 Nm Feature Size. In Proceedings of the 2020 IEEE Photonics Conference (IPC); IEEE: Vancouver, BC, Canada, September 2020; pp. 1–2.
111. Han, S.; Liu, W.; Shi, Y. Ultra-Broadband Dual-Polarization Power Splitter Based on Silicon Subwavelength Gratings. *IEEE Photon. Technol. Lett.* **2021**, *33*, 765–768, doi:10.1109/LPT.2021.3095257.
112. Herrero-Bermello, A.; Luque-Gonzalez, J.M.; Velasco, A.V.; Ortega-Monux, A.; Cheben, P.; Halir, R. Design of a Broadband Polarization Splitter Based on Anisotropy-Engineered Tilted Subwavelength Gratings. *IEEE Photonics J.* **2019**, *11*, 1–8, doi:10.1109/JPHOT.2019.2912335.
113. Pérez-Armenta, C.; Ortega-Moñux, A.; Luque-González, J.M.; Halir, R.; Reyes-Iglesias, P.; Schmid, J.H.; Cheben, P.; Molina-Fernández, íñigo; Wangüemert Pérez, J.G. Polarization Independent 2×2 Multimode Interference Coupler with Bricked Subwavelength Metamaterial. *EPJ Web Conf.* **2022**, *266*, 01009, doi:10.1051/epjconf/202226601009.
114. Xu, L.; Wang, Y.; Kumar, A.; Patel, D.; El-Fiky, E.; Xing, Z.; Li, R.; Plant, D.V. Polarization Beam Splitter Based on MMI Coupler With SWG Birefringence Engineering on SOI. *IEEE Photon. Technol. Lett.* **2018**, *30*, 403–406, doi:10.1109/LPT.2018.2794466.
115. Xu, H.; Dai, D.; Shi, Y. Ultra-Broadband and Ultra-Compact On-Chip Silicon Polarization Beam Splitter by Using Hetero-Anisotropic Metamaterials. *Laser & Photonics Reviews* **2019**, *13*, 1800349, doi:10.1002/lpor.201800349.
116. Xu, L.; Wang, Y.; El-Fiky, E.; Mao, D.; Kumar, A.; Xing, Z.; Saber, M.G.; Jacques, M.; Plant, D.V. Compact Broadband Polarization Beam Splitter Based on Multimode Interference Coupler With Internal Photonic Crystal for the SOI Platform. *J. Lightwave Technol.* **2019**, *37*, 1231–1240, doi:10.1109/JLT.2018.2890718.
117. Pérez-Armenta, C.; Ortega-Moñux, A.; Manuel Luque-González, J.; Halir, R.; Schmid, J.; Cheben, P.; Molina-Fernández, I.; Gonzalo Wangüemert-Pérez, J. Polarization Insensitive Metamaterial Engineered Multimode Interference Coupler in a 220 Nm Silicon-on-Insulator Platform. *Optics & Laser Technology* **2023**, *164*, 109493, doi:10.1016/j.optlastec.2023.109493.

118. Zhong, W.; Xiao, J. Ultracompact Polarization-Insensitive Power Splitter Using Subwavelength-Grating-Based MMI Couplers on an SOI Platform. *Appl. Opt.* **2020**, *59*, 1991, doi:10.1364/AO.382097.
119. Shiran, H.; Zhang, G.; Liboiron-Ladouceur, O. Dual-Mode Broadband Compact 2 × 2 Optical Power Splitter Using Sub-Wavelength Metamaterial Structures. *Opt. Express* **2021**, *29*, 23864, doi:10.1364/OE.423882.
120. Lu, M.; Deng, C.; Sun, Y.; Wang, D.; Liu, P.; Lin, D.; Cheng, W.; Shi, S.; Lin, T.; Hu, G.; et al. Broadband Dual-Mode 3 dB Power Splitter Using Bricked Subwavelength Gratings. *J. Opt. Soc. Am. B* **2023**, *40*, 502, doi:10.1364/JOSAB.482899.
121. Guo, Z.; Xiao, J. Ultracompact Mode-Order Converting Power Splitter for Mid-Infrared Wavelengths Using an MMI Coupler Embedded with Oblique Subwavelength Grating Wires. *Optics Communications* **2021**, *488*, 126850, doi:10.1016/j.optcom.2021.126850.
122. Tran, M.A.; Komljenovic, T.; Hulme, J.C.; Davenport, M.L.; Bowers, J.E. A Robust Method for Characterization of Optical Waveguides and Couplers. *IEEE Photon. Technol. Lett.* **2016**, *28*, 1517–1520, doi:10.1109/LPT.2016.2556713.
123. Wang, Y.; Lu, Z.; Ma, M.; Yun, H.; Zhang, F.; Jaeger, N.A.F.; Chrostowski, L. Compact Broadband Directional Couplers Using Subwavelength Gratings. *IEEE Photonics J.* **2016**, *8*, 1–8, doi:10.1109/JPHOT.2016.2574335.
124. Voigt, K. Interferometric Devices Based on 4µm SOI Material for Application in Optical Telecommunications, Elektrotechnik und Informatik der Technischen Universität Berlin, 2012.
125. González-Andrade, D. Subwavelength Metamaterials for High-Performance Photonic Microdevices, UNIVERSIDAD COMPLUTENSE DE MADRID, 2020.
126. Kan, W.K.K.; Toxqui-Rodriguez, S.; Medina-Quiroz, D.; Nuño-Ruano, P.; Melati, D.; Cassan, E.; Marris-Morini, D.; Vivien, L.; Cheben, P.; Adelmini, L.; et al. 2x2 Ultra-Broadband Multimode Interference Coupler with Subwavelength Gratings Fabricated by Immersion Lithography. In Proceedings of the 2023 Photonics North (PN); IEEE: Montreal, QC, Canada, June 12 2023; pp. 1–1.
127. Benedikovic, D.; Alonso-Ramos, C.; Guerber, S.; Le Roux, X.; Cheben, P.; Dupré, C.; Szelag, B.; Fowler, D.; Cassan, É.; Marris-

Morini, D.; et al. Sub-Decibel Silicon Grating Couplers Based on L-Shaped Waveguides and Engineered Subwavelength Metamaterials. *Opt. Express* **2019**, *27*, 26239, doi:10.1364/OE.27.026239.
128. Marchetti, R.; Lacava, C.; Carroll, L.; Gradkowski, K.; Minzioni, P. Coupling Strategies for Silicon Photonics Integrated Chips [Invited]. *Photon. Res.* **2019**, *7*, 201, doi:10.1364/PRJ.7.000201.
129. Nambiar, S.; Sethi, P.; Selvaraja, S. Grating-Assisted Fiber to Chip Coupling for SOI Photonic Circuits. *Applied Sciences* **2018**, *8*, 1142, doi:10.3390/app8071142.
130. Mu, X.; Wu, S.; Cheng, L.; Fu, H.Y. Edge Couplers in Silicon Photonic Integrated Circuits: A Review. *Applied Sciences* **2020**, *10*, 1538, doi:10.3390/app10041538.
131. Bozzola, A.; Carroll, L.; Gerace, D.; Cristiani, I.; Andreani, L.C. Optimising Apodized Grating Couplers in a Pure SOI Platform to −05 dB Coupling Efficiency. *Opt. Express* **2015**, *23*, 16289, doi:10.1364/OE.23.016289.
132. Schmid, J.H.; Cheben, P.; Janz, S.; Lapointe, J.; Post, E.; Xu, D.-X. Gradient-Index Antireflective Subwavelength Structures for Planar Waveguide Facets. *Opt. Lett.* **2007**, *32*, 1794, doi:10.1364/OL.32.001794.
133. Barwicz, T.; Peng, B.; Leidy, R.; Janta-Polczynski, A.; Houghton, T.; Khater, M.; Kamlapurkar, S.; Engelmann, S.; Fortier, P.; Boyer, N.; et al. Integrated Metamaterial Interfaces for Self-Aligned Fiber-to-Chip Coupling in Volume Manufacturing. *IEEE J. Select. Topics Quantum Electron.* **2019**, *25*, 1–13, doi:10.1109/JSTQE.2018.2879018.
134. Van Laere, F.; Bogaerts, W.; Taillaert, D.; Dumon, P.; Van Thourhout, D.; Baets, R. Compact Focusing Grating Couplers Between Optical Fibers and Silicon-on-Insulator Photonic Wire Waveguides. In Proceedings of the OFC/NFOEC 2007 - 2007 Conference on Optical Fiber Communication and the National Fiber Optic Engineers Conference; IEEE: Anaheim, CA, USA, March 2007; pp. 1–3.
135. Schmid, B.; Petrov, A.; Eich, M. Optimized Grating Coupler with Fully Etched Slots. **2009**.
136. Antelius, M.; Gylfason, K.B.; Sohlström, H. An Apodized SOI Waveguide-to-Fiber Surface Grating Coupler for Single

Lithography Silicon Photonics. *Opt. Express* **2011**, *19*, 3592, doi:10.1364/OE.19.003592.
137. Chen, X.; Li, C.; Fung, C.K.Y.; Lo, S.M.G.; Tsang, H.K. Apodized Waveguide Grating Couplers for Efficient Coupling to Optical Fibers. *IEEE Photon. Technol. Lett.* **2010**, *22*, 1156–1158, doi:10.1109/LPT.2010.2051220.
138. Letzkus, F.; Zaoui, W.S.; Berroth, M.; Kunze, A.; Vogel, W.; Butschke, J. CMOS-Compatible Nonuniform Grating Coupler with 86% Coupling Efficiency. In Proceedings of the 39th European Conference and Exhibition on Optical Communication (ECOC 2013); Institution of Engineering and Technology: London, UK, 2013; pp. 21–23.
139. Zhou, X.; Tsang, H.K. Photolithography Fabricated Sub-Decibel High-Efficiency Silicon Waveguide Grating Coupler. *IEEE Photon. Technol. Lett.* **2023**, *35*, 43–46, doi:10.1109/LPT.2022.3221527.
140. Schrauwen, J.; Van Laere, F.; Van Thourhout, D.; Baets, R. Focused-Ion-Beam Fabrication of Slanted Grating Couplers in Silicon-on-Insulator Waveguides. *IEEE Photon. Technol. Lett.* **2007**, *19*, 816–818, doi:10.1109/LPT.2007.897293.
141. Benedikovic, D.; Alonso-Ramos, C.; Cheben, P.; Schmid, J.H.; Wang, S.; Xu, D.-X.; Lapointe, J.; Janz, S.; Halir, R.; Ortega-Moñux, A.; et al. High-Directionality Fiber-Chip Grating Coupler with Interleaved Trenches and Subwavelength Index-Matching Structure. *Opt. Lett.* **2015**, *40*, 4190, doi:10.1364/OL.40.004190.
142. Zhou, Z.; Drabik, T.J. Optimized Binary, Phase-Only, Diffractive Optical Element with Subwavelength Features for 1.55 Um. *Journal of the Optical Society of America* **1995**, *12*, doi:10.1364/JOSAA.12.001104.
143. Ang, T.W.; Reed, G.T.; Vonsovici, A.; Evans, A.G.R.; Routley, P.R.; Josey, M.R. Highly Efficient Unibond Silicon-on-Insulator Blazed Grating Couplers. *Applied Physics Letters* **2000**, *77*, 4214–4216, doi:10.1063/1.1334910.
144. Wang, B.; Jiang, J.; Nordin, G.P. Systematic Design Process for Slanted Grating Couplers. *Appl. Opt.* **2006**, *45*, 6223, doi:10.1364/AO.45.006223.
145. Wang, B.; Jiang, J.; Nordin, G.P. Compact Slanted Grating Couplers. *Opt. Express* **2004**, *12*, 3313, doi:10.1364/OPEX.12.003313.

146. Benedikovic, D.; Cassan, E.; Baudot, C.; Boeuf, F.; Vivien, L.; Alonso-Ramos, C.; Guerber, S.; Perez-Galacho, D.; Le Roux, X.; Vakarin, V.; et al. Sub-Decibel Off-Chip Fiber Couplers Based on L-Shaped Waveguides and Subwavelength Grating Metamaterials. In Proceedings of the 2019 IEEE 16th International Conference on Group IV Photonics (GFP); IEEE: Singapore, Singapore, August 2019; pp. 1–2.
147. Benedikovic, D.; Alonso-Ramos, C.; Pérez-Galacho, D.; Guerber, S.; Vakarin, V.; Marcaud, G.; Le Roux, X.; Cassan, E.; Marris-Morini, D.; Cheben, P.; et al. L-Shaped Fiber-Chip Grating Couplers with High Directionality and Low Reflectivity Fabricated with Deep-UV Lithography. *Opt. Lett.* **2017**, *42*, 3439, doi:10.1364/OL.42.003439.
148. Watanabe, T.; Ayata, M.; Koch, U.; Fedoryshyn, Y.; Leuthold, J. Perpendicular Grating Coupler Based on a Blazed Antiback-Reflection Structure. *J. Lightwave Technol.* **2017**, *35*, 4663–4669, doi:10.1109/JLT.2017.2755673.
149. Chen, X.; Thomson, D.J.; Crudginton, L.; Khokhar, A.Z.; Reed, G.T. Dual-Etch Apodised Grating Couplers for Efficient Fibre-Chip Coupling near 1310 Nm Wavelength. *Opt. Express* **2017**, *25*, 17864, doi:10.1364/OE.25.017864.
150. Melati, D.; Grinberg, Y.; Kamandar Dezfouli, M.; Janz, S.; Cheben, P.; Schmid, J.H.; Sánchez-Postigo, A.; Xu, D.-X. Mapping the Global Design Space of Nanophotonic Components Using Machine Learning Pattern Recognition. *Nat Commun* **2019**, *10*, 4775, doi:10.1038/s41467-019-12698-1.
151. Kamandar Dezfouli, M.; Grinberg, Y.; Melati, D.; Cheben, P.; Schmid, J.H.; Sánchez-Postigo, A.; Ortega-Moñux, A.; Wangüemert-Pérez, G.; Cheriton, R.; Janz, S.; et al. Perfectly Vertical Surface Grating Couplers Using Subwavelength Engineering for Increased Feature Sizes. *Opt. Lett.* **2020**, *45*, 3701, doi:10.1364/OL.395292.
152. Vitali, V.; Domínguez Bucio, T.; Lacava, C.; Marchetti, R.; Mastronardi, L.; Rutirawut, T.; Churchill, G.; Faneca, J.; Gates, J.C.; Gardes, F.; et al. High-Efficiency Reflector-Less Dual-Level Silicon Photonic Grating Coupler. *Photon. Res.* **2023**, *11*, 1275, doi:10.1364/PRJ.488970.

153. Guo, R.; Zhang, S.; Gao, H.; Senthil Murugan, G.; Liu, T.; Cheng, Z. Blazed Subwavelength Grating Coupler. *Photon. Res.* **2023**, *11*, 189, doi:10.1364/PRJ.474199.
154. Fan, M.; Popovic, M.A.; Kartner, F.X. High Directivity, Vertical Fiber-to-Chip Coupler with Anisotropically Radiating Grating Teeth. In Proceedings of the 2007 Conference on Lasers and Electro-Optics (CLEO); IEEE: Baltimore, MD, USA, May 2007; pp. 1–2.
155. Alonso-Ramos, C.; Cheben, P.; Ortega-Moñux, A.; Schmid, J.H.; Xu, D.-X.; Molina-Fernández, I. Fiber-Chip Grating Coupler Based on Interleaved Trenches with Directionality Exceeding 95%. *Opt. Lett.* **2014**, *39*, 5351, doi:10.1364/OL.39.005351.
156. Benedikovic, D.; Alonso-Ramos, C.; Cheben, P.; Schmid, J.H.; Wang, S.; Xu, D.-X.; Halir, R.; Ortega-Monux, A.; Fedeli, J.-M.; Janz, S.; et al. First Experimental Demonstration of High-Directionality Fiber-Chip Grating Coupler with Interleaved Trenches. In Proceedings of the 2015 IEEE 12th International Conference on Group IV Photonics (GFP); IEEE: Vancouver, BC, Canada, August 2015; pp. 203–204.
157. Michaels, A.; Yablonovitch, E. Inverse Design of near Unity Efficiency Perfectly Vertical Grating Couplers. *Opt. Express* **2018**, *26*, 4766, doi:10.1364/OE.26.004766.
158. Mekis, A.; Gloeckner, S.; Masini, G.; Narasimha, A.; Pinguet, T.; Sahni, S.; De Dobbelaere, P. A Grating-Coupler-Enabled CMOS Photonics Platform. *IEEE J. Select. Topics Quantum Electron.* **2011**, *17*, 597–608, doi:10.1109/JSTQE.2010.2086049.
159. Roelkens, G.; Thourhout, D.V.; Baets, R. High Efficiency Grating Coupler between Silicon-on-Insulator Waveguides and Perfectly Vertical Optical Fibers. *Opt. Lett.* **2007**, *32*, 1495, doi:10.1364/OL.32.001495.
160. Wang, Y.; Wang, X.; Flueckiger, J.; Yun, H.; Shi, W.; Bojko, R.; Jaeger, N.A.F.; Chrostowski, L. Focusing Sub-Wavelength Grating Couplers with Low Back Reflections for Rapid Prototyping of Silicon Photonic Circuits. *Opt. Express* **2014**, *22*, 20652, doi:10.1364/OE.22.020652.
161. Hoffmann, J.; Schulz, K.M.; Pitruzzello, G.; Fohrmann, L.S.; Petrov, A.Yu.; Eich, M. Backscattering Design for a Focusing Grating

Coupler with Fully Etched Slots for Transverse Magnetic Modes. *Sci Rep* **2018**, *8*, 17746, doi:10.1038/s41598-018-36082-z.
162. Li, Y.; Vermeulen, D.; De Koninck, Y.; Yurtsever, G.; Roelkens, G.; Baets, R. Compact Grating Couplers on Silicon-on-Insulator with Reduced Backreflection. *Opt. Lett.* **2012**, *37*, 4356, doi:10.1364/OL.37.004356.
163. Song, J.H.; Rottenberg, X. Low-Back-Reflection Grating Couplers Using Asymmetric Grating Trenches. *IEEE Photon. Technol. Lett.* **2017**, *29*, 389–392, doi:10.1109/LPT.2017.2650558.
164. Zou, J.; Zhang, Y.; Hu, J.; Wang, C.; Zhang, M.; Le, Z. Grating Coupler With Reduced Back Reflection Using λ /4 Offset at Its Grating Sub-Teeth. *J. Lightwave Technol.* **2019**, *37*, 1195–1199, doi:10.1109/JLT.2018.2889863.
165. Vermeulen, D.; De Koninck, Y.; Li, Y.; Lambert, E.; Bogaerts, W.; Baets, R.; Roelkens, G. Reflectionless Grating Coupling for Silicon-on-Insulator Integrated Circuits. In Proceedings of the 8th IEEE International Conference on Group IV Photonics; IEEE: London, September 2011; pp. 74–76.
166. Vermeulen, D.; De Koninck, Y.; Li, Y.; Lambert, E.; Bogaerts, W.; Baets, R.; Roelkens, G. Reflectionless Grating Couplers for Silicon-on-Insulator Photonic Integrated Circuits. *Opt. Express* **2012**, *20*, 22278, doi:10.1364/OE.20.022278.
167. Song, J.H.; Snyder, B.; Lodewijks, K.; Jansen, R.; Rottenberg, X. Grating Coupler Design for Reduced Back-Reflections. *IEEE Photon. Technol. Lett.* **2018**, *30*, 217–220, doi:10.1109/LPT.2017.2783759.
168. Halir, R.; Cheben, P.; Schmid, J.H.; Ma, R.; Bedard, D.; Janz, S.; Xu, D.-X.; Densmore, A.; Lapointe, J.; Molina-Fernández, Í. Continuously Apodized Fiber-to-Chip Surface Grating Coupler with Refractive Index Engineered Subwavelength Structure. *Opt. Lett.* **2010**, *35*, 3243, doi:10.1364/OL.35.003243.
169. Ding, Y.; Ou, H.; Peucheret, C. Ultrahigh-Efficiency Apodized Grating Coupler Using Fully Etched Photonic Crystals. *Opt. Lett.* **2013**, *38*, 2732, doi:10.1364/OL.38.002732.
170. Benedikovic, D.; Alonso-Ramos, C.; Cheben, P.; Schmid, J.H.; Wang, S.; Halir, R.; Ortega-Moñux, A.; Xu, D.-X.; Vivien, L.; Lapointe, J.; et al. Single-Etch Subwavelength Engineered Fiber-Chip

Grating Couplers for 13 Mm Datacom Wavelength Band. *Opt. Express* **2016**, *24*, 12893, doi:10.1364/OE.24.012893.
171. Xu, X.; Subbaraman, H.; Covey, J.; Kwong, D.; Hosseini, A.; Chen, R.T. Complementary Metal–Oxide–Semiconductor Compatible High Efficiency Subwavelength Grating Couplers for Silicon Integrated Photonics. *Applied Physics Letters* **2012**, *101*, 031109, doi:10.1063/1.4737412.
172. Xia Chen; Tsang, H.K. Nanoholes Grating Couplers for Coupling Between Silicon-on-Insulator Waveguides and Optical Fibers. *IEEE Photonics J.* **2009**, *1*, 184–190, doi:10.1109/JPHOT.2009.2031685.
173. Liu, L.; Pu, M.; Yvind, K.; Hvam, J.M. High-Efficiency, Large-Bandwidth Silicon-on-Insulator Grating Coupler Based on a Fully-Etched Photonic Crystal Structure. *Applied Physics Letters* **2010**, *96*, 051126, doi:10.1063/1.3304791.
174. Taillaert, D.; Bienstman, P.; Baets, R. Compact Efficient Broadband Grating Coupler for Silicon-on-Insulator Waveguides. *Opt. Lett.* **2004**, *29*, 2749, doi:10.1364/OL.29.002749.
175. Marchetti, R.; Lacava, C.; Khokhar, A.; Chen, X.; Cristiani, I.; Richardson, D.J.; Reed, G.T.; Petropoulos, P.; Minzioni, P. High-Efficiency Grating-Couplers: Demonstration of a New Design Strategy. *Sci Rep* **2017**, *7*, 16670, doi:10.1038/s41598-017-16505-z.
176. Yang, J.S.; O, B.-H.; Hong, S.H.; Lee, S.G.; Park, S.-G.; Kim, J.-H.; Chung, D.-J.; Chang, S.-P.; Lee, E.-H. Novel Grating Design for Out-of-Plane Coupling With Nonuniform Duty Cycle. *IEEE Photon. Technol. Lett.* **2008**, *20*, 730–732, doi:10.1109/LPT.2008.921083.
177. Sobu, Y.; Jeong, S.-H.; Tanaka, Y.; Morito, K. 300-Mm ArF-Immersion Lithographytechnology Based Si-Wire Grating Couplers with High Coupling Efficiency and Low Crosstalk. 3.
178. Zhao, Z.; Fan, S. Design Principles of Apodized Grating Couplers. *J. Lightwave Technol.* **2020**, *38*, 4435–4446, doi:10.1109/JLT.2020.2992574.
179. Li, C.; Chee, K.S.; Tao, J.; Zhang, H.; Yu, M.; Lo, G.Q. Silicon Photonics Packaging with Lateral Fiber Coupling to Apodized Grating Coupler Embedded Circuit. *Opt. Express* **2014**, *22*, 24235, doi:10.1364/OE.22.024235.
180. Tang, Y.; Wang, Z.; Wosinski, L.; Westergren, U.; He, S. Highly Efficient Nonuniform Grating Coupler for Silicon-on-Insulator

Nanophotonic Circuits. *Opt. Lett.* **2010**, *35*, 1290, doi:10.1364/OL.35.001290.
181. Fowler, D.; Grosse, P.; Gays, F.; Szelag, B.; Baudot, C.; Vuillet, N.; Planchot, J.; Boeuf, F. Fiber Grating Coupler Development for Si-Photonics Process Design Kits at CEA-LETI. In Proceedings of the Smart Photonic and Optoelectronic Integrated Circuits XXI; Lee, E.-H., He, S., Eds.; SPIE: San Francisco, United States, March 4 2019; p. 4.
182. Xu, J.; Jin, X.; Zhao, Y. Apodized Fully-Etched Surface Grating Coupler Using Subwavelength Structure for Standard Silicon-on-Insulator Waveguide. *Opt Quant Electron* **2017**, *49*, 158, doi:10.1007/s11082-017-0997-4.
183. Corning® SMF-28® ULL Optical Fiber.
184. APC Connectors and Adapters (Corning).
185. Halir, R.; Cheben, P.; Janz, S.; Xu, D.-X.; Molina-Fernández, Í.; Wangüemert-Pérez, J.G. Waveguide Grating Coupler with Subwavelength Microstructures. *Opt. Lett.* **2009**, *34*, 1408, doi:10.1364/OL.34.001408.
186. Mack, C.A. Corner Rounding and Line-End Shortening in Optical Lithography.; Mack, C.A., Yuan, X., Eds.; Singapore, Singapore, October 20 2000; pp. 83–92.
187. Snyder, B.; O'Brien, P. Packaging Process for Grating-Coupled Silicon Photonic Waveguides Using Angle-Polished Fibers. *IEEE Trans. Compon., Packag. Manufact. Technol.* **2013**, *3*, 954–959, doi:10.1109/TCPMT.2012.2237052.
188. Khalighi, M.A.; Uysal, M. Survey on Free Space Optical Communication: A Communication Theory Perspective. *IEEE Commun. Surv. Tutorials* **2014**, *16*, 2231–2258, doi:10.1109/COMST.2014.2329501.
189. Kaushal, H.; Kaddoum, G. Free Space Optical Communication: Challenges and Mitigation Techniques. **2015**.
190. Henniger, H.; Wilfert, O. An Introduction to Free-Space Optical Communications. **2010**, *19*.
191. Kaushal, H.; Jain, V.K.; Kar, S. Overview of Wireless Optical Communication Systems. In *Free Space Optical Communication*; Optical Networks; Springer India: New Delhi, 2017; pp. 1–39 ISBN 978-81-322-3689-4.

192. Bloom, S.; Korevaar, E.; Schuster, J.; Willebrand, H. Understanding the Performance of Free-Space Optics [Invited]. *J. Opt. Netw.* **2003**, *2*, 178, doi:10.1364/JON.2.000178.
193. Maharjan, N.; Devkota, N.; Kim, B.W. Atmospheric Effects on Satellite–Ground Free Space Uplink and Downlink Optical Transmissions. *Applied Sciences* **2022**, *12*, 10944, doi:10.3390/app122110944.
194. Trichili, A.; Cox, M.A.; Ooi, B.S.; Alouini, M.-S. Roadmap to Free Space Optics. *J. Opt. Soc. Am. B* **2020**, *37*, A184, doi:10.1364/JOSAB.399168.
195. Dios, F.; Rubio, J.A.; Rodríguez, A.; Comerón, A. Scintillation and Beam-Wander Analysis in an Optical Ground Station-Satellite Uplink. *Appl. Opt.* **2004**, *43*, 3866, doi:10.1364/AO.43.003866.
196. Hajjarian, Z.; Fadlullah, J.; Kavehrad, M. MIMO Free Space Optical Communications in Turbid and Turbulent Atmosphere (Invited Paper). *JCM* **2009**, *4*, 524–532, doi:10.4304/jcm.4.8.524-532.
197. Guo, Y.; Guo, Y.; Li, C.; Zhang, H.; Zhou, X.; Zhang, L. Integrated Optical Phased Arrays for Beam Forming and Steering. *Applied Sciences* **2021**, *11*, 4017, doi:10.3390/app11094017.
198. Heck, M.J.R. Highly Integrated Optical Phased Arrays: Photonic Integrated Circuits for Optical Beam Shaping and Beam Steering. *Nanophotonics* **2017**, *6*, 93–107, doi:10.1515/nanoph-2015-0152.
199. Zhao, S.; Chen, J.; Shi, Y. All-Solid-State Beam Steering via Integrated Optical Phased Array Technology. **2022**.
200. Zhang, X.; Kwon, K.; Henriksson, J.; Luo, J.; Wu, M.C. A Large-Scale Microelectromechanical-Systems-Based Silicon Photonics LiDAR. *Nature* **2022**, *603*, 253–258, doi:10.1038/s41586-022-04415-8.
201. Guerber, S.; Fowler, D.; Mollard, L.; Dieppedale, C.; Le Rhun, G.; Hamelin, A.; Faugier-Tovar, J.; Abdoul-Carime, K. Active Optical Phased Array Integrated within a Micro-Cantilever. *Commun Eng* **2024**, *3*, 76, doi:10.1038/s44172-024-00224-1.
202. Frantz, J.A.; Myers, J.D.; Bekele, R.Y.; Spillmann, C.M.; Naciri, J.; Kolacz, J.; Gotjen, H.G.; Nguyen, V.Q.; McClain, C.C.; Brandon Shaw, L.; et al. Chip-Based Nonmechanical Beam Steerer in the Midwave Infrared. *J. Opt. Soc. Am. B* **2018**, *35*, C29, doi:10.1364/JOSAB.35.000C29.

203. Hulme, J.C.; Doylend, J.K.; Heck, M.J.R.; Peters, J.D.; Davenport, M.L.; Bovington, J.T.; Coldren, L.A.; Bowers, J.E. Fully Integrated Hybrid Silicon Two Dimensional Beam Scanner. *Opt. Express* **2015**, *23*, 5861, doi:10.1364/OE.23.005861.
204. Komatsu, K.; Kohno, Y.; Nakano, Y.; Tanemura, T. Large-Scale Monolithic InP-Based Optical Phased Array. *IEEE Photon. Technol. Lett.* **2021**, *33*, 1123–1126, doi:10.1109/LPT.2021.3107277.
205. Chow, C.-W.; Chang, Y.-C.; Kuo, S.-I.; Kuo, P.-C.; Wang, J.-W.; Jian, Y.-H.; Ahmad, Z.; Fu, P.-H.; Shi, J.-W.; Huang, D.-W.; et al. Actively Controllable Beam Steering Optical Wireless Communication (OWC) Using Integrated Optical Phased Array (OPA). *J. Lightwave Technol.* **2023**, *41*, 1122–1128, doi:10.1109/JLT.2022.3206843.
206. Tyler, N.A.; Fowler, D.; Malhouitre, S.; Garcia, S.; Grosse, P.; Rabaud, W.; Szelag, B. SiN Integrated Optical Phased Arrays for Two-Dimensional Beam Steering at a Single near-Infrared Wavelength. *Opt. Express* **2019**, *27*, 5851, doi:10.1364/OE.27.005851.
207. Poulton, C.V.; Byrd, M.J.; Raval, M.; Su, Z.; Li, N.; Timurdogan, E.; Coolbaugh, D.; Vermeulen, D.; Watts, M.R. Large-Scale Silicon Nitride Nanophotonic Phased Arrays at Infrared and Visible Wavelengths. *Opt. Lett.* **2017**, *42*, 21, doi:10.1364/OL.42.000021.
208. Shuai, Y.; Zhou, Z.; Su, H. Toward Practical Optical Phased Arrays through Grating Antenna Engineering. *Photonics* **2023**, *10*, 520, doi:10.3390/photonics10050520.
209. Doylend, J.K.; Heck, M.J.R.; Bovington, J.T.; Peters, J.D.; Coldren, L.A.; Bowers, J.E. Two-Dimensional Free-Space Beam Steering with an Optical Phased Array on Silicon-on-Insulator. *Opt. Express* **2011**, *19*, 21595, doi:10.1364/OE.19.021595.
210. Sun, J.; Timurdogan, E.; Yaacobi, A.; Hosseini, E.S.; Watts, M.R. Large-Scale Nanophotonic Phased Array. *Nature* **2013**, *493*, 195–199, doi:10.1038/nature11727.
211. Kwong, D.; Hosseini, A.; Covey, J.; Zhang, Y.; Xu, X.; Subbaraman, H.; Chen, R.T. On-Chip Silicon Optical Phased Array for Two-Dimensional Beam Steering. 5.
212. Hutchison, D.N.; Sun, J.; Doylend, J.K.; Kumar, R.; Heck, J.; Kim, W.; Phare, C.T.; Feshali, A.; Rong, H. High-Resolution Aliasing-Free Optical Beam Steering. *Optica* **2016**, *3*, 887, doi:10.1364/OPTICA.3.000887.

213. Fatemi, R.; Khachaturian, A.; Hajimiri, A. A Nonuniform Sparse 2-D Large-FOV Optical Phased Array With a Low-Power PWM Drive. *IEEE J. Solid-State Circuits* **2019**, *54*, 1200–1215, doi:10.1109/JSSC.2019.2896767.
214. Chung, S.; Abediasl, H.; Hashemi, H. A Monolithically Integrated Large-Scale Optical Phased Array in Silicon-on-Insulator CMOS. *IEEE J. Solid-State Circuits* **2018**, *53*, 275–296, doi:10.1109/JSSC.2017.2757009.
215. Poulton, C.V.; Yaccobi, A.; Su, Z.; Byrd, M.J.; Watts, M.R. Optical Phased Array with Small Spot Size, High Steering Range and Grouped Cascaded Phase Shifters. In Proceedings of the Advanced Photonics 2016 (IPR, NOMA, Sensors, Networks, SPPCom, SOF); OSA: Vancouver, 2016; p. IW1B.2.
216. Phare, C.T.; Shin, M.C.; Sharma, J.; Ahasan, S.; Krishnaswamy, H.; Lipson, M. Silicon Optical Phased Array with Grating Lobe-Free Beam Formation Over 180 Degree Field of View. In Proceedings of the Conference on Lasers and Electro-Optics; OSA: San Jose, California, 2018; p. SM3I.2.
217. Miller, S.A.; Chang, Y.-C.; Phare, C.T.; Shin, M.C.; Zadka, M.; Roberts, S.P.; Stern, B.; Ji, X.; Mohanty, A.; Jimenez Gordillo, O.A.; et al. Large-Scale Optical Phased Array Using a Low-Power Multi-Pass Silicon Photonic Platform. *Optica* **2020**, *7*, 3, doi:10.1364/OPTICA.7.000003.
218. Liu, Y.; Hu, H. Silicon Optical Phased Array with a 180-Degree Field of View for 2D Optical Beam Steering. *Optica* **2022**, *9*, 903, doi:10.1364/OPTICA.458642.
219. Poulton, C.V.; Yaacobi, A.; Cole, D.B.; Byrd, M.J.; Raval, M.; Vermeulen, D.; Watts, M.R. Coherent Solid-State LIDAR with Silicon Photonic Optical Phased Arrays. *Opt. Lett.* **2017**, *42*, 4091, doi:10.1364/OL.42.004091.
220. Hsu, C.-P.; Li, B.; Solano-Rivas, B.; Gohil, A.R.; Chan, P.H.; Moore, A.D.; Donzella, V. A Review and Perspective on Optical Phased Array for Automotive LiDAR. *IEEE J. Select. Topics Quantum Electron.* **2021**, *27*, 1–16, doi:10.1109/JSTQE.2020.3022948.
221. He, J.; Dong, T.; Xu, Y. Review of Photonic Integrated Optical Phased Arrays for Space Optical Communication. *IEEE Access* **2020**, *8*, 188284–188298, doi:10.1109/ACCESS.2020.3030627.

222. Hsu, C.-Y.; Yiu, G.-Z.; Chang, Y.-C. Free-Space Applications of Silicon Photonics: A Review. *Micromachines* **2022**, *13*, 990, doi:10.3390/mi13070990.
223. Polishuk, A. Communication Performance Analysis of Microsatellites Using an Optical Phased Array Antenna. *Opt. Eng* **2003**, *42*, 2015, doi:10.1117/1.1579491.
224. Fatemi, R.; Abiri, B.; Khachaturian, A.; Hajimiri, A. High Sensitivity Active Flat Optics Optical Phased Array Receiver with a Two-Dimensional Aperture. *Opt. Express* **2018**, *26*, 29983, doi:10.1364/OE.26.029983.
225. Abediasl, H.; Hashemi, H. Monolithic Optical Phased-Array Transceiver in a Standard SOI CMOS Process. *Opt. Express* **2015**, *23*, 6509, doi:10.1364/OE.23.006509.
226. Zhang, Y.; Wang, R.; Liu, H.; Zhao, G.; Wei, M.; Jiang, R.; Du, K. Intensive and Efficient Design of a Two-Dimensional 8 × 8 Silicon-Based Optical Phased Array Transceiver. *Sensors* **2023**, *23*, 9396, doi:10.3390/s23239396.
227. Poulton, C.V.; Byrd, M.J.; Russo, P.; Timurdogan, E.; Khandaker, M.; Vermeulen, D.; Watts, M.R. Long-Range LiDAR and Free-Space Data Communication With High-Performance Optical Phased Arrays. *IEEE J. Select. Topics Quantum Electron.* **2019**, *25*, 1–8, doi:10.1109/JSTQE.2019.2908555.
228. Rhee, H.-W.; You, J.-B.; Yoon, H.; Han, K.; Kim, M.; Lee, B.G.; Kim, S.-C.; Park, H.-H. 32 Gbps Data Transmission With 2D Beam-Steering Using a Silicon Optical Phased Array. *IEEE Photon. Technol. Lett.* **2020**, *32*, 803–806, doi:10.1109/LPT.2020.2998162.
229. Li, Y.; Chen, B.; Na, Q.; Tao, M.; Liu, X.; Zhi, Z.; Peng, T.; Li, X.; Luo, X.; Lo, G.-Q.; et al. High-Data-Rate and Wide-Steering-Range Optical Wireless Communication via Nonuniform-Space Optical Phased Array. *J. Lightwave Technol.* **2023**, *41*, 4933–4940, doi:10.1109/JLT.2023.3252166.
230. Wang, K.; Nirmalathas, A.; Lim, C.; Wong, E.; Alameh, K.; Li, H.; Skafidas, E. High-Speed Indoor Optical Wireless Communication System Employing a Silicon Integrated Photonic Circuit. *Opt. Lett.* **2018**, *43*, 3132, doi:10.1364/OL.43.003132.
231. Kwong, D.; Hosseini, A.; Zhang, Y.; Chen, R.T. 1 × 12 Unequally Spaced Waveguide Array for Actively Tuned Optical Phased Array

on a Silicon Nanomembrane. *Appl. Phys. Lett.* **2011**, *99*, 051104, doi:10.1063/1.3619847.
232. Poulton, C.V. Integrated LIDAR with Optical Phased Arrays in Silicon Photonics.
233. Van Acoleyen, K. Nanophotonic Beamsteering Elements Using Silicon Technology for Wireless Optical Applications, Universiteit Gent, 2012.
234. Van Acoleyen, K.; Bogaerts, W.; Jágerská, J.; Le Thomas, N.; Houdré, R.; Baets, R. Off-Chip Beam Steering with a One-Dimensional Optical Phased Array on Silicon-on-Insulator. *Opt. Lett.* **2009**, *34*, 1477, doi:10.1364/OL.34.001477.
235. Dostart, N.; Zhang, B.; Khilo, A.; Brand, M.; Al Qubaisi, K.; Onural, D.; Feldkhun, D.; Wagner, K.H.; Popović, M.A. Serpentine Optical Phased Arrays for Scalable Integrated Photonic Lidar Beam Steering. *Optica* **2020**, *7*, 726, doi:10.1364/OPTICA.389006.
236. Ashtiani, F.; Aflatouni, F. N × N Optical Phased Array with 2N Phase Shifters. *Opt. Express* **2019**, *27*, 27183, doi:10.1364/OE.27.027183.
237. Aflatouni, F.; Abiri, B.; Rekhi, A.; Hajimiri, A. Nanophotonic Projection System. *Opt. Express* **2015**, *23*, 21012, doi:10.1364/OE.23.021012.
238. Chalupnik, M.; Singh, A.; Leatham, J.; Lončar, M.; Soltani, M. Scalable and Ultralow Power Silicon Photonic Two-Dimensional Phased Array. *APL Photonics* **2023**, *8*, 051305, doi:10.1063/5.0139538.
239. Jiang, R.; Wang, R.; Guo, J.; Liu, H.; Du, K.; Zhang, Y.; Wu, Y.; Li, Y. Design and Analysis of a Two-Dimensional Large-Scale Silicon-Photonic Optical Phased Array. *Optics & Laser Technology* **2022**, *156*, 108551, doi:10.1016/j.optlastec.2022.108551.
240. Zhang, H.; Zhang, Z.; Lv, J.; Peng, C.; Hu, W. Fast Beam Steering Enabled by a Chip-Scale Optical Phased Array with 8 × 8 Elements. *Optics Communications* **2020**, *461*, 125267, doi:10.1016/j.optcom.2020.125267.
241. Zhang, Y.; Wang, R.; Wei, M.; Zhao, G.; Jiang, R.; Du, K. Design of High-Efficiency and Large-Field Silicon-Based Transceiver Integrated Optical Phased Array. *Optics & Laser Technology* **2024**, *171*, 110421, doi:10.1016/j.optlastec.2023.110421.

242. Komljenovic, T.; Helkey, R.; Coldren, L.; Bowers, J.E. Sparse Aperiodic Arrays for Optical Beam Forming and LIDAR. *Opt. Express* **2017**, *25*, 2511, doi:10.1364/OE.25.002511.
243. Yang, B.; Chen, H.; Yang, S.; Chen, M. An Improved Aperiodic OPA Design Based on Large Antenna Spacing. *Optics Communications* **2020**, *475*, 125852, doi:10.1016/j.optcom.2020.125852.
244. Zhang, F.; Zhang, D.; Pan, S. Fast and Wide-Range Optical Beam Steering with Ultralow Side Lobes by Applying an Optimized Multi-Circular Optical Phased Array. *Appl. Opt.* **2018**, *57*, 4977, doi:10.1364/AO.57.004977.
245. Zeng, S.; Zhang, Y.; Zhu, J.; Wu, Z.; Chen, Y.; Yu, S. 360° on Chip Optical Beam Steering Based on Superposition of Planar Spiral Orbital Angular Momentum Waves. In Proceedings of the 2019 Conference on Lasers and Electro-Optics Europe & European Quantum Electronics Conference (CLEO/Europe-EQEC); IEEE: Munich, Germany, June 2019; pp. 1–1.
246. Liu, Q.; Benedikovic, D.; Smy, T.; Atieh, A.; Cheben, P.; Ye, W.N. Circular Optical Phased Arrays with Radial Nano-Antennas. *Nanomaterials* **2022**, *12*, 1938, doi:10.3390/nano12111938.
247. Benedikovič, D.; Liu, Q.; Sánchez-Postigo, A.; Atieh, A.; Smy, T.; Cheben, P.; Ye, W.N. Circular Optical Phased Array with Large Steering Range and High Resolution. *Sensors* **2022**, *22*, 6135, doi:10.3390/s22166135.
248. Sylvain Guerber; Daivid Fowler; Ismael Charlet; Philippe Grosse; Kim Abdoul-Carime; Jonathan Faugier-Tovar; Bertrand Szelag Development, Calibration and Characterization of Silicon Photonics Based Optical Phased Arrays.; March 5 2021; Vol. 11690, p. 1169006.
249. Kim, S.; Westly, D.A.; Roxworthy, B.J.; Li, Q.; Yulaev, A.; Srinivasan, K.; Aksyuk, V.A. Photonic Waveguide to Free-Space Gaussian Beam Extreme Mode Converter. *Light Sci Appl* **2018**, *7*, 72, doi:10.1038/s41377-018-0073-2.
250. Luque-González, J.M.; Halir, R.; Wangüemert-Pérez, J.G.; de-Oliva-Rubio, J.; Schmid, J.H.; Cheben, P.; Molina-Fernández, Í.; Ortega-Moñux, A. An Ultracompact GRIN-Lens-Based Spot Size Converter Using Subwavelength Grating Metamaterials. *Laser*

& *Photonics Reviews* **2019**, *13*, 1900172, doi:10.1002/lpor.201900172.
251. Abbaslou, S.; Gatdula, R.; Lu, M.; Stein, A.; Jiang, W. Ultra-Short Beam Expander with Segmented Curvature Control: The Emergence of a Semi-Lens. *Opt. Lett.* **2017**, *42*, 4383, doi:10.1364/OL.42.004383.
252. Asaduzzaman, M.; Bakaul, M.; Skafidas, E.; Khandokar, M.R.H. A Compact Silicon Grating Coupler Based on Hollow Tapered Spot-Size Converter. *Sci Rep* **2018**, *8*, 2540, doi:10.1038/s41598-018-20875-3.
253. Li, D.; Liu, Y.; Song, Q.; Du, J.; Xu, K. Millimeter-Long Silicon Photonic Antenna for Optical Phased Arrays at 2-Mm Wavelength Band. *IEEE Photonics J.* **2021**, *13*, 1–7, doi:10.1109/JPHOT.2021.3059844.
254. Yu, L.; Ma, P.; Luo, G.; Cui, L.; Zhou, X.; Wang, P.; Zhang, Y.; Pan, J. Adoption of Large Aperture Chirped Grating Antennas in Optical Phase Array for Long Distance Ranging. *Opt. Express* **2022**, *30*, 28112, doi:10.1364/OE.464358.
255. Chen, J.; Wang, J.; Li, J.; Yao, Y.; Sun, Y.; Tian, J.; Zou, Y.; Zhao, X.; Xu, X. Subwavelength Structure Enabled Ultra-Long Waveguide Grating Antenna. *Opt. Express* **2021**, *29*, 15133, doi:10.1364/OE.421529.
256. Ginel-Moreno, P.; Pereira-Martín, D.; Hadij-ElHouati, A.; Ye, W.N.; Melati, D.; Xu, D.-X.; Janz, S.; Ortega-Moñux, A.; Wangüemert-Pérez, J.G.; Halir, R.; et al. Highly Efficient Optical Antenna with Small Beam Divergence in Silicon Waveguides. *Opt. Lett.* **2020**, *45*, 5668, doi:10.1364/OL.404012.
257. Seo, D.-J.; Ryu, H.-Y. Accurate Simulation of a Shallow-Etched Grating Antenna on Silicon-on-Insulator for Optical Phased Array Using Finite-Difference Time-Domain Methods. *Current Optics and Photonics* **2019**, *3*, 522–530, doi:10.3807/COPP.2019.3.6.522.
258. Guerber, S.; Fowler, D.; Virot, L. PHASED-GRATING-ANTENNA-ARRAY OPTOELECTRONIC EMITTER IN WHICH EACH OPTICAL ANTENNA HAS A LARGE EMISSION AREA 2023.
259. Bock, P.J.; Cheben, P.; Delâge, A.; Schmid, J.H.; Xu, D.-X.; Janz, S.; Hall, T.J. Demultiplexer with Blazed Waveguide Sidewall Grating and Sub-Wavelength Grating Structure. **2008**, 10.

260. Bock, P.J.; Cheben, P.; Schmid, J.H.; Velasco, A.V.; Delâge, A.; Janz, S.; Xu, D.-X.; Lapointe, J.; Hall, T.J.; Calvo, M.L. Demonstration of a Curved Sidewall Grating Demultiplexer on Silicon. *Opt. Express* **2012**, *20*, 19882, doi:10.1364/OE.20.019882.
261. Ginel-Moreno, P.; Hadij-ElHouati, A.; Sánchez-Postigo, A.; Wangüemert-Pérez, J.G.; Molina-Fernández, Í.; Schmid, J.H.; Cheben, P.; Ortega-Moñux, A. Metamaterial Antenna Array Fed by Distributed Bragg Deflector for Beam Steering on SOI Platform. In Proceedings of the 2023 IEEE Silicon Photonics Conference (SiPhotonics); IEEE: Washington, DC, USA, April 2023; pp. 1–2.
262. Hadij-ElHouati, A.; Cheben, P.; Ortega-Moñux, A.; Wangüemert-Pérez, J.G.; Halir, R.; Schmid, J.H.; Molina-Fernández, Í. Distributed Bragg Deflector Coupler for On-Chip Shaping of Optical Beams. *Opt. Express* **2019**, *27*, 33180, doi:10.1364/OE.27.033180.
263. Stoll, H.M. Distributed Bragg Deflector: A Multifunctional Integrated Optical Device. *Appl. Opt.* **1978**, *17*, 2562, doi:10.1364/AO.17.002562.
264. Davis, R.L.; Long, W.; Wang, C.-J.; Lam, T.; Ho, J.G.; Nachman, P.M.; Poylio, J.; Mishechkin, O.V.; Fallahi, M. Distributed Bragg Deflectors Fabricated in Sol-Gel Based Waveguides. *IEEE Photon. Technol. Lett.* **2004**, *16*, 464–466, doi:10.1109/LPT.2003.821255.
265. Houati, A.H.E. Highly efficient distributed Bragg deflectors for silicon photonic waveguide devices.
266. Hadij-ElHouati, A.; Cheben, P.; Ortega-Moñux, A.; Wangüemert-Pérez, J.G.; Halir, R.; de-Oliva-Rubio, J.; Schmid, J.H.; Molina-Fernández, I. High-Efficiency Conversion from Waveguide Mode to an on-Chip Beam Using a Metamaterial Engineered Bragg Deflector. *Opt. Lett.* **2021**, *46*, 2409, doi:10.1364/OL.420993.
267. Zhang, Y.; Ling, Y.-C.; Zhang, K.; Gentry, C.; Sadighi, D.; Whaley, G.; Colosimo, J.; Suni, P.; Ben Yoo, S.J. Sub-Wavelength-Pitch Silicon-Photonic Optical Phased Array for Large Field-of-Regard Coherent Optical Beam Steering. *Opt. Express* **2019**, *27*, 1929, doi:10.1364/OE.27.001929.
268. Kut King Kan, W.; Guerber, S.; Garcia, S.; Fowler, D.; Alonso-Ramos, C. Antenna for a Two-Dimensional Integrated Optical Phased Array Designed for Optical Wireless Communications.; Eindhoven, Netherlands, December 2023.

269. Zhang, X.; Zhou, H.; Ge, Z.; Vaid, A.; Konduparthi, D.; Osorio, C.; Ventola, S.; Meir, R.; Shoval, O.; Kris, R.; et al. Addressing FinFET Metrology Challenges in 1× Node Using Tilt-Beam Critical Dimension Scanning Electron Microscope. *J. Micro/Nanolith. MEMS MOEMS* **2014**, *13*, 041407, doi:10.1117/1.JMM.13.4.041407.
270. Van Kessel, L.; Huisman, T.; Hagen, C.W. Understanding the Influence of Three-Dimensional Sidewall Roughness on Observed Line-Edge Roughness in Scanning Electron Microscopy Images. *J. Micro/Nanolith. MEMS MOEMS* **2020**, *19*, doi:10.1117/1.JMM.19.3.034002.

9 LIST OF PUBLICATIONS

International Journal Papers

[1] Vakarin, V.; Melati, D.; Dinh, T.T.D.; Le Roux, X.; Kut King Kan, W.; Dupré, C.; Szelag, B.; Monfray, S.; Boeuf, F.; Cheben, P.; et al. Metamaterial-Engineered Silicon Beam Splitter Fabricated with Deep UV Immersion Lithography. *Nanomaterials* **2021**, *11*, 2949, doi:10.3390/nano11112949

International Conference Papers

[1] Kut King Kan, W.; Toxqui-Rodriguez, S.; Medina-Quiroz, D.; Nuño-Ruano, P.; Melati, D.; Cassan, E.; Marris-Morini, D.; Vivien, L.; Cheben, P.; Adelmini, L.; et al. 2x2 Ultra-Broadband Multimode Interference Coupler with Subwavelength Gratings Fabricated by Immersion Lithography. In Proceedings of the 2023 Photonics North (PN); IEEE: Montreal, QC, Canada, June 12 2023; pp. 1–1

[2] Kut King Kan, W.; Guerber, S.; Garcia, S.; Fowler, D.; Alonso-Ramos, C. Antenna for a Two-Dimensional Integrated Optical Phased Array Designed for Optical Wireless Communications.; Eindhoven, Netherlands, December 2023.